UNIVERSITY OF ILLINOIS AT CHICAGO

Final Technical Report: Continued Development of the AF/SGR "Tricorder" Program – Laser Eye Protection, Biomarkers of Laser Injury, and Sensor Development

Final Technical Report

Reporting Period: 30 September 2007 – 28 March 2012

Prepared for:
DEPARTMENT OF THE AIR FORCE
Office of the Surgeon General
5201 Leesburg Pike, Suite 1501
Falls Church VA 22041

Contract Number:
FA7014-07-C-0047

Submitted by:
Dr. Larry Danziger, Executive Director (CADRE)
312-413-9811 e-mail: danziger@uic.edu

UNCLASSIFIED

REPORT DOCUMENTATION PAGE

Form Approved
OMB No. 0704-0188

1. REPORT DATE *(DD-MM-YYYY)*
05/15/2012

2. REPORT TYPE
Final Technical Report

3. DATES COVERED *(From - To)*
09/30/2007-03/28/2012

4. TITLE AND SUBTITLE
Final Technical Report: Continued Development of the AF/SGR "Tricorder" Program – Laser Eye Protection, Biomarkers of Laser Injury and Sensor Development

5a. CONTRACT NUMBER
FA7014-07-C-0047

5b. GRANT NUMBER

5c. PROGRAM ELEMENT NUMBER

6. AUTHOR(S)
Dr. Larry Danziger, Ms. Melissa Naiman, Dr. Luke Hanley, Dr. Igor Gavin, Dr. Robert Gordon, Dr. Richard Preston, Dr. Preston Snee, Dr. Mitra Dutta, Dr. Andrew Boyd, Dr. Annette Valenta

5d. PROJECT NUMBER

5e. TASK NUMBER

5f. WORK UNIT NUMBER

7. PERFORMING ORGANIZATION NAME(S) AND ADDRESS(ES)
Center for Advanced Design Research and Exploration (CADRE)
University of Illinois - Chicago (UIC)
1737 W. Polk Street, B14 AOB, MC 800
Chicago, IL 60612

8. PERFORMING ORGANIZATION REPORT NUMBER

9. SPONSORING/MONITORING AGENCY NAME(S) AND ADDRESS(ES)
DEPARTMENT OF THE AIRFORCE
Office of the Surgeon General
5201 Leesburg Pike, Suite 1501
Falls Church VA 22041

10. SPONSOR/MONITOR'S ACRONYM(S)

11. SPONSOR/MONITOR'S REPORT NUMBER(S)

12. DISTRIBUTION/AVAILABILITY STATEMENT
Approved for public release; distribution is unlimited.

13. SUPPLEMENTARY NOTES

14. ABSTRACT

Laser misuse poses a unique challenge to the public health and medical communities. The rapid pace of laser technology development warrants exploratory research into mitigation strategies for emerging laser threats. This report compiles the findings from a multidisciplinary research program to address public health and force health protection capability gaps that emerged as unanticipated laser exposure incidents increased. Research efforts were directed to improve capabilities in three key areas: 1) LEP performance, 2) laser characterization in the field, and 3) laser eye injury diagnosis. Complimentary projects explored other sensing modalities that could be combined with laser characterization.

15. SUBJECT TERMS
Laser, laser eye protection, laser safety, biomarkers, laser injury, laser characterization, molecular beacon, non-linear optical limiting

16. SECURITY CLASSIFICATION OF:			**17. LIMITATION OF ABSTRACT**	**18. NUMBER OF PAGES**	**19a. NAME OF RESPONSIBLE PERSON**
a. REPORT	**b. ABSTRACT**	**c. THIS PAGE**			Larry Danziger, PharmD
Unclassified	Unclassified	Unclassified	UU	200	**19b. TELEPHONE NUMBER** *(Include area code)* 312-413-9811

Table of Contents

ii. Report Documentation Page

Form Approved
OMB No. 0704-0188

1. REPORT DATE *(DD-MM-YYYY)*
28-03-2012

2. REPORT TYPE
Final Technical Report

3. DATES COVERED *(From - To)*
30 September 2007 – 28 March 2012

4. TITLE AND SUBTITLE
Final Technical Report: Continued Development of the AF/SGR "Tricorder" Program - Laser Eye Protection, Biomarkers of Laser Injury, and Sensor Development

5a. CONTRACT NUMBER
FA7014-07-C-0047

5b. GRANT NUMBER

5c. PROGRAM ELEMENT NUMBER

6. AUTHOR(S)
Dr. Larry Danziger
Ms. Melissa Naiman
Dr. Luke Hanley
Dr. Robert Gordon
Dr. Richard Preston
Dr. Timothy Keiderling
Dr. Preston Snee
Dr. Brian Kay
Dr. Igor Gavin
Dr. Mitra Dutta
Dr. Annette Valenta
Dr. Andrew Boyd

5d. PROJECT NUMBER

5e. TASK NUMBER

5f. WORK UNIT NUMBER

7. PERFORMING ORGANIZATION NAME(S) AND ADDRESS(ES)
Center for Advanced Design Research and Exploration (CADRE)
University of Illinois - Chicago (UIC)
1737 W. Polk Street, B14 AOB, MC 800
Chicago, IL 60612

8. PERFORMING ORGANIZATION REPORT NUMBER

9. SPONSORING/MONITORING AGENCY NAME(S) AND ADDRESS(ES)
DEPARTMENT OF THE AIRFORCE
Office of the Surgeon General
5201 Leesburg Pike, Suite 1501
Falls Church VA 22041

10. SPONSOR/MONITOR'S ACRONYM(S)
AF/SGR

11. SPONSORING/MONITORING AGENCY REPORT NUMBER

12. DISTRIBUTION AVAILABILITY STATEMENT
Approved for public release; distribution is unlimited.

13. SUPPLEMENTARY NOTES

14. ABSTRACT

Laser misuse poses a unique challenge to the public health and medical communities. The rapid pace of laser technology development warrants exploratory research into mitigation strategies for emerging laser threats. In 2007, the University of Illinois at Chicago (UIC) embarked on a large-scale, multidisciplinary research program to address public health and force health protection capability gaps that emerged as unanticipated laser exposure incidents increased. Research efforts were directed to improve capabilities in three key areas: 1) LEP performance, 2) laser characterization in the field, and 3) laser eye injury diagnosis. In addition, several projects explored other sensing modalities and targets that might be combined with laser detection and characterization to provide a flexible and diverse tool that would be attractive to the wide range of end users.

15. SUBJECT TERMS
Laser, laser eye protection, laser safety, biomarkers, laser injury, laser characterization, molecular beacon, non-linear optical limiting

16. SECURITY CLASSIFICATION OF:			**17. LIMITATION OF ABSTRACT**	**18. NUMBER OF PAGES**	**19a. NAME OF RESPONSIBLE PERSON**
					Larry Danziger Pharm. D
a. REPORT	**b. ABSTRACT**	**c. THIS PAGE**			**19b. TELEPONE NUMBER** (*Include area code*)
Unclassified	Unclassified	Unclassified			312-413-9811

iii. Abstract

Laser misuse poses a unique challenge to the public health and medical communities. At this time there is limited data to quantify the full scope and severity of this threat. However, it is generally accepted among many stakeholders from a variety of backgrounds that laser misuse, and therefore laser exposure, is likely to increase in the future. The rapid pace of laser technology development warrants exploratory research into mitigation strategies for emerging laser threats. In 2007, the University of Illinois at Chicago (UIC) embarked on a large-scale, multidisciplinary research program to address public health and force health protection capability gaps that emerged as unanticipated laser exposure incidents increased. Research efforts were directed to improve capabilities in three key areas: 1) LEP performance, 2) laser characterization in the field, and 3) laser eye injury diagnosis. In addition, several projects explored other sensing modalities and targets that might be combined with laser detection and characterization to provide a flexible and diverse tool that would be attractive to the wide range of end users.

iv. List of Figures and Tables

Figures

Tables

A. Program Overview and Management

1. Introduction

As laser technology becomes more sophisticated, powerful, affordable, and portable, it will present new challenges to the public health and medical communities. Lasers are associated with a myriad of beneficial applications but are also increasingly associated with threats to health and safety. Since the Federal Aviation Administration initiated mandatory laser incident reporting in 2005, the number of recorded incidents in the United States has increased every year [1]. There were 2,587 aircraft illumination events recorded by the Federal Aviation Administration between 2004 and 2008 [2]. Pilots are not the only population affected by the misuse of lasers. There are documented cases of eye injury among teens and young adults following exposure during recreational laser light shows [3] and experimentation with high power laser pointers [4]. Military personnel assigned to a checkpoint were injured by laser “dazzlers” [5]. Law enforcement officials have expressed concerns that lasers will become increasingly attractive to terrorists and criminal actors due to a combination of factors: the relative ease of procurement, potential to cause damage (both to health and property), and the lack of forensic techniques capable of tying a specific laser to an incident [6].

The actual impact of laser misuse on public health is difficult to quantify. Despite popular perceptions of laser injury propagated by science fiction, real-world wounds can be subtle and challenging to diagnose. Currently, lasers pose the greatest risk to ocular tissue. The effective dose of non-ionizing radiation delivered to the eye by a laser will fluctuate based on a variety of environmental, technical, and clinically relevant factors that are likely unknown or not measured at the time of exposure. For example, a patient reporting exposure to a “green” laser would not be able to confirm the exact wavelength, distinguish between pulsed or continuous wave, or estimate the power or fluence of the beam. This information would all be extremely helpful in assessing the likelihood of eye injury. Even if laser eye protection (LEP) is deployed, there are a variety of circumstances in which eye injury can still occur. For example, a pilot wearing LEP could be exposed to a laser with a wavelength that falls outside of the protected range (i.e., out of band) or is so powerful that it defeats the goggle. Minor retinal lesions are not necessarily painful; thus definitive diagnosis of laser injury requires a thorough ophthalmological assessment using specialized equipment. This equipment and expertise may not be readily available to those who require an examination, particularly if the exposure occurred in a remote setting, such as during military operations. In such circumstances, medical personnel must determine whether to evacuate personnel for full assessment (which is possibly unnecessary) or risk further injury by delaying treatment, based on very little data. There are also anecdotal accounts of pilot resistance to eye examinations following possible laser exposure due to concerns about being arbitrarily grounded.

In summary, laser misuse poses a unique challenge to the public health and medical communities. At this time there is limited data to quantify the full scope and severity of this threat. However, it is generally accepted among many stakeholders from a variety of backgrounds that laser misuse, and therefore laser exposure, is likely to increase in the future. The rapid pace of laser technology development warrants exploratory research into mitigation strategies for emerging laser threats. In 2007, the University of Illinois at Chicago (UIC) embarked on a large-scale, multidisciplinary research program to address public health and force health protection capability gaps that emerged as unanticipated laser exposure incidents increased. Research efforts were directed to improve capabilities in three key areas: 1) LEP performance, 2) laser characterization in the field, and 3) laser eye injury diagnosis. In addition, several projects explored other sensing modalities and targets that might be combined with laser detection and characterization to provide a flexible and diverse tool that would be attractive to the wide range of end users. Figure 1 summarizes each project and the interrelationships between research efforts.

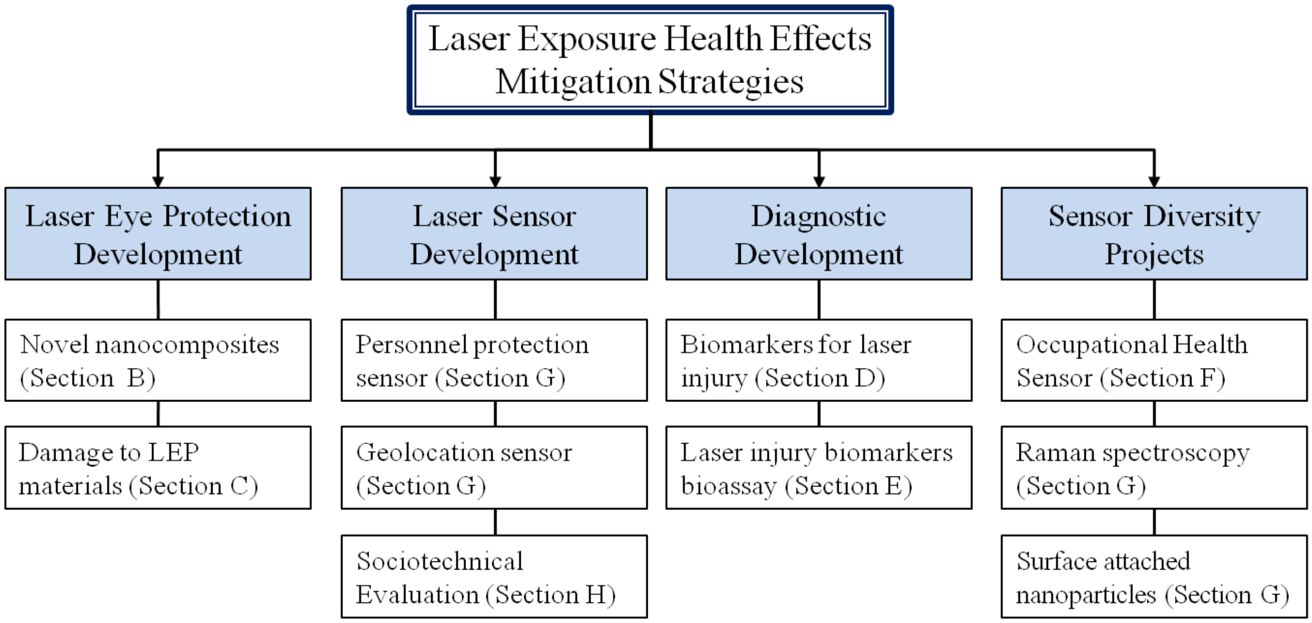

Figure 1. Program overview and project relationships

2. Methods, Assumptions and Procedures

This program was designed from a public health perspective and sought to integrate projects that addressed the full range of health effects associated with unanticipated exposure to lasers (and more broadly direct energy). While protection, detection, and diagnosis were key components of addressing the public health risks associated with laser misuse (whether intentional or accidental), the emerging nature of the threat raised concerns regarding user adoption of any sensor products developed under this effort. In order to address this risk, emphasis was also placed on sociotechnical issues of user acceptance (i.e., reasons users might reject sensors beyond the technical performance). Finally, the complexity of the program warranted the application of formal project management principles throughout the period of performance. Assigning a specific group (the Center for Advanced Design, Research and Exploration) to oversee technical and financial performance allowed greater flexibility in research design and resource allocation over the period of performance, which is outlined in the project reports in the sections that follow.

3. Conclusions

This program has successfully and significantly advanced scientific knowledge and technologic capabilities in the area of directed energy protection. Research in nanocomposites revealed valuable information on the mechanisms by which optical limiting coatings work which will be exploited in next generation protective coatings. New understanding of damage mechanisms caused by femtosecond pulsed lasers was documented. A panel of biomarkers for laser injury was developed, validated, and then translated into a biosensor based on a commercial platform currently in use by the Air Force. Two prototype laser sensors were constructed and evaluated in multiple settings, including a field demonstration with a deployed rescue squadron. Sociotechnical evaluations revealed similarities and differences among user groups for these laser sensors and provided guidance for future development spirals. Detailed performance metrics are provided in the project sections that follow.

4. References

1. *US: 2011 total: 3,591 laser/aircraft incidents*. 2012 [cited 2012 May 2]; Available from: http://www. .com/news/news/other-news_files/76b9d278e1a00ab36eea51cff1c5cab1-244.php.
2. Nakagawara, V., R.W. Montgomery, and K.J. Wood, *The Illumination of Aircraft at Altitude by Laser Beams: A 5-Year Study Period (2004-2008)*. 2010, FAA Civil Aerospace Medical Institute: Washington, DC. p. 1-16.
3. Baldwin, C., *Ravers lose sight at laser show*, in *Reuters*. 2008: Moscow.
4. Wyrsch, S., P.B. Baenninger, and M.K. Schmid, *Retinal Injuries from a Handheld Laser Pointer*. New England Journal of Medicine, 2010. **363**(11): p. 1089-1091.
5. Hambling, D. *Soldiers Blinded, Hospitalized by Laser 'Friendly Fire' (Updated)*. 2009 [cited 2012 February 13]; Available from: http://www.wired.com/dangerroom/2009/03/dont-lase-me-br/.
6. Bunker, R.J., *Terrorists and Laser Weapons Use: An Emergent Threat*. Studies in Conflict & Terrorism, 2008. **31**: p. 434-455.

B. Optical Limiting Nanocomposites for Laser Eye Protection

1. Summary

Eye tissue can be damaged by a wide range of laser wavelengths in the visible spectrum. Laser radiation-eye interactions have been widely studied for decades and the susceptibility of human eye tissue to laser damage is well known [1]. Current laser eye protection (LEP) eyewear can shield against fixed laser wavelengths, but eyewear that continuously shields against all potentially damaging wavelengths at all intensities would also not be transparent, thereby blocking vision. The ideal solution would be agile LEP eyewear, such as that which blocks only high intensity laser radiation across a wide spectrum while allowing low intensity light transmission for vision.

Agile LEP eyewear based upon optical limiters can be designed to block only high intensity laser radiation across a wide spectrum while allowing low intensity light transmission for vision. Optical limiting occurs when a bulk material transmits low light intensities, but blocks a wide spectrum of high intensity radiation and is related to third or higher order nonlinear optical properties.

The results presented here show that both colloidal synthesis and gaseous deposition can be used to prepare metal chalcogenide nanocrystals (nanoparticles) with novel morphology and surface chemistry. Furthermore, it is shown that these nanocomposite materials can be utilized for optical limiters with large nonlinear absorption and scattering coefficients. Surface properties play a dominant role in controlling their nonlinear optical response in the visible region. Post-synthesis washing generated surface lattice defects or free dangling-bonds states quench the radiative emission and stimulate the nonlinear absorption and scattering processes with limiting that approach the human eye damage limit in a day vision goggle configuration.

2. Introduction

The last three decades have seen intense study of a variety of semiconductor nanocrystals which promise unique optical and electronic properties [2]. The synthesis and characterization of semiconductor nanocrystals and nanocomposites composed thereof have garnered much attention due to their potential for nonlinear optical materials, photovoltaics, and other novel technologies. It was determined early in the project that nanocrystals of lead selenide (PbSe), lead sulfide (PbS) and other group IV-VI semiconductors have shown great potential as nonlinear optical materials [3]. These metal chalcogenide nanocrystals have size-tunable bandgaps across the near infrared [3, 4] and large extinction coefficients [5]. Nanoscale PbS films have also been considered as infrared absorbers for photovoltaics incorporating anatase titanium dioxide nanocrystals [6, 7].

Third order nonlinear optical properties been studied for lead chalcogenide nanocrystal systems which were found to exhibit both saturable [8-17] and reverse saturable absorption (RSA) [10, 16, 18-23], depending on the preparation method and laser parameters used.

The large surface to volume ratio of lead chalcogenide nanocrystals and their large excitonic Bohr radii (18 nm for PbS and 46 nm for PbSe) predict that photogenerated carriers will have strong interactions with the nanocrystal surface. Thus, surface properties of lead chalcogenide nanocrystals strongly affect their optical properties [24, 25]. Surface properties, especially those leading to the formation of trap states; have been shown to play important roles in nonlinear optical processes [24-27]. Site-substituted impurities, lattice distortion, and defects [26, 28-30] that exist at the surface have an effect on the properties of traps states. Differences in these properties and their effect on the nanocrystal optical properties have often been studied by examining photoluminescence [28, 31, 32] or band gap relaxation [24, 25, 28, 33, 34].

It has been found that both nanocrystal synthetic procedure and after-synthesis treatment [35, 36] can affect the surface properties of nanocrystals, motivating study of their optical response after synthesis and during various stages of processing. Nanocrystal oxidation specifically, and surface chemistry generally have a strong effect on photovoltaic performance by modulating the surface density of states, charge transfer efficiency, excited state lifetimes, and in other ways that remain poorly understood [37, 38]. It was shown that removing surface oxides (i.e., sulfates) or carboxy-containing ligands (i.e., oleic acid) from the surface of PbS(Se) nanocrystals dramatically improves carrier and/or photovoltaic efficiency [39-44]. Annealing or chemical treatment of nanocrystal-organic composites removes capping ligands and leads to strong enhancements in photovoltaic efficiency (although the absolute photovoltaic efficiency remained low) [44-47]. By contrast, PbS nanocrystal films with oxides at their surface behave as photodetectors rather than photovoltaics [48-50]. Surface passivation of PbS nanocrystals also strongly affects their optical properties [51]. One explanation for this improvement in photovoltaic properties was that ligand exchange passivated charge traps at the nanocrystal surface [39, 40, 52]. It was further argued that lightly oxidized PbS nanocrystals in composite films increased the number of charge traps which lead to higher photoconductivity, presumably by increasing the film capacitance and dropping the film resistance [48-50]. These charge traps exist as surface states on the nanocrystal surface. *Overall, surface chemical tuning of nanocrystals allow control of these charge traps, which in turn affects their photovoltaic properties.*

There are several types of nonlinear optical (NLO) materials that might be utilized for nonlinear absorption, scattering or refraction in power limiting applications. One promising type includes compounds with large RSA involves a unique NLO property of materials in which the cross-section for optical absorption from the excited state is larger than that from the ground state [53]. PbS and PbSe nanocrystals have been demonstrated to display optical limiting under various conditions [10, 18, 19, 54-56]. Other very common types include compounds with two-photon absorption (TPA), for example chalcogenides of cadmium and zinc.

This report examines procedures for synthesizing metal chalcogenide nanocrystals of various shapes and sizes and studies their third order nonlinear optical properties. These nanocrystals were subjected to post-synthesis processing to improve their optical limiting properties.

3. Methods, Assumptions and Procedures

The project was focused on two major synthesis strategies for organic–inorganic nanostructured materials. The first strategy was colloidal synthesis of inorganic nanocrystals with various organic capping agents, which then can mixed with the organic semiconductor. Colloidal synthesis is extremely popular due to its great potential, simplicity, and low cost. Colloidal synthesis controls nanocrystal size, shape, and surface functionality by selection and exchange of ligand capping agents.

The second strategy for formation of inorganic nanostructures within an organic matrix was via gaseous deposition. This *in situ* strategy has several major advantages compared to colloidal synthesis, especially when the nanocrystals are to be incorporated into films for application in photovoltaics or other devices. No separate nanocrystal synthesis step is necessary and no capping agents are required to control nanocrystal size, producing ‘naked’ nanocrystals whose surfaces can be readily modified. Nanocomposite films are produced in a vacuum environment without any solvents, reducing health risks and environmental impacts.

These two synthetic approaches allow an almost infinite number of combinations of inorganic and organic nanostructured materials. New methods of synthesizing PbS, PbSe, and other metal chalcogenides nanocrystals within an organic phase were developed to optimize optical limiting in both films and colloidal solutions with selected post-synthesis treatment. Details of both synthesis procedures are shown in the synthesis section.

It was concluded that various lead salt nanocomposites would be prepared by colloidal synthesis and gaseous deposition, and then evaluated by optical methods at both UIC and at the Air Force Research Laboratory at Wright Patterson Air Force Base in Dayton, OH. These evaluations lead to the experiments whose results are described below.

NPs have been characterized by electron microscopy, UV/Vis absorption, fluorescence, nonlinear absorption, and optical pump-probe techniques [20, 22, 57-63]. TEM (JEOL 3010, operated at 300 KeV) was used to determine nanocrystal size, shape and elemental content by energy dispersive spectroscopy. Nanocrystal crystallinity was probed by selected area electron diffraction too. Nanocrystal surface and film chemistry was analyzed with a photoelectron spectrometer equipped with a monochromatic X-ray source (Al-K_α, 1487 eV photons).

Optical limiters based upon metal chalcogenide semiconductor nanocrystals dispersed in carbonaceous matrices were evaluated at UIC by use of 1064 and 532 nm nanosecond pulse length Z-scan experiments [64]. Thus, both near-IR and visible wavelength regions were examined. The Z-scan apparatus was developed to simultaneously record signals of four channels [22, 57, 61, 62] as shown schematically in Figure 1. A limited set of Z-scan experiments were performed with 800 nm femtosecond laser pulses, but they are not reported here.

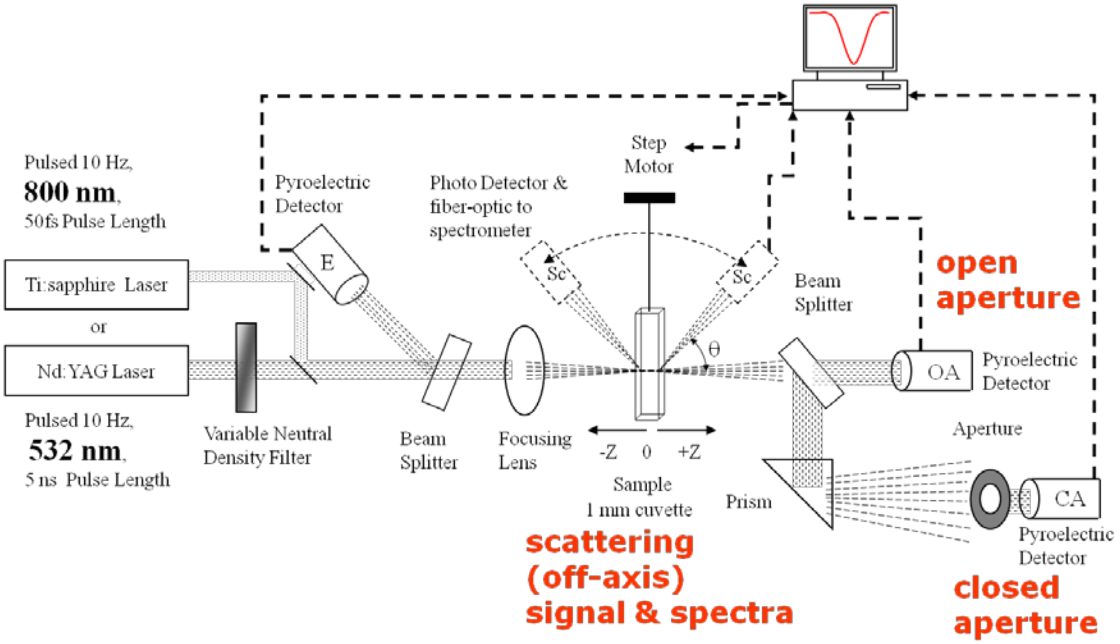

Figure 1. Schematic diagram of multichannel data acquisition Z-scan apparatus at UIC

Nonlinear absorption measurements were performed with a close-field detector in open aperture Z-scan configuration, where nonlinear refraction was measured using the far-field detector in closed aperture Z-scan configuration. Nonlinear scattering at various angles was obtained by a photodetector that was attached to a sample stage and could be rotated around the cuvette in an angular range of 20°-160°. Measurements of the nonlinear performance factors were deduced from the fitting of experimental curves. The spectra are plotted as normalized transmittance versus sample distance, Z, from the focus. The nonlinear absorption and refraction coefficients, β and n_2, for nanocrystals were determined directly as grown, as well as after the post-synthesis procedures.

Most of the Z-scan data reported were as open aperture Z-scans and used a configuration consisting of a pulsed laser (Continuum, model Surelite SL-I-30), variable neutral density filter (ThorLabs, model NDC-50C-2M), beam splitter, 125 mm focal length lens, and two pyroelectric detectors (Coherent, J4-09; with EPM 2000 dual channel power meter) to measure changes in laser transmission. A 1 mm glass cuvette sample cell (for colloidal samples) or film coated glass samples was gradually moved by computer controlled translation stage with a full range of 25 mm along the axis of light propagation, increasing the laser fluence as it reached the focal point. A frequency doubled Nd:YAG laser produced 532 nm pulses with energies that could be varied from 1 to 100 μJ/pulse, a repetition rate of 10 Hz, and a pulse length of ~5 ns. The value of the beam waist at the focal point was ~16 – 22 μm (the Rayleigh ranges were 1.5 – 2.5 mm) and the corresponding peak intensities were $10^7 – 10^9$ W/cm^2. These values were deduced from the fitting of experimental curves of transmittance, *T(z)*, versus sample distance, *z*, from the focal plane normalized with the linear transmittance. The *Z*-scan transmittance was normalized such that the transmittance far from the focus was unity.

Additional optical testing was performed with collaborators at the Air Force Research Laboratories (AFRL) and the corresponding procedures are discussed in the AFRL data sections.

a) *Synthesis Procedures*

The procedures are reported here divided by section for liquid nanocomposites (LNCs) and film nanocomposites (FNCs). PbS, PbSe and other nanocrystals were prepared in various polymeric and organic matrices. Other sections describe procedures for the preparation of films of polystyrene (PMMA) blended with colloidally synthesized nanocrystals. This type of film is referred to here as FNCs from LNC solutions. An additional task was completed by varying matrix polymer and nanocrystal concentration.

LNC-1: Procedures for synthesizing PbS nanocrystals in the presence of conjugated polymers were developed where a sulfur precursor is injected into a degassed solution containing solvent, a lead precursor and a polymer [18, 28, 43, 56, 65]. The polymer is the only species present to act as the size-limiting agent in which the composites form a unique particle/polymer interface otherwise free of the surfactant capping groups used in typical colloidal syntheses. LNCs composed of PbS nanocrystals in solutions of the six polymers were synthesized by these colloidal methods, whose details were published [20, 57, 58]. PbS nanocrystals were synthesized in the presence of the polymer, which limited the growth of the particles. The polymers used for these experiments were: polystyrene (CAS #9003-53-6, Sigma–Aldrich, St. Louis, MO, USA), MEH-PPV (CAS #138184-36-8, Sigma–Aldrich), poly(vinyl alcohol) (CAS #9002-89-5, Sigma–Aldrich), poly(1-decene) (CAS #68037-01-04, Sigma–Aldrich), poly(1-butene) (CAS #9003-28-5, Sigma–Aldrich), and polyethylene (CAS #9002-88-4, Sigma–Aldrich). The sources of lead in these synthesis was lead nitrate (CAS #10099-74-8, Fisher Scientific, Fair Lawn, NJ, USA) for poly(vinyl alcohol) (PVA) synthesis and lead acetate trihydrate (CAS #6080-56-4, Sigma–Aldrich) for the other polymers. The sulfur precursors used were sodium sulfide nonahydrate (CAS #1313-84-4, Sigma–Aldrich), in the PVA synthesis, and elemental sulfur flakes (CAS #7704-34-9, Sigma–Aldrich) for the other syntheses.

Each of the polymers acted as size limiters in the nanocrystal growth in a procedure adapted from that employed for growing nanocrystals in MEH-PPV [43], with the exception that the amount of dimethyl sulfoxide was decreased in this synthesis to promote solubility of the polymers. A solution consisting of 0.01 g of the polymer and 0.10 g of lead acetate trihydrate dissolved in a solution of 20.0 ml of toluene and 2.5 ml of DMSO was degassed for an hour under nitrogen at 110° C in a three neck flask. The sulfur precursor was prepared by dissolving 0.2 g of elemental sulfur flakes in 10 ml of nitrogen-degassed toluene. The sulfur solution was placed in a sonicator to aid in dissolution of the sulfur then briefly heated prior to injection. 1 ml of the sulfur solution was injected into the polymer-containing flask under maximum stirring. The nanocrystals grew in the solution and given 15 minutes for the reaction to progress to completion and grow to maximum size.

The growth of PbS nanocrystals in the conjugated polymer MEH-PPV used two different strategies to control nanocrystal size [43, 65]. The first strategy involved changing the average molecular weight of the polymer in the solution, where a decrease in molecular weight led to an increase in the size of the nanocrystals. However, attempts to achieve control of nanocrystal size distribution by changing molecular weight of the poly(1-decene) and polystyrene showed little effect on the nanocrystal size. The second method varied the ratio of the toluene and DMSO in the solution which in the case of MEH-PPV changed the solubility of the polymer that gave rise to different nanocrystal sizes. However, this second strategy also lead to problems in the synthesis with optically clear polymers, as increasing the ratio of toluene:DMSO to nearly 3:1 (compared with 10:1 in the initial reaction) rendered the polymer much less soluble. This reduced solubility dramatically reduced the ability to control nanocrystal size and lead to the formation of large, >25 nm sized PbS nanocrystals.

An additional task was completed in which PbS nanocrystals were synthesized, then annealed into different shapes and sizes in a microwave oven.

LNC-2: The growth of oleic acid capped PbSe and PbS nanocrystals with various shapes was carried out using newly developed methods [61, 62]. PbSe cubes, stars, spheres and rods were synthesized from 1 mmol of lead (II) acetate trihydrate (99.98%, Sigma-Aldrich), 1-3 mmol of oleic acid (99%, Sigma-Aldrich), 4-7 mL of squalane (Acros), and 1 mL of trioctylphospine (TOP, 97%, Strem) degassed under vacuum at 110°C for one hour. Nanocrystal size was selected via adjusting solution temperature to 135°C for rods synthesis, 150°C for spheres, 175°C for stars or 225°C for cubes, after which a mixture of 1-4 mL TOP and 1mL 1M TOP:Se (made with 97% TOP and 99.999% Se shot, Strem) was rapidly injected under nitrogen. Different volumes of TOP were also required to combine with the 1 mL of TOP:Se in the last step for shape control: rods and spheres required 1 mL, starts required 1-2 mL, and cubes required 4 mL. The nanocrystals were then allowed to grow in solution for 5-10 min. PbSe nanorod synthesis additionally required (instead of standard squalane) a mixture of 4 mL squalene, 2 mmol acetic acid, and 3 mmol H_2O heated to 110^oC under N_2 for 3 hours to remove excess acetic acid.

The nanocrystal colloids were then centrifuged and the nanocrystals re-dispersed in anhydrous hexane: these represent the “as grown” nanocrystals.

Post-synthesis washing of the nanocrystals was carried out by the addition of a 1:1 ethanol/hexane solution to crash the nanocrystals out of the colloidal solution, followed by centrifugation and redispersion in hexane. In some cases, the washing procedure was repeated 2-3 times.

An additional task was completed in which post-synthesis washing of the nanocrystals was carried in hexane mixture with pyridine, acetone, isopropanol and butanol.

Post-synthesis treatments were including doping of synthesized nanocrystals by various metal ions and dodecanethiol or aminodecane capping exchange of originally oleic acid capped PbSe nanocrystals. Zn, Cd, Cu ions for PbS and PbSe nanocrystals, Cu and Fe ions for ZnSe nanocrystals were selected.

FNC: Metal chalcogenide clusters were prepared by DC magnetron sputtering of a solid Pb metal target in a Haberland type source [66], which undergoes gaseous condensation and reaction in a background gas mixture of hydrogen sulfide (or hydrogen selenide), helium, and argon [59, 60, 67]. These components underwent reaction and gaseous condensation to form lead chalcogenide clusters. A U.S. patent was submitted on this process [68]. Cluster beam deposition apparatus was adapted from a commercially available source (Nanogen-50, Mantis Deposition Ltd., Oxfordshire, UK), as shown schematically in Figure 2. Careful manipulation of working power, wall temperature, gas flow or pressure in the aggregation zone, and volume of aggregation zone (or magnetron target/skimmer position) enables a control over the structure and size of the nanocrystals. One of the limitation of the work was that only smaller nanocrystals were formed, many of which could not be observed by TEM [59].

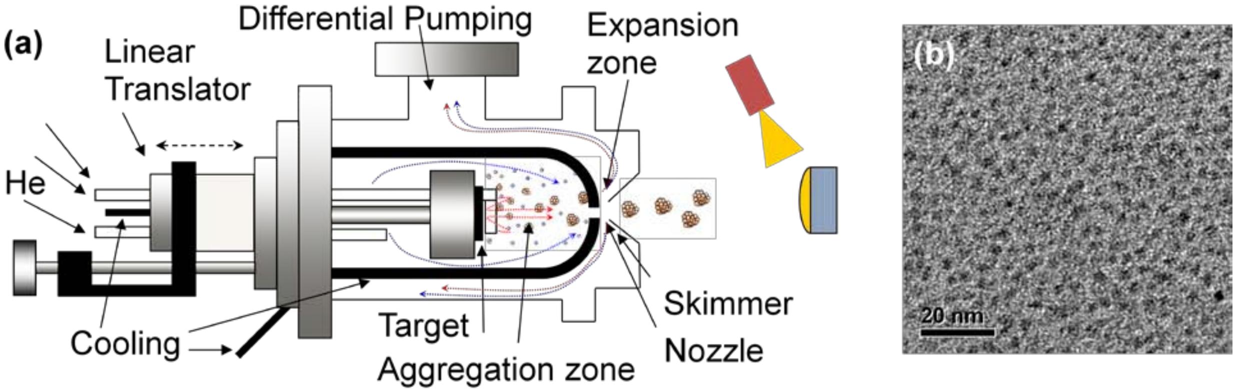

Figure 2. a) Schematic diagram of cluster beam deposition apparatus for the preparation of PbS clusters by magnetron sputtering and gaseous condensation. Also shown is separate evaporator of organics. b) TEM of 3-5 nm PbS nanocrystals deposited into titanyl phthalocyanine (TiOPc). Crystallinity verified by selected area electron diffraction (not shown)

Cluster beam deposition can be expanded to nearly any metal or metal chalcogenide nanocrystal simply by using different target for magnetron sputtering and introducing reagent gases into the source as needed (see Figure 6 for the example of Cu_xS and PbSe nanocrystal formation). Ternary metal chalcogenide (for example, PbS_xSe_{1-x}) nanocrystals can also be prepared by cluster deposition by mixing H_2S and H_2Se gas flows.

An additional task demonstrated deposition of PbS nanocrystals whose surface-termination varied from predominantly Pb to S [20, 69] by adjustment of the gas flow.

Nanocrystals prepared by cluster beam deposition will undergo aggregation and oxidation unless they are isolated and trapped within an organic film. TEM images indicate clumping and aggregation of the nanocrystals occurred in the absence of a co-deposited organic. Tuning the cluster vs. organic deposition rate controls the nanocrystal to organic ratio in the film, allowing control of the nanocrystal packing. The deposition rates of the organic layer and nanocrystals were monitored *in situ* by quartz crystal microbalance. Typical flux for investigated samples was $\sim 1\text{-}3 \times 10^{15}$ molecules/cm^2s.

Organic matrix can be evaporated directly onto the substrate before, after, or simultaneously with cluster beam deposition and SPIAD. Evaporation of neutral matrix compounds titanyl phthalocyanine (TiOPc) and sexithiophene (6T, CAS 88493-55-4, Sigma-Aldrich, St. Louis, MO, USA) was achieved with a resistively heated ceramic crucible (LTE 11000K, 1 cc, Kurt J. Lesker, Pittsburgh, PA, USA). $C_2H_x^+$ ions used also directly for deposition of amorphous carbon (a-C:H) and diamond-like carbon films [70] as a beneficial type of carbon-based organic phase with attractive properties for many applications.

A Kaufman broad beam ion source (Veeco-CS, 3 cm Ion Source) using acetylene gas metered with an (MKS Mass Flow controller model 1479A21) accelerated ions at ~50 eV. Typical ion current ~3 µA with an ion fluence of $\sim 1.6 \times 10^{16}$ ions/cm^2 s was used.

Post-synthesis treatment was evaluated for post-deposition of polystyrene spin-cast overlayer on top of vacuum deposited films. This kind of film is referred to here as sandwiched FNCs. Preparation of a polystyrene spin-cast overlayer was prepared for protection against ablation.

4. Results and Discussions

a) *Nanocomposite Preparation*

i. Preparation of Liquid Nanocomposites (LNCs)

This work began in 2008 with the development of procedures for synthesizing PbS nanocrystals in the presence of conjugated polymers using a procedure based upon a previously published method [43]. LNCs composed of PbS nanocrystals in solutions of the six polymers were synthesized by these colloidal methods, whose details were published [20, 57, 58] (see “Synthesis section, LNC-1”). Oleic acid capped PbS nanocrystals were also prepared by established methods [71] later replaced with a new procedure in conjunction with PbSe nanocrystal synthesis. All the resultant LNCs were characterized by UV/Vis linear optical absorption, TEM and selected area electron diffraction.

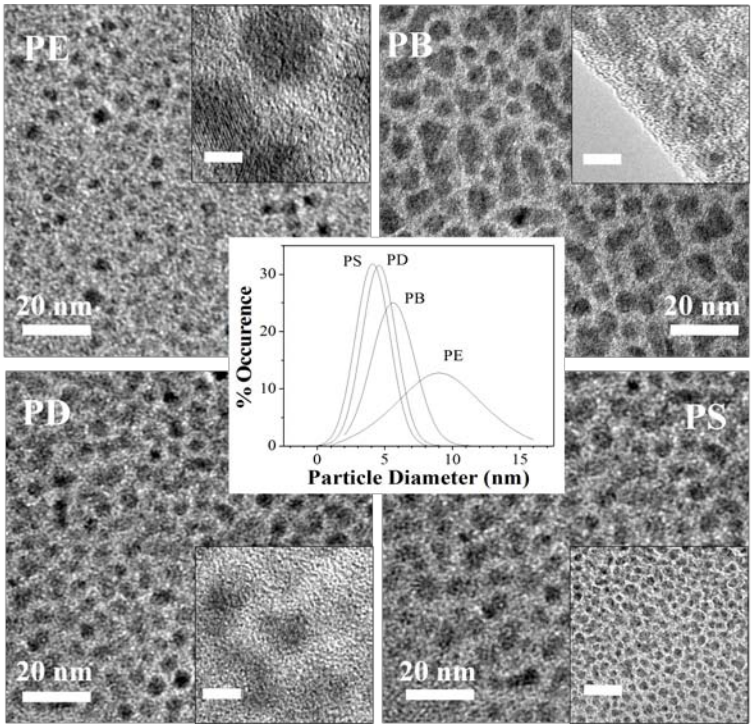

Figure 3. Transmission electron microscope (TEM) images of lead sulfide nanocrystals grown in (PE) polyethylene, (PB) poly(1-butene), (PD) poly(1-decene,) and (PS) polystyrene. Scale bar on the inset is 5 nm. Size distributions fitted from TEM analysis are also shown.

Figure 3 shows PbS nanocrystals synthesized in four different polymers, all prepared under conditions that lead to 4 – 10 nm diameter particles. TEM images of individual PbS nanocrystals clearly revealed lattice fringes of nanocrystals. Selected area electron diffraction showed the expected ring structure for the rocksalt PbS crystal structure for nanocrystals formed from all nanocrystals from all four polymers. Similar results were also observed for PbS nanocrystals synthesized in MEH-PPV and poly(vinyl alcohol), as well as oleic acid capped PbS nanocrystals (data not shown).

During the next stage (2009-2010), a procedure was developed for synthesizing surfactant (mostly oleic acid) capped PbSe nanocrystals of different shapes and sizes followed by a post-synthesis treatment developed to optimize optical limiting in colloidal solutions. The details of this procedure are described in the “Synthesis section, LNC-2”. TEM results showed that size and shape of nanocrystals was not changed by this post-synthesis procedure, which was also applied to previously evaluated oleic acid capped PbS nanocrystals. An additional task was completed by varying and exchanging ligand capping agents.

Figure 4 shows oleic acid capped PbSe nanocrystals of four different shapes and sizes between 5 to 20 nm which were selected for optical limiting evaluation. TEM images of individual PbSe nanocrystals and selected area electron diffraction showed the rocksalt crystal structure for all four selected sizes nanocrystals (data not shown).

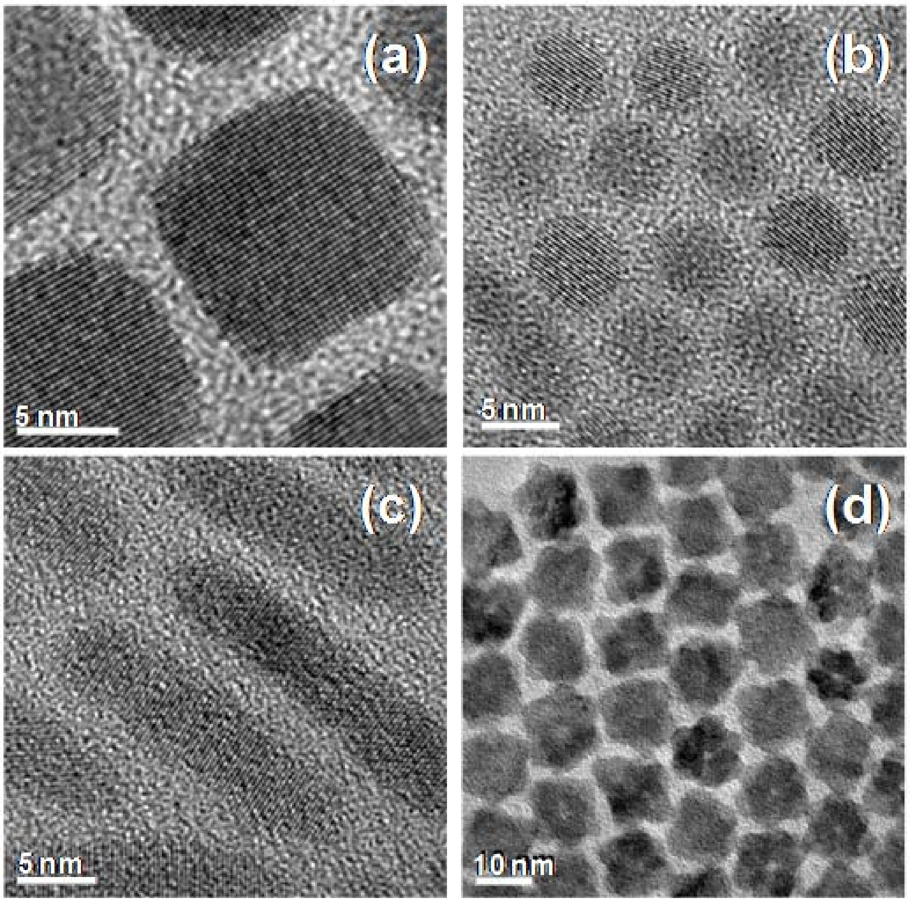

Figure 4. TEM images of the oleic acid capped as grown PbSe nanoscrystals. The nanocrystals take the shape of cubes - (a), spheres - (b), rods - (c), and stars - (d) with narrow size distributions and sizes ranging from ~5 (spheres) to ~20 nm (rods, dimension for length). TEM images of individual PbSe nanocrystals clearly revealed lattice fringes of nanocrystals.

Finally, during 2011, a procedure was developed for post-synthesis treatment of non-lead chalcogenide nanocrystals (ZnS, ZnSe, CdS, CdS/ZnS, CdS/ZnSe nanoshells). Those nanocrystals were already synthesized in the laboratory of Preston Snee at UIC and the synthetic procedure was not part of the reported project. An additional task was completed for mixture of PbSe nanocubes with ZnO tetrapods.

ii. Preparation of Film Nanocomposites (FNCs)

Laser blocking eyewear requires that an optical limiting film be prepared on a transparent substrate. The first stage for FNCs from LNC solutions was reported in 2008 and included procedures to prepare films of polystyrene blended with colloidally synthesizing PbS nanocrystals.

During the next stage (through 2010), a separate technique was developed for direct gaseous deposition of film nanocomposites (see "Synthesis section, FNC"). Figures 2b and 5 display the TEM images of PbS nanocrystals deposited into evaporated titanium phthalocyanine (TiOPc) and sexithiophene (6T) films. Cluster source produced nanocrystals up to 2 – 3 nm in diameter of a narrow size distribution which could be surface-termination tuned by adjustment of the gas flow [60].

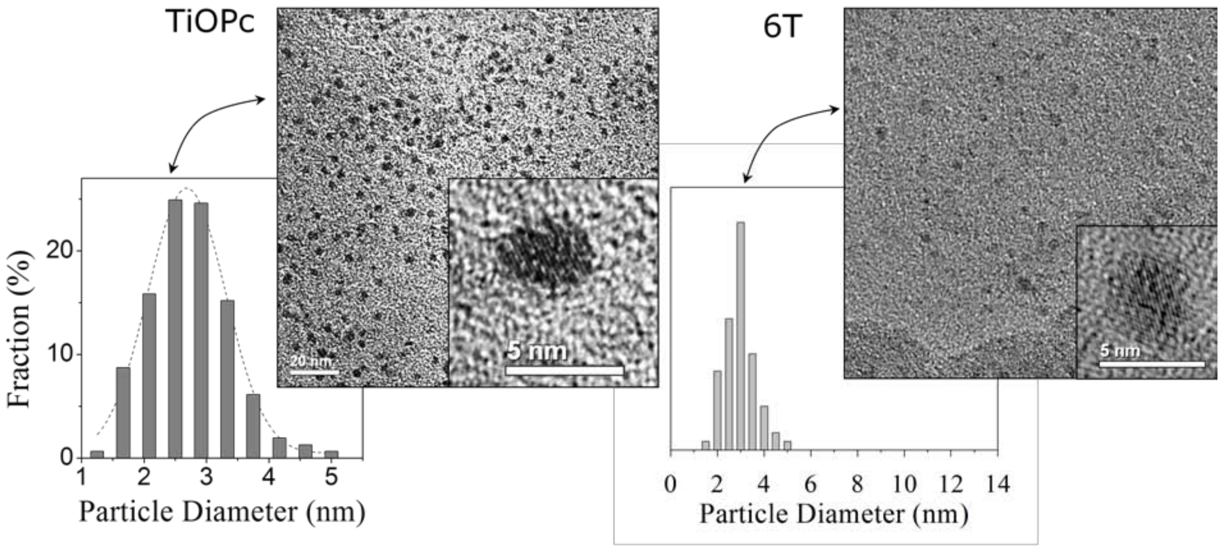

Figure 5. TEM images and particle size distributions of FNCs of PbS nanocrystals embedded in titanium phthalocyanine (TiOPc, left) and sexithiophene (6T, right) films.

Ion-assisted deposition of diamond-like carbon was achieved as an alternate organic phase in FNCs. However, 50 eV $C_2H_x^+$ ions destroyed the carbon film on TEM grids, preventing the collection of TEM data. Therefore, only UV-Vis and X-ray photoelectron spectra (XPS) were available to confirm the presence of PbS nanocrystals in diamond-like carbon and no size classification was performed.

As was reported in 2008, FNCs and films from LNC solutions were characterized by XPS to determine the state of surface oxidation which strongly affects optical limiting. Oxidation of the PbS and PbSe or strong bonding of the nanocrystals to the matrix without oxygen groups was not present in these composites [58]. An additional task was completed for calibration of nanocrystal surface termination which can be varied from metal to S (or Se) in cluster beam deposition by control of the $H_2S(Se)$:Ar gas flow, as demonstrated for PbS nanocrystals and reported previously [60].

Until this aspect was terminated in 2010 (see below), cluster beam deposition was evaluated for PbSe and Cu_xS nanocrystal formation. PbSe clusters were prepared by substituting H_2Se gas for H_2S in the cluster source, Cu_xS clusters were prepared by using a Cu target. Figure 5 shows an example of TEM images and XP spectra of Cu_xS (Figure 6a) and PbSe (Figure 6b) nanocrystals deposited into diamond-like carbon and TiOPc films, respectively (on silicon substrates). The Cu:S and Pb:Se ratios observed were ~4-5, and ~2 respectively, indicating that the H_2S(or H_2Se):Ar gas ratio had not been optimized for these new systems. Nevertheless, these results show the ability of cluster beam deposition to produce a variety of metal chalcogenide nanocrystals.

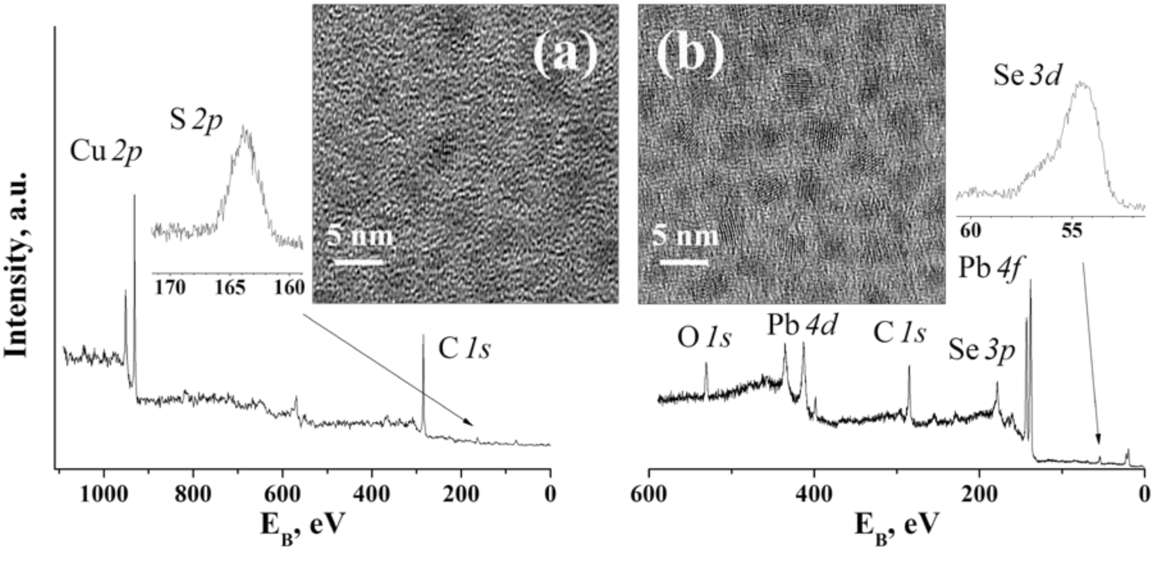

Figure 6. TEM images and X-ray photoelectron spectrum (XPS) for Cu_xS nanocrystals in diamond-like carbon (a) and PbSe nanocrystals into TiOPc (b) using cluster beam deposition (films on silicon substrates). ***Crystallinity verified by lattice fringes.***

b) *Evaluation of Optical Limiting*

i. <u>Evaluation of Optical limiting of LNCs</u>

The main method used at UIC was the Z-scan technique with nanosecond pulses which characterized the third order nonlinear optical properties of nanocrystals such as nonlinear absorption, scattering and refraction. Supplemental method includes quenching of near-IR emission.

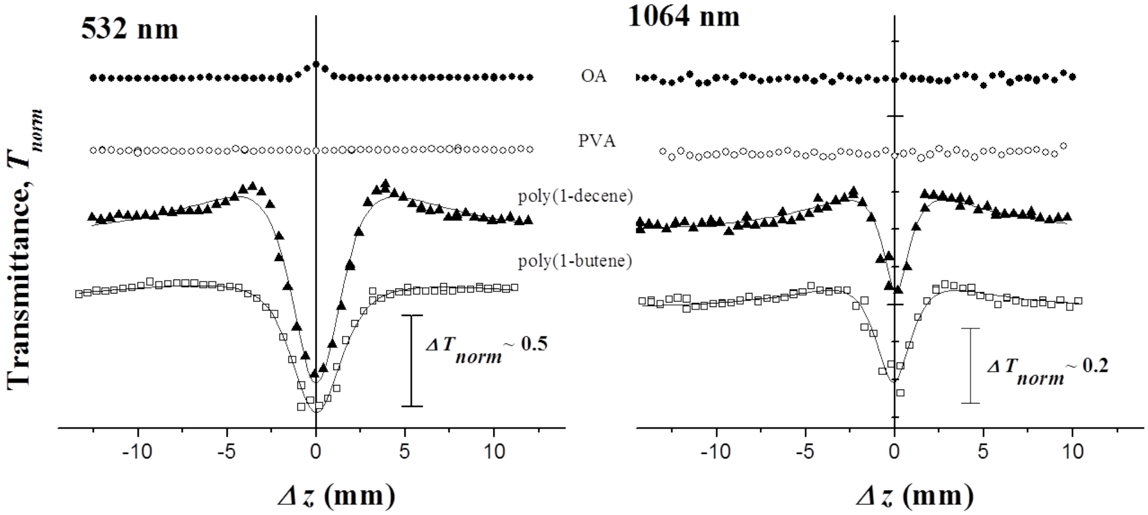

Figure 7. Open aperture Z-scan with 10 μJ pulses of 532 nm and 25 μJ pulses of 1064 nm radiation (symbols) for PbS nanocrystals in poly(1-decene), poly(1-butene), poly(vinyl alcohol) or PVA and for oleic acid (OA) capped PbS nanocrystals (without post-synthesis treatment) dispersed in toluene. Data fit to models of nonlinear optical absorption with contribution of saturable absorption (line).

Figure 7 displays previously reported open aperture Z-scans at 532 and 1064 nm of 4 – 5 nm PbS nanocrystals synthesized in poly(1-decene), poly(1-butene), poly(vinyl alcohol) and oleic acid capped PbS nanocrystals *before post-synthesis treatment* (see below for new samples) dispersed in toluene [22]. All the hydrocarbon polymer synthesized nanocomposites were found to exhibit a large decrease in normalized transmittance *T(z)*, down to as low as 14% for the poly(1-decene) sample. This Z-scan data indicates optical limiting was occurring, which was also observed for PbS nanocrystals in polystyrene, MEH-PPV, and polyethylene (data not shown). All the normalized transmittance data from Z-scans showed saturable absorption nonlinear behavior at low laser power, which changed to reverse saturable absorption as the fluence increased. No nanocrystal size dependence was observed for those materials that displayed optical limiting.

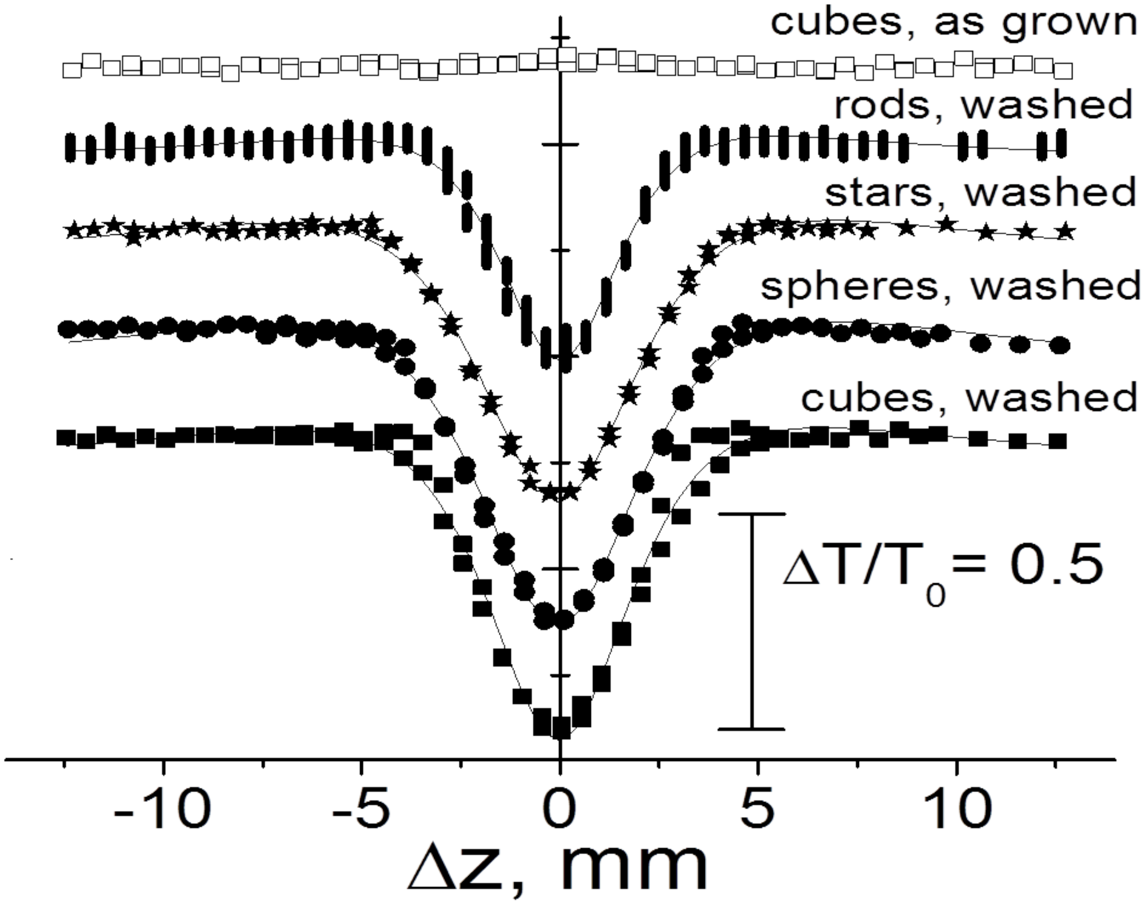

Figure 8. Typical 532 nm Z-scan traces for the oleic acid capped PbSe cubic nanocrystals as grown (top, open square symbols) and after washing in ethanol/hexane mixture for cubes (solid squares), spheres (solid circles), stars (solid stars) and rods (solid vertical bars). Lines are numerical fits using a model including saturable absorption. For all experiments, the transmittance of these composites was measured at an input laser energy, I_0, of ~ 7 μJ or laser peak power density of ~ 1 GW/cm^2 at focal plane. Transmittance T(z) versus sample distance z along the focal plane was normalized to linear transmittance such that the transmittance far from the focal point, 0 mm, was unity. The linear transmittance, T_0, of the samples was ~80-85% for all nanocrystals solutions.

Colloidal PbS nanocrystals prepared in polymer matrix did not show favorable results due to solubility problems and were replaced by more soluble, oleic acid capped PbS and PbSe nanocrystals prepared with the post-synthesis treatment. The advantage of PbS in polymer matrix nanocrystals was that they showed limiting directly after synthesis without any supplemental steps.

Figure 8 displays open aperture Z-scans at 532 nm for four different shapes and sizes oleic acid capped PbSe nanocrystals shown previously on Figure 4. PbSe nanocrystals directly after growth (open squares, Figure 8, top) did not show sizable changes in absorption, but small amounts of saturable absorption were observed. However, when washed in ethanol/toluene mixture (the post-synthesis treatment mentioned above) the nanocrystals were found to exhibit a large decrease in normalized transmittance *T(z)*, down to as low as 33% (cubes, spheres), 35% (stars) and 40% (rods) at peak laser peak power density of ~1 GW/cm^2 at the focal point. This is evidence of reverse saturable absorption for all shapes of PbSe nanocrystals after washing.

Similar results were obtained for oleic acid caped PbS nanocrystals after washing in ethanol/toluene mixture (data not shown). No significant nanocrystal shape/size dependence was observed for those materials that displayed optical limiting. The normalized transmittance Z-scan traces obtained from this function were symmetrical, similar direct and back-scan, reproducible, and almost unchanged for small and medium concentration of particles with $T_0 > 70\%$.

Ligand control of nanocrystal photoelectrical properties has been repeatedly demonstrated and originally was one of the main goals of this work. However, Z-scan screening of dodecanethiol or aminodecane capping exchange of originally oleic acid capped PbSe nanocrystals did not show significant improvement in limiting, and this negative result lead to a curtailing of the study of those post-synthesis treatments. The discovery of a simpler limiting control by washing in ethanol/toluene mixture shifted work in this direction.

Several sets of experiments washing PbSe cubes and spheres in hexane mixed with pyridine, acetone, ethanol, isopropanol and butanol showed similar ability to convert PbSe nanocrystals into optical limiters (data not shown). However, more aggressive washing resulted in crashing the PbSe nanocrystals from solution.

Z-scan measurements of PbSe nanocrystals with Cu and Zn doped shell, PbSe/CdSe core shell nanocrystals, and PbSe nanocrystals coupled with ZnO tetrapods did not show positive limiting results. These post-synthesis treatments were not evaluated further.

Finally, Figure 9 displays open aperture Z-scans at 532 nm for four different ZnSe nanocrystals in oleylamine. TEM images showed the nanocrystal sizes were 3 nm or less, close to the sensitivity level of the TEM equipment. Furthermore, they did not display crystallinity in the TEM. ZnSe nanocrystals directly after growth (open squares, Figure 9, top) or either after washing procedure described previously did not show sizable changes in absorption. However, doping by Fe(III) ions (yet another post-synthesis treatment mentioned above) caused these ZnSe nanocrystals to exhibit a decrease in normalized transmittance $T(z)$, down to as low as 70-80% at peak laser peak power density of ~0.7 GW/cm^2 at the focal point. This is evidence of reverse saturable absorption for ZnSe nanocrystals after surface doping with the magnitude of limiting close to washed PbS samples (stars, Figure 9, bottom). Synthesis and doping procedures were not optimized completely for these non-lead chalcogenide nanocrystals systems and optical limiting was obtained only for ZnSe Fe(III) doped nanocrystals. Nevertheless, these results show the ability of nanocrystals (or nanoparticles) with two-photon absorbing (TPA) properties to display optical limiting after appropriate post-synthesis treatment.

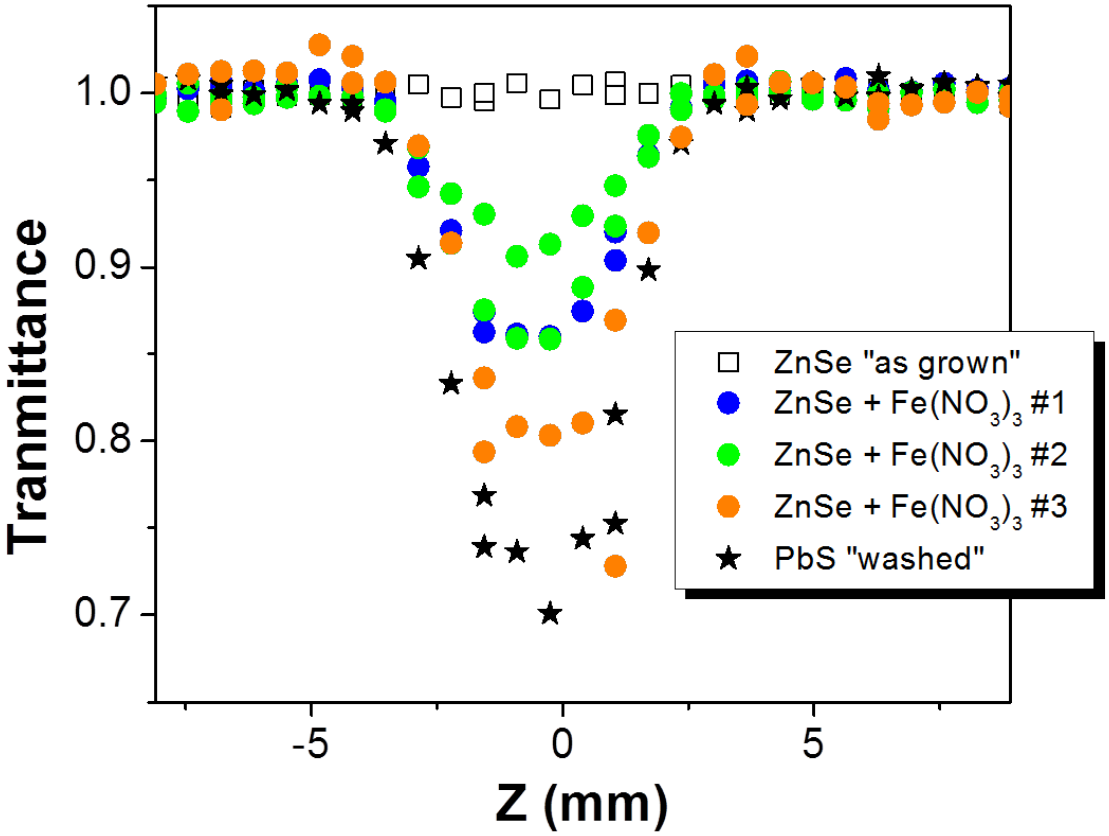

Figure 9. Typical 532 nm Z-scan traces for the ZnSe nanocrystals as grown (top, open square symbols) and after doping by Fe(III) ions. For all experiments, the transmittance of these composites was measured at an input laser energy, I_0, of ~ 5 μJ or laser peak power density of ~0.7 GW/cm^2 at focal plane. Transmittance T(z) versus sample distance z along the focal plane was normalized to linear transmittance such that the transmittance far from the focal point, 0 mm, was unity. The linear transmittance, T_0, of the samples was ~90-95% for all nanocrystals solutions.

A relationship between quenching of near-IR emission and nonlinear optical absorption observed by Z-scan was demonstrated for PbSe and PbS nanocubes after the nanocrystals were washed in the ethanol/hexane mixture (Figure 10) [62]. Quenching of emission could be due to the appearance of deep trap states leading to nonradiative recombination of the photogenerated carriers. A similar trend of quenched emission signals was observed for all shapes of PbSe nanocrystals (data not shown), supporting the same conclusion.

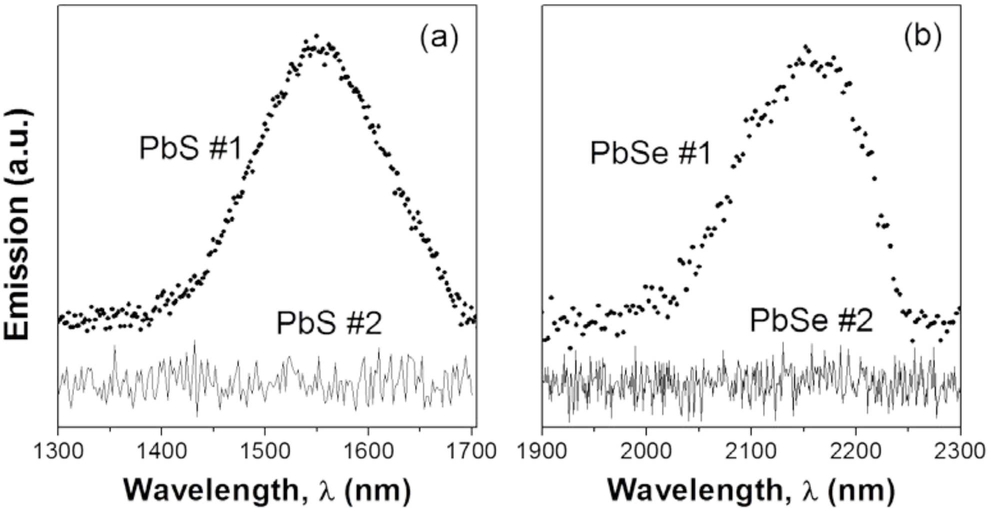

Figure 10. Near-IR emission spectra for the oleic acid capped (a) PbS and (b) PbSe nanocrystals after synthesis (dots or "#1") and after washing in ethanol/hexane mixture (lines or "#2").

Unfortunately, quenching of emission cannot be used as an indicator of optical limiting, since such quenching can also result from nanocrystal oxidation after contact with air. To alleviate this concern, nanocrystal colloidal solutions were transported in vacuum sealed glass tubes for AFRL testing. Control experiments showed that this procedure prevented oxidation of nanocrystals and kept emission intensity level at reasonable levels. Nevertheless, samples unwashed in ethanol or without vacuum sealing lost emission signal after one week, without any adjacent appearance of reverse saturable absorption.

In addition to large reversed saturable absorption, investigations showed the presence of an associated nonlinear scattering and sign change of nonlinear refraction coefficient in post-synthesis treatment nanocrystals that was postulated to be induced by thermal relaxation [62]. Experiments simultaneously detected off-axis light scattering and direct transmittance signals and indicated strong inverse correlation between scattering and transmittance signals with increasing laser beam flux. Furthermore, this nonlinear scattering displayed a classical Mie-type intensity distribution that is typically observed for >100 nm nanocrystals with a characteristic high intensity front lobe ($\theta<90°$) (data not shown) [62]. A similar Mie-type scattering pattern was previously observed for different nanocomposite systems [72-74], albeit those with much larger, ~100 nm nanocrystals.

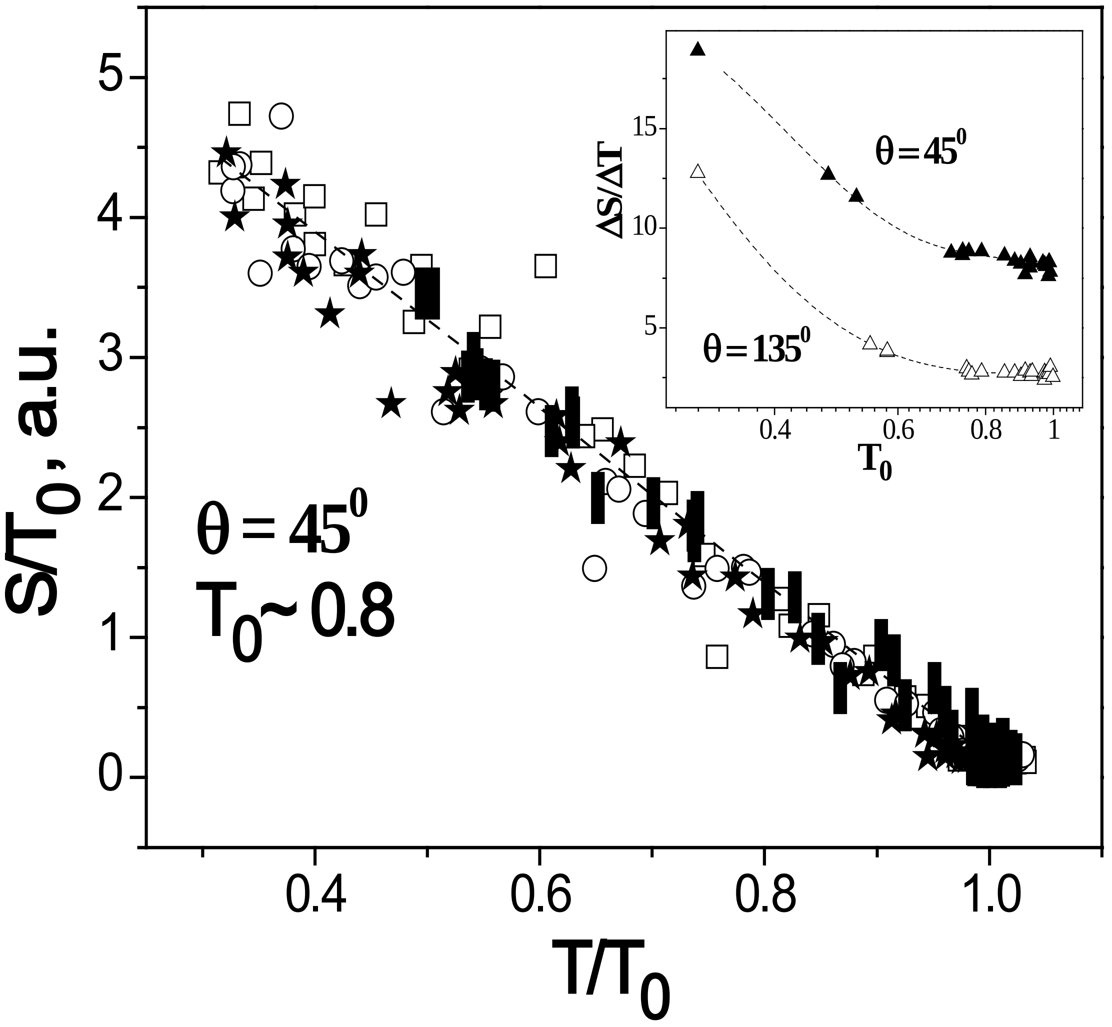

Figure 11. Correlation between forward-scattering (θ =45°) and transmittance of oleic acid capped PbSe nanocrystals with different shapes after washing in ethanol/hexane, corresponding to curves in Figures 8. Cubes represent open squares, spheres - open circles, star-like shapes - solid stars, and rods - solid bar symbols. Inset - graph of slope values as a function cubic nanocrystal concentration (as reflected in linear transmittances, T$_0$) for back-scattering (θ =135°) and forward-scattering (θ =45°) measurements.

Figure 11 summarizes the correlation between nonlinear scattering and transmittance signals for four different shapes of PbSe washed nanocrystals [61]. A similar inverse correlation between nonlinear scattering and transmittance was also observed for all shapes of washed PbS nanocrystals (data not shown). The Figure 11 data compares the signal from the forward scattering detector (positioned at a scattering angle of θ=45°) to the nonlinear transmittance signal shown in Figure 8 at different Z-positions of the sample (different laser beam flux), all normalized to the linear transmittance, T_0 = 0.8. A slight difference in the transmittance dip in Figure 8 for rods compared with other nanocrystals shapes could be related to a lower absorption cross-section due to the anisotropic rod shape, but this appears to not affect the values of slopes in Figure 11.

Analysis of various concentration levels of PbSe nanocrystals demonstrated that backscattering signal was not proportional to the concentration of nanocrystals and was better correlated with the cubic root of concentration. Forward scattering signal showed another correlation function, but those results were not confirmed. Forward- and back-scattering signals vs. transmittance loss correlation slopes showed similar behavior and can be divided to two regions. At low concentrations scattering (the main Z-scan testing conditions at UIC), the contribution linearly dropped until transmittance level 70-75% and almost did not change afterwards (day vision goggle or DVG and "bubble scattering" measurements at AFRL, see below). One possible explanation includes contribution of multiscattering, increasingly effective light path through media and increasing absorption losses. This mechanism was tested in conjunction with DVG analysis and scattering experiments at AFRL, as described further below.

ii. Evaluation of Optical limiting of FNCs (UIC)

The main method used here was the open-aperture Z-scan technique with nanosecond pulses which characterized the nonlinear absorption. Nonlinear scattering and quenching of near-IR emission was not studied since those methods were implemented after termination of the FNCs aspect of the program.

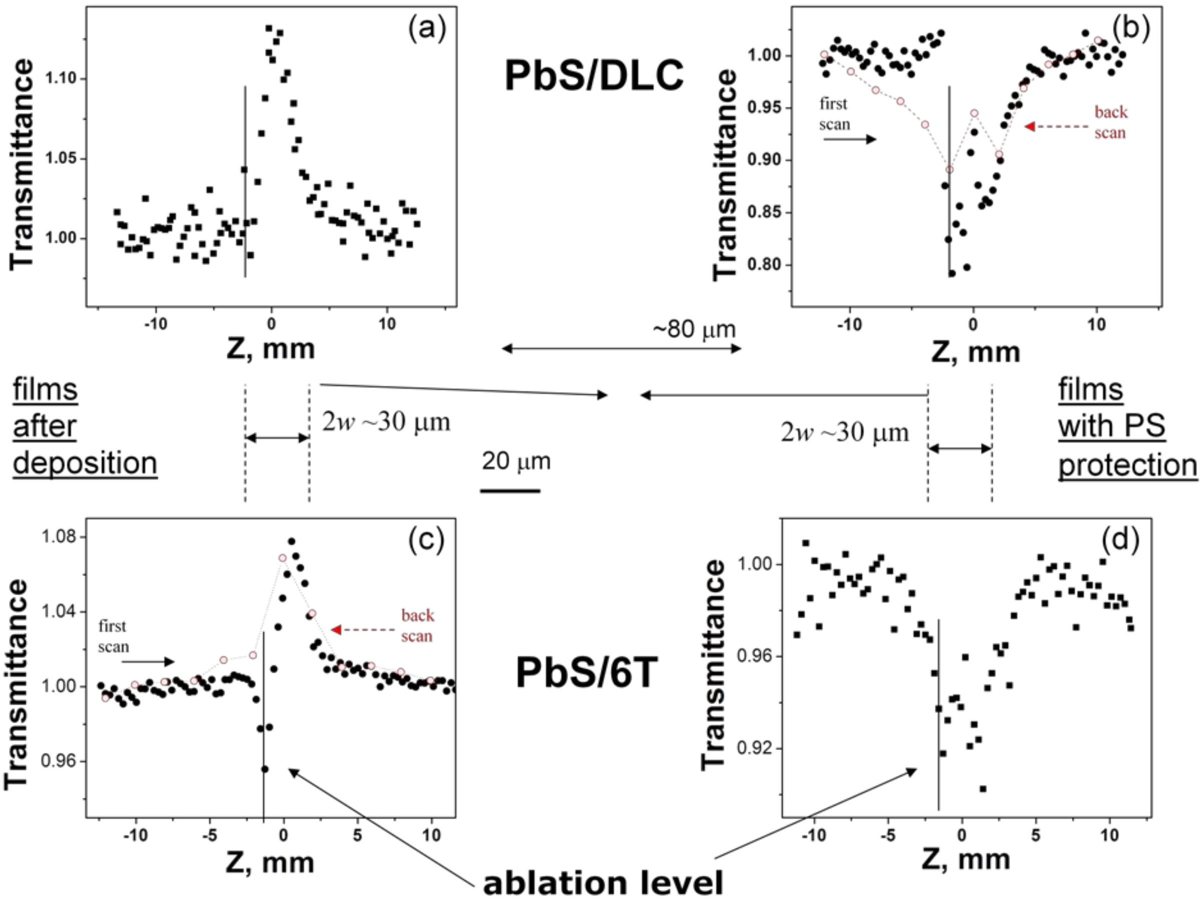

Figure 12. Ablation-type of open aperture Z-scan with 5 μJ pulses of 532 nm radiation (points) for PbS nanocrystals in diamond-like carbon (a,b) and 6T film after deposition (a,c) and sandwiched films with polystyrene overlayer protection (b,d). Optical image of damage shows a hole in the film of a diameter close to that of the laser beam-waist diameter.

Main difficulties for evaluation of optical limiting of FNCs were from film ablation and crater-hole formation for all kind of FNCs. Figure 12 (in parts a & c) displays open aperture Z-scans at 532 nm of PbS nanocrystals embedded in diamond-like carbon (DLC) and 6T films with clear ablation of the films occurring close to the focusing plane. This Z-scan data indicates that some optical limiting is occurring before the onset of ablation. Preparation of a polystyrene spin-cast overlayer (sandwiched FNCs) showed promise for at least partial protection against ablation (Figure 12 in parts b & d), but would require much lower nonlinear optical absorption thresholds for practical application. Similar results were observed for TiOPc films (data not shown).

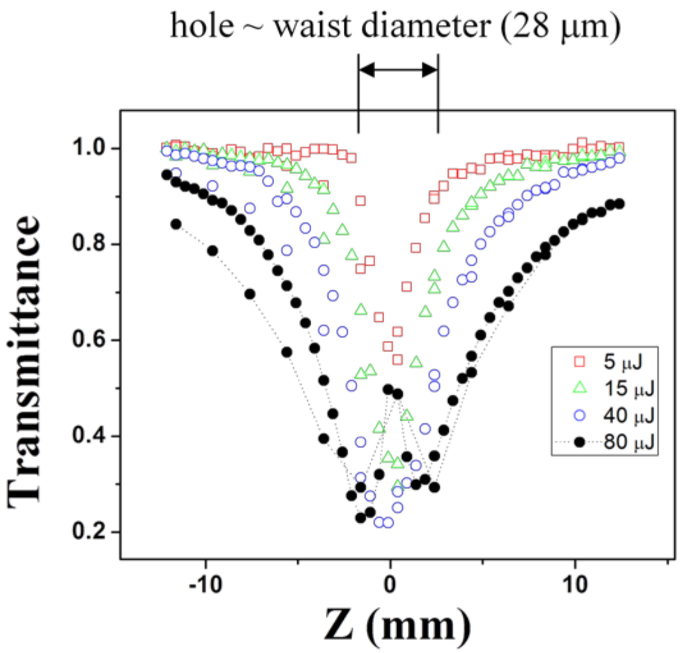

Figure 13: Open aperture Z-scan with 5 – 80 μJ pulses of 532 nm radiation for films of polystyrene blended with PbS nanocrystals in poly(1-butene).

Figure 13 displays open aperture Z-scan at 532 nm for films dried on glass under nitrogen atmosphere of polystyrene blended with PbS nanocrystals originally synthesized in poly(1-butene) (FNCs from LNC solutions). However, films with uniform thicknesses after spin-coating did not show optical limiting (data not shown).

c) *Determination of limiting characteristics of LNCs and FNCs.*

All the normalized transmittance data from Z-scans showed saturable absorption nonlinear behavior at low laser power, which changed to reverse saturable absorption as the fluence increased. The solid lines in Figures 7 and 8 represent the best fit of open-aperture Z-scan experimental data based on the Gaussian beam decomposition method of Sheik-Bahae *et al.* [64] in the quasi-steady-state approximation. Transmission *T(z)* for an open-aperture Z-scan is described by the modified equation [57]:

$$T(z) = C(1-R)^2 \exp\left(-\left\{\frac{\alpha_1}{1+I/I_S}+\alpha_2\right\}L\right)\sum_{m=0}^{\infty}\frac{[-q_0(z)]^m}{(m+1)^{3/2}} \quad . \qquad (1)$$

This equation gives the best fit of the Z-scan measurement. The linear absorption coefficient is in the form $\alpha_0 = \frac{\alpha_1}{1+I/I_S}+\alpha_2$, where α_1 and α_2 are constants; I_S is the saturation intensity; and $I(z)$ is the laser intensity. C is a normalization constant in Equation 1, R is the surface reflectivity, and q_0 is a function of z distance. The parameters I_0, z_0, w_0, λ, L and β correspond to the maximum incident radiation intensity, Rayleigh length, beam waist, wavelength, sample pathlength and two-photon absorption coefficient, respectively.

A modified fitting function for analysis of the Z-scan data was used to determine the nonlinear absorption coefficient, β_{eff}, which incorporates both saturable and reverse saturable components [22, 57, 62]. The β_{eff} values in these materials showed no obvious dependence on nanocrystal size/shape or organic phase. Table 1 presents results for various nanocomposites.

Table 1: Nonlinear absorption coefficient (β_{eff}), beam waist parameter (w_{eff}), limiting thresholds (F_{min}) and nanocrystal size for different LNCs nanocomposites. β_{eff} and w_{eff} were determined from the fitting of Z-scan data and nanocrystal sizes were determined from the TEM measurements.

SAMPLE	$\beta_{EFF,}$ CM/GW		$W_{EFF,}$ µM		$F_{MIN,}$ MJ/CM^2		NANOCRYSTAL SIZE/DIMENTIONS
	532 nm	1064 nm	532 nm	1064 nm	532 nm	1064 nm	nm
LNCs							
PbS/Poly(1-decene)	163±30	5.4±0.2	21.0	17.3	<250	<1000	4.6
PbS/Poly(1-butene)	121±18	9.3±0.4	15.7	21.8	<300	<1000	5.6
PbS/OA (cubes)	150±40	3.4±0.8	18.9	~20	<150	<1200	~10
PbSe/OA (cubes)	130±30	4.8±0.7	17.7	~20	<150	<1100	~10
PbSe/OA (spheres)	111±17	-	16.9	-	<200	-	5
PbSe/OA (stars)	138±33	-	19.1	-	<250	-	20
PbSe/OA (rods)	98±11	-	15-19	-	<200	-	5-25
PbSe/thiol (cubes)	78±11	-	~20	-	<150	-	~10
PbSe/amine (cubes)	45±11	-	~20	-	<250	-	~10

ZnSe	85±31		~20		<200		2-3
Gaseous FNCs							
PbS/DLC	?				<30		?
PbS/TiOPc	?				<40		3-5
Cu_xS/DLC	?				<40		?
FNCs from LNCs							
PbS/Poly(1-butene)	14000				<100		~5
Sandwiched FNCs							
PbS/DLC	~900				<7		?
PbS/TiOPc	>300				<30		3-5
Cu_xS/DLC	>500				<15		?

An important point to consider when evaluating the data presented in Table 1 is that the contribution to the nonlinear absorption and refraction from Z-scan traces due to photogenerated carriers and nanocrystal concentration has not been directly included in the equations for analysis and consolidated values of β_{eff} and n_2 [62] (data not shown). Thus, values of β_{eff} and n_2 are impacted by several interrelated phenomena. Similar β_{eff} values were attributed to the dependence of nonlinear absorption on the surface chemistry of the nanocrystals, rather than their size. Further theoretical and experimental investigation will be required to explain the primary events involved in the reversal of sign and the magnitude of third or higher order optical nonlinearities of nanocrystals by changes in nanocrystal surface in the absence of changes in nanocrystal core bandgap or laser beam parameters. Most importantly, these results demonstrate that the value of the sign on the nonlinear absorption and refractive index coefficient can be reversed by a relatively simple post-synthetic treatment.

In addition, for evaluation of the optical limiting and comparison with results from AFRL, all original raw Z-scan data for transmittance vs. position can be converted to transmission vs. input laser intensity (analogous to encircled transmission from DVG, see below) or energy vs. input intensity (analogous to encircled energy from DVG and bubble scattering measurements, see below).

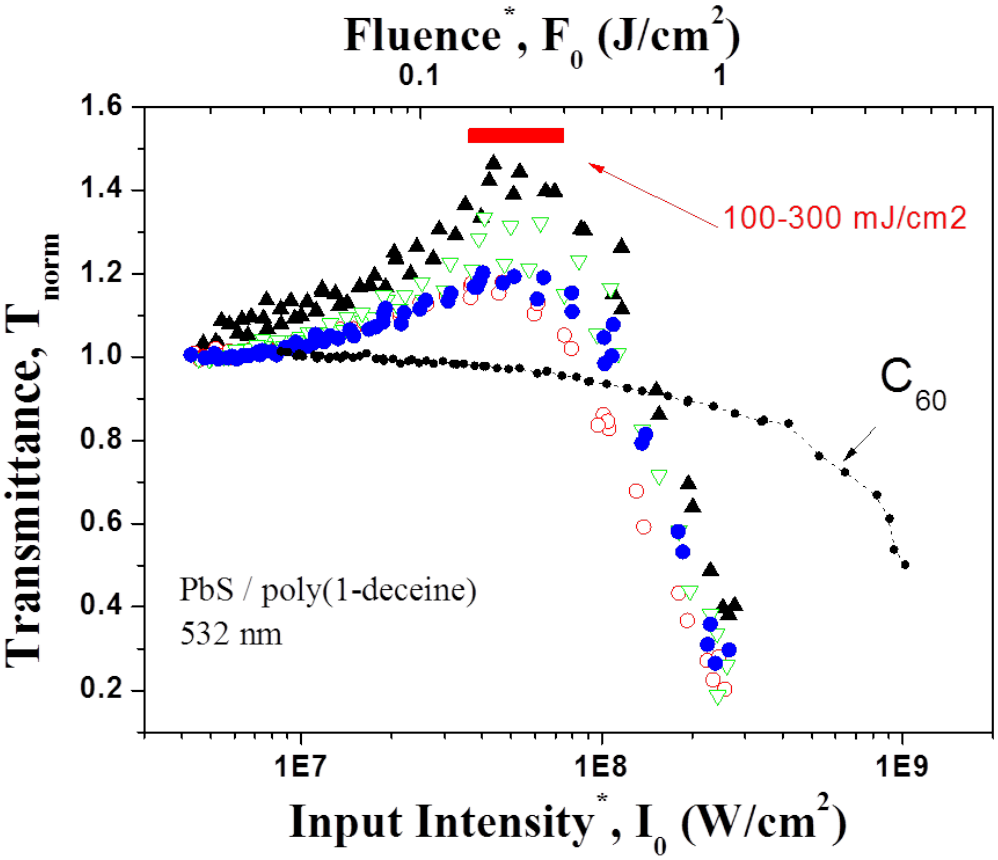

Figure 14. Evaluation of intensity (fluence) dependencies of normalized transmittance from open aperture Z-scan measurements of 532 nm radiation (symbols) for LNCs PbS nanocrystals in poly(1-decene) dispersed in toluene. C_{60} was used as a standard.

Figure 14 displays previously reported evaluation of optical limiting from fitted data of open aperture Z-scans at 532 nm of LNCs of PbS nanocrystals synthesized in poly(1-decene) dispersed in toluene (compared with C_{60} standard). Data for four different samples prepared with various concentrations and sizes of PbS nanocrystals show similar behavior with limiting thresholds of 200-300 mJ/cm^2.

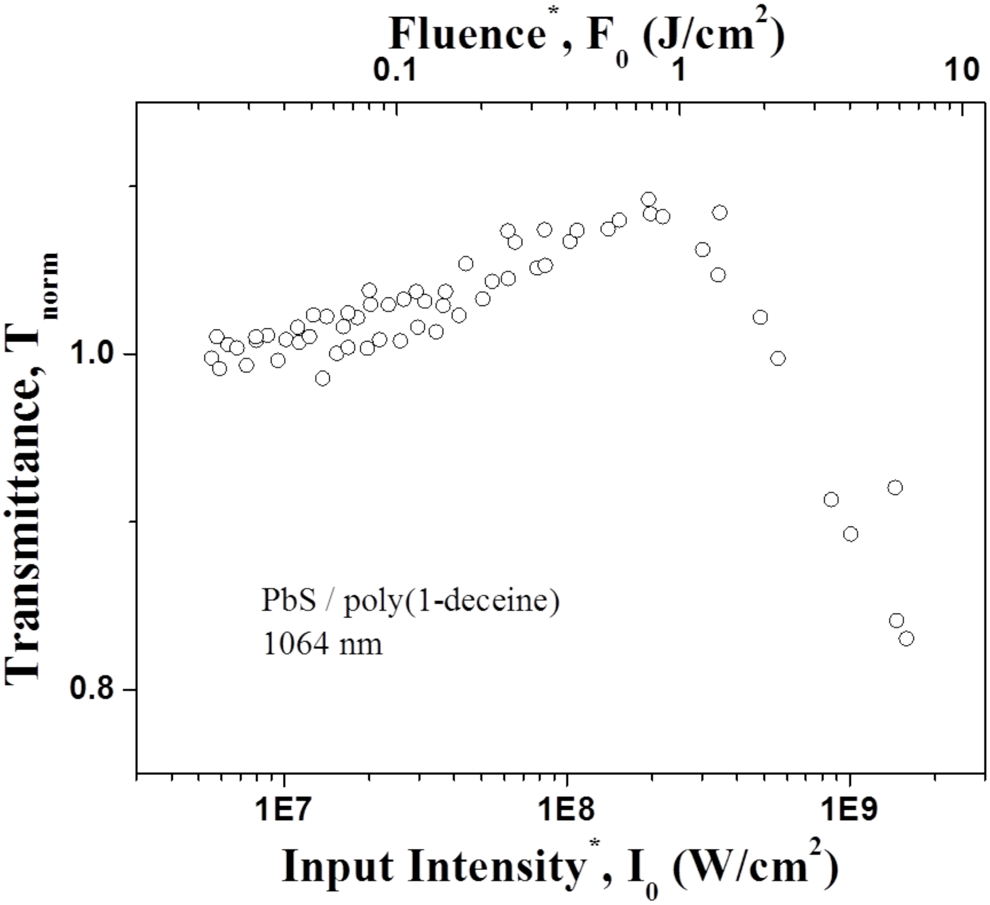

Figure 15. Evaluation of intensity (fluence) dependencies of normalized transmittance from open aperture Z-scan measurements of 1064 nm radiation for PbS nanocrystals in poly(1-decene) dispersed in toluene.

Figure 15 displays evaluation of optical limiting (from fitted data of open aperture Z-scans at 1064 nm presented on Figure 7b) for LNCs of PbS nanocrystals synthesized in poly(1-decene), then dispersed in toluene. C_{60} did not show reverse-saturable absorption for 1064 nm and therefore, could not be used as a standard. Data show limiting thresholds of ~1 J/cm^2, nearly an order of magnitude higher than at 532 nm, presumably as a result of a reduced absorption cross-section for this near-infrared wavelength.

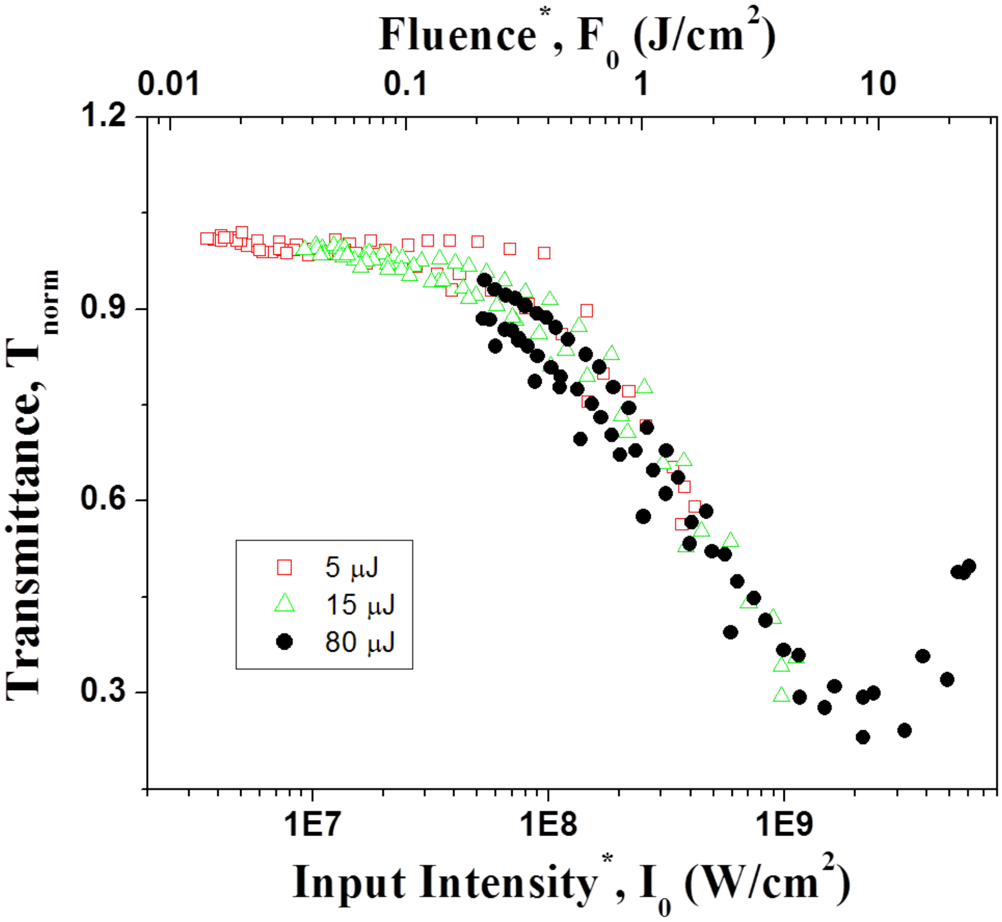

Figure 16. Evaluation of intensity (fluence) dependencies of normalized transmittance from Z-scan measurements for films of polystyrene blended with PbS nanocrystals in poly(1-butene).

Figure 16 displays open aperture Z-scan at 532 nm and evaluation of optical limiting for films dried on glass under nitrogen atmosphere of polystyrene blended with PbS nanocrystals originally synthesized in poly(1-butene). Data for optical limiting used parameters obtained from liquid phase Z-scans and show similar behavior with limiting thresholds of ~250 mJ/cm^2. However, films with uniform thickness after spin-coating did not show optical limiting (data not shown). Numerical evaluation of nonlinear optical behavior and determination of β_{eff} for the dried films was complicated by their non-uniform and unknown thicknesses, values required for fitting. Additional difficulties in the numerical evaluation arose from potential additional mechanisms such as scattering, reflection, and photodarkening.

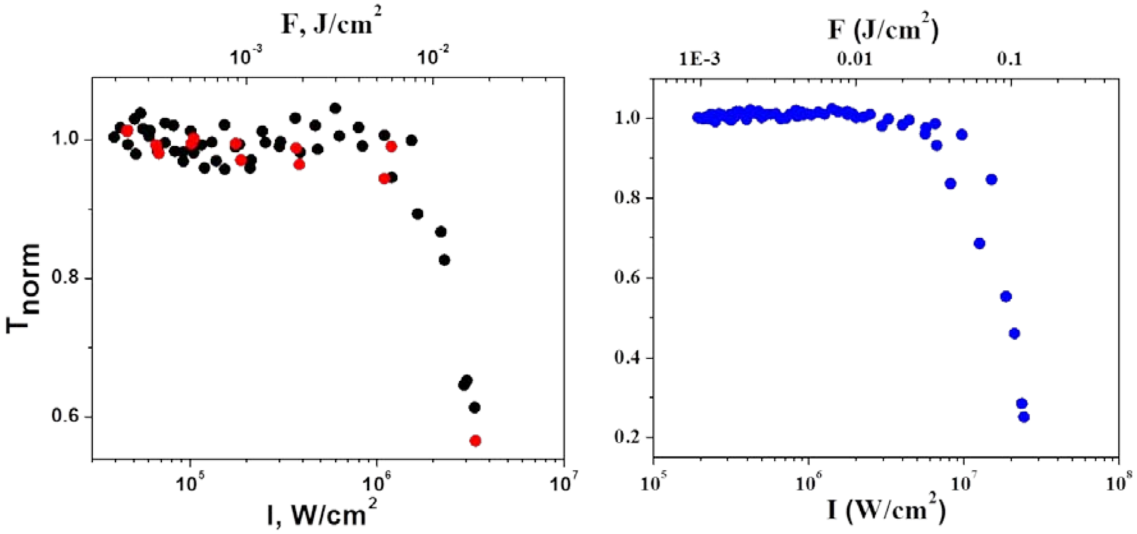

Figure 17. Evaluation of intensity (fluence) dependencies of normalized transmittance from open aperture Z-scan measurements of 532 nm radiation for sandwiched films of PbS nanocrystals in diamond-like carbon (a) and (b) TiOPc with a protective polystyrene overlayer.

Figure 17 displays the evaluation of optical limiting (from open aperture Z-scans at 532 nm) of sandwiched FNCs deposited on ITO coated glass of PbS nanocrystals in diamond-like carbon with a protective polystyrene spin-coated overlayer. The Figure 17a data show the best limiting before ablation with thresholds shifted less than 10 mJ/cm^2. This kind of film was chosen for initial evaluation at AFRL.

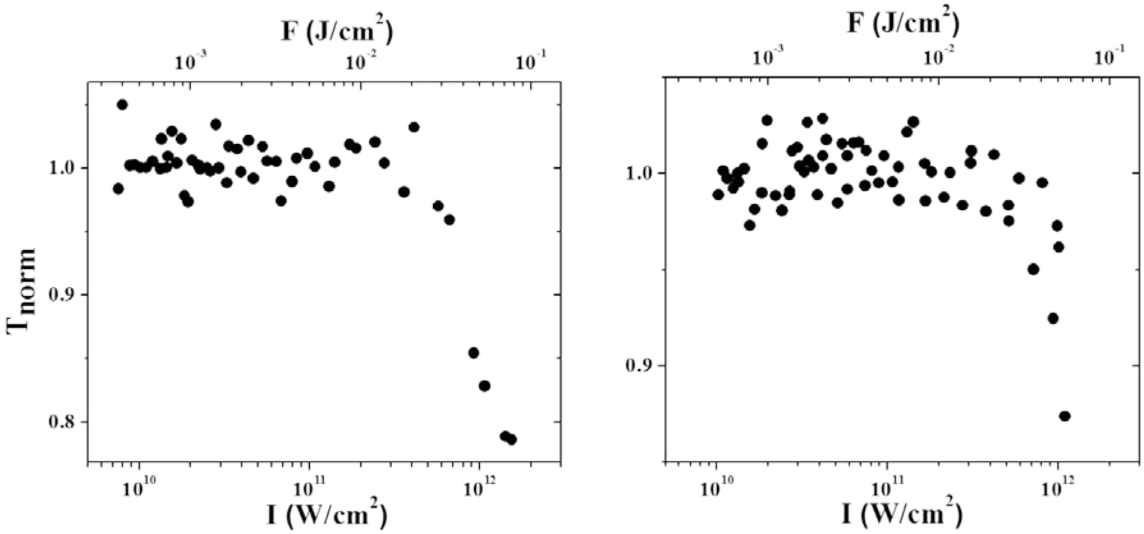

Figure 18. Evaluation of intensity (fluence) dependencies of normalized transmittance from open aperture Z-scan measurements of 50 fs, 800 nm radiation for sandwiched films (a) of polystyrene blended with PbS nanocrystals in poly(1-decene) and (b) PbS nanocrystals in TiOPc TiOPc with a protective polystyrene overlayer.

Finally, Figure 18 displays the evaluation of optical limiting (from open aperture Z-scans at 800 nm with 50 fs laser pulses) of films dried on glass under nitrogen atmosphere of polystyrene blended with PbS nanocrystals originally synthesized in poly(1-decene) and sandwiched FNCs deposited on ITO coated glass of PbS nanocrystals in TiOPc with a protective polystyrene spin-coated overlayer. The data show limiting thresholds on the order of ~30-40 mJ/cm^2. Note that femtosecond laser pulses Z-scan measurements was done only for FNCs since in colloidal systems presence of nonlinear absorption from solvents made limiting evaluation impossible.

d) *AFRL Collaborations*

i. Evaluation of Optical Limiting of LNCs

The main method used here was the day vision goggle (DVG) encircled (from 2.5 to 25 mrad) energy protocol with 537 nm, 3.5 ns, and 3 mJ maximum input laser setup for 0.5 mm cuvette of colloidal nanocomposites. Mark Brant and Paul Fleitz at AFRL ran these DVG tests. An additional task was performed with encircled forward scattering captures with 532 nm, 10 ns laser pulses (“bubble scattering” measurements).

Figure 19 displays the DVG evaluation of optical limiting of various colloidal samples of fresh and old PbSe and PbS colloidal nanocrystals which was selected for testing at AFRL in 2009 (1 PbS and 6 PbSe samples) and 2010 (1 PbS and 11 PbSe samples).

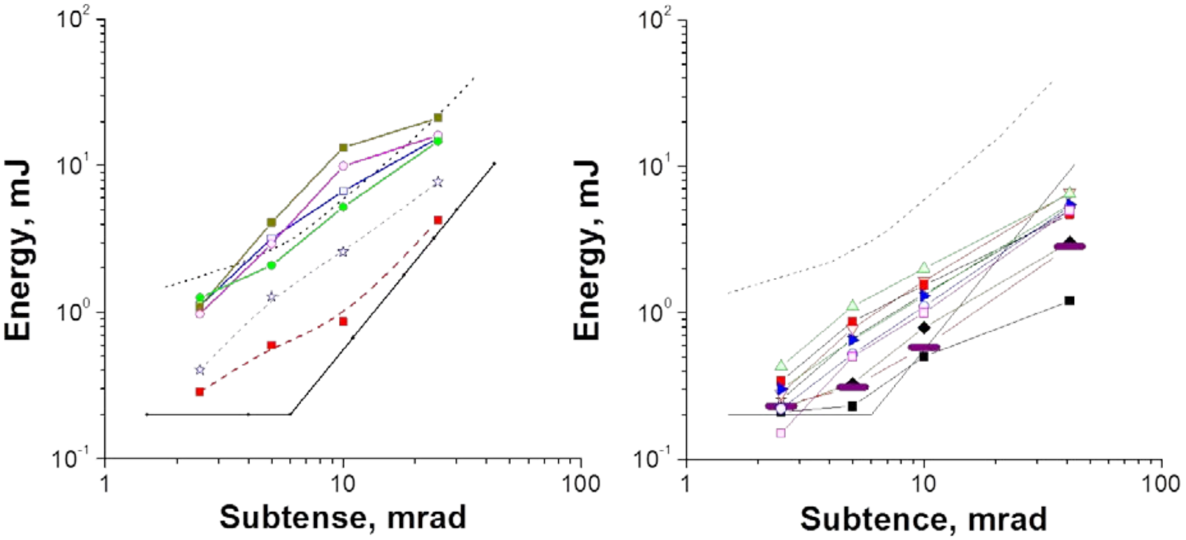

Figure 19. DVG evaluation of PbSe and PbS colloidal nanocrystals tested in a) 2009 and b) 2010. For 2009 : 1,2,3,4 – oleic acid capped spheres and thiol and amine capped cubes of PbSe; 5 – oleic acid capped stars of PbSe; 6 – oleic acid capped cubes of PbSe. PbS/poly(1-butane) samples obtained poor DVG results and data not shown. For 2010 results shown for oleic acid capped PbSe cubed except: 4 - PbS cubes; 8 – PbSe stars; and 9 – PbSe rods. All 2010 samples were analyzed after washing in ethanol/hexane mixture. ED50 – 50% probability of damaged determined from rhesus monkey tests; MPE(lim) – maximum permissible exposure.

2009 DVG tests showed varying degrees of limiting for all samples except PbS/poly(1-butane). Cube and star-shaped PbSe nanocrystals demonstrated the most favorable nonlinear optical behavior approaching MPE(lim) – human eye damage limit [75, 76]. Those systems were chosen as the basis for the next test in 2010. Colloidal PbS in polymer matrix nanocrystals did not show favorable results due to solubility problems and were replaced by newly synthesized oleic acid capped PbS nanocrystals after post-synthesis treatment.

2010 DVG tests showed improvement in optical limiting performance compared with the samples which were tested in 2009. Samples tested in 2010 at AFRL included oleic acid capped cubes, stars, rods PbSe and cubes PbS nanocrystals freshly synthesized or after storage up to 6 months. All samples showed good optical limiting performance and significant improvement compared with samples which were tested in 2009. On the other hand, even with the best performing samples #10 (PbS cubes), #9 (PbSe rods) and #8 (PbSe stars) could not be evaluated properly due to excessive nanocrystal concentrations in solution and the resultant drop in transmittance levels below the lower testing limit. Concentration levels must be considered for any new potential tests of these systems.

A different series of tests at AFRL during 2010 were performed with the “bubble scattering” apparatus. For this kind of test, images of scattered light are directly captured at various input energies to characterize the limiting performance. The pixel counts of the total beam is summed for each image and subtracted off the dark count, then the input energy is divided by the pixel count for each case to determine the average energy per pixel count. Measurement of the energy within various circle sizes provides a characterization of the distribution of light. Large circles collect the majority of the forward scattered light. This method allowed calculation of the energy contained within specified regions of an image.

Figure 20 displays the encircled forward scattering evaluation for 5 oleic acid capped PbSe samples with various shapes: spheres, cubes, stars and tees+crosses. All samples had absorbance of ~1 in a 2 mm pathlength at 400 nm. The two samples of cubes differed in that they were before and after washing for comparative studies. All other samples were after washing and showed nonlinear response via Z-scan measurements.

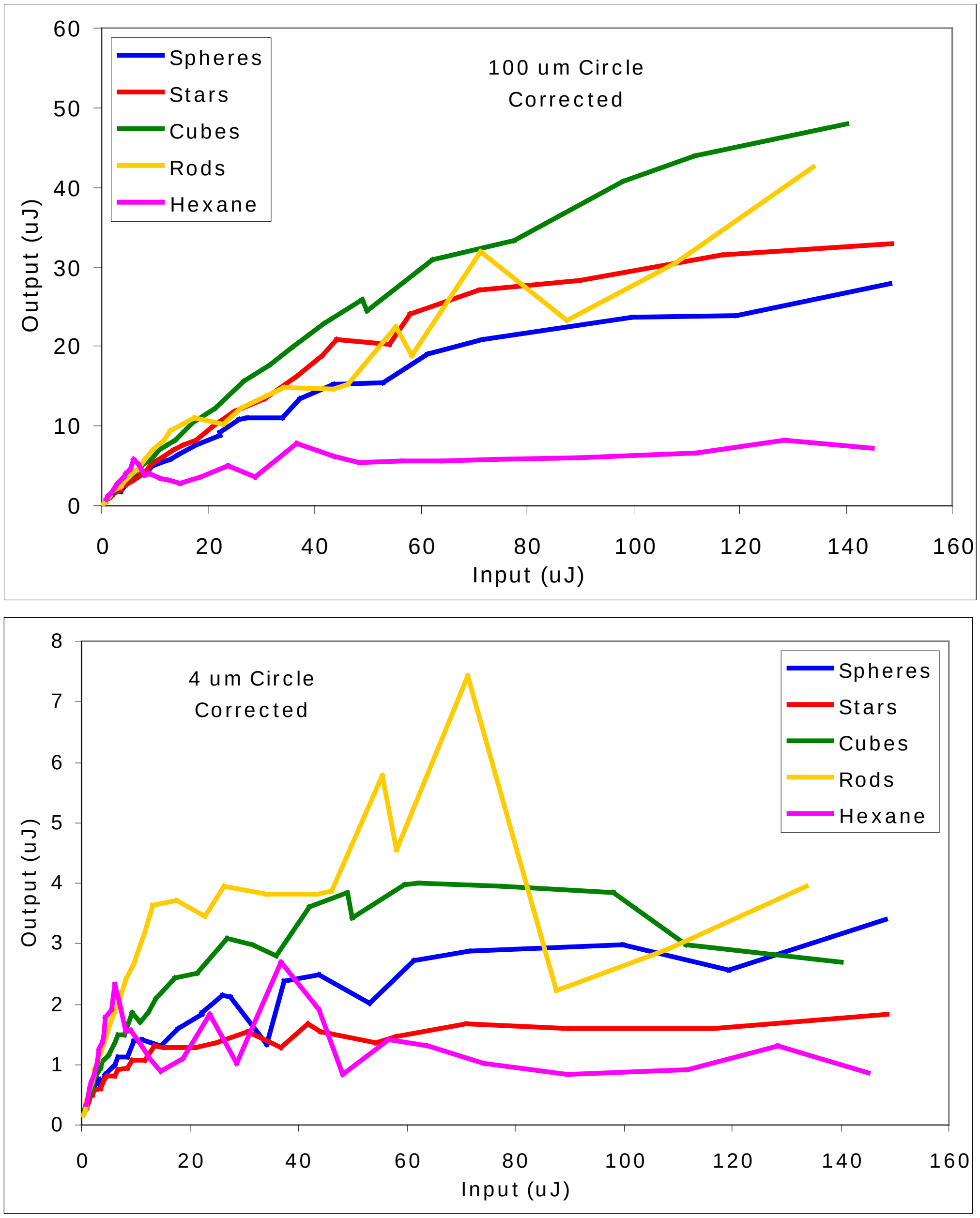

Figure 20. Encircled forward scattering evaluation ("bubble scattering") with two collection circle sizes. Examined five oleic acid capped PbSe samples with various shapes: spheres, cubes, stars and tees+crosses.

Limiting of all investigated systems were explained by the concurrent presence of nonlinear absorption (NLA) and scattering (NLS) events. It was confirmed that by increasing the collection circle, the largest NLS signals of all the PbSe systems were for cubes and rods. However, the highest scattering fraction NLS/NLA (or increasing rate of scattering vs collection circle) was obtained for star-shaped nanocrystals.

Finally, an additional sub-task was performed in collaborative femtosecond transient absorption experiments performed with Joy E. Haley of AFRL. Samples that displayed optical limiting were studied as well as samples that did not display optical limiting. All samples were excited with a

390 nm (3 μJ, 100 fs) pulse and probed from 425 to 775 nm. Prepared 3 sets of PbS and PbSe samples before and after washing in ethanol/hexane mixture. Samples were tested by Z-scan and shows reverse saturable absorption response after washing and strong IR emission before washing. All colloidal samples in vacuum sealed glass tubes were sent by UPS overnight.

Transient absorption experiments confirmed that washing in ethanol/hexane mixture for oleic acid capped PbS and PbSe cubes and spheres did not show the prominent changes in transient absorption decays behavior (data not shown) which was previously observed in various polymer-PbS nanocomposites [22].

ii. Evaluation of Optical limiting of FNCs

The main method used here was the DVG encircled energy protocol with 537 nm, 3.5 ns laser setup for fiber optic faceplates. Fiber optic faceplates are used to transfer an image without the use of lenses. They are commonly used on displays, CCD coupling, and image intensification.

For this task, the best performing optical limiting FNCs films were sandwiched nanocomposites of the original colloidal PbS/poly(1-butane) and gaseous deposited on faceplates PbS nanocrystals in DLC matrix, prepared specially for testing at AFRL. Similar films were deposited on glass slides (as imitation faceplates) and examined by 532 nm Z-scan. Originally, these films showed a degradation of the optical limiting threshold to ~100 mJ/cm^2 compared with the ~20-25 mJ/cm^2 values for films deposited on ITO-coated glass. The degradation in performance is thought to derive from the deposition on uncoated glass, which is electrically insulating compared with the electrically conductive ITO-coated glass substrates. Diamond-like carbon/PbS nanocomposites on ITO-coated glass showed an optical limiting threshold of ~5-10 mJ/cm^2.

DVG tests (not shown) for all films showed good limiting for small aperture but lost performance at larger apertures. Loss of overall performance, due to photodarkening and/or ablation, was the main reason that this aspect of the project was terminated without any future attempt at optimizing the FNCs.

These results showed that both colloidal synthesis and gaseous deposition can be used to prepare metal chalcogenide nanocrystals with novel morphology and surface chemistry which can be utilized for optical limiters with large nonlinear absorption and scattering coefficients. Surface properties of the nanocrystals were found to play a dominant role in controlling their nonlinear optical response in the visible region.

Linear absorption, Z-scan experiments, DVG and “buble scattering” tests showed that nanocrystal surface chemistry, especially after post-synthesis treatment, controlled the nonlinear optical absorption of colloidally synthesized nanocrystals. The surface chemical dependence of the nonlinear optical absorption for the PbS and PbSe nanocrystals contrasted with its relative independence of nanocrystal size and shape [22, 57, 61, 62].

Cumulative analysis of results presented here indicates that oleic acid capped PbSe nanocrystals of various shapes with large nonlinear absorption coefficients can be synthesized and these nanocrystals show promise for potential application in nonlinear optical devicesIt was found that *simple* post-synthesis treatment – washing in ethanol/hexane mixture - eliminated fluorescence of optically excited PbSe nanocrystals and induced nonlinear absorption [61, 62].

These results show that nanocrystal surface chemistry can select between nonradiative and radiative energy transfer. The TEM results show that the size and shape of the particles does not change during this washing process. Rather, the washing changes the nanocrystal surface chemistry and is thought to lead to the formation of deep trap states required for the nonlinear absorption, nonlinear scattering, and quenching of near-IR radiative emission. Paradoxically, transient absorption experiments did not show prominent changes in transient absorption decays behavior for which was previously obtained in various polymer-PbS nanocomposites [22].

All PbSe nanocrystal shapes show strong inverse correlation between scattering and transmittance with similar slopes that are independent of nanocrystal shape. Nonlinear scattering appears to occur via a separate mechanism. However, the slope values ($\Delta S/\Delta T$) are a function of scattering angle and nanocrystal concentration (as measured by the linear transmittance, T_0), as shown in the inset of Figure 11 for washed cubic PbSe nanocrystals. Nonlinear scattering is not explained by the same mechanisms as reverse saturable absorption, but the two phenomena appear to be directly related. A potential explanation is that the nanocrystals after the post-synthesis treatment are highly light absorbing and undergo nonradiative cooling in the laser beam, where the energy is transferred to the surrounding solvent causing the formation of bubbles due to the evaporation of hexane [77-79]. These bubbles then become new scattering centers with an effective size of an order of magnitude larger than the actual ~10 nm particle size which originally did not show Mie scattering. Such *nonlinear scattering* can be related to other effects such as laser-induced refractive index mismatch between particles and solvent [74]. In nanocrystals colloids that had undergone the post-synthetic washing, the change of n_2 from negative to positive can also be attributed to optical Kerr effect and thermal effect originating from the heat released by the nonradiative relaxation, similar to what was discussed for nonlinear scattering [62].

However, scattering did not show better limiting than well known scattering media as carbon-black. This indicates that the PbSe system had a more complicated limiting mechanism than carbon black which appears related to nonlinear absorption. Nevertheless, from bubble and DVG (AFRL) and Z-scan (UIC) experiments, the overall performance at different concentration levels of oleic acid capped PbSe nanocubes after washing in ethanol/hexane mixture can be chosen as the best limiting nanocomposite of those investigated in this project.

It seems contradictory that nonlinear transmittance and scattering depend on PbSe nanocrystal surface chemistry rather than shape or size, given that geometry will affect the nanocrystal surface to volume ratio. However, surface chemistry controls trap states which essentially turn on or off the third order nonlinear optical absorption which then leads to nonlinear scattering. If all nanocrystals have similar nonlinear absorption cross sections, then this would explain the dependence on nonlinear transmittance on washed nanocrystal concentration rather than size or shape. Nevertheless, further experiments are needed for a more detailed understanding the mechanisms and their relative contributions to the overall third order nonlinear optical properties of PbSe nanocrystals.

Figure 21 displays an energy level diagram for the nanocrystals with the excitation and relaxation process to and from deep trap intermediate states which explained obtained optical limiting. In this mechanism, limiting includes several steps

1. Excited state absorption (ESA) with intraband relaxation followed by band gap relaxation then trapping into shallow traps (ST). Surface chemistry controls whether ST leads to electron-hole recombination, transfer to deep trap (DT), or DT electron-hole recombination, and either excited state absorption (ESA) via DT or near-IR emission via 1, 2, or 3 [22].
2. Bubble formation and shadowing (at high nanocrystal concentration levels) where energy absorbed by nanocrystals induces ~100 nm-sized bubble formation and those bubbles effectively scatter laser light. Correlation between NLA and scattering may arise from bubbles shadowing incoming light, reducing total excited state absorption by the ensemble [62]. This stage directly causes ablation in films and lost performance in DVG tests.

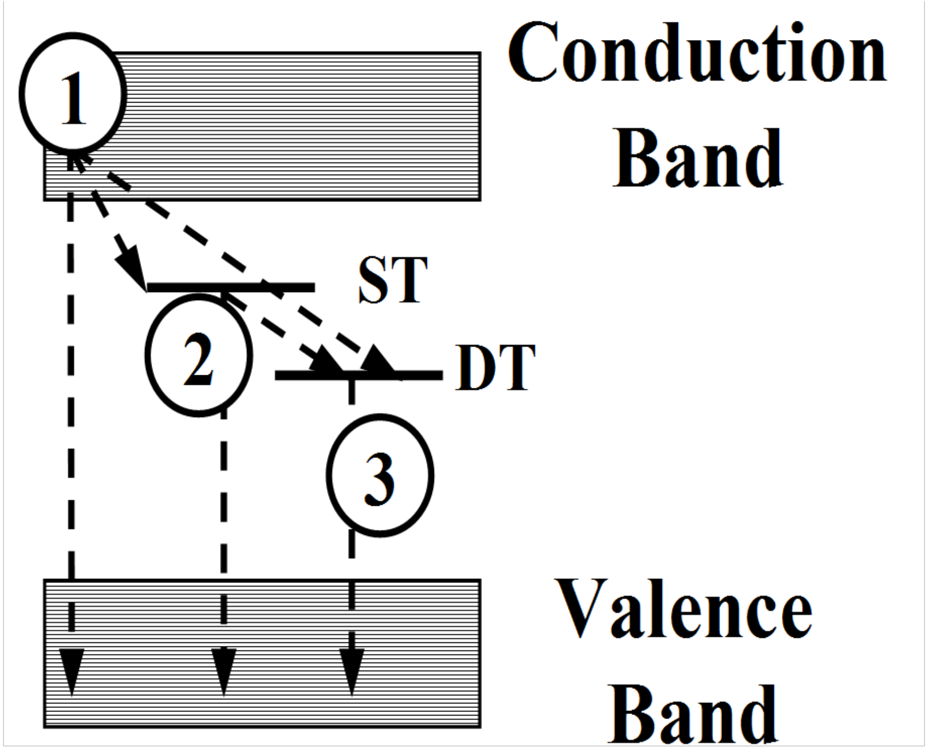

Figure 21. An energy level diagram for semiconducting nanocrystals with the excitation and relaxation process to and from deep trap intermediate states.

Films were prepared of these materials and some of them displayed optical limiting below the ablation threshold. Films prepared by a novel gaseous deposition method also displayed optical limiting with thresholds near ~100 mJ/cm^2; slightly below the ablation threshold for these very thin films. However, protective polymer layers were required to achieve optical limiting below the ablation threshold. Lower thresholds for optical limiting must be achieved with these PbS nanocrystal containing materials before they can be used as film-based optical limiters, since the laser eye damage threshold is ~3 × 10^{-7} J/cm^2 at 532 nm and ~2 × 10^{-5} J/cm^2 at 1064 nm (based upon the ANSI standard). Further work will also be required to prepare these materials in films.

Nevertheless, there are several shortcomings to the preparation of lead chalcogenide NCs, especially for their use in LEP. UV-exposure and even trace oxygen exposure can alter their optoelectronic properties. Casting NCs as films can lead to uncontrolled aggregation and can be related to unsuccessful DVG tests.

Finally, all lead chalcogenide are opaque and cannot used at high concentration levels as they inhibit normal vision. However, two photon absorbing (TPA), linearly transparent materials can serve as alternatives that can overcome these obstacles. Results for ZnSe nanocrystals showed that those TPA nanocomposites can also be utilized for optical limiters [80], provided they undergo post-synthesis treatment via Fe(III) ion doping. TPA allows material transparency and improved energy dispersion would suppress bubble formation that damages films. However, further work is required to optimizing synthetic and post-synthesis procedures for different TPA metal chalcogenides, for instance, cadmium chalcogenides limiters [21, 81-88]. For example, other works have shown that the presence of Ag improves two-photon absorption of 2-9 nm sized CdS nanoparticles [21, 88]. The results presented here indicate that optical limiting via TPA in various metal chalcogenide nanocrystals can be improved by post-synthetic treatment and greater attention to surface chemistry.

5. Conclusions

a) *Key Research Accomplishments in Liquid Nanocomposite (LNC) Preparation:*

A variety of new LNCs were synthesized in house by colloidal methods. LNC morphology and chemistry were analyzed by UV/Vis absorption, X-ray photoelectron spectroscopy, selected energy area diffraction, and transmission electron microscopy. New methods of synthesizing PbS and PbSe nanocrystals within an organic phase with post-synthesis treatment were developed to optimize optical limiting in colloidal solutions. All nanocrystals were examined by Z-scan and were found to display optical limiting after appropriate post-synthesis procedures. Extra optical testing (DVG and scattering measurements) was performed at AFRL.

Oleic acid capped PbSe nanocrystals of various shapes with large nonlinear absorption coefficients were synthesized and these nanocrystals were found to be promising materials for potential application in nonlinear optical devices. Simple post-synthesis treatment, or washing in ethanol/hexane mixture, eliminated fluorescence of optically excited PbSe nanocrystals and revealed nonlinear absorption and scattering. This washing changed the nanocrystal surface chemistry and lead to the formation of deep trap states needed for the nonlinear absorption, nonlinear scattering, and quenching of near-IR radiative emission.

All lead chalcogenides are opaque and cannot used at high concentration level. Two photon absorbing (TPA) transparent materials such as ZnSe were found to be promising alternatives for LEP. Results for ZnSe nanocrystals showed that those TPA nanocomposites can be utilized for optical limiters. The post-synthesis treatment that worked for these ZnSe nanocrystals was Fe(III) ion doping. Furthermore, TPA allows material transparency and improved energy dispersion that should suppress bubble formation that damages films. However, further work will be required to optimize synthetic and post-synthesis procedures. It is speculated here that ZnSe nanocrystals or other TPA nanostructures could display lower nonlinear absorbing thresholds that might allow optical limiting films to be developed as optical coatings on lenses for effective LEP. However, further work will be required to discovery such TPA materials such as CdS or $CdAg_xS_{1-x}$ [88] nanocrystals. Overall, optical limiting via TPA in various metal chalcogenide nanocrystals can be improved by post-synthetic treatment and greater attention to surface chemistry.

b) *Key Research Accomplishments in Film Nanocomposite (FNC) Preparation:*

A magnetron sputtering, gaseous deposition method was developed for producing PbS nanocrystals. This method can be applied to the production of films containing various metal or semiconductor nanocrystals embedded in any film that can be prepared by a gaseous deposition process.

FNCs were analyzed by open aperture Z-scan at 532 and 1064 nm (5 ns pulse) and 800 nm (50 fs pulse) and indicated results consistent with optical limiting before ablation for films with a protective polystyrene overlayer. It should be possible to use the magnetron sputtering, gaseous deposition method developed here to prepare TPA films for LEP.

These results demonstrated that the value of the nonlinear absorption, scattering and refractive index can be optimized or switched by simple post-synthetic procedure. The Z-scan technique directly monitored the appearance of the trap states in the nanocrystals that occurred after the post synthesis treatment. Further investigations are required to better understand the mechanisms, absolute value, and total contribution of each mechanism on the overall third order nonlinear optical properties of nanocrystals.

Similar effect of post-treatment can be applied for any new class of nanocrystals. Results with post-synthesis treated ZnSe nanocrystals confirm and support this statement.

One U.S. patent [68] is pending for this work and nine referred papers were published [20, 22, 57-63, 89].

6. References

1. Vogel, A. and V. Venugopalan, *Mechanisms of pulsed laser ablation of biological tissues.* Chemical Reviews, 2003. **103**(2): p. 577-644.
2. Talapin, D.V., et al., *Prospects of Colloidal Nanocrystals for Electronic and Optoelectronic Applications.* Chemical Reviews, 2010. **110**(1): p. 389-458.
3. Wise, F.W., *Lead salt quantum dots: The limit of strong quantum confinement.* Accounts of Chemical Research, 2000. **33**(11): p. 773-780.
4. Rogach, A.L., et al., *Infrared-emitting colloidal nanocrystals: Synthesis, assembly, spectroscopy, and applications.* Small, 2007. **3**(4): p. 536-557.
5. Cademartiri, L., et al., *Size-dependent extinction coefficients of PbS quantum dots.* Journal of the American Chemical Society, 2006. **128**(31): p. 10337-10346.
6. Bayon, R., et al., *Highly structured TiO2/In(OH)(x)S-y/PbS/PEDOT : PSS for photovoltaic applications.* Solar Energy Materials and Solar Cells, 2005. **89**(1): p. 13-25.
7. Biancardo, M. and F.C. Krebs, *Microstructured extremely thin absorber solar cells.* Solar Energy Materials and Solar Cells, 2007. **91**(18): p. 1755-1762.
8. Guerreiro, P.T., et al., *PbS quantum-dot doped grasses as saturable absorbers for mode locking of a Cr:forsterite laser.* Applied Physics Letters, 1997. **71**(12): p. 1595-1597.
9. Buso, D., et al., *PbS-doped mesostructured silica films with high optical nonlinearity.* Chemistry of Materials, 2005. **17**(20): p. 4965-4970.
10. Kim, H.S., et al., *Very high third-order nonlinear optical activities of intrazeolite PbS quantum dots.* Journal of the American Chemical Society, 2006. **128**(47): p. 15070-15071.

11. Malyarevich, A.M., et al., *Nonlinear spectroscopy of PbS quantum-dot-doped glasses as saturable absorbers for the mode locking of solid-state lasers.* J. Appl. Phys., 2006. **100**(2): p. 5.
12. Yu, B., et al., *Optical nonlinear properties of PbS nanoparticles studied by the Z-scan technique.* Optical Materials, 1998. **11**(1): p. 17.
13. Yu, B.L., et al., *Optical non-linearities of PbSe microcrystallites doped in glass.* Journal of Materials Science Letters, 1997. **16**(24): p. 2001-2004.
14. Aleksejenko, G., V. Pacebutas, and A. Krotkus, *Optical nonlinearities in PbSe nanocrystals.* Acta Phys. Pol., A, 2005. **107**: p. 294-297.
15. Moreels, I., et al., *The non-linear refractive index of colloidal PbSe nanocrystals: Spectroscopy and saturation behaviour.* J. Lumin., 2006. **121**(2): p. 369-374.
16. Neo, M.S., et al., *Size-Dependent Optical Nonlinearities and Scattering Properties of PbS Nanoparticles.* Journal of Physical Chemistry C, 2009. **113**(44): p. 19055-19060.
17. Xiang, W., et al., *Glasses doped with PbS nanocrystals.* J. Alloys Compd., 2009. **471**(1-2): p. 498-501.
18. Yu, B.L., et al., *Optical nonlinear properties of PbS nanoparticles studied by the Z-scan technique.* Optical Materials, 1998. **11**(1): p. 17-21.
19. Kurian, P.A., et al., *Two-photon-assisted excited state absorption in nanocomposite films of PbS stabilized in a synthetic glue matrix.* Nanotechnology, 2007. **18**(7): p. 7.
20. Asunskis, D.J., et al., *Lead sulfide nanocrystal-polymer composites for optoelectronic applications.* Macromol. Symp., 2008. **268**: p. 33-37.
21. Jia, W.L., et al., *Two-photon absorption and degenerate four-wave mixing studies of sulfide semiconductor nanoparticles in polymeric solutions.* Journal of Nanoscience and Nanotechnology, 2008. **8**(3): p. 1364-1370.
22. Asunskis, D.J., et al., *Effects of Surface Chemistry on Nonlinear Absorption of PbS Nanocrystals.* Journal of Physical Chemistry C, 2009. **113**(46): p. 19824-19829.
23. Li, C., et al., *Nonlinear optical properties of the PbS nanorods synthesized via surfactant-assisted hydrolysis.* Materials Letters, 2007. **61**(8-9): p. 1809-1811.
24. Guyot-Sionnest, P., *Intraband Spectroscopy and Semiconductor Nanocrystals*, in *Structure & Bonding*. 2005, Springer: Berlin, Heidelberg. p. 59.
25. Guyot-Sionnest, P., B. Wehrenberg, and D. Yu, *Intraband relaxation in CdSe nanocrystals and the strong influence of the surface ligands.* J. Chem. Phys., 2005. **123**: p. 074709.
26. Gomez, D.E., M. Califano, and P. Mulvaney, *Optical properties of single semiconductor nanocrystals.* Phys. Chem. Chem. Phys., 2006. **8**(43): p. 4989-5011.
27. Zhang, J.Z., *Interfacial Charge Carrier Dynamics of Colloidal Semiconductor Nanoparticles.* J. Phys. Chem. B, 2000. **104**(31): p. 7239-7253.
28. Patel, A.A., et al., *Synthesis, Optical Spectroscopy and Ultrafast Electron Dynamics of PbS Nanoparticles with Different Surface Capping.* J. Phys. Chem. B, 2000. **104**(49): p. 11598.
29. Tamulaitis, G., et al., *Optical nonlinearities of glass doped with PbS nanocrystals.* J. Appl. Phys., 2000. **88**(1): p. 178.
30. Du, M.-H., S.C. Erwin, and A.L. Efros, *Trapped-Dopant Model of Doping in Semiconductor Nanocrystals.* Nano Lett., 2008. **8**(9): p. 2878-2882.
31. Pendyala, N.B. and K. Rao, *Identification of surface states in PbS quantum dots by temperature dependent photoluminescence.* J. Lumin., 2008. **128**(11): p. 1826-1830.

32. Fernée, M.J., P. Jensen, and H. Rubinsztein-Dunlop, *Bistable Switching between Low and High Absorbance States in Oleate-Capped PbS Quantum Dots.* ACS Nano, 2009. **3**(9): p. 2731-2739.
33. Wehrenberg, B.L., C.J. Wang, and P. Guyot-Sionnest, *Interband and intraband optical studies of PbSe colloidal quantum dots.* J. Phys. Chem. B, 2002. **106**(41): p. 10634-10640.
34. Istrate, E., et al., *Carrier Relaxation Dynamics in Lead Sulfide Colloidal Quantum Dots.* J. Phys. Chem. B, 2008. **112**(10): p. 2757-2760.
35. Beard, M.C., et al., *Variations in the Quantum Efficiency of Multiple Exciton Generation for a Series of Chemically Treated PbSe Nanocrystal Films.* Nano Lett., 2009. **9**(2): p. 836-845.
36. Fernée, M.J., et al., *Inorganic surface passivation of PbS nanocrystals resulting in strong photoluminescent emission.* Nanotechnology, 2003. **14**(9): p. 991-997.
37. Hillhouse, H.W. and M.C. Beard, *Solar cells from colloidal nanocrystals: Fundamentals, materials, devices, and economics.* Current Opinion in Colloid & Interface Science, 2009. **14**(4): p. 245-259.
38. Nozik, A.J., *Multiple exciton generation in semiconductor quantum dots.* Chemical Physics Letters, 2008. **457**(1-3): p. 3-11.
39. Johnston, K.W., et al., *Schottky-quantum dot photovoltaics for efficient infrared power conversion.* Applied Physics Letters, 2008. **92**(15): p. 151115.
40. Koleilat, G.I., et al., *Efficient, stable infrared photovoltaics based on solution-cast colloidal quantum dots.* Acs Nano, 2008. **2**(5): p. 833-840.
41. Luther, J.M., et al., *Schottky Solar Cells Based on Colloidal Nanocrystal Films.* Nano Letters, 2008. **8**(10): p. 3488-3492.
42. Luther, J.M., et al., *Structural, optical and electrical properties of self-assembled films of PbSe nanocrystals treated with 1,2-ethanedithiol.* Acs Nano, 2008. **2**(2): p. 271-280.
43. Watt, A., et al., *Carrier transport in PbS nanocrystal conducting polymer composites.* Applied Physics Letters, 2005. **87**(25): p. 253109.
44. Zhang, S., et al., *Enhanced infrared photovoltaic efficiency in PbS nanocrystal/semiconducting polymer composites: 600-fold increase in maximum power output via control of the ligand barrier.* Applied Physics Letters, 2005. **87**(23): p. 233101.
45. Dissanayake, D., et al., *A PbS nanocrystal-C-60 photovoltaic device for infrared light harvesting.* Applied Physics Letters, 2007. **91**(13): p. 133506
46. Fritz, K.P., et al., *IV-VI nanocrystal-polymer solar cells.* Journal of Photochemistry and Photobiology a-Chemistry, 2008. **195**(1): p. 39-46.
47. Kim, S.J., et al., *Carrier multiplication in a PbSe nanocrystal and P3HT/PCBM tandem cell.* Applied Physics Letters, 2008. **92**(19): p. 191107
48. Clifford, J.P., et al., *Fast, sensitive and spectrally tuneable colloidal quantum-dot photodetectors.* Nature Nanotechnology, 2009. **4**(1): p. 40-44.
49. Konstantatos, G., et al., *Ultrasensitive solution-cast quantum dot photodetectors.* Nature, 2006. **442**(7099): p. 180-183.
50. Konstantatos, G., et al., *Engineering the temporal response of photoconductive photodetectors via selective introduction of surface trap states.* Nano Letters, 2008. **8**(5): p. 1446-1450.

51. Fernee, M.J., et al., *Direct observation of mixed-parity excited states in surface-passivated PbS nanocrystals.* Nanotechnology, 2004. **15**(9): p. 1351-1355.
52. Barkhouse, D.A.R., et al., *Thiols Passivate Recombination Centers in Colloidal Quantum Dots Leading to Enhanced Photovoltaic Device Efficiency.* Acs Nano, 2008. **2**(11): p. 2356-2362.
53. de la Torre, G., et al., *Role of Structural Factors in the Nonlinear Optical Properties of Phthalocyanines and Related Compounds.* Chemical Reviews, 2004. **104**(9): p. 3723-3750.
54. Yu, B.L., et al., *Nonlinear optical properties of PbS nanoparticles under CW laser illumination.* Journal of Nonlinear Optical Physics & Materials, 2000. **9**(1): p. 117-125.
55. Lu, S.W., et al., *Nonlinear optical properties of lead sulfide nanocrystals in polymeric coatings.* Nanotechnology, 2002. **13**(5): p. 669-673.
56. Lyakhovetsky, V.R., et al., *New optical Nonlinear material based upon PVA with PbS quantum dots.* Molecular Crystals and Liquid Crystals, 2005. **426**: p. 205-217.
57. Asunskis, D.J., I.L. Bolotin, and L. Hanley, *Nonlinear optical properties of PbS nanocrystals grown in polymer solutions.* Journal of Physical Chemistry C, 2008. **112**(26): p. 9555-9558.
58. Asunskis, D.J. and L. Hanley, *Valence band and core level X-ray photoelectron spectroscopy of lead sulfide nanoparticle-polymer composites.* Surface Science, 2007. **601**(19): p. 4648-4656.
59. Zachary, A.M., et al., *Cluster Beam Deposition of Lead Sulfide Nanocrystals into Organic Matrices.* Acs Applied Materials & Interfaces, 2009. **1**(8): p. 1770-1777.
60. Zachary, A.M., I.L. Bolotin, and L. Hanley, *Cluster Beam Deposition of Metal, Insulator, and Semiconductor Nanoparticles*, in *Nanofabrication using focused ion and electron beams: Principles and applications*, S. Moshkalev, Editor. 2011: New York.
61. Bolotin, I.L., et al., *Effects of surface chemistry and shape on nonlinear absorption, scattering, and refraction of PbSe nanocrystals.* Proceedings of SPIE, 2011. **7935**: p. 79350P/1-79350P/7.
62. Bolotin, I.L., et al., *Effects of Surface Chemistry on Nonlinear Absorption, Scattering, and Refraction of PbSe and PbS Nanocrystals.* Journal of Physical Chemistry C, 2010. **114**(39): p. 16257-16262.
63. Zhou, M., et al., *Synthesis of PbS nanocrystal/functionalized conducting polymers for plastic solar cells.* Int. J. Nanosci., 2011. **10**: p. 521-532.
64. Sheik-Bahae, M., et al., *Sensitive Measurement of Optical Nonlinearities Using a Single Beam.* IEEE J. Quantum Electron., 1990. **26**(4): p. 760.
65. Watt, A., et al., *A new approach to the synthesis of conjugated polymer–nanocrystal composites for heterojunction optoelectronics.* Chem. Commun., 2004. **20**: p. 2334.
66. Haberland, H., et al., *THIN-FILMS FROM ENERGETIC CLUSTER IMPACT - A FEASIBILITY STUDY.* Journal of Vacuum Science & Technology a-Vacuum Surfaces and Films, 1992. **10**(5): p. 3266-3271.
67. Wegner, K., et al., *Cluster beam deposition: a tool for nanoscale science and technology.* Journal of Physics D-Applied Physics, 2006. **39**(22): p. R439-R459.
68. Hanley, L., et al., *All-gaseous deposition of nanocomposite films*. 2008, The Board of Trustees of the University of Illinois, USA . p. 54pp.
69. Zachary, A.M., *Cluster beam deposition of nanoparticles in organic matrices for optoelectronic applications*, in *PhD Theses*. 2009, University of Illinois at Chicago.

70. Robertson, J., *Diamond-like amorphous carbon.* Materials Science & Engineering R-Reports, 2002. **37**(4-6): p. 129-281.
71. Steckel, J.S., et al., *On the mechanism of lead chalcogenide nanocrystal formation.* Journal of the American Chemical Society, 2006. **128**(40): p. 13032-13033.
72. King, S.M., et al., *Scattering indued optical limiting in Si/SiO2 nanostructure dispersions.* Opt. Commun., 2007. **276**(2): p. 305-309.
73. Li, Q.S., et al., *Broadband optical limiting in the suspensions of lead sulfide nanoparticles.* Laser Physics, 2008. **18**(4): p. 434-437.
74. Joudrier, V., et al., *Characterization of nonlinear scattering in colloidal suspensions of silica particles.* Appl. Phys. B: Lasers Opt., 2000. **70**(1): p. 105-109.
75. Hollins, R.C., *Materials for optical limiters.* Current Opinion in Solid State & Materials Science, 1999. **4**(2): p. 189-196.
76. Hollins, R.C., et al., *Optical Limiters: Spatial, Temporal, and Bio-Optical Effects.* MRS Proceedings, 1999. **597**: p. 447.
77. Goh, H.W., et al., *Optical Limiting Properties of Double-C60-End-Capped Poly(ethylene oxide), Double-C60-End-Capped Poly(ethylene oxide)/Poly(ethylene oxide) Blend, and Double-C60-End-Capped Poly(ethylene oxide)/Multiwalled Carbon Nanotube Composite.* J. Phys. Chem. B, 2003. **107**(25): p. 6056-6062.
78. Mishra, S.R., et al., *Optical limiting in single-walled carbon nanotube suspensions.* Chemical Physics Letters, 2000. **317**(3-5): p. 510-514.
79. Vivien, L., et al., *Pulse duration and wavelength effects on the optical limiting behavior of carbon nanotube suspensions.* Optics Letters, 2001. **26**(4): p. 223-225.
80. Lad, A.D., et al., *Three-photon absorption in ZnSe and ZnSe/ZnS quantum dots.* Applied Physics Letters, 2007. **90**(13).
81. Venkatram, N., R.S.S. Kumar, and D.N. Rao, *Nonlinear absorption and scattering properties of cadmium sulphide nanocrystals with its application as a potential optical limiter.* Journal of Applied Physics, 2006. **100**(7).
82. Venkatram, N., D.N. Rao, and M.A. Akundi, *Nonlinear absorption, scattering and optical limiting studies of CdS nanoparticles.* Optics Express, 2005. **13**(3): p. 867-872.
83. Lin, Y., et al., *Third-order optical nonlinearity and figure of merit of CdS nanocrystals chemically stabilized in spin-processable polymeric.* Journal of Materials Science, 2004. **39**(3): p. 993-996.
84. Creekmore, S., et al., *Nonlinear optical properties of cadmium telluride semiconductor nanocrystals for optical power-limiting application.* Journal of the Korean Physical Society, 2003. **42**: p. S143-S148.
85. Seo, J.T., et al., *Evaluation of nonlinear optical properties of cadmium chalcogenide nanomaterials.* Physica E-Low-Dimensional Systems & Nanostructures, 2003. **17**(1-4): p. 101-103.
86. Han, M.Y., et al., *Characterization and third-order optical nonlinearities of uniform surface-modified CdS nanoparticles.* Talanta, 1998. **45**(4): p. 735-738.
87. Han, M.Y., et al., *Large nonlinear absorption in coated Ag2S/CdS nanoparticles by inverse microemulsion.* Journal of Physical Chemistry B, 1998. **102**(11): p. 1884-1887.
88. Jia, W.L., et al., *Optical limiting of semiconductor nanoparticles for nanosecond laser pulses.* Applied Physics Letters, 2004. **85**(26): p. 6326-6328.
89. Jawaid, A.M., et al., *Shape controlled colloidal synthesis of rock-salt lead selenide nanocrystals.* Abstracts of 240th ACS National Meeting, 2010: p. INOR-128.

C. Laser Eye Protection: Damage of Materials

1. Summary

Low cost fiber and other lasers that produce short- and ultrashort (from nano- to femtosecond) pulses have begun to appear in the operational theater. The goal of this work was to examine atypical damage induced by ultrashort pulses in various materials to facilitate evaluation of the threat from ultrashort pulsed lasers. Damage mechanisms were studied using two techniques: ablation time-of-flight mass spectrometry (ATOF-MS) and laser-induced breakdown spectroscopy (LIBS).

a) *LIBS*

Trains of femtosecond laser pulses were designed to maximize damage to a material. The principle diagnostics used were laser-induced breakdown spectroscopy (LIBS) and optical and atomic force microscopy. The LIBS signal was found to increase by an order of magnitude with the separation between a pair of identical pulses, with evidence that the amount of ablated material is also enhanced by the double pulse. Still greater enhancement of the LIBS signal was observed with trains of three and five pulses. Strong second harmonic generation far from the specular angle is still another indication of enhanced surface damage. The phenomenon of polarization-resolved LIBS was discovered, and a mechanism based on surface reflection of unpolarized plasma photoemission was deduced.

b) *ATOF-MS*

A custom mass spectrometer was designed and built to allow correlation of the effects of pulse trains on the surface morphology of an ablated surface with the photoluminescence spectrum and the ion signal formed by ablation. Demonstration experiments were performed at high vacuum and at intermediate pressures. This system allowed a rare opportunity to obtain this range of diagnostics for the same process which lead to additional insights into damage mechanisms not obtained by other methods.

2. Introduction

When an intense laser is focused onto a surface, a complex series of events is launched, ending ultimately in the melting and ablation of the material [1]. The initial step is always excitation of electrons, which couple to the electric field of the laser. Subsequent behavior depends on the nature of the material and the properties of the laser pulse. In the case of a metal, the high density of conduction electrons and their low heat capacity leads to a very rapid increase in the electronic temperature, followed by thermal equilibration of the electrons and lattice on a time scale of several picoseconds (ps). For semiconductors and dielectrics, several photons are required to bridge the bandgap and promote electrons to the conduction band. After this multiphoton process, collisional absorption by the electrons (also known as inverse Bremsstrahlung) initiates an avalanche, which creates a plasma. Following these initial steps, the lattice is heated to several thousand degrees until its temperature exceeds the melting and boiling points of the material. Non-equilibrium paths may produce super-heated phases, resulting in a phase explosion, ablation, and spallation. For transparent materials, an additional damage route is self-focusing of the laser beam inside the material. The resulting energy confinement can create voids, cracks, and material compaction. In competition with all of these processes, thermal and mechanical waves radiating from the focal zone transfer energy to surrounding areas and induce collateral damage.

The duration of the laser pulse is a key parameter in determining the extent of laser damage. For a given pulse energy, the intensity, I, varies inversely with the pulse width. Since the rate of multiphoton absorption of n photons is proportional to I^n, short pulses are much more effective in damaging wide bandgap materials. An additional consideration is the rate of thermal and mechanical dissipation of energy. For sub-ps pulses, damage to the focal area occurs before thermal and mechanical diffusion to surrounding areas has time to develop. A third consideration is the possibility of creating trains of very short pulses, such that the target is bombarded multiple times before energy dissipation occurs. During this period of vulnerability, successive pulses may cause more damage than a single pulse of the same total energy. This factor is especially relevant for a moving target. By way of illustration, if a target moving at mach 3 is struck by a pair of pulses separated by 100 femtoseconds (fs), the typical pulse width of a Ti:Sapphire laser, the target will have moved only 0.1 nm between pulses. The same target hit by a pulse-pair separated 1 µs (the pulse width of a typical CO_2 laser) will have moved 1 mm, well beyond the spot size of a tightly focused laser beam. Still a further consideration is the possibility of using a feedback loop to convert fs pulses into complex pulse trains designed to produce maximal damage.

The goals of this research project are to study the damage produced by femtosecond laser pulses to a variety of materials, including metals, semiconductors, and transparent dielectrics. We have evaluated the effects of pulse energy, spacing, focal position, and polarization. The principle tools we have used to assess the effects of the laser pulse are laser-induced breakdown spectroscopy (LIBS) [2, 3] and optical and atomic force miscroscopy (AFM). In the course of this work we discovered two new phenomena: (a) polarization of the LIBS spectrum and (b) second harmonic generation (SHG) at non-specular angles, which is an indicator of surface damage.

In addition, the ionized part of the plume can be used for mass spectrometric **(**MS) image analysis of known and unknown species within inorganic, organic, polymeric, or biological samples, while maintaining information on their spatial distribution, allowing correlation of chemical ion signals with macroscopic structures [4-7]. However, it is unclear which pressure is optimal for imaging. As pressure increases, collisions of laser desorbed species with background gas lead to internal cooling and collision induced dissociation [8, 9]. Elevated pressures might also lead to analyte oxidation and/or alteration of desorption plume dynamics. Analysis at atmospheric pressure (AP) occurs without samples suffering the dehydrating effects (and resultant structural modifications) of vacuum.

Some prior work using ultrashort laser pulses for desorption and/or ablation has been performed under vacuum, but most studies been done at AP. This work demonstrated how to design and build instruments which allow ion signal recording during experiments performed both at high vacuum or intermediate pressures.

3. Methods, Assumptions and Procedures

a) *LIBS*

A schematic drawing of the basic apparatus is shown in Figure 1. A Titanium Sapphire laser generates pulses of 800 nm radiation with a duration of 60 fs. In a typical experiment the beam is divided in two by a beam-splitter (BS). The two components are sent into the arms of a Michelson interferometer to create a delay between them and then recombined into a single beam. The energy of the beam is adjusted with a combination of a half wave plate (λ/2) and a polarizer (P). In some experiments, additional half wave plates are used to select the polarizations of the pulses generated in each arm of the interferometer. A lens or microscope objective (L) is next used to focus the beam onto the target in open air. A computer-controlled translation stage moves the sample so that a fresh surface is exposed to each laser shot. An interference filter (not shown) is used to reject scattered laser light, a second lens is used to focus luminescence from the crystal onto a spectrograph, and a second polarizer is used to measure the polarization of the emission.

In some experiments, a spatial light modulator (SLM) is used instead of the interferometer to generate complex pulse trains [10]. In this apparatus, shown schematically in Figure 2, the beam is dispersed by a grating, and different frequency components of the beam are focused onto a mask consisting of 640 liquid crystals. The refractive index of each pixel is set by a computer-controlled voltage so that different frequency components of the laser beam travel faster or slower through the crystal. The components of the beam are recombined with a second lens and grating. By adjusting the voltages on the liquid crystals, we can program the spectral phase of the beam and thereby synthesize pulse shapes of arbitrary complexity. To assure that the beam entering the SLM has a Gaussian, transform-limited profile, we first clean up the pulse using the multiphoton intrapulse interference phase scan (MIIPS) technique [11].

Laser-induced damage to the sample is measured in some experiments using optical and atomic force microscopy.

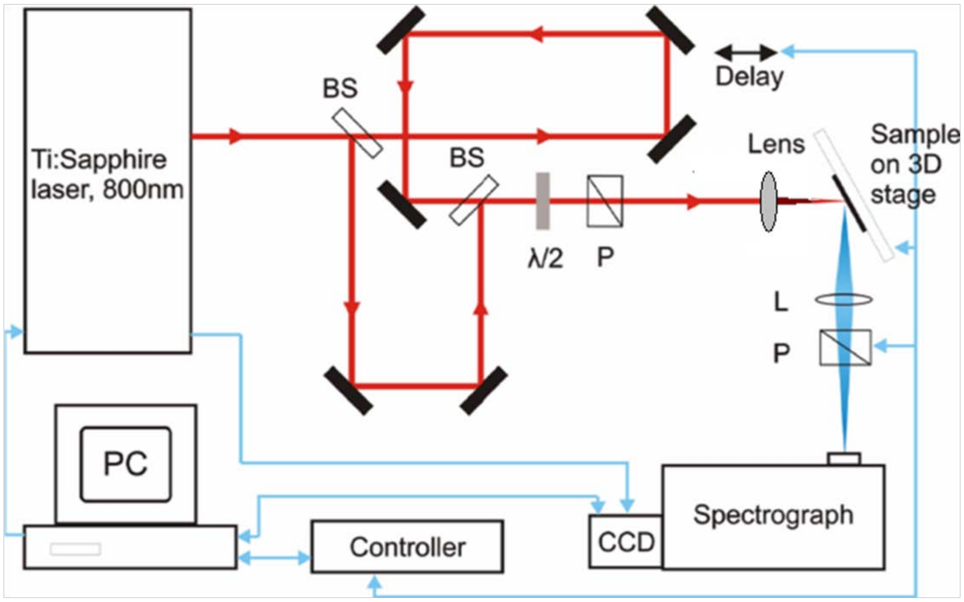

Figure 1. Experimental setup for double pulses

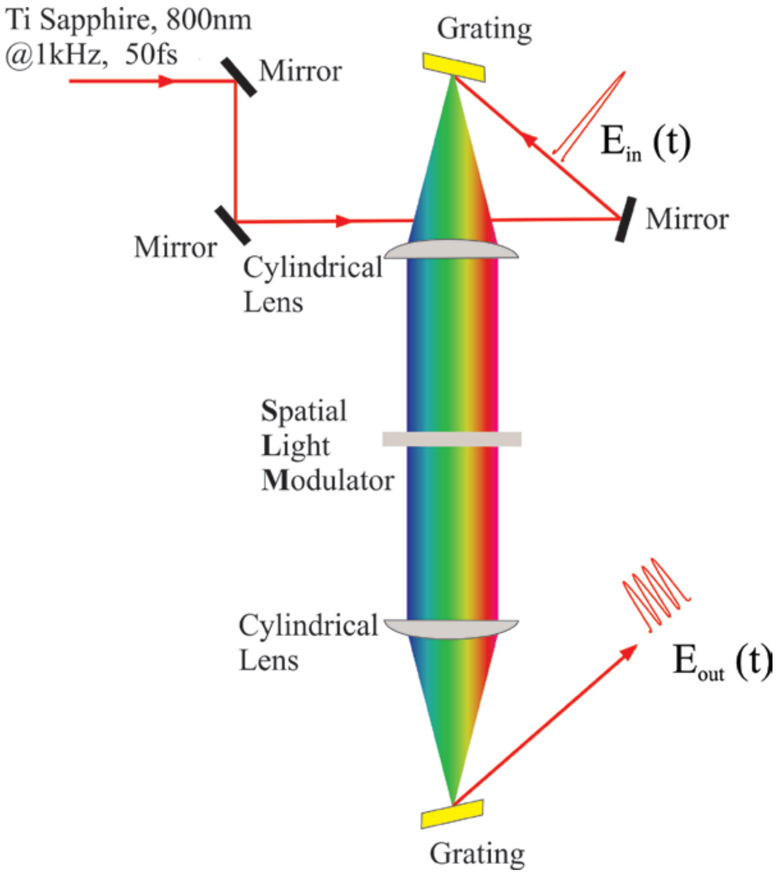

Figure 2. Optical setup for spatial light modulator

b) *ATOF-MS*

The project was focused on construction and development of a novel instrument with variable pressure, femtosecond (fs) laser ablation TOF-MS (ATOF-MS). Components of the ATOF-MS had been installed and were functioning by the end of 2011. The setup of ATOF-MS instrument is shown schematically in Figure 3.

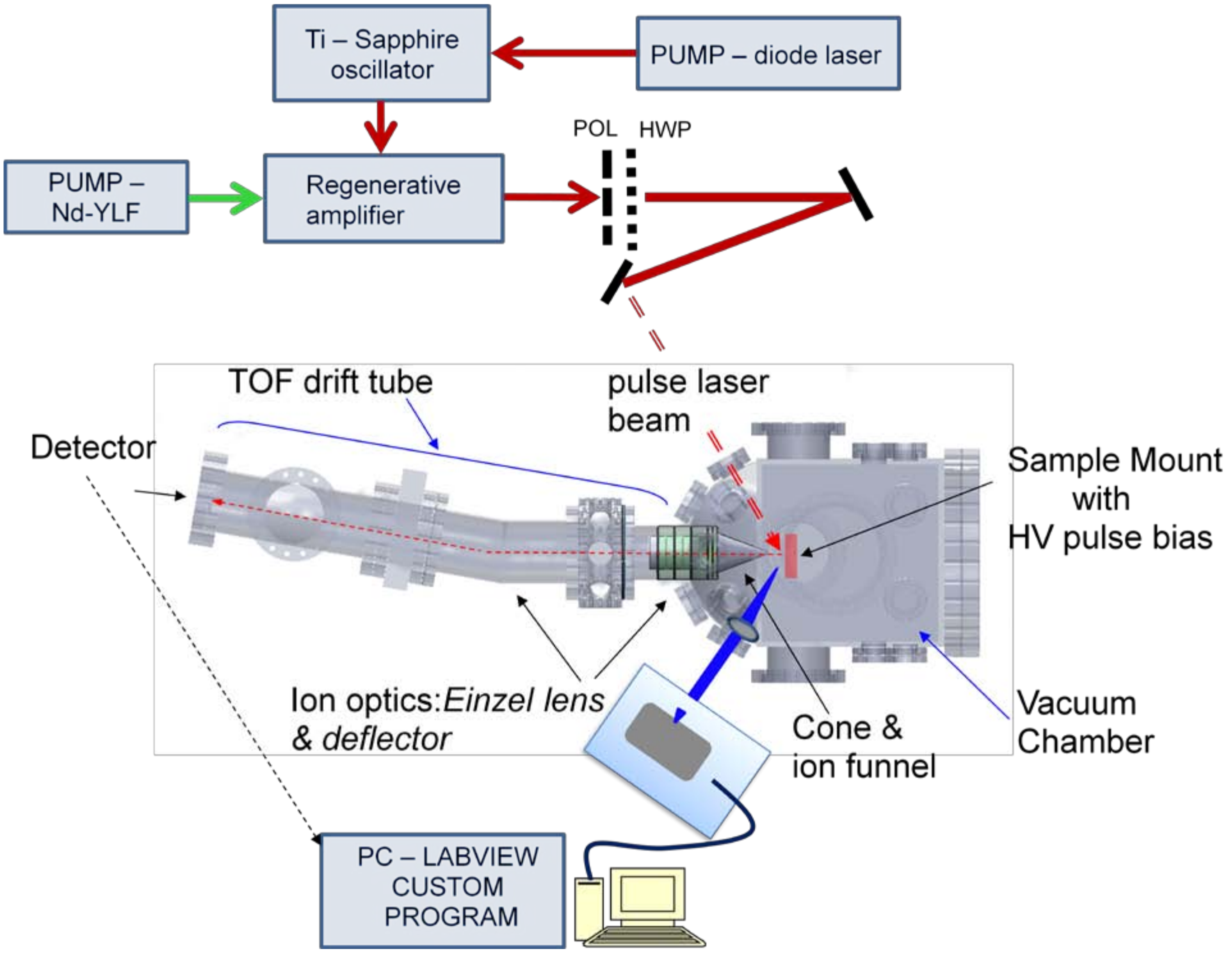

Figure 3. Schematic of ATOF-MS instrument setup.

Samples were placed on a vacuum compatible, high velocity x-y-z motion stage. The fs and ns lasers were incident at 30° from grazing, as shown by the line. At recent configuration instrument was coupled rigidly only to a Ti:sapphire laser system from Spectra Physics capable of delivering 45 fs, 800 nm pulses at 1 mJ/pulse energy and 1 kHz repetition rate. Currently, this beam is focused through a high damage threshold, long working distance microscope to deliver ~75 fs pulses to a sample with a focus of ~8 µm.

The unique features of the ATOF-MS included ~10 µm or better spatial and depth resolution source that can operate both under vacuum and at elevated pressures. The ATOF-MS setup employs a hybrid funnel–cone interface to couple the ion source with the linear time of flight (TOF) mass analyzer, allowing the ion source to operate in three different pressure ranges: $<10^{-6}$ torr or high vacuum, 10^{-3} torr or mid-pressure, and atmospheric pressure (AP). The laminar flow ion funnel enables efficient ion transport at higher pressures. Ions then pass through an expansion cone to a series of transport lenses that focused the ions onto a second differentially-pumped aperture and the remainder of the TOF path. Finally, very high speed data acquisition permitted collection of mass at up to 1 kHz, and a 1×1 mm sample area to be analyzed in 2 µm steps in less than 10 minutes.

4. Results and Discussions

a) *LIBS*

In the following sections we consider first the effects of double pulses on LIBS and SHG. Next we examine the LIBS signal produced by more complex pulse trains. These results are followed by several studies of the surface damage. Finally we describe the new phenomenon of polarization resolved laser-induced breakdown spectroscopy.

i. Double-pulse enhancement of LIBS.

A typical LIBS spectrum is shown in Figure 4 for Si(111). Measuring the signal at a fixed wavelength, we compared the LIBS intensity for a single pulse to that of a double pulse having the same total energy. The ratio of the two signals is plotted in Figure 4 for a semiconductor (Si(111) at 505.6 nm), a metal (Cu at 324.75 nm), and a dielectric (CaF_2 at 317.93 nm) as a function of the delay between the pulses. In all the cases we see a dramatic enhancement of the signal with time delay, leveling off around 100 ps. The panel on the right shows the asymptotic enhancement as a function of laser fluence. The metal and semiconductor display similar behavior, with the enhancement ratio reaching a maximum value of 11 for Cu and 6.5 for Si at fluences near 10 J/cm^2, whereas the dielectric enhancement rises gradually to a broad maximum of 2. Our results demonstrate a general phenomenon in which the first pulse produces an excited non-equilibrium state that is more susceptible to damage than the ground state. In the cases of the metal and semiconductor, the first pulse melts the material. The liquid film that is produced has different optical properties than that of the solid and interacts more strongly with the second pulse. For Si, the liquid layer is a metal, which has a much stronger extinction coefficient at 800 nm than the solid semiconductor. In the case of Cu, the liquid has a higher resistivity and therefore confines ballistic electrons generated by the laser in a smaller volume. The asymptotic growth of the enhancement with time is caused by propagation of the melt front into the bulk material at near sonic speed until its depth equals the photon absorption or electron recoil distance. The different fluence dependence of CaF_2 is a consequence of its large bandgap (10.2 eV as compared with 1.12 eV for Si). The material is much less susceptible to melting and probably undergoes a phase explosion. This work has been published in reference [12].

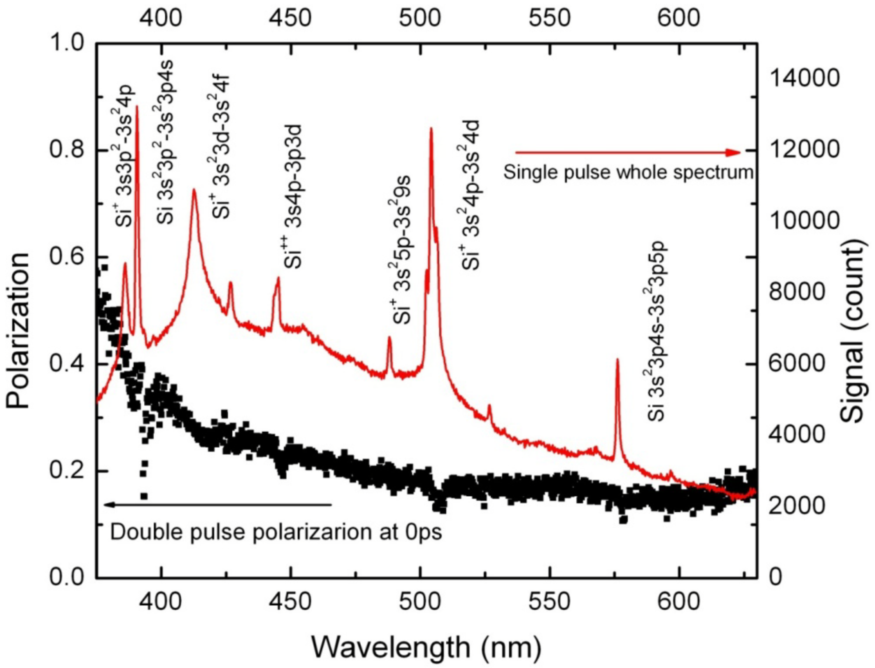

Figure 4. A typical LIBS spectrum of Si

ii. Double-Pulse SHG.

In the course of our studies of double-pulse LIBS, we discovered that under certain controlled conditions a strong second harmonic signal near 400 nm dominates the spectrum. This effect is illustrated in Figure 5, where the LIBS spectrum of Si(111) is shown for different focal positions and pulse separations. These spectra were obtained with a laser beam incident at 30^0 from the normal and detected at right angles (i.e., at 60^0 from the normal). For focal positions 50 µm above the surface (upper left panel) and 100 µm below the surface (lower right), we obtain normal multi-line LIBS spectra, with maximum intensity occurring for a pulse spacing of 93 ps. Very different behavior is observed when the laser is focused on the surface (upper right) and 50 µm below the surface (lower left). In these cases, a single 400 nm peak is observed that much stronger than any of the atomic lines. This signal, which reaches maximum intensity at a pulse separation of 20-40 ps, is the second harmonic of the Ti:Sapphire laser. Its appearance far from the specular angle of 30^0 is indicative of surface damage, which scatters light in a cone about that angle. Similar behavior was observed for BK7 glass. Figures 6-9 show in more detail the dependence of the SH signal on pulse delay, focal distance, and pulse energy. The stronger-than-quadratic energy dependence below 10 µJ is evidence that the effect we are seeing is caused by harmonic generation in a plasma and is not simply a surface effect [13]. A manuscript describing this work, which is part of the doctoral thesis of John Penczak, is in preparation.

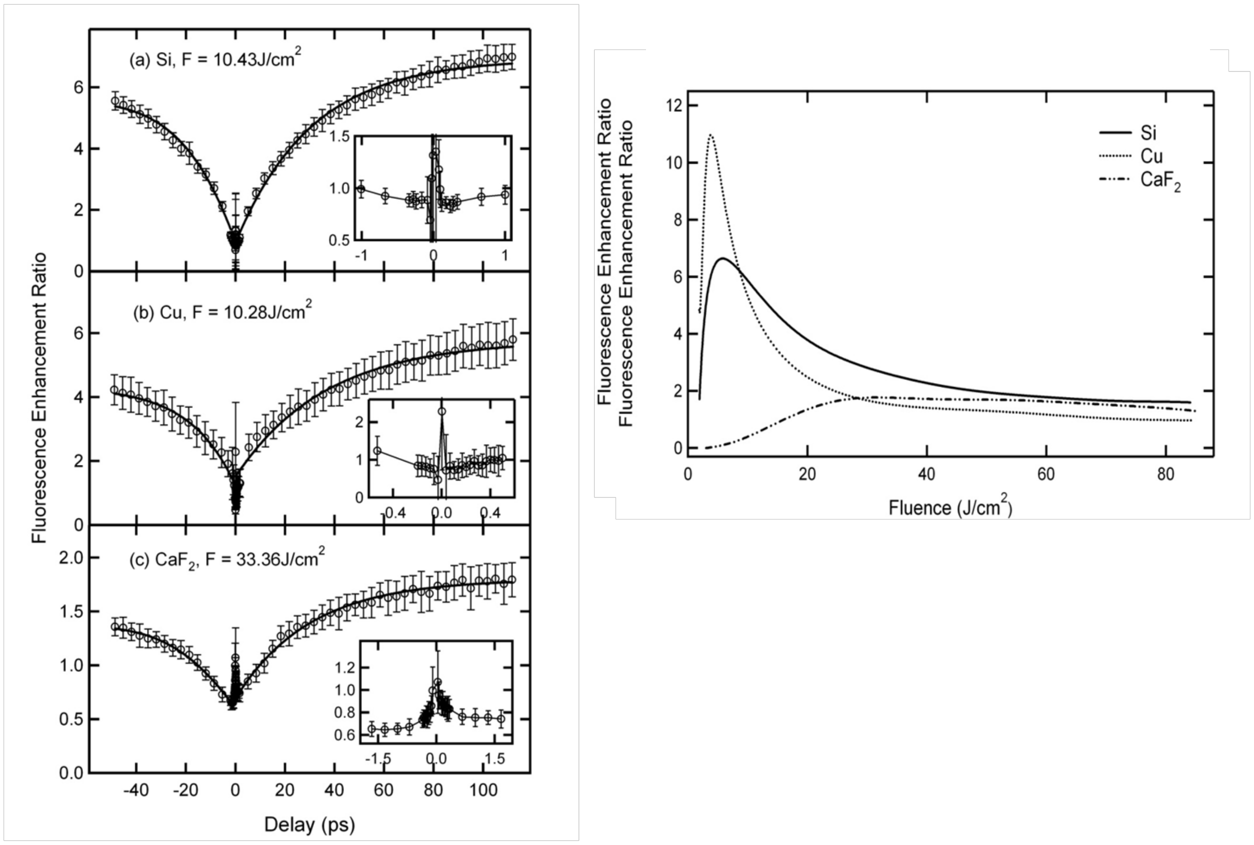

Figure 5. Double pulse enhancement of LIBS signal

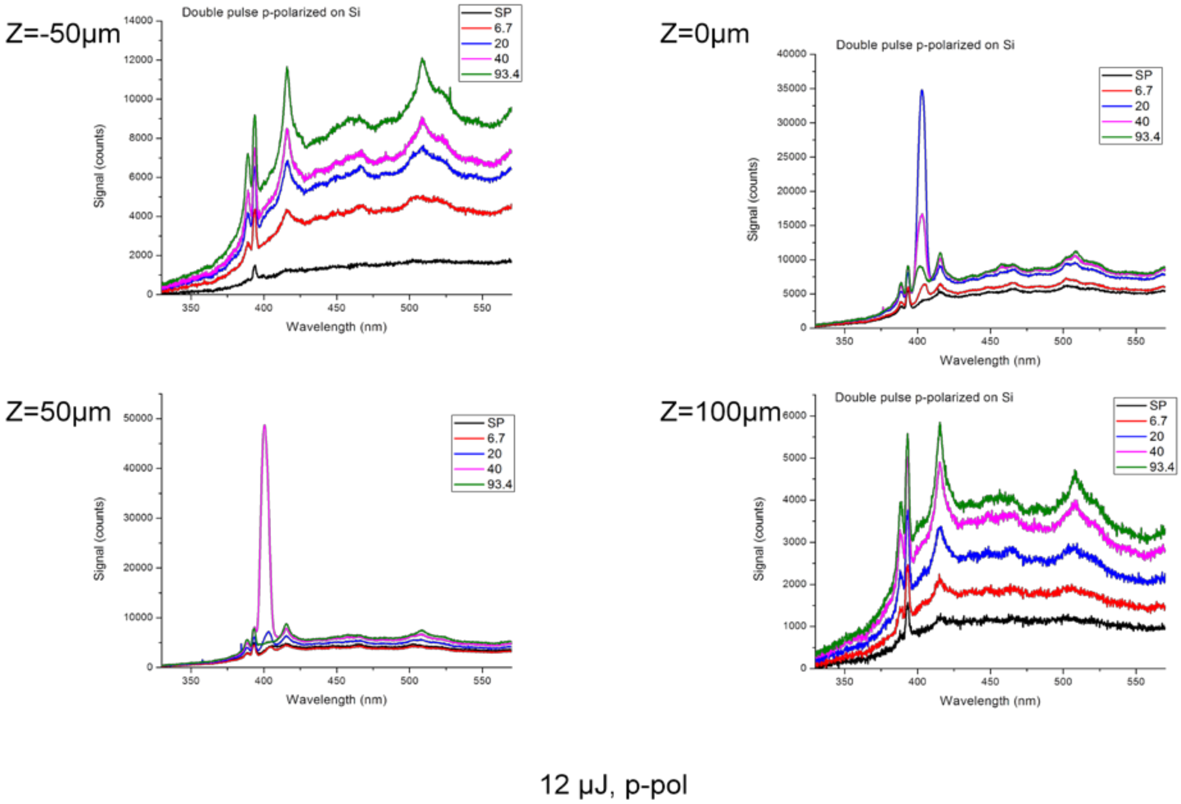

Figure 6. Double pulse second harmonic generation in Si(111). a) -50µm b) 0 µm, c) 50µm, d) 100µm.

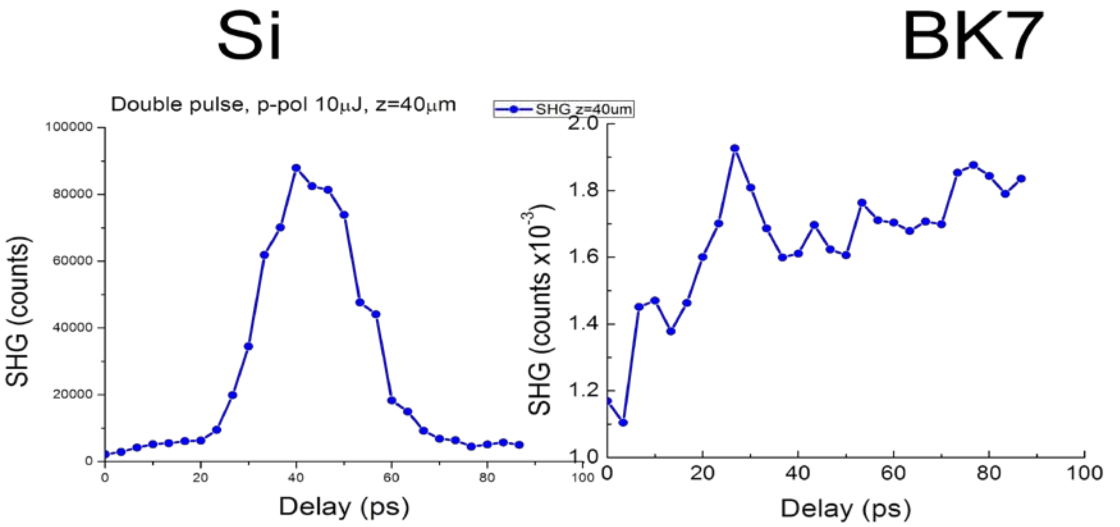

Z=40 µm, E=10 µJ, p-pol

Z=40 µm, E=20 µJ, s-pol

Figure 7. Double pulse SHG vs. time delay

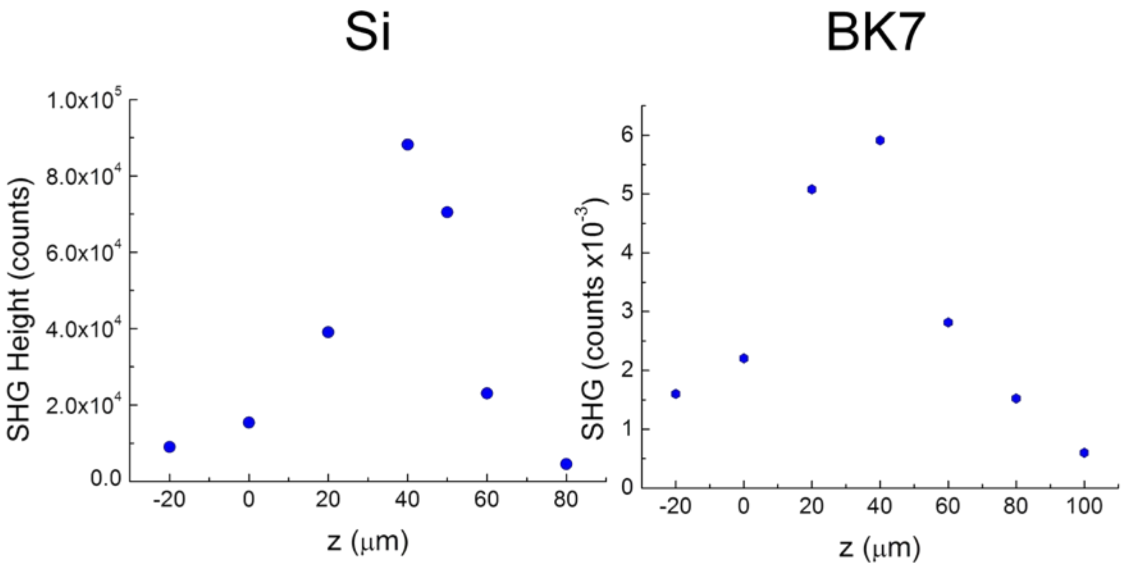

10 μJ, p-pol

20 μJ, s-pol

Figure 8. Double pulse SHG vs. focal distance

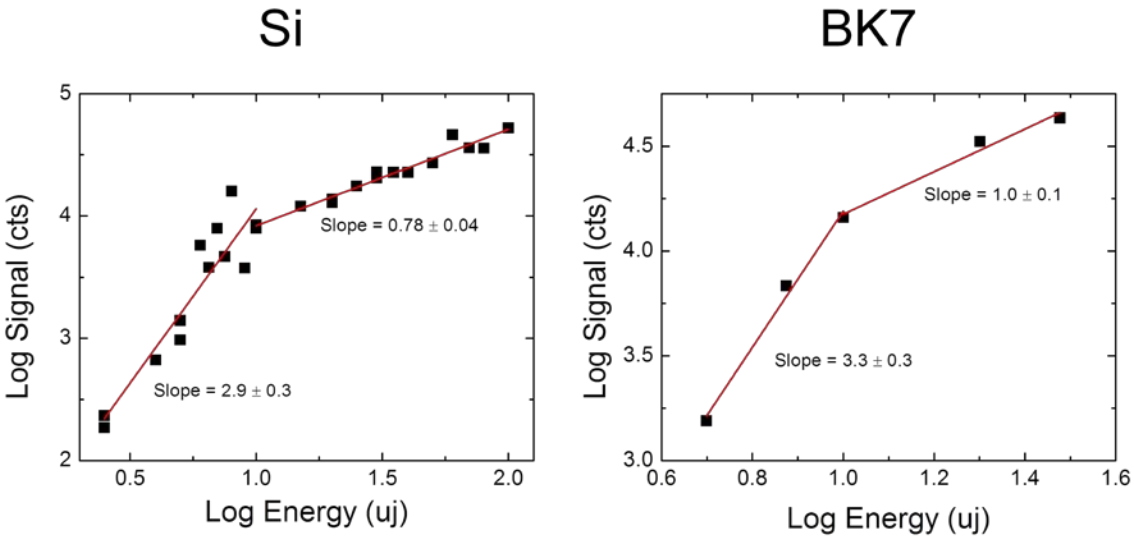

Figure 9. Double pulse SHG vs. pulse energy

iii. LIBS Spectra from Complex Pulse Trains.

In the next step we increased the number of pulses from 2 to 3 and then 5. This was accomplished by replacing the interferometer with a 640 pixel spatial light modulator (SLM, Figure 2). By employing a spectral phase that varies sinusoidally with pixel number, we generated trains consisting of odd numbers of equally spaced pulses with controllable spacing and amplitudes. In addition, a double pulse was generated by using a V-shaped phase function. Preliminary results are shown in Figures 10 and 11 for BK7 and Si(111), with the laser focused 50 μm below the surface for BK7 and on the surface for Si. The various panels correspond to different spacing of the pulse trains. We see that in general the spectrum is a sensitive function of the number and spacing of the sub-pulses for a fixed total energy.   A systematic study of the pulse shape effect remains to be done. A particularly exciting prospect is to use a feedback loop to create pulse trains that induce specific outcomes, such as to maximize the spectral output in a particular wavelength range or to minimize/maximize the overall damage. We have already achieved such an effect for GaAs as part of a different research program [14].

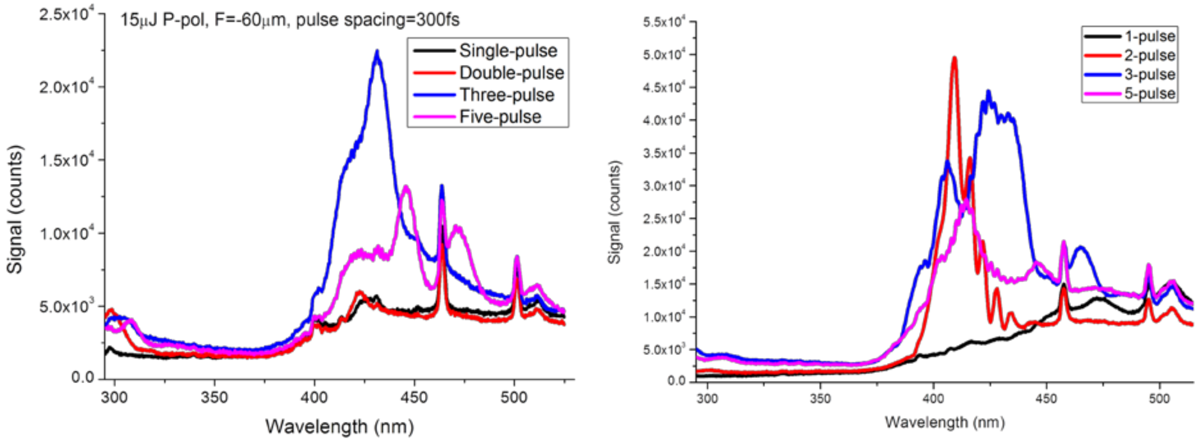

15 μJ, z=60 μm, pulse spacing: 300 fs

20 μJ, z=60 μm, pulse spacing: 220 fs

Figure 10: Plasma emission from BK7 produced by complex pulse trains

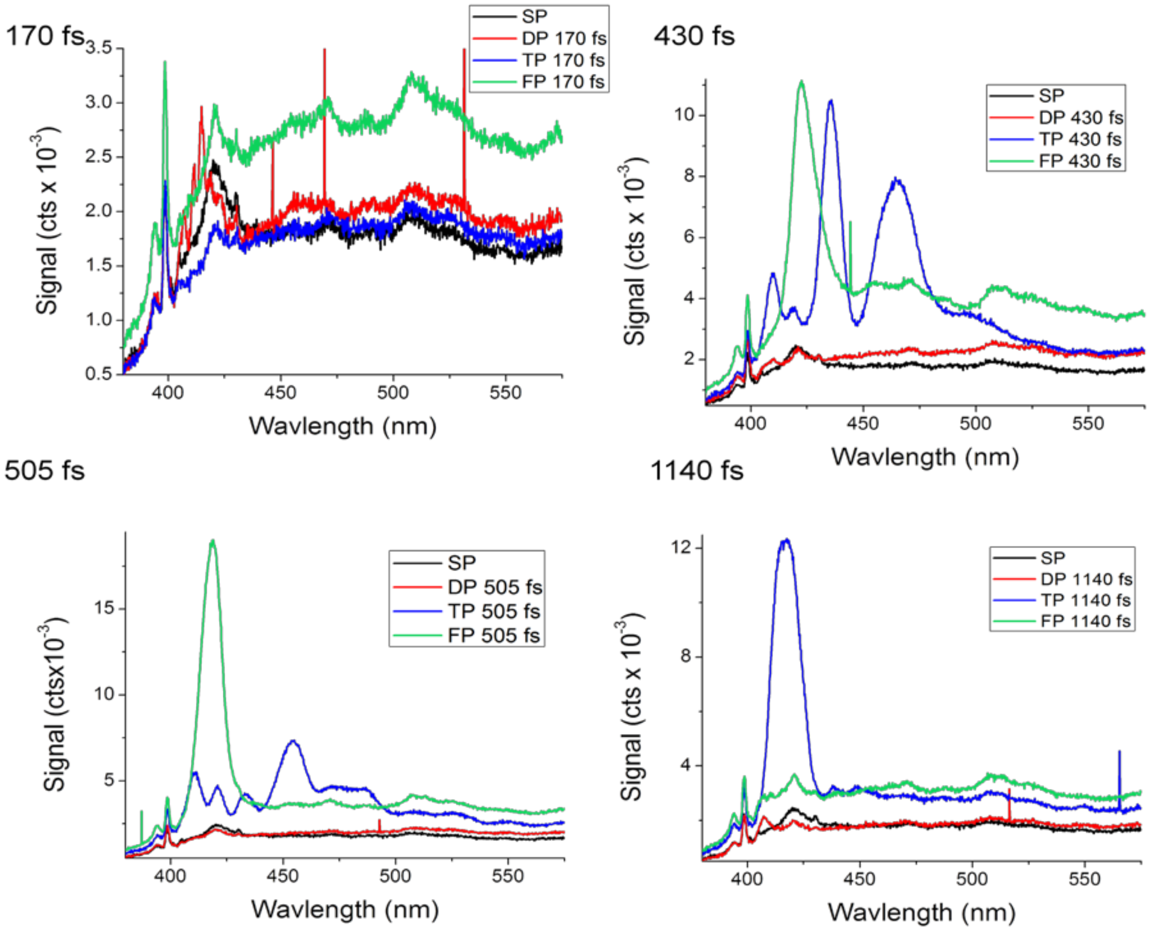

Figure 11: Plasma emission from Si produced by complex pulse trains

iv. Diagnostics of Surface Damage.

Several techniques were used to determine the surface damage created by laser pulse trains. Figure 12 shows optical microscope images of craters produced by a pair of pulses focused 100 µm beneath the surface of PDMS polymer. The images show maximum damage for pulse separations between 10 and 100 ps. Figure 13 shows atomic force microscope (AFM) images of craters produced in Si(111) and CaF_2. The V-shape of the Si crater is typical of a melting mechanism, which does not occur for CaF_2. The bottom three panels are AFM images of Si that was etched for 1 hour with 44% KOH solution after irradiation. The pulse delays were (a) 1.5, (b) 66, and (c) 86 ps.

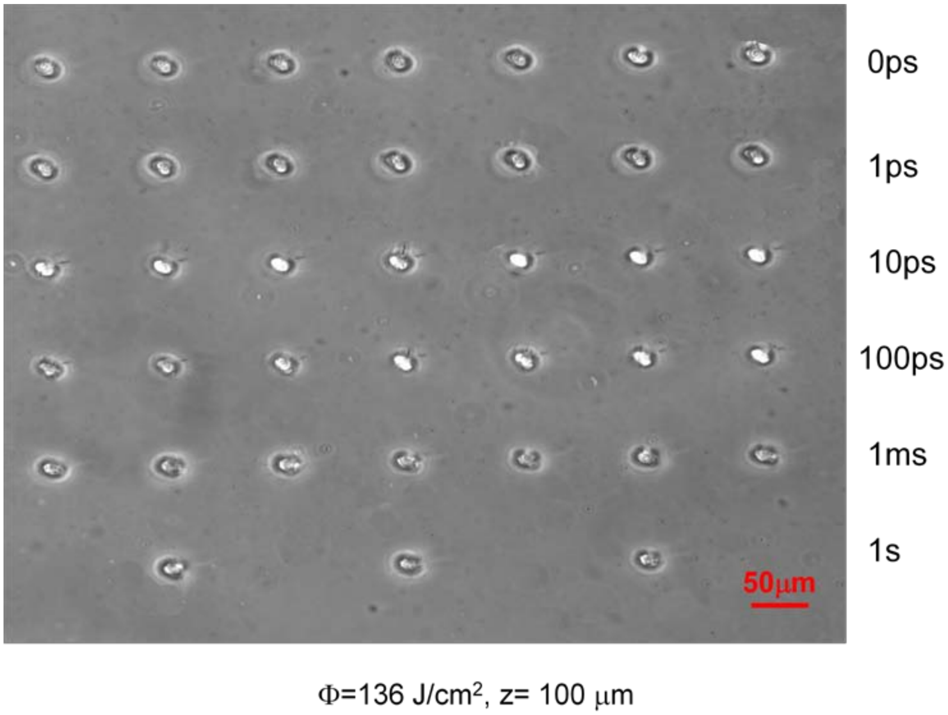

Figure 12. Optical imaging of craters in PDMS

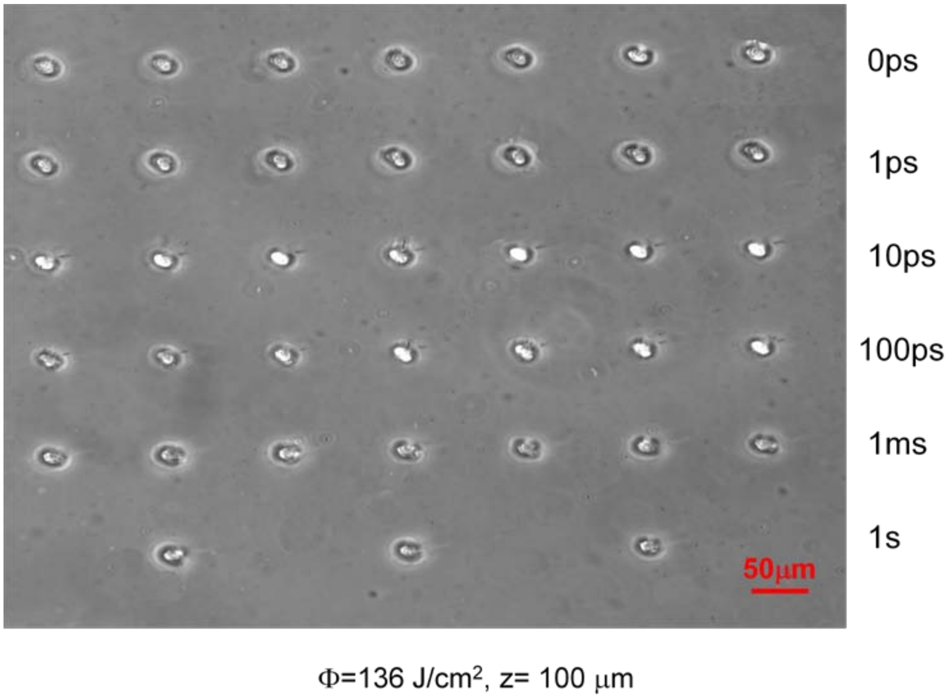

Figure 13. AFM images of Si and CaF_2 craters

The white areas in the center of panels (b) and (c) are produced by amorphous Si, which is much more resistant to etching than the crystal. The large amount of amorphous material in the crater is likely caused by condensation of material in the plume. The presence of this material highlights the difficulty of using only microscopy to assess material damage, inasmuch as the amount of material ablated by the laser may far exceed the volume of the observed crater. This point is brought home in the Figure 14, which compares crater volume and LIBS intensity under various conditions. The open circles show that for single pulses the crater volume is roughly proportional to the LIBS signal, although some re-condensation may have occurred. The laser fluence is increased from 6.2 to 91.4 J/cm^2, going from left to right. The solid points are for a double pulse having a fixed fluence of 44.5 J/cm^2, with the pulse separation increasing from 0 to 105 ps. The arrow indicates the corresponding point for a single pulse with a fluence of 44.5 J/cm^2. At first glance it appears that increasing the pulse delay has no effect on the amount of material ablated, even though we showed in Figure 4 that the LIBS signal increases with delay. The effect of the second pulse is the subject of some controversy, with some researchers maintaining that the increased LIBS signal is caused by laser heating of the plasma (e.g., by vaporization of particulates in the plume) created by the first pulse. If this were the case, however, the crater volumes for the solid points would be only half the values shown in the figure because the total energy is divided equally between the two pulses. Figure 15 presents definitive proof that the second pulse reaches the surface and does more damage than a single pulse of the same total energy. In this experiment we ablated a bilayer consisting of a 100 nm Au film deposited on a Si substrate. The single pulse spectrum shows only Au lines, whereas the double pulse shows not only a more intense Au signal but also clear evidence of ablation of the Si substrate. More systematic experiments are planned.

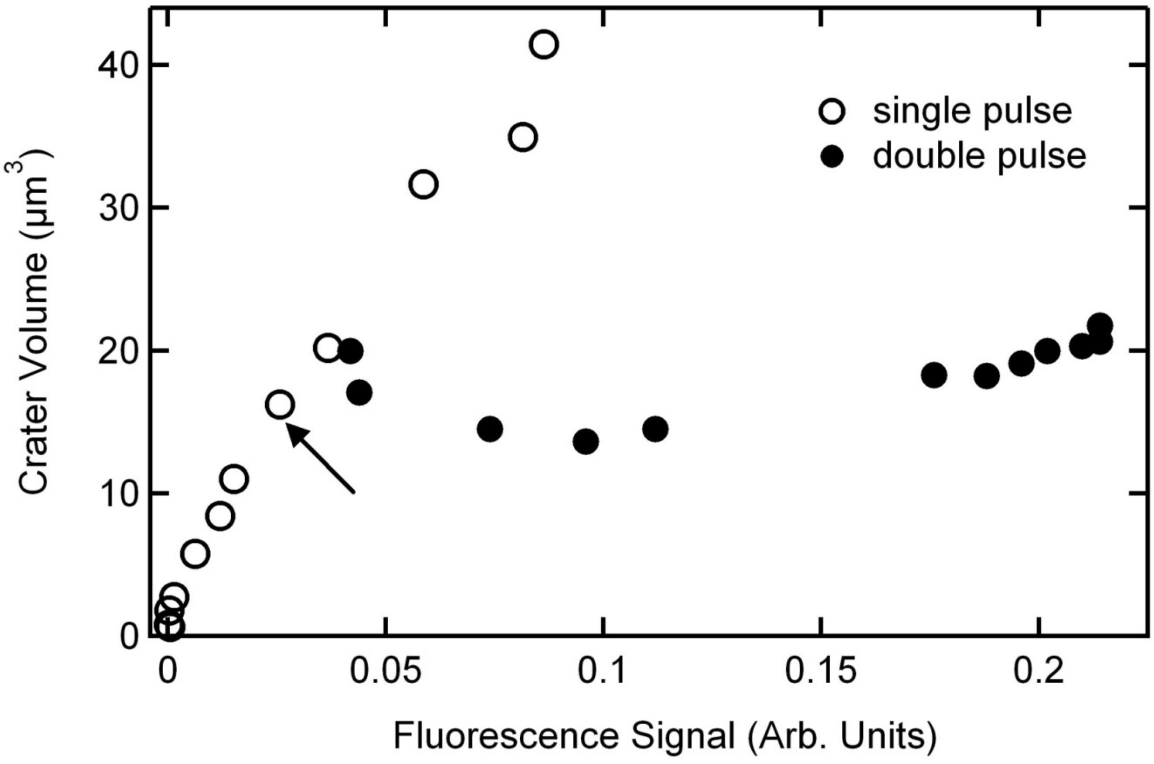

Figure 14. Volume of Si craters

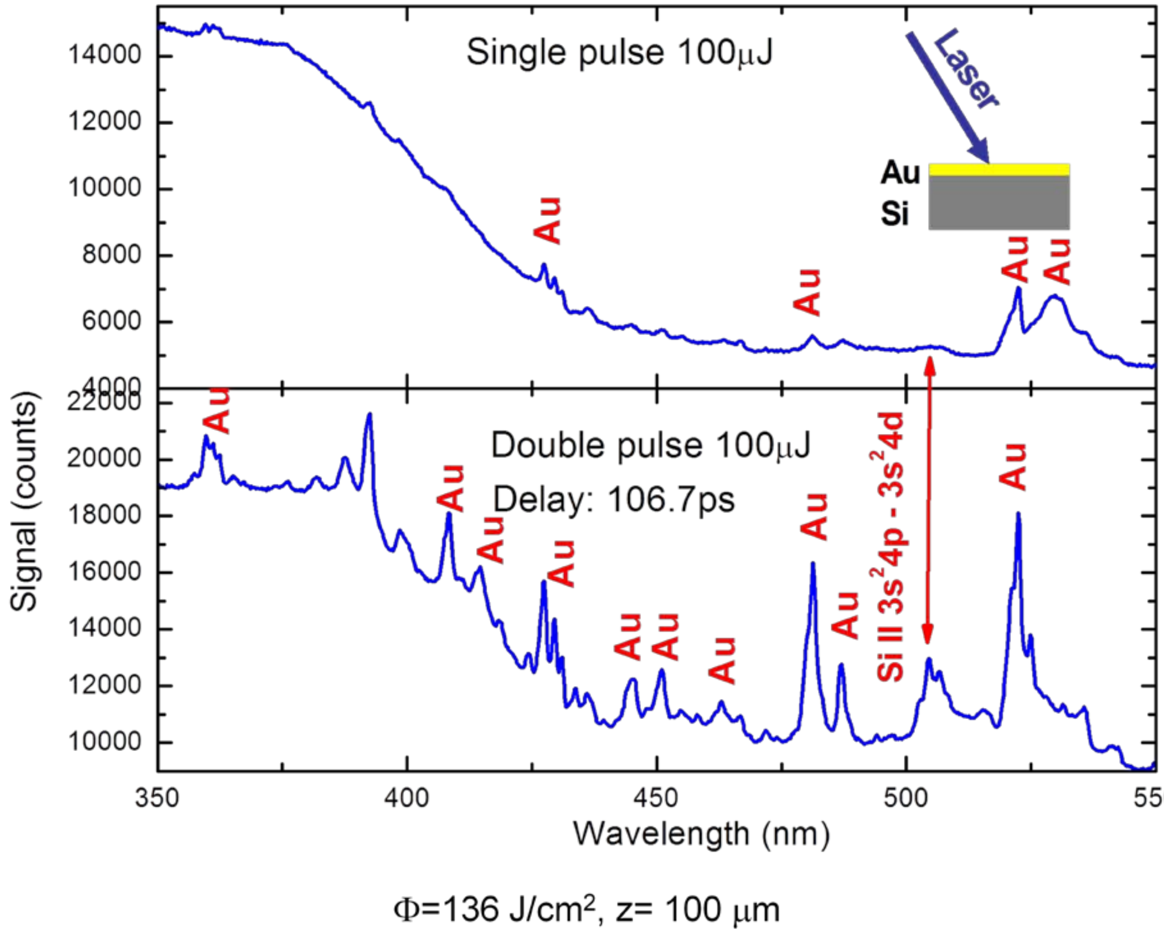

Figure 15. Double pulse ablation of Au (100nm)/Si bilayer

v. Polarization-Resolved Laser-Induced Breakdown Spectroscopy (PRLIBS).

Early in this research program we observed that under some conditions the LIBS signal may be strongly polarized, both for ns and fs ablation pulses [15-19]. An example of this phenomenon is evident in Figure 4. In order to elucidate the mechanism, we repeated the experiment at the Center for Nanoscale Materials at Argonne National Laboratory, where we had access to a ps streak camera, which allowed us to measure the polarization as a function of time. After a number of false starts, we obtained strong evidence that the mechanism for this effect is reflection of the plasma emission by the liquid layer generated by the laser. Key results are shown in Figures 16-19.

Figure 16 shows the temporal evolution of (a) the LIBS signal, (b) the amount of polarization, and (c) the angle of the polarized emission produced by single fs laser pulses. The horizontal line in panel (c) corresponds to s-polarized emission. The data show that (a) the signal level and polarization properties are independent of laser polarization, (b) the amount of polarization grows with time delay, even as the level of the signal falls off by several orders of magnitude, and (c) the emission is always s-polarized. Figure 17 shows that for ns pulses the amount of polarization is constant for fluences below 30 J/cm^2 and falls exponentially at higher fluences. Figure 18 shows the dependence of the level of polarization on the detection angle for a fixed angle of incidence. The data show a maximum polarization for a near- grazing angle (80^0) detection. A mechanism, shown schematically in Figure 19, which is consistent with all of our data is that the s-polarization is the result of Fresnel reflection of unpolarized plasma emission by the surface. Assuming that half of the light reaches the detector directly without being polarized and that the other half is s-polarized by the surface, we obtain quantitative agreement with the calculated polarization from a reflecting layer of liquid Si. This discovery was the subject of an invited paper presented at the 11th Euro-Mediterranean Symposium on LIBS in Cesme, Turkey and has been accepted for publication in Spectrochimica Acta B [20].

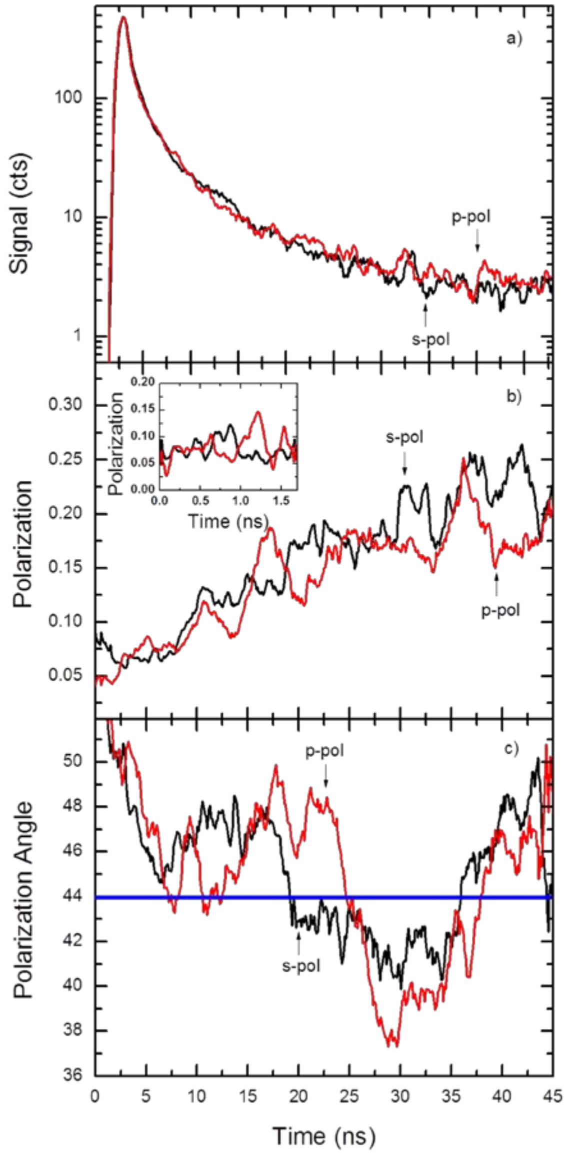

fs pulses, 100 µj, obj. lens,

18 Hz, 500 nm

Figure 16. Time-resolved PRLIBS of Si

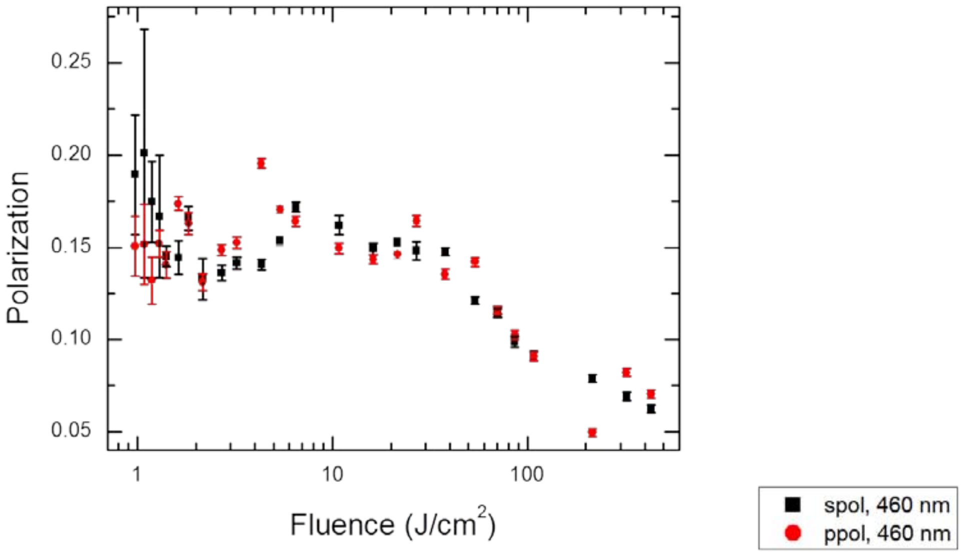

Figure 17. Energy dependence of ns PRLIBS

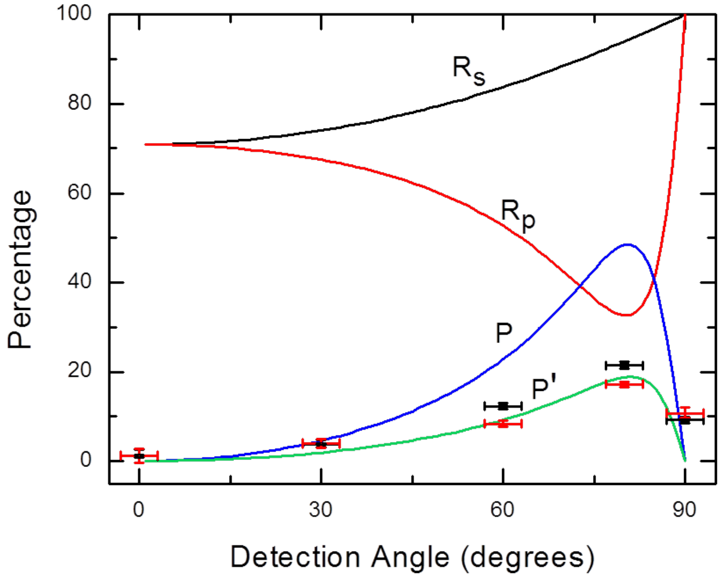

100 uj, obj lens, 18 Hz, 500 nm

Figure 18. Angle-resolved PRLIBS of Si

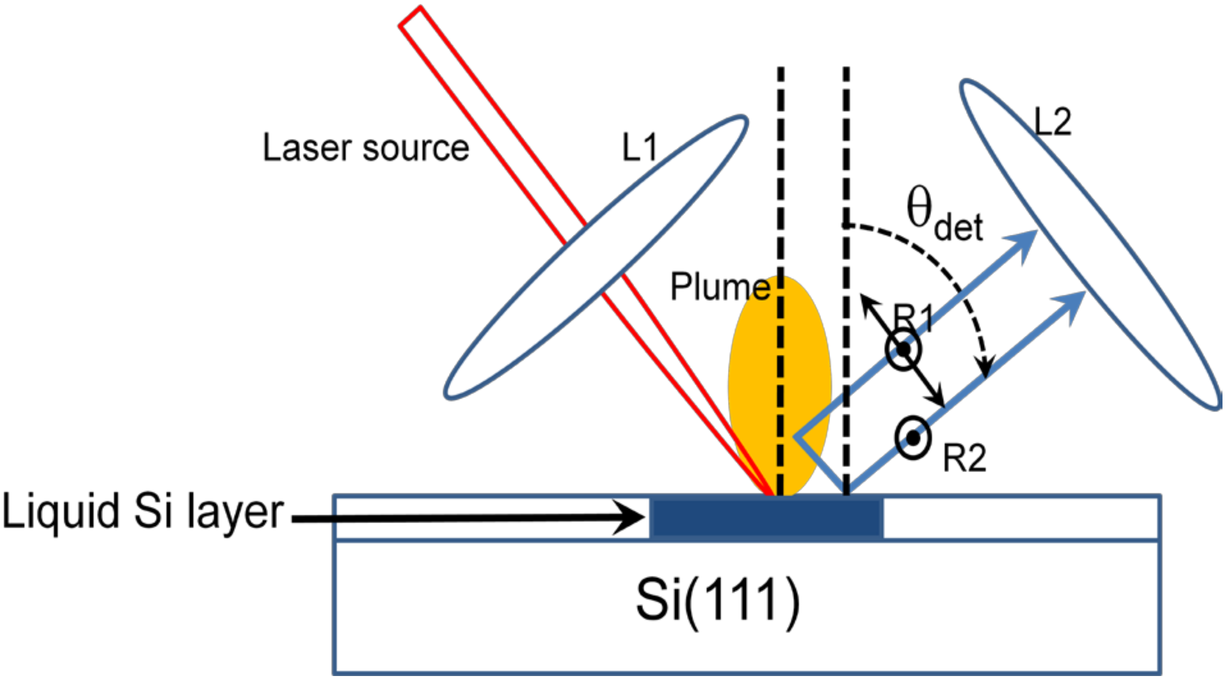

Figure 19. PRLIBS Mechanism

b) *ATOF-MS*

The beginning stage of the ATOF-MS construction was completed at the start of 2011 and included setting up of the ion optics (Einzel lens and deflector), high voltage pulsing grids and the cone that separates the ion source from the main chamber. Experiments with ablation of various targets (Ag, Cu, Ta, Mo, and Au) allowed the determination of experimental parameters, improved MS resolution and signal/noise ratio.

Figure 20 shows a typical MS of a silver (Ag) target with correct isotopes (^{109}Ag, ^{109}Ag) ratio and mass resolution R ~ 400. It was founded that mass resolution was best near laser ablation threshold for all metal targets.

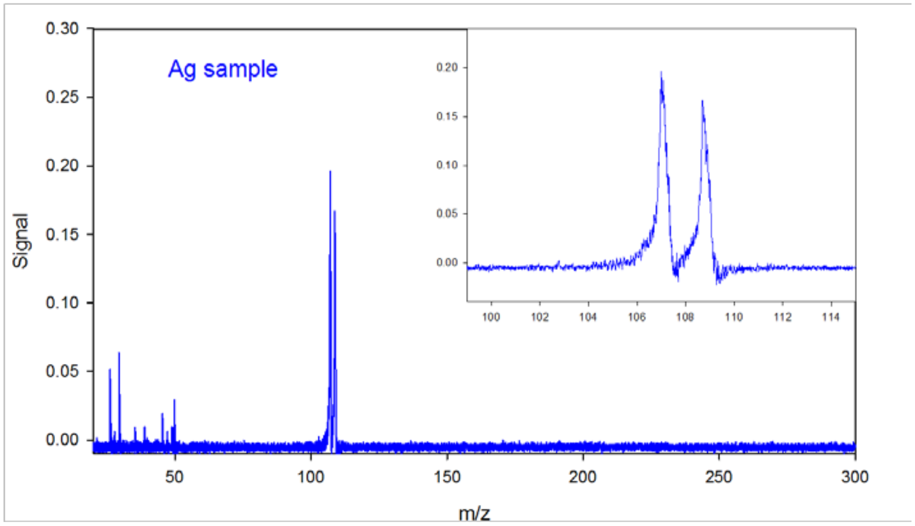

Figure 20. TOF-MS of Ag target ablated by fs laser pulses.

The next stage of ATOF-MS construction was completed at the end of 2011 and included mid-vacuum ablation experiments which demonstrated how collisions of laser ablated species with background gas lead to internal cooling, collision induced dissociation, cluster formation, protonation, charge transfer, and other gas phase collision events. The complicating factors of integrated ionization are shown for the example of laser ablated N-(1-pyrenyl) maleimide (NPM) in Figure 24. At high vacuum, the parent ion of NPM forms along with several large mass fragments where were suppressed at the elevated pressure of 10^{-3} Torr of He. The additional appearance of the m/z 55 ion at 10^{-3} Torr at the expense of the M-55 ion (observed at high vacuum) can be interpreted as resulting from charge transfer events.

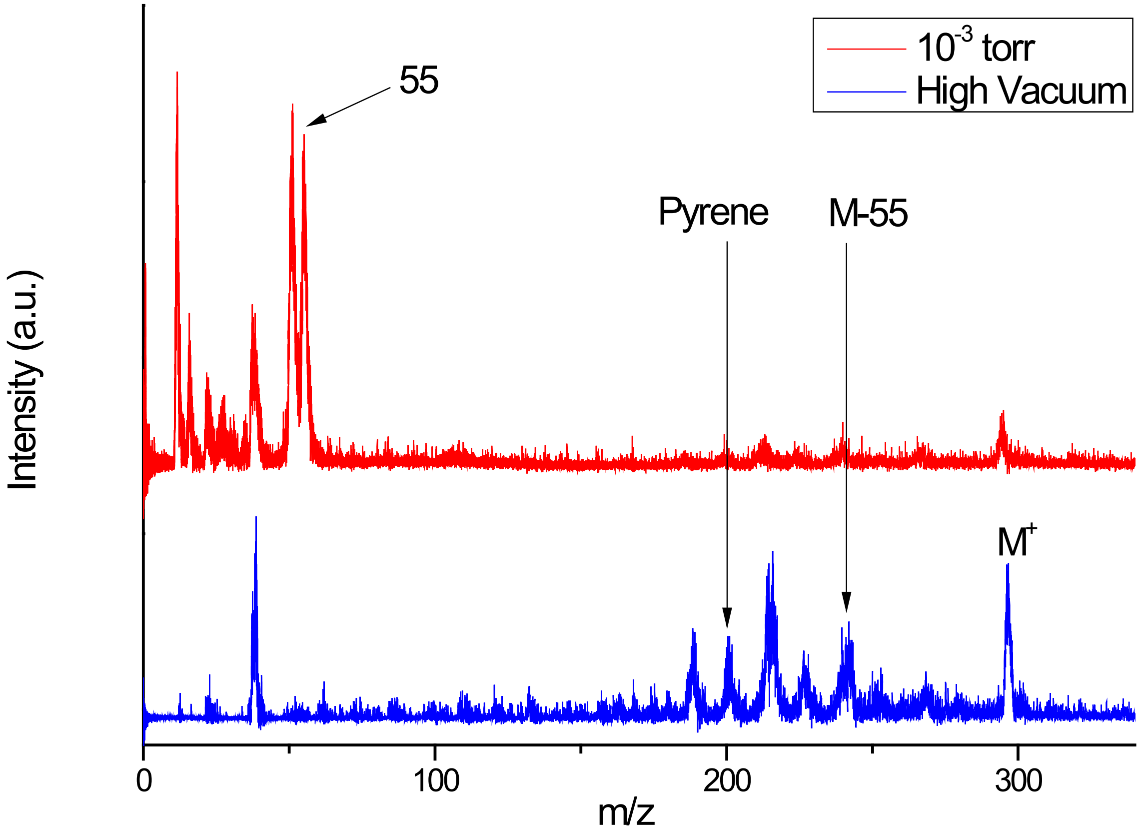

Figure 21. TOF-MS of N-(1-pyrenyl) maleimide (NPM) from 800 nm, ~70 fs laser ablation at a fluence of 10 J/cm^2 from a crystalline film. Under high vacuum (10^{-5} Torr or below, bottom spectrum in blue) the molecular ion (M^+) is observed. At the higher pressure of 10^{-3} Torr of He (top spectrum in red), the higher mass ions are suppressed or undergo collision induced dissociation. The daughter ion from the characteristic loss at M-55 is seen at 10^{-3} Torr, indicating charge transfer processes not present at high vacuum.

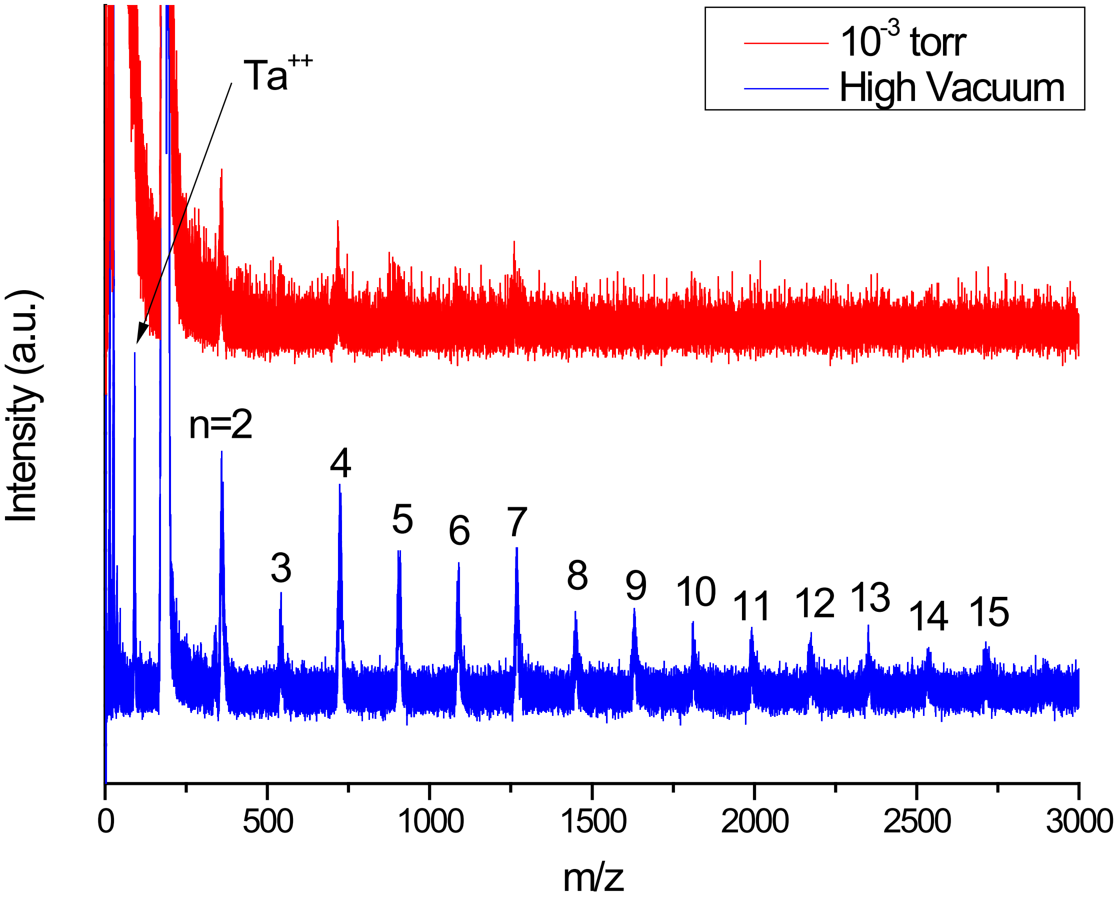

Figure 22. Tantalum cluster mass spectra from ablation by 800 nm, ~70 fs laser pulses at a fluence of 8 J/cm^2 from a laser-cleaned area of chemically etched bulk Ta. Under high vacuum ($\leq 10^{-5}$ Torr, bottom spectrum in blue) a series of Ta clusters to at least Ta$_{15}$ are observed within factors of 1-3 above the ablation threshold. Approaching higher pressures (10^{-3} Torr He, top spectrum in red) significant ion suppression and collision induced dissociation is observed, and only a few clusters are seen.

Further evidence of the role of post-ablation collisions in femtosecond laser desorption is shown in Figure 25. The TOF-MS of tantalum atomic and cluster ions observed in high vacuum mostly disappear due to ion suppression and/or collision induced dissociation when the ablation occurs into 10^{-3} Torr of He. Ablation of semiconductor targets (Si, GaAs) at threshold conditions obtained similar results for cluster suppression at mid-vacuum conditions (data not shown). Measurements of the ATOF-MS under vacuum of undoped GaAs yielded high resolution GaAs MS displaying individual isotope peaks as well as dimers, trimers, tetramers and pentamers.

Figure 26 shows a photo of the ablation plume for NPM formed by 800 nm, ~70 fs laser pulses at two different He background pressures. The photo at 10 Torr pressure shows more NPM fluorescence due to an increase in gaseous collisional cooling and plume confinement compared with 10^{-5} Torr.

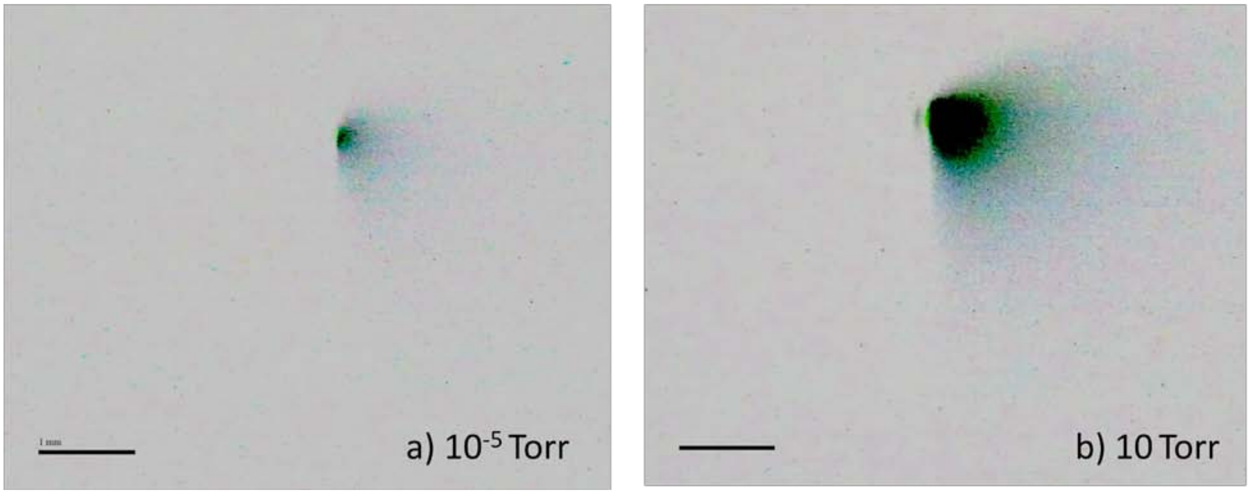

Figure 26. Photographs of fluorescent plumes from a film of N-(1-pyrenyl) malemide (NPM) ablated from a metal surface using 800 nm, ~70 fs laser pulses at a fluence of 10 J/cm^2 (several times ablation threshold). The sample is in profile with the femtosecond laser incident near the center of the field of view. Both photos have been inverted, noise filtered and levels adjusted identically. a) The high vacuum (10^{-5} Torr) photo shows a diffuse plume from the uncooled, high translational energy molecules. b) The photo recorded at a background pressure of 10 Torr of He shows a significantly brighter plume is observed which indicates that collisional cooling is confining the ablated molecules. The energy of the ionized portion of the ablated material extends to over 100 eV, as determined by an electrostatic energy analyzer. The scale bar in each photo corresponds to 1 mm.

Finally, an additional task was performed at the end of 2011 that tested a new microfocusing light optic and software for MS-imaging measurements for 2D analysis and depth profiling for 3D analysis. MS-imaging scans of metal TEM grids achived 20 micron resolution with 25 cm focal length lens. Another 17.5 cm focal length objective lens was installed and a 5 micron laser spot was archived. Due to the objective lens outgasing, pressures below 10^{-5} torr could not be achieved. Depth profiling was successively performed through 300 nm thick Ta_2O_5 on Ta Foil and collodially synthesized, ~4 nm PbS nanocrystals nanocomposites on stainless steel were also analyzed (data not shown).

5. Conclusions

a) *LIBS*

Double pulses of femtosecond laser radiation produce an order-of-magnitude more intense laser-induced breakdown spectrum. There is substantial evidence that the enhanced photoemission is accompanied by greater material damage. Complex pulse trains produce even more intense LIBS spectra, and there are prospects for optimizing this effect by using feedback to shape the laser pulse. A strong second harmonic signal was observed far from the specular angle. This effect is produced by a double laser pulse and is sensitive to the pulse separation and focal position. Polarization of the LIBS spectrum was observed for the first time, and evidence was found for a surface-reflection mechanism.

This work opens up several promising new lines of inquiry. A learning algorithm may be used to create laser pulses designed to maximize or minimize damage to a surface. This methodology may also be used as a powerful diagnostic tool, with the pulse shape optimized to maximize the LIBS spectrum in specified spectral regions. Bilayers of material consisting of metal or semiconductor films deposited on selected substrates may be used to obtain quantitative information about the ability of a laser to penetrate the surface. Feedback techniques may be used to enhance this effect.

b) *ATOF-MS*

Construction of an ATOF-MS was completed and the instrument was found to display sufficient MS resolution. This instrument incorporates a time of flight (TOF) mass analyzer and a variable pressure vacuum ion ablation, which currently operate under transition gas flow conditions up to pressures of ~10^{-3} Torr. Operation at intermediate pressures facilitates comparison with photoluminescence studies of femtosecond laser ablation.

6. References

1. Haglund, R.F., *Laser Ablation and Desorption*, ed. J.C.M.a.R.F. Haglund. 1998, San Diego: Academic Press.
2. Cremers, D.A. and L.J. Radziemski, *Handbook of Laser-Induced Breakdown Spectroscopy*. 2006, New York: Wiley.
3. Singh, J.P. and S.N. Thakur, *Laser-Induced Breakdown Spectroscopy*. 2007, Boston: Elsevier.
4. Rubakhin, S.S., et al., *Imaging mass spectrometry: fundamentals and applications to drug discovery.* Drug Discovery Today, 2005. **10**(12): p. 823-837.
5. Reyzer, M.L. and R.M. Caprioli, *MALDI-MS-based imaging of small molecules and proteins in tissues.* Current Opinion in Chemical Biology, 2007. **11**(1): p. 29-35.
6. Seeley, E.H. and R.M. Caprioli, *Molecular imaging of proteins in tissues by mass spectrometry.* Proceedings of the National Academy of Sciences of the United States of America, 2008. **105**(47): p. 18126-18131.
7. Chughtai, K. and R.M.A. Heeren, *Mass Spectrometric Imaging for Biomedical Tissue Analysis.* Chemical Reviews, 2010. **110**(5): p. 3237-3277.
8. Bae, Y.J., J.H. Moon, and M.S. Kim, *Expansion Cooling in the Matrix Plume is Under-Recognized in MALDI Mass Spectrometry.* Journal of the American Society for Mass Spectrometry, 2011. **22**(6): p. 1070-1078.
9. Soltwisch, J., et al., *Effect of Gas Pressure and Gas Type on the Fragmentation of Peptide and Oligosaccharide Ions Generated in an Elevated Pressure UV/IR-MALDI Ion Source Coupled to an Orthogonal Time-of-Flight Mass Spectrometer.* Analytical Chemistry, 2009. **81**(8): p. 2921-2934.
10. Wiener, A.M., *Femtosecond pulse shaping using spatial light modulators.* Rev. Sci. Inst., 2000. **71**: p. 1929.
11. Lozovoy, V.V., I. Pastirk, and M. Dantus, *Multiphoton intrapulse interference. IV. Ultrashort laserpulse spectral phase characterization and compensation.* Opt. Lett., 2004. **29**(7): p. 775-777.
12. Singha, S., Z. Hu, and R.J. Gordon, *Ablation and plasma emission produced by dual femtosecond laser pulses*. Journal of Applied Physics, 2008. **104**(11): p. 113520.
13. Engers, T., et al., *Second-harmonic generation in plasmas produced by femtosecond laser pulses.* Physical Review A, 1991. **43**(8): p. 4564-4567.
14. Singha, S., Z. Hu, and R.J. Gordon, *Closed Loop Coherent Control of Electronic Transitions in Gallium Arsenide.* The Journal of Physical Chemistry A, 2011. **115**(23): p. 6093-6101.

15. Liu, Y., J.S. Penczak, and R.J. Gordon, *Nanosecond polarization-resolved laser-induced breakdown spectroscopy.* Opt. Lett., 2010. **35**(2): p. 112-114.
16. Liu, Y., et al., *Observation of near total polarization in the ultrafast laser ablation of Si.* Applied Physics Letters, 2008. **93**(16): p. 161502-3.
17. Penczak, J.S., Y. Liu, and R.J. Gordon, *Polarization Resolved Laser-Induced Breakdown Spectroscopy of Alâ€* The Journal of Physical Chemistry A, 2009. **113**(47): p. 13310-13317.
18. Penczak, J.S., Y. Liu, and R.J. Gordon, *Polarization and fluence dependence of the polarized emission in nanosecond laser-induced breakdown spectroscopy.* Spectrochimica Acta Part B: Atomic Spectroscopy, 2011. **66**(2): p. 186-188.
19. Zhao, Y., et al., *Polarization-resolved laser-induced breakdown spectroscopy.* Opt. Lett., 2009. **34**(4): p. 494-496.
20. Penczak, J.S., et al., *The mechanism for continuum polarization in laser induced breakdown spectroscopy of Si(111).* Spectrochimica Acta Part B: Atomic Spectroscopy, 2012. **(accepted for publication)**.

D. Biomarkers in Laser Induced Retinal Injury in Rabbits

1. Summary

Laser-based devices are used by the armed forces in a wide range of applications, these include range determination, target designation, defensive counter measures, and as guides [1]. Although many safety standards for laser use have been established by the Occupational Safety and Health Administration (OSHA), injuries still occur, including in military settings [2-6].

Both military personnel and first responders are vulnerable to blinding laser eye injuries in combat or from inadvertent exposure to laser radiation from enemy or friendly sources. Regardless of the origins of the exposure, the retina is the most vulnerable to tissue damage from laser radiation due to its natural function of focusing light. The mechanism of damage can be photothermal, photomechanical, or photochemical [7] and lead to damage or death of retinal neuronal and retinal pigment epithelial (RPE) cells and disruption of the outer blood-retinal barrier [7-11]. Laser induced retinal injuries at the posterior pole of the eye are often asymptomatic immediately following injury [12]; however an undiagnosed retinal lesion can result in a loss of visual acuity or blindness over time. Currently, diagnosis of retinal lesions requires specialized equipment and ophthalmological expertise. Therefore, because the potential for exposure (whether accidental or intentional) to laser is increasing, the need to more rapidly diagnose laser eye injuries is crucial. In this project, we were able to establish panels of protein biomarkers indicative of laser induced retinal injury in the rabbit. These biomarkers were detected in the serum and saliva of laser treated animals. The same series of experiments also established a panel of anti-retinal antibodies that are detected in the serum in response to laser lesions in the retina twelve weeks following injury [13]. Experimental outcomes in this project and previous projects [14] support the hypothesis that proteins from the laser damaged retina can leak into the systemic circulation and can be detected in body fluids. Varying experimental conditions, such as lesion grade, dosage, and exposure patterns, influenced the protein biomarker response. These proteins could be used as potential biomarkers for diagnosis for retinal injuries that result from exposure to laser.

2. Introduction

Lasers (light amplification by stimulated emission of radiation) were discovered in the 1960s [15] and quickly became part of daily life. Laser implementation in the armed forces has increased rapidly and has been used in range determination, target acquisition, as guides “smart weapons” as well as in many other applications [1]. Exposure to these lasers may result in retinal injuries or damage because of the concentration of the visible and near-infrared radiation to the retina [16]. Military personnel and emergency responders are the most vulnerable individuals to such damage.

Laser induced retinal injury at the posterior pole of the eye is often symptomatic [12] and detection of inadvertent laser exposure of wavelengths beyond the visible spectrum has been difficult, especially if the exposure is away from the macula [1]. Retinal laser damage could involve the entire retinal thickness and has been studied in animal models [7, 8, 11, 17].

Laser retinal damage can occur by photothermal, photomechanical, photodisruptive or photochemical mechanisms [7], leading to varying degrees of retinal neuronal and retinal pigment epithelial (RPE) cell damage or death [7-10]. In addition, the blood–retina barrier is disrupted, which is associated with local inflammation and the upregulation of immunoregulatory molecules, such as prostaglandin E2 [18], cellular adhesion molecules, intercellular adhesion molecule 1 and vascular cell adhesion molecule 1 in the retina [19]. Disruption of the blood-retinal barrier following laser photocoagulation may lead to the release of retinal proteins into the blood circulation. We hypothesized that these proteins could be detected in body fluids such as serum and saliva immediately after the injury or could initiate an immune response, resulting in autoantibodies that are detectable in the serum. These proteins and autoantibodies could serve as molecular biomarkers for retinal injuries caused by laser. The concept of a systemic immune response to retinal injuries is not new and has been described in chronic diseases that affect the retina, such as age-related macular degeneration [20], diabetic retinopathy [21] and glaucoma [22]. In this project, we describe the detection of retinal proteins and anti-retinal antibodies in the body fluids of rabbits whose eyes were treated with laser and establishment of biomarker panels that could help in the diagnosis of retinal injuries caused by lasers in military settings.

3. Methods, Assumptions and Procedures

a) *Animals*

A total of 303 Dutch Belted (DB) rabbits were used for the project which consisted of 3 different experiments (experiment 1: n=90, experiment 2: n=72 (x2) and experiment 3: n=69). Experiments varied laser power used, the time from treatment to sample collection, and the number of laser treatments (Table 1). Experiment 2 was performed twice to clarify inconclusive results.

Table 1: Project experimental design

Experiment	Laser grade	Number of laser lesions	Timer points for sample collection	Number of laser treatments	Number of animals
Experiment 1	MVL	50	1h, 4h, 24h, 1w,12w	1	6 saliva 24 serum
	GII	50	1h, 4h, 24h, 1 w,12w	1	6 saliva 24 serum
	GIII	50	1h, 4h, 24h, 1w,12w	1	6 saliva 24 serum
Experiment 2	MVL	5	1h, 4h, 24h,12w	1	6 saliva 18 serum
	MVL	10	1h, 4h, 24h,12w	1	6 saliva 18 serum

	MVL	50	1H, 4H, 24H,12W	1	6 SALIVA 18 SERUM
EXPERIMENT 3	MVL	50	24H, 12W	1	6 SALIVA 9 SERUM
	MVL	50	24H, 12W	2	6 SALIVA 18 SERUM
	MVL	50	24H,12W	3	6 SALIVA 24 SERUM

MVL: minimally visible lesion, GII: Grade two, GIII, Grade III, h: hour, w: week

Animals were purchased from Myrtle's Rabbitry, Inc. (Thompsons Station, TN) and were housed at the Comparative Medicine Unit Animal Facility at the Northeastern Ohio Medical University (NEOMED). All experimental protocols were approved by the North Eastern University of Ohio College of Medicine Institutional and Animal Care and Use Committee (#10-039 and 08-022) and US Air Force Animal Use Programs (AFDW-2011-003A).

All animal procedures were carried out under general anesthesia using a combination of subcutaneous injection of dexmedetomidine (approximately 0.25–0.5 mg/kg; Pfizer Animal Health, New York, NY) and ketamine (15–20 mg/kg; Fort Dodge Animal Health, Fort Dodge, IA). Upon completion of the procedures, atipamazole (0.5 mg/kg) was administered as a reversing agent. At the end of the experiment, animals were euthanized using a pentobarbital-containing solution (Fatal Plus) (80–100 mg/kg) intravenously.

b) *Laser treatment*

Retinal laser lesions were created, after pupillary dilation with one drop each of tropicamide 1.0% (Bausch & Lomb, Tampa, FL) and phenylephrine HCl 2.5% (Alcon Laboratories, Fort Worth, TX), using a double frequency Nd:YAG laser at 532 nm mounted on a Haag-Streit BQ-900 slit lamp. A Goldmann contact lens was used to help aim the laser beam into the retina. The laser settings for power (mW), duration (ms), and spot size (µm) that were used to create the three grades of lesions were as follows: MVL (100 mW, 100 ms, 500 µm), GII (150 mW, 200 ms, 500 µm), and GIII (300 mW, 200 ms, 500 µm). The control animals for each group were treated in the same manner, except for the laser application. Fundus photography was performed after laser treatment and in control animals following slit lamp examination.

c) *Clinical assessment of lesions by direct examination and photography*

Fundus photography was performed after laser treatment and in control animals following slit lamp examination. Pictures were taken for every animal.

d) *Histological confirmation of lesions and clinicopathologic correlation of injury*

Rabbit eyes at each time point and at the end of the procedure were enucleated, fixed in 10% buffered formalin, processed, and embedded in paraffin. 5-µm-thick sections were prepared for histological examination of the laser lesions.

e) *Saliva collection*

Saliva was collected from each rabbit following a subcutaneous injection of pilocarpine (1.0 mg/kg) to stimulate salivation under general anesthesia before laser treatment and at 1hr, 4hrs and 24hrs after laser treatment. Samples were collected on ice and shipped on dry ice to the lab where they were stored at –80°C until processing.

f) *Blood Collection*

Blood was collected by cardiac puncture from both laser-treated and control animals separately. Blood collection was performed under deep anesthesia using a combination of ketamine (50–70 mg/kg) and dexmedetomidine (1–2 mg/kg). The collected blood was incubated at room temperature for approximately 15 minutes to allow clotting, and then centrifuged for 15 minutes before serum collection. Contact with the blood cells (bottom layer) was avoided to prevent possible contamination. The serum was aliquoted and stored at -80°C until processing.

g) *Retinal protein preparation*

Normal DB rabbit retinal protein lysates were prepared as previously described [23] with some modifications. Briefly, whole retinas containing sensory retina, RPE and choroid collected from the animals at the time of enucleation were disrupted in 0.5 mL of homogenization buffer (10 mM Tris-HCl pH 7.4, 1 mM EDTA, 200 mM sucrose, 1 mM phenylmethylsulfonyl fluoride), and cell debris was removed by centrifugation at 1000 x g for 5 minutes at 4°C. The supernatant was centrifuged at 16,000 x g for 30 minutes at 4°C. The resulting supernatant was solubilized in Triton X-100 solubilization buffer (50 mM Tris-HCl pH 7.5, 100 mM NaCl, 5 mM EDTA, 0.05% SDS, 2.5% glycerol, 1.0 mM phenylmethylsulfonyl fluoride, 1% Triton X-100) for at least 4 hours at 4°C. Protein concentration was measured using the bicinchoninic acid Protein Assay Kit (Thermo Scientific, Rockford, IL). Proteins were concentrated using Amicon Ultra-4 centrifugal filter devices (Millipore, Billerica, MA).

h) *Two-dimensional polyacrylamide gel electrophoresis (2D-PAGE)*

Retinal proteins (80 µg/strip) were diluted in ReadyPrep 2-D Starter Kit Rehydration/Sample Buffer (8 M urea, 2% CHAPS, 50 mM DTT, 0.2% Bio-Lyte 3/10 ampholyte, 0.001% bromophenol blue; Bio-Rad, Hercules, CA), loaded onto 11 cm Immobiline Dry Strips, pH 3–11 non-linear (GE Healthcare, Piscataway, NJ) and rehydrated for 16 hours at room temperature. The first-dimension separation was performed in a Protean isoelectric focusing cell (Bio-Rad, Hercules, CA) at 250 V for 15 minutes, followed by an increase to 8000 V for 30 kVh. After the first-dimension separation, gel strips were rinsed in 1X Tris-Glycine (TG) running buffer (25 mM Tris, 192 mM glycine + 0.1% SDS) for 10 minutes, equilibrated for 15 minutes in equilibration buffer I (6 M urea, 0.375 M Tris-HCl pH 8.8, 20% glycerol, 2% SDS, 2% DTT), followed by 15 minutes in equilibration buffer II (6 M urea, 0.375 M Tris-HCl pH 8.8, 20% glycerol, 2% SDS, 2.5% iodoacetamide), then loaded onto 12.5% criterion Tris-HCl gels (Bio-Rad, Hercules, CA). Proteins were subjected to electrophoresis at 175 V in 1X TG running buffer for the second-dimension separation.

i) *Western blot*

Following 2D-PAGE, the proteins were transferred to a polyvinylidene fluoride (PVDF) membrane overnight at 10 V in 1X TG transfer buffer (25 mM Tris, 192 mM glycine + 0.05% SDS + 20% methanol). Membranes were blocked with 5% bovine serum albumin (BSA) in Tris-buffered saline + 0.1% Tween 20 (TBS-T) for 8 hours at 4°C, then probed with sera from the 12-week laser-treated or control animals. Sera from each rabbit were tested individually and not pooled. The serum was applied at a 1:100 dilution in 2% BSA in TBS-T overnight at 4°C, followed by 3 washes with TBS-T for 10 minutes each. Goat anti-rabbit IgG- Horseradish peroxidase (HRP) conjugated secondary antibody (SantaCruz Biotechnologies, Santa Cruz, CA) was applied at a 1:25,000 dilution in 2% BSA in TBS-T for 1 hour at room temperature, followed by 4 washes with TBS-T for 10 minutes each. The signal was visualized using SuperSignal West Pico Chemiluminescent substrate (Thermo Scientific, Rockford, IL).

j) *Protein Spot Analysis*

Western blot images were scanned and analyzed using Ludesi Redfin software basic analysis (http://www.ludesi.com/redfin/).Western blot images probed with sera from laser-treated animals were compared to those probed with sera from control animals. Spots that were present in the blots from at least two laser-treated animals and absent in all of the control blots within a group were selected for protein identification. The membranes were matched using all-to-all spot matching. The integrated intensity of each spot was measured, background-corrected and normalized. The normalization removes differences originating from variations in staining, scanning time and protein loading by mathematically minimizing the median expression difference between the matched spots [24]. For spot excision, gels were run with 11 cm Immobiline Dry Strips, pH 3–11 non-linear, rehydrated with 120 µg of protein as described above, then silver stained as previously described [25, 26]. Briefly, gels were fixed in 45% methanol + 7% acetic acid for at least 30 minutes and washed 3 times for 5 minutes each to remove the fixer. Gels were sensitized by incubation in 0.02% sodium thiosulfate pentahydrate for 90 seconds, followed by 3 washes with water for 30 seconds each. Gels were incubated for a minimum of 25 minutes in 0.2% silver nitrate solution, followed by 3 washes with water for 1 minute each. Gels were then developed by incubation in 6% sodium carbonate + 0.018% formaldehyde + 0.0004% sodium thiosulfate pentahydrate until stained. Development was terminated by incubation in 45% methanol + 7% acetic acid. The selected spots were excised from the silver-stained gels for analysis by LC-MS/MS.

k) *Liquid chromatography mass spectrometry (LC-MS/MS)*

i. Sample preparation

a. Saliva and serum

Sample preparation and nano-LC/MS/MS were performed as described previously [27]. Briefly, after trypsin digestion, peptide mixtures were separated using a C18 reverse phase column (0.75A internal diameter at a flow rate of 1 µl/min) in line with the mass spectrometer. The mobile phases consisted of 0.1% formic acid containing 5% acetonitrile (A) and 0.1% formic acid in 95% acetonitrile (B) respectively. A 180-minute linear gradient was used followed by 60 minutes of equilibration in solvent A. The ions eluted from the column were electrosprayed at a voltage of 1.75 kV. Nano-HPLC-mass spectrometry was performed using an LTQ mass spectrometer (Thermo Fisher Scientific; Waltham, MA) coupled to a Surveyor HPLC system (Thermo-Fisher Scientific, Waltham, MA) equipped with a Micro AS autosampler.

b. 2D gel spots

The excised 2D spot gel pieces were processed individually as previously described [14] with minor modifications to the gel washing steps. The gel pieces were fixed in 1 ml of 40% methanol, 7% acetic acid for 30 minutes and destained by washing with water once, followed by washing for 30 minutes with 50 mM sodium thiosulfate and 15 mM potassium ferricyanide until the silver color disappeared. Pieces were then washed four times with water, once with 200 mM ammonium bicarbonate, and twice with 100 mM ammonium bicarbonate in 50% acetonitrile, then dried under vacuum using a SpeedVac. To each gel piece, 200 µl of 100 mM ammonium bicarbonate (pH 8.0) containing 0.5 µg trypsin (Promega; Madison, WI) was added and incubated overnight at 37ºC. Peptides in each gel piece were extracted with three washes of 70% acetonitrile and 0.1% formic acid. The extracts were then pooled together and dried. 20 µl of 6 M guanidine-HCl in 5 mM potassium phosphate and 1 mM DTT (pH 6.5) was added to each dried sample and sonicated. Peptides were then extracted using a C18 ZipTip (Millipore, Billerica, MA) and subjected to nanospray LC-MS/MS analysis. Each sample was run once on the mass spectrometer using an extended linear gradient as described below.

ii. Nanospray LC-MS/MS spectrometry

Automated nanospray liquid chromatography tandem mass spectrometry (nanospray LC-MS/MS) was performed using an LTQ-LC/MS (ThermoFisher Scientific, Waltham, MA). Peptide mixtures were separated using a C18 reverse phase column (0.75-Å internal diameter at a flow rate of 1 µl/min) in line with the mass spectrometer. The mobile phases consisted of 0.1% formic acid containing 5% acetonitrile (A) and 0.1% formic acid in 95% acetonitrile (B), respectively. A 180 minute linear gradient was used, followed by 60 minutes of equilibration in solvent A. The ions eluted from the column were electrosprayed at a voltage of 1.75 kV. The LC-MS/MS cycle was 6 MS/MS scans per full MS scan, with dynamic exclusion enabled, +/- 1.5 Da tolerance and 12 second exclusion duration.

l) *Data analysis*

The MS data collected were analyzed using the SEQUEST algorithm (Thermo Fisher Scientific; Waltham, MA) searched against the mammalian including the rabbit subset of the UniProt database [28] using a peptide mass tolerance of 2.5 Da, a fragment mass tolerance of "0", which is effectively 1 Da, and monoisotopic masses. For the spectral counting, Relative quantitative expression of proteins was determined using scan counts as previously described [28, 29]. To determine the proteins with significantly different levels between laser and control samples, data from each group were combined using “Visualize” (Medical College of Wisconsin, Milwaukee, WI). Normalized p-values were determined using the G test (log likelihood ratio test for goodness of fit) as previously described [30]. Post-hoc adjustment of the p-value was performed using the Holm-Sidak test to correct for multiple comparisons. Proteins with an adjusted p-value <0.05 were sorted into up-regulated or down-regulated sets based on a log 2 ratio of greater than 1 or less than1 as previously described [31].

m) *Validation studies*

Validation assays that included immunohistochemistry and western blot were performed to confirm the expression of the candidate autoantigens identified from the autoantibody experiment in the rabbit retina as described below:

i. Immunohistochemistry

Deparaffinized slides from normal DB rabbit eyes were rehydrated using graded ethanol. Antigen retrieval was performed using 1X antigen retrieval solution (Dako; Carpinteria, CA) per the manufacturer's instructions. The sections were blocked for 45 minutes using 10% normal goat or donkey serum and subsequently labeled by overnight incubation at 4°C with antibodies to the following proteins: dihydropyrimidinase-related protein 2 (DRP-2) (1:100; LifeSpan BioSciences, Seattle, WA), fructose-bisphosphate aldolase C (ALDC) (1:100; SantaCruz, Santa Cruz, CA), pyruvate kinase isozyme (PKM2) (1:100; LifeSpan BioSciences, Seattle, WA) and chaperonin containing T-complex polypeptide 1 subunit zeta (TCP-1-zeta) (1:100; Abnova, Taipei, Taiwan).The sections were then incubated with DyLight 488- or Texas Red-conjugated secondary antibody (Jackson ImmunoResearch Laboratories, Inc.; West Grove, PA) for 1 hour at room temperature. Blocking and washing steps were performed in a humid chamber at room temperature. All washes were performed three times for 5 minutes each in phosphate-buffered saline (PBS). Antibody binding was detected by immunofluorescence and visualized using an Olympus BX51 fluorescent microscope (Olympus, Tokyo, Japan).

ii. Western blot

DB Retinal protein lysates (20ug/lane) were separated by sodium dodecyl sulfate polyacrylamide gel electrophoresis (SDS-PAGE) and then transferred to PVDF membrane overnight. Membranes were blocked in 2% BSA in TBS-T for 2 hours and then incubated with the primary antibody: dihydropyrimidinase related protein-2 (1:1000; LifeSpan BioSciences, Seattle, WA), fructose-bisphosphate aldolase C (1:500; SantaCruz, Santa Cruz, CA), pyruvate kinase isozyme (1:1000; LifeSpan BioSciences, Seattle, WA), and chaperonin containing T-complex polypeptide 1 subunit zeta (1:200; Abnova, Taipei, Taiwan) for 2 hours, followed by HRP-conjugated secondary antibody for 1 hour. All washes were performed 3 times for 10 minutes each in 1X TBS-T. Signal was detected using SuperSignal West Pico Chemiluminescent substrate (Thermo Scientific, Rockford, IL).

iii. Functional categories

Autoantigens were analyzed using Pathway Studio 6.0 software (Ariadne, Rockville, MD). Using the human homolog gene identifiers, the autoantigens were analyzed for their molecular function and biological process.

4. Results and Discussions

a) *Fundus imaging and histology*

MVL laser burns caused light gray retinal lesions, and GII burns produced grayish-white lesions, while GIII burns produced lesions with distinct white centers surrounded by grayish-white rings (Figure 1A, 1B and 1C respectively**)**. Hematoxylin and eosin (H&E) staining of the retina treated with MVL lesions showed minimal disruption of the retinal pigment epithelium with intact overlying retina (Figure 2A). GII lesions showed disruption of the sensory retina with mummification of the outer segments and disruption of the RPE (not shown), and GIII lesions showed RPE disruption with inflammatory reaction in the underlying choroid, mummification of the outer and inner segments and disruption and edema of the outer nuclear layer (Figure 2B).

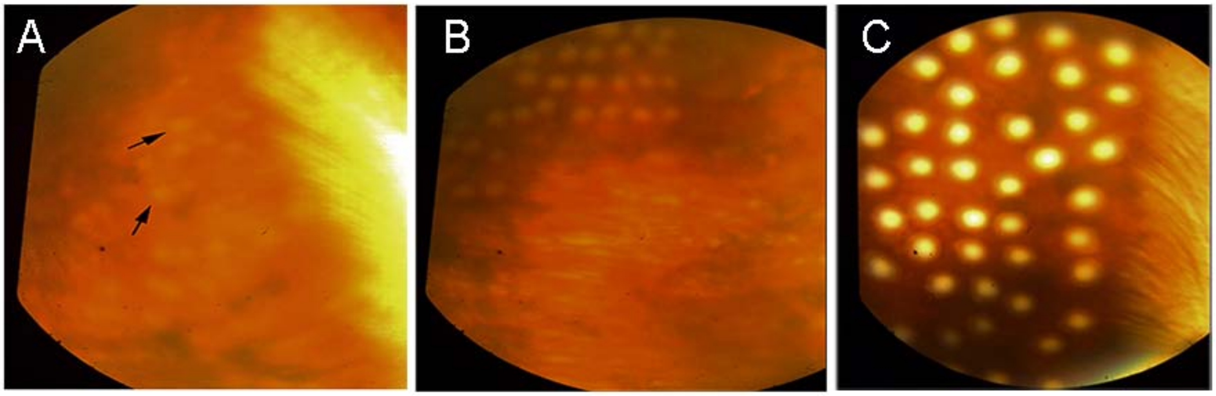

Figure 1. Fundus images of retinal lesions. A) MVL, B) GII, C) GIII

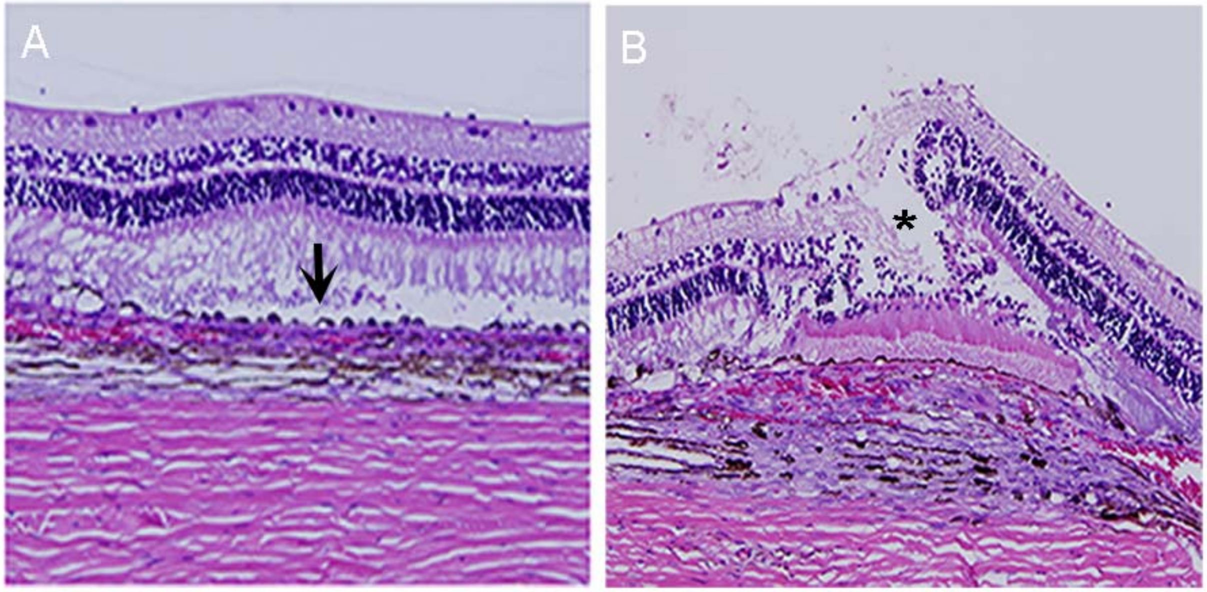

Figure 2. H&E staining of retina. A) MVL lesion, B) GIII

b) *Detection of retinal proteins in saliva and serum of laser treated rabbits*

In order to investigate whether the damage of retinal tissues caused by laser (shown with histology) also caused leakage of retinal proteins into the systemic circulation, we performed a global proteomic approach (LC-MS/MS) as described in the methods section. Identifying the total proteomes of complex mixtures using LC-MS/MS has been widely used for global molecular characterization of diseases [32-35]. Studies with label-free LC-MS/MS shotgun proteomics have demonstrated that peptide counts, and mass spectral count correlate with relative protein abundances in complex samples [28] and that the greater the number of peptide and spectral counts, the greater the relative abundance of a given protein in the analyzed samples. Using this approach, we were able to detect a total 14 retinal proteins in the serum and saliva of laser treated rabbits at 1h, 4hrs and 24hrs following the treatments (Table 2). These proteins were not detected in the control animals. These proteins however, were not detected at higher quantities possibly due to their degradation caused by the proteolytic enzymes present in the saliva and serum.

Table 2: Description of retinal proteins (biomarker candidates) detected by LC/MS/MS in saliva and serum samples of laser treated rabbits.

PROTEIN BIOMARKER	UNIPROTKB/ SWISS-PROT ID	NCBI GENE ID	FUNCTION	TISSUE LOCATION
CYCLIC NUCLEOTIDE-GATED CATION CHANNEL ALPHA-3(CNGA3/B3)	Q16281/ Q9NQW8	1261/54714	ACTIVATED BY CYCLIC GMP WHICH LEADS TO AN OPENING OF THE CATION CHANNEL AND THEREBY CAUSING A DEPOLARIZATION OF CONE PHOTORECEPTORS	CONE PHOTORECEPTOR CELLS (MEMBRANE BOUND)
PHOSPHODIESTERASE (PDE6A, 6C)	Q8K0A8/P16586	225600 /281975	METAL ION BINDING – VISUAL SIGNAL TRANSDUCTION	PDE6A IS ROD SPECIFIC, PDE6C IS CONE SPECIFIC.
ATP BINDING CASSETTE TRANSPORTER A4 (ABCA4)	Q80VS6	11304	ATP BINDING	OUTER SEGMENT DISK EDGES OF RODS AND CONES, WITH AROUND ONE MILLION COPIES/PHOTORECEPTOR
PHOSDUCIN (PHD)	P41686	751516	REGULATION OF VISUAL PHOTOTRANSDUCTION OR IN THE INTEGRATION OF PHOTORECEPTOR METABOLISM	OUTER AND INNER SEGMENTS OF THE ROD CELLS
RETINAL OXIDASE (AOX1)	P80456	100008601	OXIDOREDUCTASE	CYTOPLASM (OCULAR TISSUES)
VOLTAGE-DEPENDENT L-TYPE CALCIUM CHANNEL SUBUNIT ALPHA-1F	O60840	778	CALCIUM ION BINDING	RETINA (MEMBRANE BOUND)

(CACNAF1)				
CALCIUM-BINDING PROTEIN 4 (CABP4)	P57796	57010	SIGNAL TRANSDUCTION	ROD SPHERULES AND CONE PEDICLES OF THE PRESYNAPSES FROM BOTH TYPES OF PHOTORECEPTORS
CALCIUM-BINDING PROTEIN 1(CABP1)	Q9JLK7	29867	SIGNAL TRANSDUCTION	PHOTORECEPTOR CELLS
CLUSTERIN (CLU)	Q9XSC5	100008713	PROTEIN BINDING	MÜLLER CELL
CYSTATIN (CST3)	097862	100009450	PROTEASE INHIBITOR	RETINAL PIGMENT EPITHELIAL CELLS
FRUCTOSE-BISPHOSPHATE ALDOLASE A (ALDOA)	P00883	100009055	GLYCOLYSIS	THROUGHOUT RETINA
BETA ENOLASE (BENO)	P25704	100008769	MUSCLE DEVELOPMENT AND REGENERATION	THROUGHOUT RETINA
GELSOLIN (GSN)	Q7M2V6	100337841	ACTIN BINDING	RETINAL PIGMENT EPITHELIAL CELLS
SECRETED PROTEIN ACIDIC AND RICH IN CYSTEINE (SPARC)	P36233	100009355	CELL GROWTH	RETINAL PIGMENT EPITHELIAL CELLS

c) *Effect of the laser grade on the biomarker response*

In order to determine whether the laser grade affects the biomarker response, animals in Experiment 1 were divided in 3 groups where 1 eye in each animal in group 1 was treated with 50 lesions of minimally visible lesion (MVL), group 2 with 50 lesions of moderate grade II laser (GII) and group 3 with 50 lesions of the severe grade III laser grade (GIII). Nine retinal proteins were detected in this experiment, all 9 proteins were detected in the samples collected from the group treated with MVL, 4 in the group treated with GII and 4 in the group treated with GIII (Figure 3A).

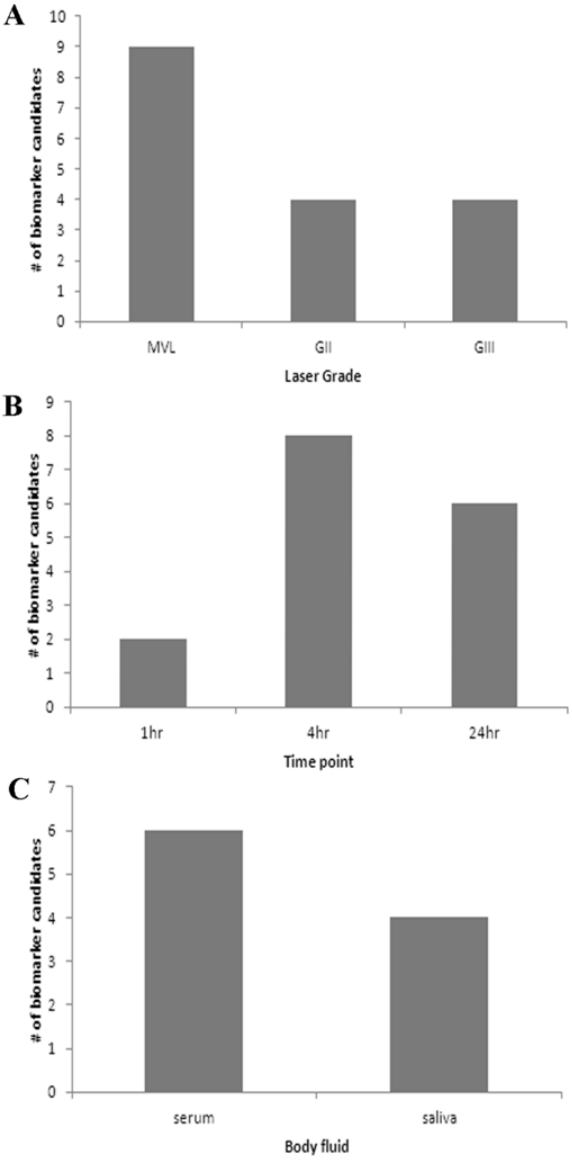

Figure 3. Experiment 1 results summary

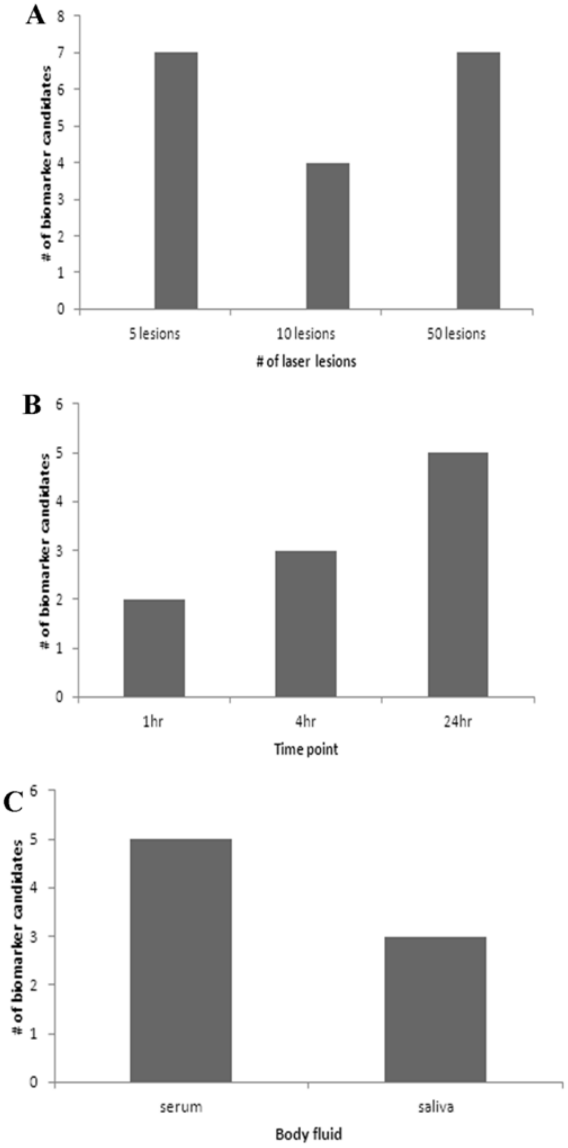

Figure 4. Experiment 2 results summary

d) *Effect of the number of lesions on the biomarker response*

In order to determine whether the number of laser lesions, affects the biomarker response, animals were treated with MVL and were divided in 3 groups where group 1 received 5 lesions, group 2 received 10 lesions and group 3 received 50 lesions. The number of retinal proteins detected was 7, 4 and 7 in the 5, 10 and 50 lesions respectively (Figure 4A). This suggests that the number of the lesions did not affect the biomarker response.

e) *Effect of the laser dose on the biomarker response*

In order to determine whether the laser dose affects the biomarker response, animals in experiment 3 were divided in 3 groups were group 1 received 1 MVL laser treatment, group 2 received 2 MVL laser treatments and group 3 received 3 MVL laser treatments, treatments were 1 month apart. Each treatment consisted of 50 laser lesions applied to one eye and all samples (saliva and serum) were collected at 24hrs following the final treatment. The number of the retinal proteins detected was 3 and 2 in the groups that received one and two treatments respectively. No retinal proteins were detected in the group that received 3 treatments (Figure 5). This suggests that the laser dose affects the biomarker response. Repetitive laser exposures may cause greater damage to tissues leading to the degradation of the proteins at the site of injury.

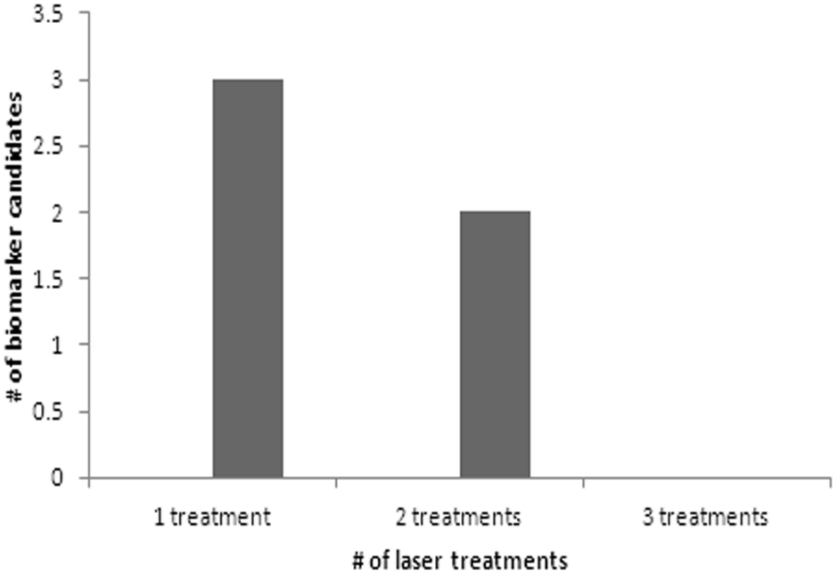

Figure 5. Biomarker response by dose

f) *Effect of the sample collection time on the biomarker response*

Samples from Experiment 1 and 2 were collected at 1hr, 4hrs and 24hrs. In Experiment 1, a 1 week time point was also included but no retinal proteins were detected in the laser treated samples. This suggests that the biomarker response is transient. Of the 9 retinal proteins detected in serum and saliva of laser treated animals in Experiment 1, 2 were detected at the 1hr time point, 8 were detected at the 4hrs time point, 6 at the 24hrs time point (Figure 3B), In Experiment 2, a total of 8 retinal proteins were detected in serum and saliva of the laser treated animals, 2, 3 and 5 were detected at 1hr, 4hrs and 24hrs time point respectively (Figure 4B). This suggests that the biomarker response is transient. When combining experiment 1 and 2, of the 14 proteins retinal proteins detected in serum and saliva of laser treated animals, 4 were detected at the 1hr time point, 9 were detected at the 4hrs time point, 11 at the 24hrs time point (Figure 6).

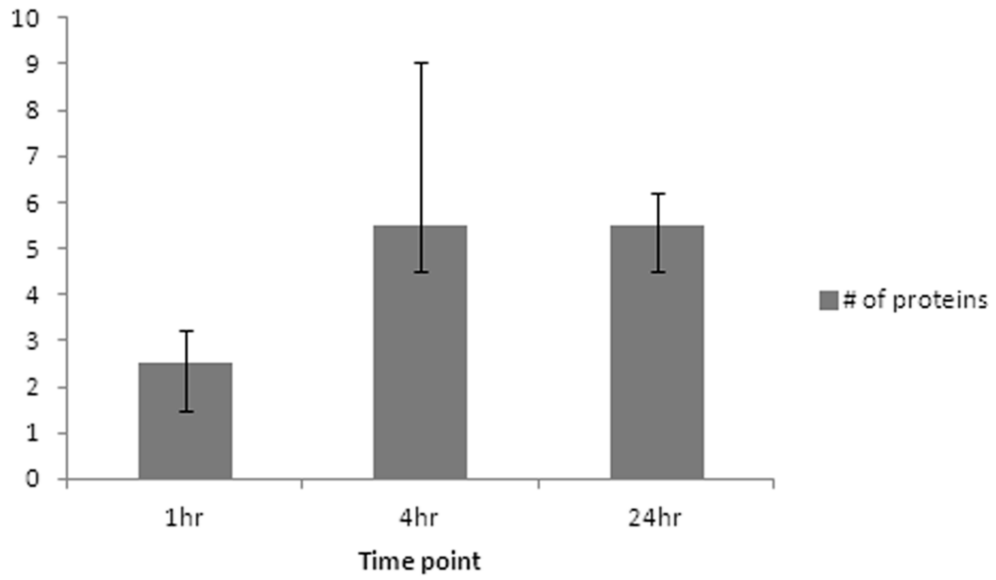

Figure 6. Effect of time on biomarker response

g) *Effect of type of body fluid used*

a. Saliva

Saliva was collected from all animals used in this project as paired; the same animal was used to collect saliva at different time points. Saliva samples were analyzed individually. Combining results from all 3 experiments, 7 of the 14 retinal proteins detected were in saliva. No retinal proteins were detected in saliva in Experiment 3 (Figure 7).

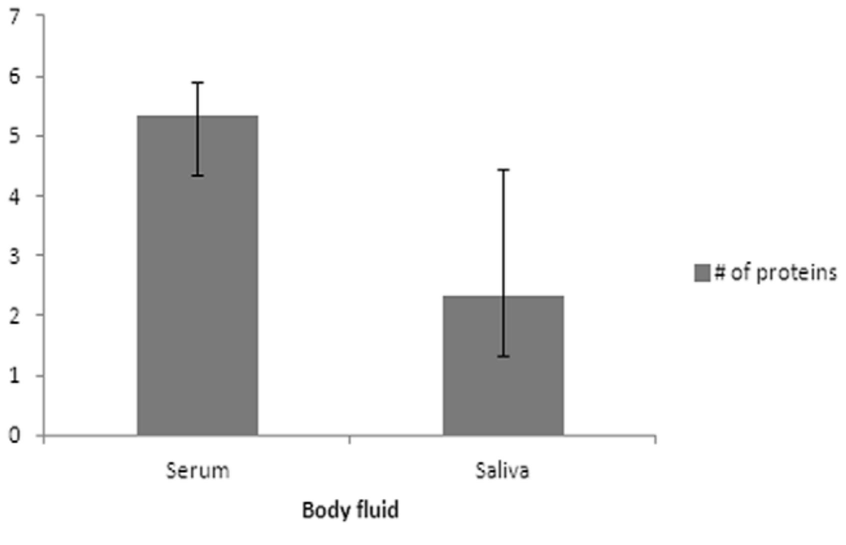

Figure 7: Biomarkers in serum and saliva

b. Serum

Serum was also analyzed for biomarkers in this project. Serum is more complex than saliva and was prefractionated prior to analysis. Each serum sample was prefractionated into 10 different fractions based on the isoelectric point of the proteins. Since each individual sample became 10 samples, serum samples from each time point were pooled when used for LC-MS/MS. Nine retinal proteins were detected in the serum suggesting that serum may be a better body fluid for detection of leaking proteins (Figure 7).

Saliva is clearly the most accessible body fluid and therefore easiest to collect which may have advantages to the clinical workflow, particularly in austere settings. However, in our study, using blood for the detection of biomarkers yielded more definitive results. This could be due to the large number of proteolytic enzymes present in saliva**.** This also made it difficult to perform validation studies. Western blot and ELISA experiments using antibodies against the 14 retinal proteins detected were performed; however, accurate quantitation of proteins and peptides in serum is challenging because of its complexity [36] and the high abundance of the other proteins such as Albumin. Therefore, no signal could be detected in the laser treated samples compared to the controls. Attempts using affinity removal columns to deplete the highly abundant proteins in the serum were also unsuccessful. The retinal proteins were still below the detection threshold. The less abundant serum proteins including our retinal proteins could have been removed along with albumin, hemoglobin and other depleted proteins. Other attempts using Multiple Monitoring reaction (MRM) to detect these retinal proteins were not successful. MRM is an MS based approach but more sensitive that LC-MS/MS. It is used for quantitation of peptides in complex mixtures such tryptic digests of plasma [37]. Studies are needed to establish assays for validation of these biomarkers.

h) *Suggested biomarker panel using LC-MS/MS*

Based on our results, 3 of the 14 protein biomarkers detected were detected repeatedly in the serum and saliva of the laser treated animals. These included: Cyclic nucleotide gated channel alpha 3 (CNGA3) and beta 3 (CNGB3) and Cone and rod cGMP-specific 3',5'-cyclic phosphodiesterases (PDE6A, 6B and 6C).

i) *Detection of anti-retinal antibodies in the serum of laser treated rabbits*

In addition to the direct search for leaked retinal proteins following laser treatments, and based on our hypothesis that these leaking proteins may initiate an immune response that can be detected at later time points, we used a two dimensional Western blot (2D WB) followed by LC/MS/MS to search for any antibodies that were raised to retinal proteins in the serum of laser treated rabbits 12 weeks after exposure [13]. A total of 18 anti-retinal antibodies were identified in this study. Four of these candidate antibodies were common between MVL and GII. No anti-retinal antibodies were detected in GIII treated samples (Table 3). Sera from GII laser-treated animals had 11 reactive protein spots (Figure 8); while sera from MVL-treated animals had 7 reactive protein spots**.** Sera from GIII laser-treated animals did not show any reactive protein spots**.** The spot patterns were similar among animals within a group.

Table 3: Biomarker candidates identified by two dimensional western blotting in the 12 week serum of laser treated rabbits (MVL: minimally visible lesion, GII: Grade two laser)

PROTEIN DESCRIPTION	LASER GRADE
FRUCTOSE BISPHOSPHATE ALDOLASE C	MVL, GII
DIHYDROPYRIMIDINASE RELATED PROTEIN 2	MVL, GII

T-complex protein 1 subunit zeta	MVL,GII
Pyruvate kinase isozymes M1/M2	MVL,GII
Transketolase	GII
Transitional endoplasmic reticulum ATPase	GII
Serotransferrin	GII
Cofilin-1	GII
Alpha enolase	GII
Elongation factor 1-alpha 1	GII
Glutamine synthase	MVL
Triosephosphate isomerase	MVL
Ubiquilin-1	MVL
Tubulin Alpha	MVL
Tubulin Beta	MVL
Bifunctional purine biosynthesis protein	MVL
Aspartate aminotransferase	MVL
Heme binding protein 2	MVL

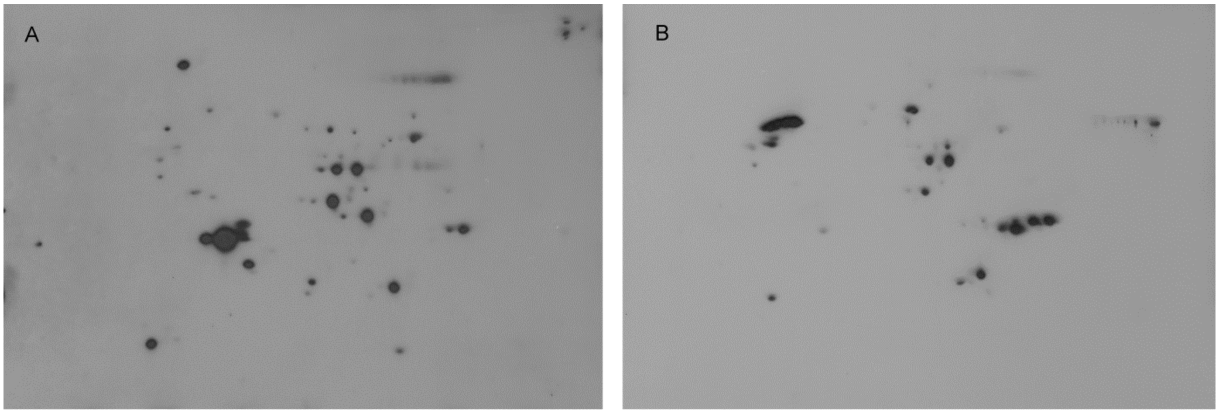

Figure 8. 2D Western blot. A) GII, B) MVL

It is important to note that even the MVL retinal laser lesions, which represent a mild response to laser-retina interaction, initiated an autoantibody response. Clinically, these lesions are often transient and may not be detected after a few weeks [38]. A serum autoantibody response could potentially serve as an indicator of a transient retinal injury, a possibility that needs to be further investigated.

The immune response appeared to be more robust after the MVL and GII laser lesions than after the severe GIII lesions. The more severe GIII lesions may have led to protein degradation at the site of injury, to the extent that they did not appear in the serum and therefore did not result in an immune reaction that could be detected in serum similar to MVL and GII lesions. Antibodies against some proteins such as Serotransferrin and ubiquilin were detected in only one group for reasons that are not clear. It could be that these responses are specific to the laser grade used for each group.

Although the autoantigens identified in this study are not retinal-specific proteins, immunohistochemistry and Western blot demonstrated that at least four antigens that were common to MVL and GII lesions were expressed in the retina in a diffuse fashion including the outer retina. Other autoantibodies detected in this study were raised against proteins that were previously known to be expressed in the retina [39, 40]. Furthermore, this observation suggests that only abundant, and possibly upregulated by injury, retinal proteins act as autoantigens when they leak into the systemic circulation and result in an immune response.

i. Identification of the candidate autoantigens by LC-MS/MS

A total of 18 protein spots from the 2D WB were selected for analysis by LC-MS/MS from the MVL (7) and GII (11) treated animals (Figure 9). Four of these spots yielded the same protein. The analysis of these spots revealed a total of 14 proteins. Four proteins, Dihydropyrimidinase related protein 2 (DRP-2), Fructose bisphosphate aldolase C (ALDC), T-complex protein 1 subunit zeta (TCP-1-zeta,) and Pyruvate kinase isozymes M1/M2 (PKM2), were common to both MVL- and GII-treated animals, while the remaining 10 proteins were seen in either the MVL- or GII-treated animals (Table 3).

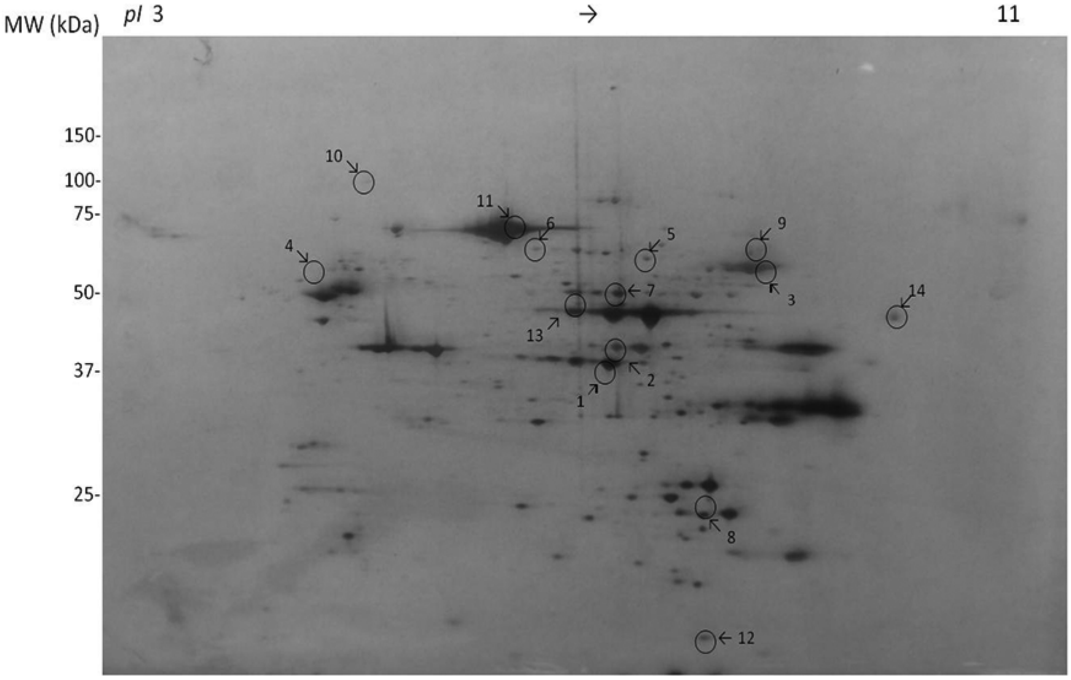

Figure 9. 2D Western blot to identify autoantigens

The 4 autoantigens present in both the MVL- and GII-treated samples were further characterized to confirm their expression in the retina using immunohistochemistry and Western blot.

ii. Expression of the identified proteins (candidate autoantigens) in the retina

To confirm that the candidate autoantibodies identified in this study following laser injury were developed against antigens expressed in the rabbit retina, we performed immunohistochemistry and Western blot using normal DB retina probed with commercially available antibodies to the 4 autoantigens that were common between the MVL and GII laser treated samples. We confirmed that these 4 common (DRP-2, ALDC, PKM2 and TCP-1-zeta) candidate autoantigens were expressed in the normal DB retina (Figure 10). The proteins were mainly cytoplasmic and were expressed diffusely in all retinal layers. Except for DRP2, all antibodies were specific and did not cross react with other proteins in the retina as shown in the Western blot (Figure 11).

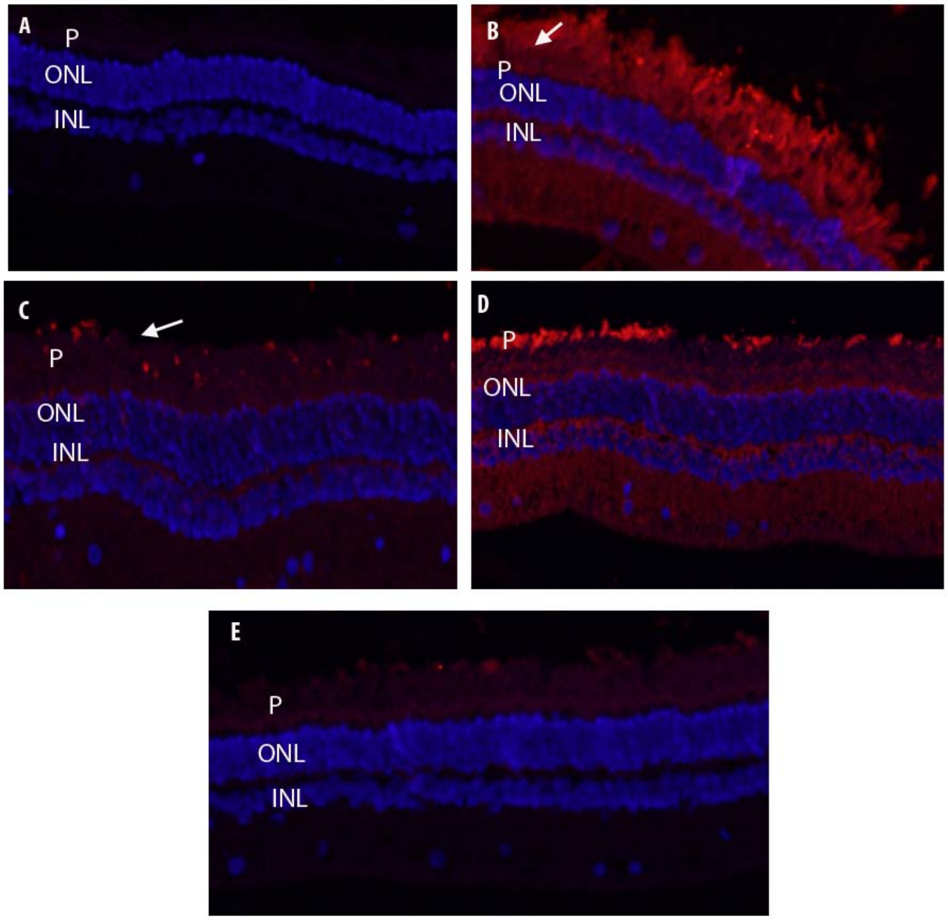

Figure 10. Autoantibody confirmation

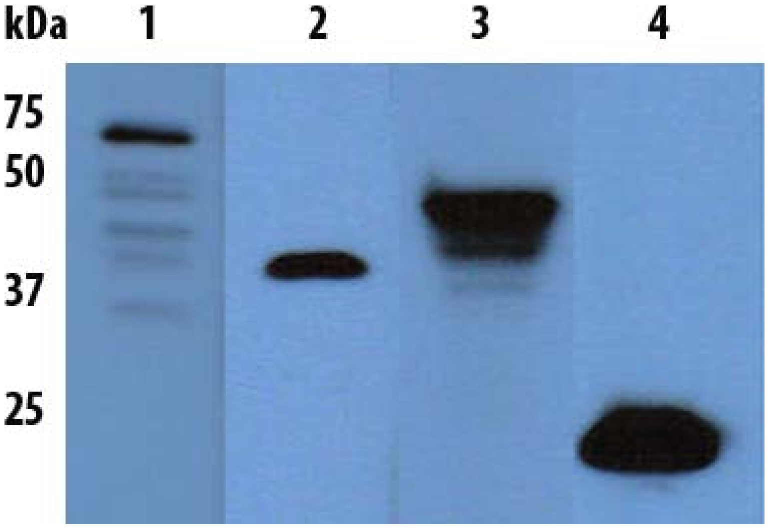

Figure 11. Except for DRP2, all antibodies were specific and did not cross react with other proteins in the retina.

iii. Molecular function/biological process for the candidate autoantigens

The 14 candidate autoantigens identified in this study as potential biomarkers for laser induced retinal injuries, were analyzed for their molecular function and biological process (Table 4) using Pathway Studio 6.0. Eleven of these autoantigens appeared to have a protein binding function. Four were involved in glycolysis. Two autoantigens had an anti apoptotic role while others were involved in actin filament depolymerization, the glyceraldehydes-3-phosphate metabolic process, neural fold formation, cell size or regulation of neurotransmitter levels with cofilin 1 being involved in most of these processes.

Table 4: Molecular functions/biological processes of the autoantigens as analyzed by Pathway Studio.

MOLECULAR FUNCTION/ BIOLOGICAL PROCESS	PROTEINS
Protein binding	ALDC, TCP-1-zeta, Cofilin-1, DRP-2. Elongation factor 1-alpha 1, Alpha-enolase, PKM2, Transketolase, Tubulin beta-2 chain, Ubiquilin, Transitional endoplasmic reticulum ATPase
Glycolysis	ALDC, PKM2, Alpha-enolase, Triosephosphate isomerase
Anti-apoptosis	Cofilin-1, Elongation factor 1-alpha 1
Positive regulation of actin filament depolymerization	Cofilin-1
Glyceraldehyde-3-phosphate metabolic process	Triosephosphate isomerase
Neural fold formation	Cofilin-1
Negative regulation of cell size	Cofilin-1
Regulation of neurotransmitter levels	Glutamine synthetase

j) *Suggested biomarker panels using the autoantibody approach*

Using results from this study, we suggest a panel of 4 anti-retinal proteins that could be used as candidate biomarkers for detection of laser induced retinal injury, these are: DRP2, ALDC, TCP-1-zeta and PKM2.

k) *Detection of biomarkers using spectral counting*

Using the approach we used in a previous study [14], compared the protein profiles between laser treated and non-laser treated samples. LC-MS/MS-based shotgun proteomics is a highly sensitive technique for detection of alterations in the proteome of diseased tissue or body fluid. Label-free quantitative proteomics is based on the assumption that increased abundance of protein will cause a measurable increase in its number of tryptic peptides. The resultant observable indices include chromatographic ion peak intensity, sequence coverage, peptide number, and spectral count [41]. We used the spectral counting approach to label-free relative quantification of proteins in serum of laser treated animals compared to non laser treated animals. For this approach, we used samples that gave optimal biomarker response (serum-GII-24hrs- 50 lesion, serum-MVL-24hrs-different lesion number and serum-GII-4hrs-50 lesions). Comparison of the total number of MS/MS spectra detected for a given protein (spectral counting) is a reliable and highly reproducible method for relative quantitation. It has been shown that spectral count is the factor with strongest correlation (r^2=0.9997) to protein abundance [42]. We used the G statistic to assess significant differences and then applied a post-hoc Holm-Sidak adjustment of the p-value to correct for multiple testing as described in the methods section. The G-test was found to be the most appropriate method of statistical analysis for our experiments [30, 43]. Additional layers of stringency were applied in order to increase confidence in the final protein biomarker candidate list. For example, proteins must have appeared in at least 50% of laser treated samples and have had a ratio of at least 2.0 where upregulation occurred. In this way, the rate of false discovery was minimized and a list of proteins that were both significantly present in each sample and significantly different between treatment groups was compiled. Based on theses analyses, we were able to identify a total of 10 proteins that were 2 fold or more upregulated in the group treated with the GII at 24hrs time point (Figure 12), 3 in the group treated with MVL (Figure 13) and 11 in the group treated with GII at 4hrs time point (Figure 14).

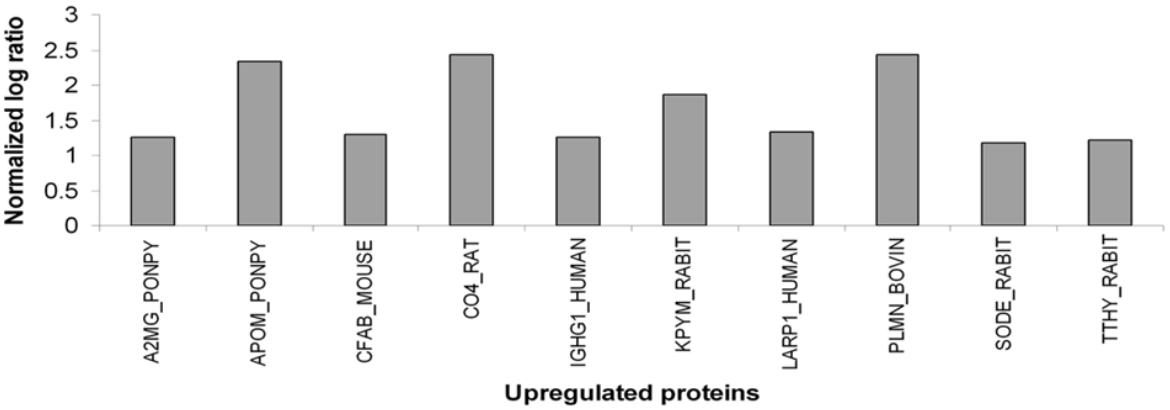

Figure 12. Protein response in GII treated group at 24 hours post exposure

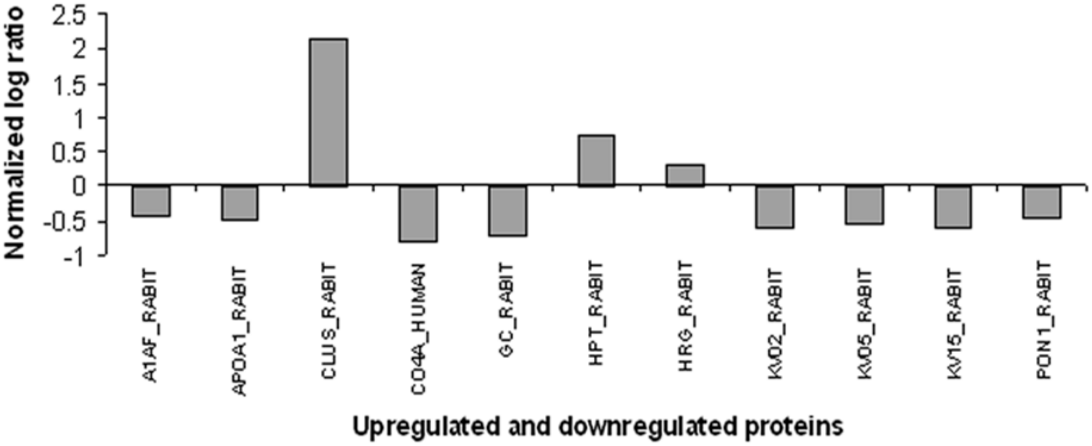

Figure 13. Protein response in MVL treated group at 24 hours post exposure

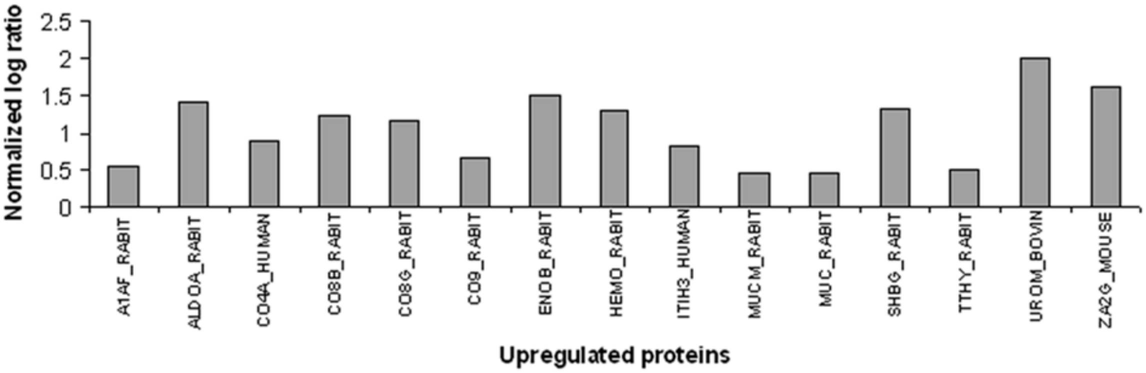

Figure 14. Protein response in GII treated group at 4 hours post exposure

Tables 5, 6 and 7 list all the differentially expressed proteins in the 3 different groups, their scan count number in each of the laser treated and mock-control, the fold change, the normalized log ratio and the P value. It is interesting to find that some proteins such as ALDC, Beta enolase, and PKM2 were consistently upregulated and those proteins were also found to be autoantigens in this study [13]. Thansthyretin (TTR), which is also expressed in the ocular tissues, was upregulated in both groups treated with GII laser. Clusterin was also upregulated in the group treated with MVL. Clusterin (Clu) is shown to be upregulated in various pathological conditions in retina suggesting that there might be a correlation between clusterin expression and cell death in the retina [27, 44]. In the animals treated with MVL, most of the differentially expressed proteins were down-regulated (Figure 13). These proteins could also be used as potential biomarkers for laser induced retinal injury. Further studies are needed to confirm these results.

Table 5: List of the differentially expressed proteins in the 24hr serum of GII laser treated rabbits using 50 laser lesions.

PROTEIN	ACCESSION	DESCRIPTION	MOCK SC	LASER SC	NORM LOG RATIO	FOLD	NORM P -VALUE
A2MG_PONPY	Q5R4N8	ALPHA-2-MACROGLOBULIN PRECURSOR (ALPHA-2-M)	17	36	1.253902	2.117647	0.002158
APOM_PONPY	Q5R894	APOLIPOPROTEIN M (APO-M) (APOM)	2	9	2.341365	4.5	0.017073
CFAB_MOUSE	P04186	COMPLEMENT FACTOR B PRECURSOR FACTOR B	11	24	1.296971	2.181818	0.010115
CO4_RAT	P08649	COMPLEMENT C4 PRECURSOR CHAIN	10	48	2.434474	4.8	1.71E-08
IGHG1_HUMAN	P01857	IG GAMMA-1 CHAIN C REGION	23	49	1.262588	2.130435	0.00032
KPYM_RABIT	P11974	PYRUVATE KINASE ISOZYMES M1/M2	8	26	1.871879	3.25	0.000455
LARP1_HUMAN	Q6PKG0	LA-RELATED PROTEIN 1	8	18	1.341365	2.25	0.022237
PLMN_BOVIN	P06868	PLASMINOGEN PRECURSOR	22	106	2.439929	4.818182	4.81E-17
SODE_RABIT	P41975	EXTRACELLULAR SUPEROXIDE DISMUTASE	10	20	1.17144	2	0.030301
TTHY_RABIT	P07489	TRANSTHYRETIN (PREALBUMIN)	299	614	1.209533	2.053512	7.75E-35

SC: scan count, Norm: Normalized, GII: Grade two, hr: hour

Table 6. A list of the differentially expressed proteins in the 24hr serum of MVL laser treated rabbits using 5, 10 and 50 laser lesions

PROTEIN	ACCESSION	DESCRIPTION	MOCK SC	LASER SC	NORM LOG RATIO	FOLD	NORM P -VALUE
A1AF_RABIT	P23035	Alpha-1-antiproteinase F precursor	193	495	-0.42378	2.564767	0.000715
APOA1_RABIT	P09809	Apolipoprotein A-I precursor (Apo-AI)	940	2298	-0.49296	2.444681	7.73E-18
CLUS_RABIT	Q9XSC5	Clusterin precursor (Apolipoprotein J) (Apo-J)	4	60	2.124286	15	0.000382
CO4A_HUMAN	P0C0L4	Complement C4-A precursor A	35	70	-0.7826	2	0.01137
GC_RABIT	P01870	Ig gamma chain C region	636	1323	-0.72589	2.080189	6.3E-24
HPT_RABIT	P19007	Haptoglobin precursor	122	695	0.727528	5.696721	5.28E-08
HRG_RABIT	Q28640	Histidine-rich glycoprotein precursor	184	798	0.334079	4.336957	0.003738
KV02_RABIT	P01683	Ig kappa chain V region 3315	63	143	-0.60001	2.269841	0.007569
KV05_RABIT	P01686	Ig kappa chain V region BS-1	64	152	-0.53468	2.375	0.015489
KV15_RABIT	P01696	Ig kappa chain V region K29-213	63	141	-0.62033	2.238095	0.005899
PON1_RABIT	P27170	Serum paraoxonase/arylesterase 1	119	301	-0.4438	2.529412	0.005521

SC: Scan count, Norm: Normalized, MVL: minimally visible lesion.

Table 7. A list of the differentially expressed proteins in the 4hr serum of GII laser treated rabbits using 50 laser lesions

PROTEIN	ACCESSION	DESCRIPTION	MOCK SC	LASER SC	NORM LOG RATIO	FOLD	NORM P-VALUE
A1AF_RABIT	P23035	Alpha-1-antiproteinase F precursor	231	547	0.536817	2.367965	1.22E-06
ALDOA_RABIT	P00883	Fructose-bisphosphate aldolase A	18	78	1.408647	4.333333	4.29E-05
CO4A_HUMAN	P0C0L4	Complement C4-A precursor	25	75	0.878132	3	0.005813
CO8B_RABIT	P98137	Complement component C8 beta chain precursor	15	58	1.24426	3.866667	0.001319
CO8G_RABIT	Q28679	Complement component C8 gamma chain precursor	11	40	1.155666	3.636364	0.011798
CO9_RABIT	P48747	Complement component C9 precursor	27	70	0.667565	2.592593	0.035158
ENOB_RABIT	P25704	Beta-enolase	20	93	1.5104	4.65	2.58E-06
HEMO_RABIT	P20058	Hemopexin precursor	20	81	1.311091	4.05	7.8E-05
ITIH3_HUMAN	Q06033	Inter-alpha-trypsin inhibitor heavy chain H3 precursor	16	46	0.816731	2.875	0.042147
MUCM_RABIT	P04221	Ig mu chain C region membrane-bound form	56	125	0.451599	2.232143	0.047423
MUC_RABIT	P03988	Ig mu chain C region secreted form	56	125	0.45159	2.23214	0.04742

					9	3	3
SHBG_RABIT	P15196	Sex hormone-binding globulin precursor	10	41	1.328793	4.1	0.004521
TTHY_RABIT	P07489	Transthyretin (Prealbumin)	181	417	0.497227	2.303867	7.72E-05
UROM_BOVIN	P48733	Uromodulin precursor	7	46	2.009376	6.571429	5.88E-05
ZA2G_MOUSE	Q64726	Zinc-alpha-2-glycoprotein precursor	3	15	1.615098	5	0.047619

SC: Scan count, Norm: normalized, GII: grade two.

5. Conclusions

Retinal injuries affecting the photoreceptors and/or the retinal pigment epithelium (RPE) result in leakage of retinal proteins into the systemic circulation. These proteins could be detected by LC-MS/MS. These proteins also initiate an immune response resulting in detectable autoantibodies that could serve as additional molecular biomarkers for retinal injuries. The biomarker response may vary with the degree of the laser injury and the amount of time from injury to detection. The findings in this study lay the foundation for further research into biomarker response and the development of diagnostics to detect injury in humans following laser exposure.

6. References

1. Harris, M.D., et al., *Laser eye injuries in military occupations.* Aviat Space Environ Med, 2003. **74**(9): p. 947-52.
2. Alhalel, A., et al., *Long-term follow up of accidental parafoveal laser burns.* Retina, 1993. **13**(2): p. 152-4.
3. Cai, Y.S., D. Xu, and X. Mo, *Clinical, pathological and photochemical studies of laser injury of the retina.* Health Phys, 1989. **56**(5): p. 643-6.
4. Gabel, V.P., et al., *Clinical observations of six cases of laser injury to the eye.* Health Phys, 1989. **56**(5): p. 705-10.
5. Modarres-Zadeh, M., et al., *Accidental parafoveal laser burn from a standard military ruby range finder.* Retina, 1995. **15**(4): p. 356-8.
6. Smiljanic, N.S. and D.O. Vicic, *Combat eye injury: laser photocoagulation prophylaxis of retinal detachment.* J Trauma, 1996. **40**(3 Suppl): p. S157-8.
7. Marshall, J., *Thermal and mechanical mechanisms in laser damage to the retina.* Invest Ophthalmol, 1970. **9**(2): p. 97-115.
8. Peyman, G.A., M. Raichand, and R.C. Zeimer, *Ocular effects of various laser wavelengths.* Surv Ophthalmol, 1984. **28**(5): p. 391-404.
9. Pollack, J.S., et al., *Tissue effects of subclinical diode laser treatment of the retina.* Arch Ophthalmol, 1998. **116**(12): p. 1633-9.
10. Wallow, I.H., M.O. Tso, and B.S. Fine, *Retinal repair after experimental xenon arc photocoagulation. I. A comparison between rhesus monkey and rabbit.* Am J Ophthalmol, 1973. **75**(1): p. 32-52.
11. Wallow, I.H. and M.O. Tso, *Repair after xenon arc photocoagulation. 2. A clinical and light microscopic study of the evolution of retinal lesions in the rhesus monkey.* Am J Ophthalmol, 1973. **75**(4): p. 610-26.
12. Curtin, T.L. and D.G. Boyden, *Reflected laser beam causing accidental burn of retina.* Am J Ophthalmol, 1968. **65**(2): p. 188-9.
13. Scott, S., et al., *Anti-retinal Antibodies in Serum of Laser-Treated Rabbits.* Invest Ophthalmol Vis Sci.
14. Dunmire, J.J., et al., *Novel serum proteomic signatures in a non-human primate model of retinal injury.* Mol Vis. **17**: p. 779-91.
15. Maiman, T., *Stimulated optical radiation in ruby.* Nature, 1960: p. 187-493.
16. Barkana, Y. and M. Belkin, *Laser eye injuries.* Surv Ophthalmol, 2000. **44**(6): p. 459-78.

17. Wallow, I.H. and M.O. Tso, *Repair after xenon arc photocoagulation. 3. An electron microscopic study of the evolution of retinal lesions in rhesus monkeys.* Am J Ophthalmol, 1973. **75**(6): p. 957-72.
18. Naveh, N. and C. Weissman, *Corticosteroid treatment of laser retinal damage affects prostaglandin E2 response.* Invest Ophthalmol Vis Sci, 1990. **31**(1): p. 9-13.
19. Richardson, P.R., et al., *Immunocytochemical study of retinal diode laser photocoagulation in the rat.* Br J Ophthalmol, 1996. **80**(12): p. 1092-8.
20. Gurne, D.H., et al., *Antiretinal antibodies in serum of patients with age-related macular degeneration.* Ophthalmology, 1991. **98**(5): p. 602-7.
21. Ahn, B.Y., et al., *Identification of an anti-aldolase autoantibody as a diagnostic marker for diabetic retinopathy by immunoproteomic analysis.* Proteomics, 2006. **6**(4): p. 1200-9.
22. Wax, M.B., J. Yang, and G. Tezel, *Serum autoantibodies in patients with glaucoma.* J Glaucoma, 2001. **10**(5 Suppl 1): p. S22-4.
23. Matveev, A.V., et al., *Native cone photoreceptor cyclic nucleotide-gated channel is a heterotetrameric complex comprising both CNGA3 and CNGB3: a study using the cone-dominant retina of Nrl-/- mice.* J Neurochem, 2008. **106**(5): p. 2042-55.
24. Chaves, I., et al., *Proteomic evaluation of wound-healing processes in potato (Solanum tuberosum L.) tuber tissue.* Proteomics, 2009. **9**(17): p. 4154-75.
25. Shevchenko, A., et al., *Mass spectrometric sequencing of proteins silver-stained polyacrylamide gels.* Anal Chem, 1996. **68**(5): p. 850-8.
26. Blum, H., H. Beier, and H. Gross, *Siver staining of proteins in polyacrylamide gels.* Electrophoresis, 1987. **8**: p. 93-99.
27. Yu, H., et al., *Quantifying raft proteins in neonatal mouse brain by 'tube-gel' protein digestion label-free shotgun proteomics.* Proteome Sci, 2007. **5**: p. 17.
28. Old, W.M., et al., *Comparison of label-free methods for quantifying human proteins by shotgun proteomics.* Mol Cell Proteomics, 2005. **4**(10): p. 1487-502.
29. Bantscheff, M., et al., *Quantitative mass spectrometry in proteomics: a critical review.* Anal Bioanal Chem, 2007. **389**(4): p. 1017-31.
30. Hendrickson, E.L., et al., *Comparison of spectral counting and metabolic stable isotope labeling for use with quantitative microbial proteomics.* Analyst, 2006. **131**(12): p. 1335-41.
31. Mesrobian, H.G., et al., *Candidate urinary biomarker discovery in ureteropelvic junction obstruction: a proteomic approach.* J Urol, 2010. **184**(2): p. 709-14.
32. Duan, X., et al., *Proteomic analysis of aqueous humor from patients with myopia.* Mol Vis, 2008. **14**: p. 370-7.
33. Niwa, T., *Biomarker discovery for kidney diseases by mass spectrometry.* J Chromatogr B Analyt Technol Biomed Life Sci, 2008. **870**(2): p. 148-53.
34. Davidsson, P. and M. Sjogren, *Proteome studies of CSF in AD patients.* Mech Ageing Dev, 2006. **127**(2): p. 133-7.
35. Srinivas, P.R., et al., *Proteomics for cancer biomarker discovery.* Clin Chem, 2002. **48**(8): p. 1160-9.
36. Anderson, N.L. and N.G. Anderson, *The human plasma proteome: history, character, and diagnostic prospects.* Mol Cell Proteomics, 2002. **1**(11): p. 845-67.

37. Kuhn, E., et al., *Quantification of C-reactive protein in the serum of patients with rheumatoid arthritis using multiple reaction monitoring mass spectrometry and 13C-labeled peptide standards.* Proteomics, 2004. **4**(4): p. 1175-86.
38. Paulus, Y.M., et al., *Healing of retinal photocoagulation lesions.* Invest Ophthalmol Vis Sci, 2008. **49**(12): p. 5540-5.
39. Farkas, R.H., et al., *Gene expression profiling of purified rat retinal ganglion cells.* Invest Ophthalmol Vis Sci, 2004. **45**(8): p. 2503-13.
40. Bhattacharya, S.K., *Retinal deimination in aging and disease.* IUBMB Life, 2009. **61**(5): p. 504-9.
41. Washburn, M.P., D. Wolters, and J.R. Yates, 3rd, *Large-scale analysis of the yeast proteome by multidimensional protein identification technology.* Nat Biotechnol, 2001. **19**(3): p. 242-7.
42. Liu, H., R.G. Sadygov, and J.R. Yates, 3rd, *A model for random sampling and estimation of relative protein abundance in shotgun proteomics.* Anal Chem, 2004. **76**(14): p. 4193-201.
43. Zhang, B., et al., *Detecting differential and correlated protein expression in label-free shotgun proteomics.* J Proteome Res, 2006. **5**(11): p. 2909-18.
44. Gwon, J.S., et al., *Expression of clusterin in Muller cells of the rat retina after pressure-induced ischemia.* Glia, 2004. **47**(1): p. 35-45.

E. Portable Biosensor for Protein Targets

1. Summary

The specific physiological response associated with exposures to directed energy and the biomarkers of resultant tissue injuries are poorly characterized. We are lacking in our ability to diagnose and quantify any subsequent degree of exposure-related damage. Cellular injury results in release of tissue-specific proteins into the circulatory system triggering immunological responses. It is possible to detect these biochemical signatures associated with the cellular damage and determine the extent of inflicted injuries in exposed individuals. Our goal is to develop a field-ready portable biosensor platform for detecting protein biomarkers appearing in human bodily fluids (saliva, serum, etc.) which are the direct result of focused energy impact. A recently developed method based on modifications to sandwich enzyme-linked immunosorbent assay (ELISA) in conjunction with electro-chemical detection (ECD) possesses both the sensitivity and specificity required to competently identify protein biomarkers in serum. Current technology utilizes microarrays of 12,000 electrodes; each electrode can be used either individually or in blocks as a substrate for customized multiplex ELISA. We optimized this technology further by introducing both customized substrates to increase antibody immobilization, and chemical signal amplification to boost the signal. The combination of these improvements with modifications to the assay parameters aimed at reducing the background, significantly increased the sensitivity of protein detection. The resulting device will have the capability of detecting protein targets in a fully automated sample-to-answer field test, which can be readily reconfigured to change target selection.

2. Introduction

The need for a portable diagnostic and monitoring device capable of rapidly detecting specific proteins in bodily fluids, viruses, or microorganisms is varied and extensive. Many of these proteins are not abundant and difficult to detect by conventional methods. Enzyme-linked immunosorbent assay (ELISA) — a very sensitive, quantitative, and reproducible protein detection technique — is widely used to detect proteins in biological and environmental samples. Protein microarrays and antibody microarrays in particular have excellent potential to advance development of portable protein detection instruments and also offer a capability of detecting many protein targets in one assay. In the microarray-based sandwich immunoassay, antibodies, immobilized on the surface of a microarray bind their corresponding antigens. Labeled or tagged detection antibodies further recognize these antigens and are detected. The compact electrochemical detection (ECD) system marketed by CustomArray is well adapted for protein detection by ELISA-type immunoassays [1]. Rather than using fluorescent dyes and an optical scanning system, ECD relies on horseradish peroxidase (HRP) and common redox substrates to generate electrons that can be measured as a change in current or potential. Their core technology is a specially modified semiconductor-containing arrays of microelectrodes (Figure 1) that are individually addressable using embedded logic circuitry on the chip. Since it is possible to measure small currents precisely, the circuitry can be employed to sense peroxidase activity at each electrode. Eliminating optics from the signal detection process will also reduce the size and complexity of the hardware, making it possible to integrate microarray reader components into larger systems for automated sample processing. CustomArray's MX300 platform integrates lab-on-a-chip technology with protein microarray (Figure 2). The fully integrated fluidic device automates the entire hybridization and post hybridization processes that involve multi-stage fluidics handling.

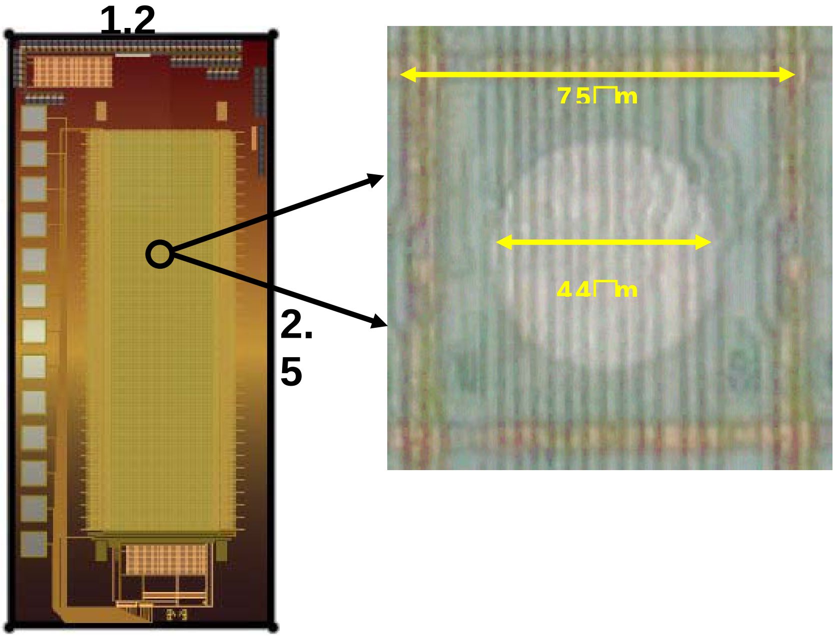

Figure 1. CORE TECHNOLOGY – CMOS MICROARRAY. Silicon microarray containing 12,544 platinum or gold coated electrodes and on-chip or off-chip counter electrode.

Figure 2. ElectraSense MX300 automated chip reading/washing station. Fully automated, contains four fluid control lines for applying four samples to the same chip. Serial address chip interface for voltage/current readout.

Phage-display technology [2] provides a method to express a large library of recombinant antibody fragments fused to the coat protein of bacteriophage in order to select for specific binding to a chosen target [3] (Figure 3). Using successive rounds of increasing selection pressures, one can isolate very strong binding antibodies for any protein sequence. Usage of recombinant antibodies in this system is advantageous because 1) Genotype and phenotype are linked providing the DNA sequence for the selected antibody, effectively immortalizing it. 2) The procedure for selection of a specific antibody can be performed quickly in a few weeks. 3) The sequence can be cloned and expressed in bacterial or yeast systems at unlimited quantities. 4) Modifications can be made to allow for site-specific attachment to surfaces, nanoparticles, or other molecule conjugates. 5) Affinity maturation through random and directed mutation can improve binding affinities to allow for more sensitive assays [4].

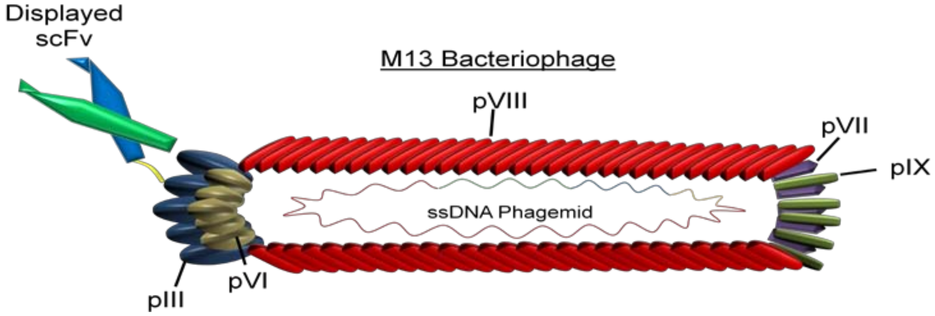

Figure 3. M13 Bacteriophage Displaying the scFv Antibody. The DNA phagemid is encapsulated inside the phage particle. This encodes for the pIII coat protein that is fused to the scFv antibody. Here the phenotype (scFv) and the genotype (ssDNA phagemid) are linked.

The single-chain fragment (scFv) of variation is an engineered version of the antigen binding region of an immune system immunoglobulin (IgG) (Figure 4). The scFv consists of a variable light (V_L) chain and a variable heavy (V_H) chain where each contains 3 complementarity-determining regions (CDRs), capable of specific recognition of a protein antigen. Although the scFv is much smaller in size to the IgG, 30kD to 150kD, low dissociation constant antibodies can be generated [5].

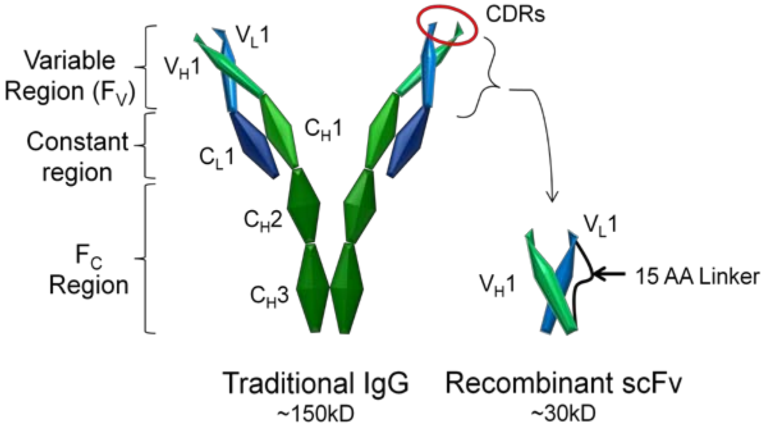

Figure 4. IgG antibody compared to engineered fragments Fab and scFv. The150kDa Immunoglobulin G (a) consists of two heavy and two light chains. The 3-25 amino acid CDRs provide recognition to antigen. Removal of the Constant regions leaves the variable regions but retains the CDRs. Engineering into a single polypeptide of variable regions is provided by a 15 AA linker, and is now a 25kDa scFv (b).

Since this project includes the discovery of unknown biomarkers for retinal injury, the recombinant antibodies can be quickly and cheaply generated [6] against any biomarker or biomarker fragment indicative of laser exposure. Traditional monoclonal antibody generation using hybridoma technology is expensive and time consuming. Many commercially available antibodies have been reported to work poorly or not at all. The ability to generate, engineer, and evaluate our own antibodies provides more opportunity for success of the biosensor aspect of this project.

3. Methods, Assumptions and Procedures

The project has three specific aims:

1. Generate a panel of custom antibodies to protein targets by using phage library display

2. Develop the assay for detecting protein biomarkers based on multiplex sandwich ELISA

3. Integrate the assay into the electrochemical detection platform

a) *Biomarker Target Preparation*

The peptides discovered by the Deepak Edward group using LC/MS/MS were chemically synthesized by the UIC Protein core facility. To allow for immobilization during antibody selection, the peptides included a biotinylation on the N-terminus, followed by a 4 residue G-S-G-S linker, and a C-terminal Amidation. The peptides were chosen since these portions of the protein were positively identified in the serum of the exposed rabbits. We could not assume that the remaining portions were present or intact.

b) *Phage-display Selection*

Wells of a Nunc Maxisorp 96-well plate (Nunc) were coated with 50ul of 10ug/ml Neutravidin in PBS and incubated at 4°C overnight. The plate was blocked with 1%Casein for 1 hr and then washed with 3xPBST. The scFv phage-display library ($1x10^9$ sequence diversity) (courtesy of Mark Sullivan, University of Rochester) was added in 50ul volumes to 4x blocked wells and incubated for 1 hr to deselect casein and Neutravidin binders. The unbound phage were transferred to wells containing 10ug/ml biotinylated-peptide and incubated for 2 hrs at room temperature with shaking. The wells were washed 5x with PBST. The phage were acid eluted using 50ul of 100 mM Glycine-HCl, pH 2.0 for 10 min. The eluted phage were neutralized with 3ul of 2 M Tris, pH 10. This was used to infect 750ul of TG-1 *E. coli* growing to OD_{600} =0.4, and incubated at 37°C without shaking for 1hr. The cells were spread on a LB agar plate containing 50ug/ml Carbenicillin (Cb) and incubated overnight at 30°C.

The following day, the lawn of growth was scraped into 15ml of Lb/cb. To 40ml of Lb/cb was added 100ul of the scraped cells, and then grown to mid-log at 37C. 1ml was infected with K07 helper phage for 1hour at 37°C with 150rpm shaking. This was added to 30ml of LB/Cb/Kanamycin (Kan, 50ug/ml) and grown overnight at 30°C to allow for phage production.

To precipitate the phage for the second round of selection, the overnight culture was spun down and the ~30ml supernatant mixed with 6ml 3 M NaCl, 24% PEG_{8000}, and incubated on ice for 1 hour. This was spun at high speed ~12,000 rpm for 15 minutes. The precipitate phage was suspended in 1ml of 0.5% casein in PBS. This was used for round 2 of selection.

Round 2 and round 3 were performed the same as round 1, except that the target was now reduced to 1ug/ml and the washes were increased to 7x PBST with harsh up and down pipetting in between.

After the final round of infecting and plating clones, 94 colonies were used to inoculate 100ul of Lb/Cb and grown to OD_{600} =0.4. To these cultures were added 200ul of K07 helper phage in Lb/Cb and allowed infection for 1 hr at 37°C, no shaking. Plates were spun down, supernatant discarded, and 400ul of LB/Cb/Kan added for overnight phage expression at 30°C with 250rpm shaking.

c) *Phage ELISA*

Two Nunc 96-well plates were coated overnight with 10ug/ml Neutravidin in PBS. The wells were blocked with 1% casein in PBS. To one plate was added the target biotinylated peptide at 10ug/ml and incubated for 1hour. After washes in PBS and PBST, 50ul of supernatant from each well of the overnight culture of expressed phage was added to the corresponding well of the coated target or background plate, and incubated for 1 hour. Washes of PBST and PBS followed. Addition of 50ul of anti-M13-HRP diluted to 1:5,000 in PBS to all wells in the Nunc plate, was used to detect the bound phage particles. Following washes of PBST and PBS, 50ul of 2,2'-azino-bis(3-ethylbenzothiazoline-6-sulphonic acid (ABTS) (Pierce) in 50mM Sodium Citrate pH 4 with 0.03% H_2O_2 was added, and color change recorded at absorbance wavelength 405nm using a BMG FluoStar OPTIMA spectrophotometer. Specific binders were identified by comparing absorbances of background and target plates.

d) *Cloning and bacterial expression*

The positive clones were grown up further and the plasmid DNA was prepared using a MiniPrep DNA purification column (Wizard MiniPrep, Promega). The scFv regions were sequenced. Unique clones were then sub-cloned into a low phosphate promoter, PhoA expression plasmid, pKP300DIIIDAP, with a N-terminal FLAG tag and C-terminal 6xHis tag. Expression is performed in low phosphate modified C.R.A.P. media overnight at 30°C. The cells are spun down and resuspended in lysis solution of 1x Bugbuster in PBS (Novagen) and Benzonase Nuclease HC (Novagen) for 20 mins. After pelleting cell debris, the scFv is purified from the supernatant through the poly-His tag using His·Mag Agarose Magnetic beads (Novagen) and a Kingfisher mL robotic purification system (ThermoScientific). Antibodies are eluted into 500 mM Imidazole, 500 mM NaCl, and 20 uM Tris-HCl, and stored at 4°C or at -20°C in 15% Glycerol.

e) *Fluorescence Polarization*

The biomarker peptides were re-synthesized to now include a Fluorescein Isothiocyanate (FITC) fluorophore on the N-terminus in place of the biotin. Fluorescence polarization measurements were performed in the antibody elution buffer (500 mM Imidazole, 500 mM NaCl, and 20 uM Tris-HCl) with 15nM FITC-peptide and a total volume of 25ul using half area 96-well plates (Costar). The scFv antibodies were expressed without the Alkaline Phosphotase fusion. A range of concentrations were used to find the upper and lower boundaries of the curve. Once an approximate EC_{50} was obtained, concentrations at least 10 times above and 10 times below this curve inflexion point were used to determine the binding constant. The data was recorded at an excitation wavelength of 485nm and an emission at 520nm using a BMG POLARStar Optima 96-well plate reader with a fluorescence polarization optic module.

f) *Photonic Crystal Biosensing*

To determine binding constants in a non-flow immobilized system, the SRU Biosystems Explorer was used. The binding on the plate surface was recorded in real-time for each of the following steps. A 96-well Streptavidin coated plate (SA1-96-M) was blocked with 5% BSA for 1 hour. The wells were washed with PBS. To these wells was added 50 ul of 10 ug/ml target peptide was added to 24 wells and the same was done for the negative peptide. The plate was incubated for 1 hour. The plate was washed and stabilized in elution buffer. Decreasing concentrations of antibody were added in triplicate to the target and control wells, and the binding response recorded. After overnight incubation at 4C, the plate was read again and the end-point values used in the curve calculations. A dose response curve was drawn using the SRU biosystems software where the EC_{50} is the dissociation constant.

g) *ELISA using soluble scFv*

Plates were coated with 50ul of 10ug/ml Neutravidin or BSA, overnight at 4°C. The plates were washed in PBST (0.1% Tween20) and 50ul 10ug/ml biotinylated peptide was added and incubated for 1 hour. After washing, 200ul of 5% Non-Fat Dried Milk in PBST was added to block the wells for 1 hour. This was followed by washing in PBST and then addition of 50ul of the purified scFv antibody in PBS for 1 hour with shaking. Wells were washed with PBST and 50ul of ABTS (2,2'-azino-bis(3-ethylbenzothiazoline-6-sulphonic acid) in 50mM Sodium Citrate pH 4, 0.03% Hydrogen Peroxide, was added to all wells. The color change was recorded at 405nm.

h) *Western of Retinal Lysates*

Retinal lysates from rabbit and mouse were obtained from Deepak Edward group and chicken eyes were obtained from a local butcher. Retinas were homogenized in 10 mM Tris-HCl, pH 7.4, 1 mM EDTA, and 200 mM Sucrose. Lysate was spun down and 5ul of the supernatant used for SDS-PAGE and western blotting. Gel electrophoresis was performed in Tris-Glycine-SDS buffer on a 12% precast Mini-Protean TGX polyacrylamide gel (Bio-Rad), at 12 mA for 1.5 hours. The protein was then transferred to PVDF membrane (Millipore) overnight at 25V in Tris-Glycine-SDS buffer with 20% Methanol. The membrane was blocked with 5% Non-Fat Dried Milk in PBST for 1 hour. One PBST and PBS wash was done for 5 minutes each. The anti-GBB5-H9 scFv was added at a concentration of 1 ug/ml in PBS and incubated with shaking for 2 hours. Blot was washed once with PBST and PBS for 5 minutes each. The secondary antibody anti-FLAG-HRP was added to the blot containing the scFv antibody and also to a negative control blot without the primary antibody, and incubated for 1 hour while shaking. The blots were washed once with PBST and PBS for 5 minutes each. Detection was performed using ECL Plus reagent (GE) and imaged using a Storm 860 Phosphorimager (Molecular Dynamics).

i) *Electrochemical Detection Based sandwich ELISA (ECD)*

The ECD-based sandwich ELISA is performed in three steps:

i. Deposition

Antibodies are deposited on the surface of each electrode by binding to polypyrrole deposits. Polymerization of pyrrole is triggered by applying voltage to each electrode and antibodies are incubated with the newly formed polypyrrole (Figure 5). Capture antibodies for multiplex detection are deposited by sequential rounds of pyrrole polymerization, incubation with the newly formed polypyrrole deposits and blocking unoccupied binding sites with casein. Polypyrrole is electro conductive and does not interfere with signal detection.

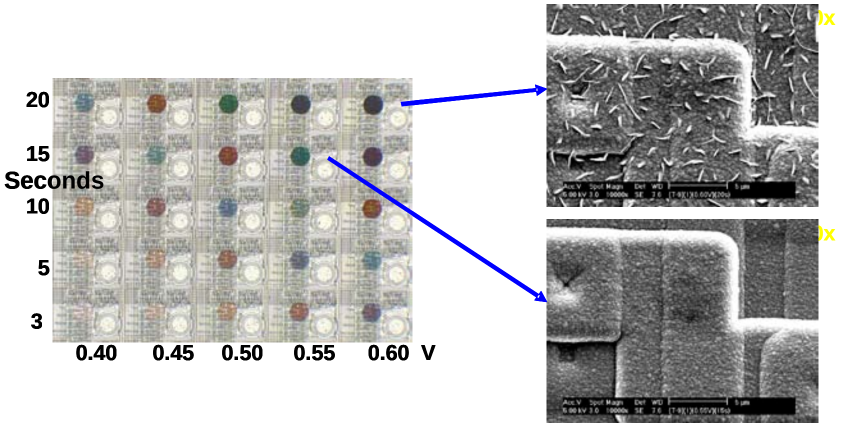

Figure 5. Polymerization of pyrrole. Pyrrole polymerization on electrodes was evaluated by increasing voltage and polymerization time.

ii. Detection

Capture antibodies deposited to polypyrrole are incubated with the antigen. Antigen can be detected by binding to labeled secondary antibody followed by electrochemical detection (Figure 6).

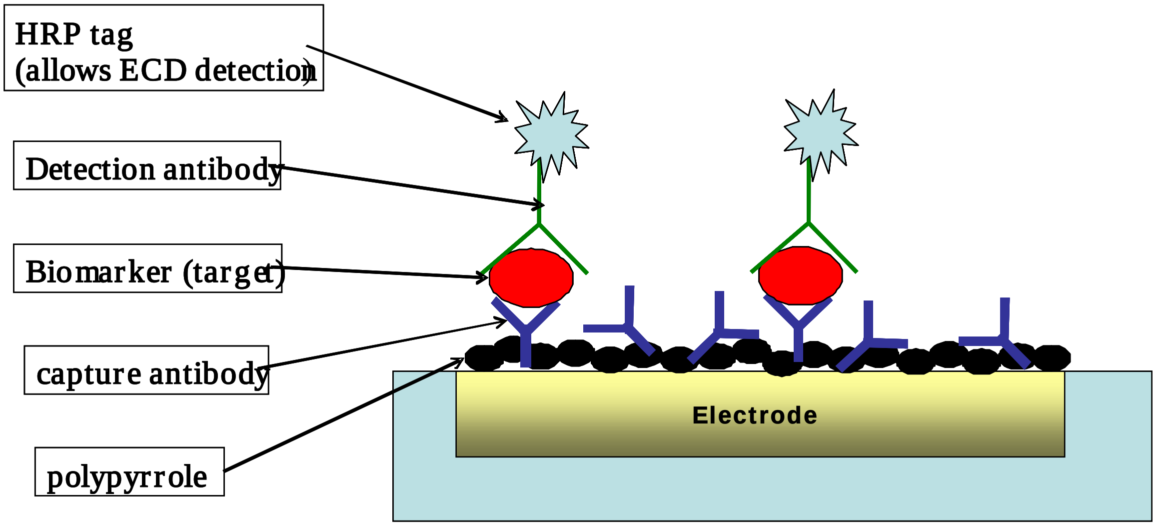

Figure 6. ELISA on protein microarrays

iii. Signal Amplification

Streptavidin-HRP binds biotin moieties of detection antibodies. HRP reacts with biotinylated tyramide resulting in deposition of multiple copies of biotin in the vicinity of the reaction site. More streptavidin-HRP binds to newly deposited biotin during the second incubation step. Amplified HRP activity is detected by ECD (Figure 7).

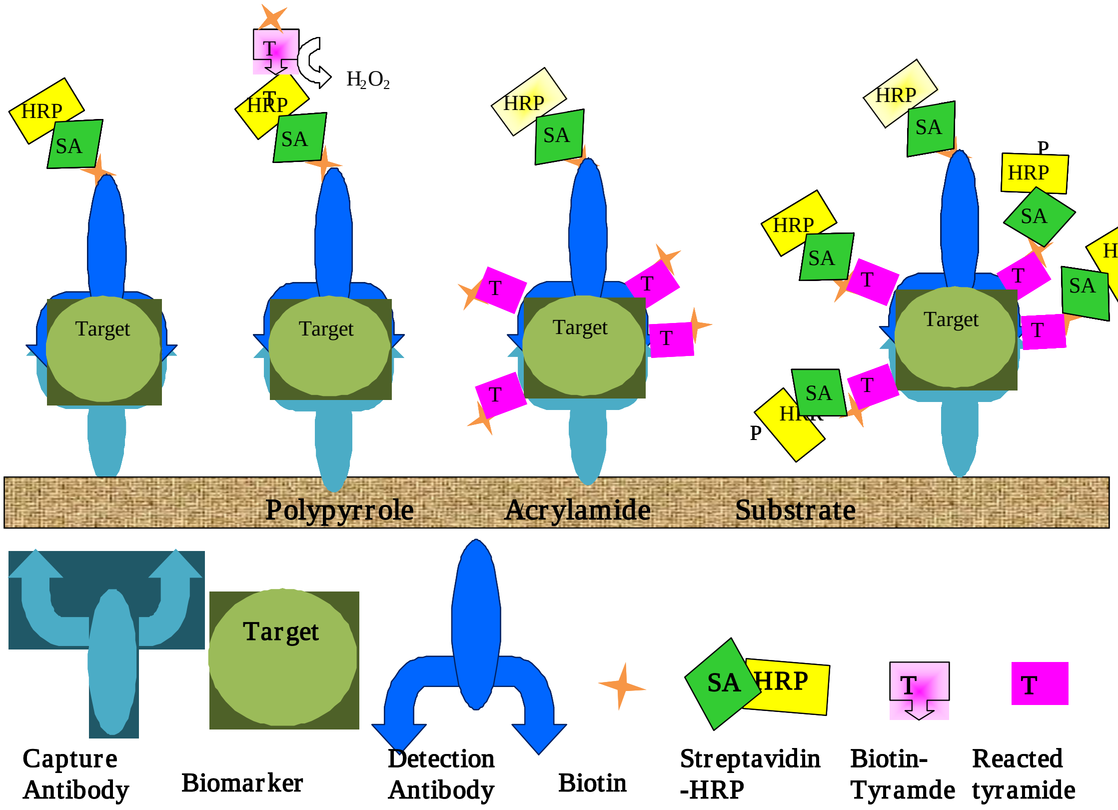

Figure 7. Tyramide signal amplification steps

iv. in Electrochemical Detection (ECD)

The CombiMatrix (now CustomArray) MX300 automated instrument was used to deposit polypyrrole onto blocks of 5x25 platinum electrodes across separate quadrants on a 12K chip containing over 12,000 electrodes. 20 ug of antibody-alkaline Phosphatase (AP) fusion protein was adsorbed to the polypyrrole, and then washed with PBST. This process of deposition and adsorption was repeated for each of the anti-biomarker antibodies (anti-CNGA3-A5, anti-CACNA1F-Pep1, anti-GBB5-A1, and casein as a negative control). The chip was spin coated and dried with casein in PBS. CNGA3-peptide was run in different concentrations over each gasket separated quadrant of the chip to allow binding. A 1:1000 dilution of poly-80-Streptavidin-HRP was added to the chip and allowed to bind the biotin on the peptide. After washing, an electrochemical current was generated with addition of the substrate 3,3',5,5'-Tetramethylbenzidine (TMB) in PBS. The current generated for each electrode was recorded in picoAmperes.

v. of Peptide-MBP fusion control

For a western blot positive control, an in-frame fusion of the biomarker peptide was made with a maltose binding protein (MBP) (Figure 8). This was constructed by designing forward PCR primers that 1) encode the respective peptide and 2) contain a complementary region that allows hybridization to the beginning sequence of the MBP. Performing PCR of the pAT224-MBP plasmid generates the newly formed peptide-MBP sequence that is cloned through NcoI and HindIII (New England Biolabs) restriction digest, and subsequent ligation back into the pAT224 with the original MBP removed. The ligation products were transformed into XL-1Blue electrocompetent E. coli. Confirmed recombinants were grown in 25ml LB/Cb + 1% Glucose in 250ml flasks, o/n at 37°C. From the overnight culture, ~10ml was used to inoculate to OD_{600} =0.12 in 250ml LB+cb+1%Glucose in 2L Flask. This was grown to OD_{600} 0.7, at 37°C where 500uM IPTG was used to induce expression. Expression was done for 6 hours at 37°C. The culture was then pelleted and frozen at -80C overnight. The pellet was then resuspended in PBS and sonicated at 51% amplitude for 5 minutes. After clearing the lysate, 0.5ml of Ni-NTA agarose slurry (Qiagen) was batch incubated for 5 hours at 4°C. This was then column purified with elution into 500mM Imidazole, 20mM Tris-HCl, 500mM NaCl.

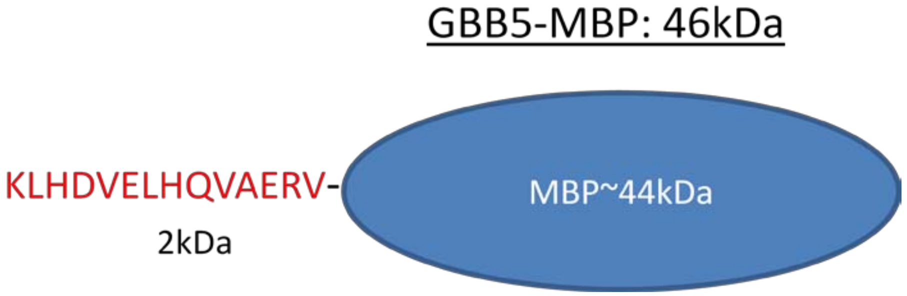

Figure 8. The GBB5-Peptide-MBP Fusion blotting control. An expression construct was made where the sequence for the biomarker peptides was cloned upstream of the sequence for Maltose Binding Protein. Upon protein expression, the peptide is fused to the N-terminus of the MBP. Since the MBP is much larger, the fusion protein can be resolved in a gel during electrophoresis and subsequently detected by the antibody in Western blot.

vi. Conversion

A construct containing the Fc portion of a rat Immunoglobulin was obtained from John McCafferty (University of Cambridge, U.K). The C-terminus has a His-Tag and a Tri-FLAG tag that allows three anti-FLAG secondary antibodies to bind. The scFvs were cloned upstream and in-frame with the Fc sequence. The plasmid was then transiently transfected into Human Embryonic Kidney Cells (HEK-293F) growing in a 40 ml suspension culture. Expression was allowed for 7 days at 37°C, 8% CO_2 while shaking. On the eighth day, the cells were spun out and to the supernatant was added 0.5ml of Ni-NTA agarose and batch incubated overnight at 4°C while tumbling. The scFv was then purified in a column and eluted in 400mM Imidazole, 200mM NaCl in PBS.

vii. Plasmon Resonance (SPR)

SPR measurements were performed using a Biacore T100 instrument (GE). 10ug/ml of the GBB5 peptide in PBS was immobilized to saturation on a flow cell of a Streptavidin SA sensor chip. Increasing concentrations of scFv or scFv-Fc were flowed over the surface at a rate of 10 ul/min in the elution buffer of 500mM Imidazole, 20mM Tris-HCl, 500mM NaCl. The binding response was recorded simultaneously with the control flow cell with immobilized RGS9 peptide. The control was subtracted from the experimental to give the mass accumulation on the surface of the chip. Real-time binding data was compiled by the evaluation software.

4. Results and Discussions

a) *Phage-display selection*

The screen of the phage-display scFv library against the various biomarkers resulted in at least one specific antibody (Table 1) per peptide. The shorter peptides yielded fewer antibodies possibly due the limited space for interaction with the peptide. The antibodies were all successfully cloned into bacterial vectors and expressed and purified. To test for specificity, an ELISA was performed using the bacterially expressed scFvs antibodies. Figure 9 shows that the scFvs recognize only the peptide they were selected to bind to and not unrelated full proteins or peptide antigens.

Table 1: Phage-display results

Biomarker Target	Peptide Synthesized with linker	Organism Match	# of AAs	# of Ab Clones
CACNA1F Peptide 1: **Voltage Dependent Calcium Channel**	Biotin-GSGS-**IRWFSHSTR**	**Human, Rat Mouse**	9	**1-4**
CACNA1F Peptide 2: **Voltage Dependent Calcium Channel**	Biotin-GSGS-**KPSFTIQCLQR**	**Human, Rat Mouse**	11	**1-4**
CACNA1F Peptide 3: **Voltage Dependent Calcium Channel**	Biotin-GSGS-**TEGNLEQANQELRIVIK**	**Human**	17	**4**
CNGA3: **Cyclic nucleotide gated channel**	Biotin-GSGS-**RLTRLESQMNRRCCGFSPDRE**	**Mouse**	21	**8**
GBB5: **Guanine nucleotide-binding protein**	Biotin-GSGS-**KLHDVELHQVAERV**	**Human, Rat, Mouse**	14	**6**
RGS9: **Regulator of G-protein**	Biotin-GSGS-**KLVEVPTKMRV**	**Rat,** **Human/Mouse:** KLVEIPTKMRV	11	**3**

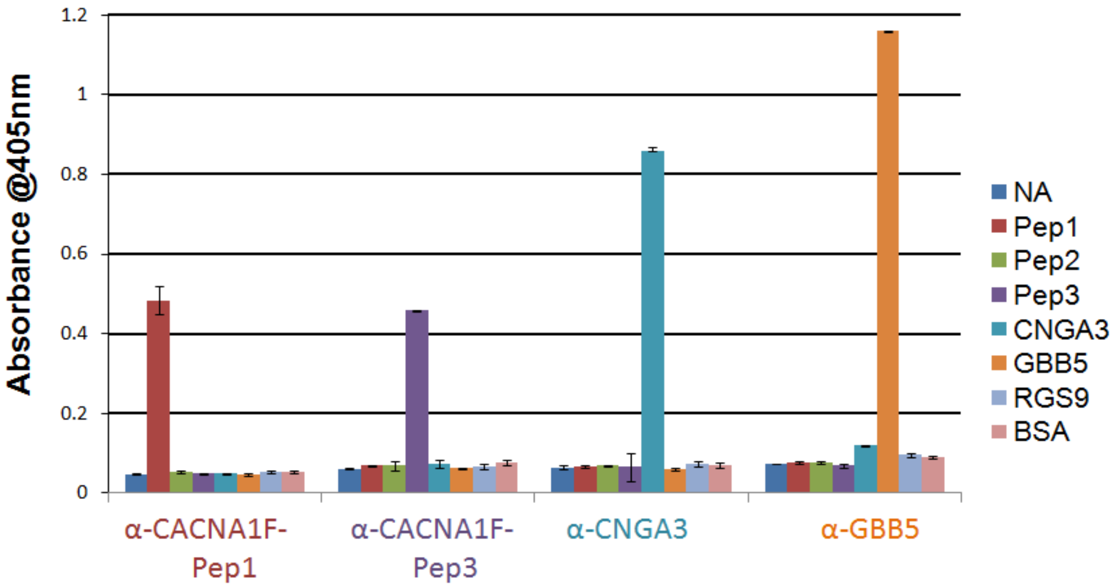

Figure 9. ELISA using purified anti-biomarker scFv. Immobilization of peptide on a plate surface and detection by the scFv shows specificity and sensitivity of the antibodies.

b) *Fluorescence Polarization*

To determine which clones bound the tightest, a more sensitive assay was needed. Fluorescence Polarization (FP) was used to determine the affinities of the antibodies by adding decreasing concentrations of scFv into wells with a fixed concentration of FITC-labeled peptide and recording the change in the polarization (fluorescence anisotropy) upon binding. A typical example of FP data appears in Figure 10, showing an increase in polarization with increasing concentration of scFv.

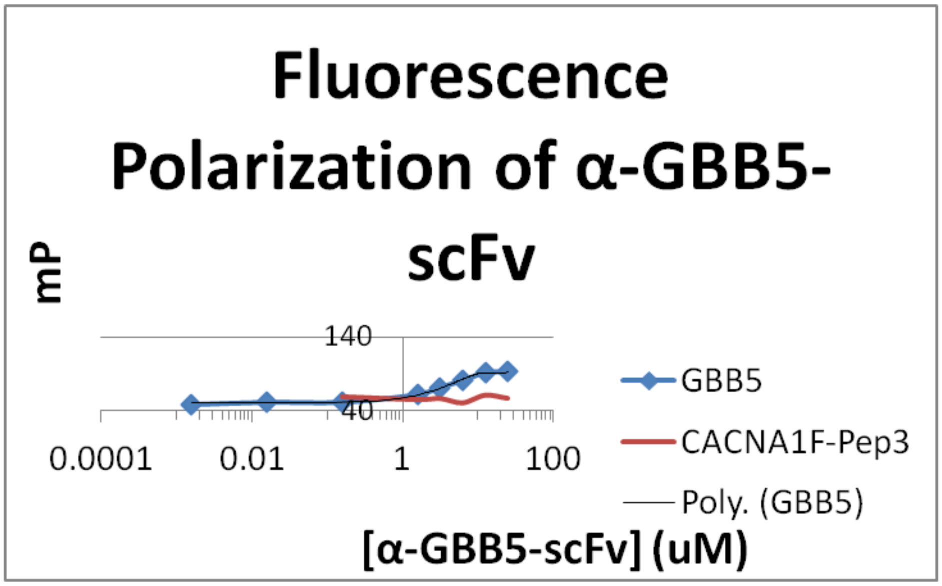

Figure 10. Fluorescence Polarization Result using the anti-GBB5-H9. The blue curve shows the concentration dependent increase in polarization units of the anti-GBB5-H9 for the GBB5 peptide. The red curve is the negative control, unrelated peptide showing no change in polarization and presumably no cross reactivity.

The inflexion point or EC_{50} of the curve gives the approximate binding constant. This was performed for many of the scFv antibodies, however, some express so poorly that not enough material was ever obtained to generate binding curves (Table 2). The majority of the antibodies had binding constants in the low micromolar range, which allows for binding and signal in the sensitive ELISA. A lower binding constant is desirable. One antibody, the anti-GBB5-H9, bound 10x stronger with a binding constant in the high nanomolar. This antibody was originally overlooked since the expression level is 10 times lower than the other antibodies and therefore gave a weaker signal as compared to the others.

Table 2: Antibody Binding

Antibody	K_d
α-CACNA1F-Pep1	2-5uM
α-GBB5-A1	3-4uM
α-GBB5-H9	250nM-500nM
α-CNGA3-A5	2-4uM
α-CNGA3-C1	4-7uM
α-RGS9-H1	1-2uM

c) *Photonic Crystal Biosensor*

To confirm the binding affinities obtained by the FP, a second technique using a photonic crystal biosensor was used. This provides approximate binding constants in a format where the target peptide is immobilized on a streptavidin coated titanium dioxide surface. As antibody binds to the surface, there is a change in the peak wavelength (PWV) of light reflected from a LED source beneath the plate. The shift in PWV is proportional to the amount of protein binding on the surface. Off rates cannot be determined but end-point binding values from different concentrations of antibody can be used to construct a dose response curve where the EC_{50} is determined to be the binding constant. As seen in table 3, many of the affinities agree with the FP measurements where again the anti-GBB5-H9 scFv antibody has a 10 fold stronger binding than the others. This also shows the ability of the photonic crystal biosensor to potentially detect the full biomarker in a diagnostic assay.

Table 3: BIND Reader results

Antibody	Kd from BIND Reader
Anti-GBB5-H9	306nM
Anti-GBB5-A1	4-6uM
Anti-RGS9-A5	2-3uM
Anti-RGS9-A6	3-8uM
Anti-RGS9-H1	2-3uM
Anti-CNGA3-A6	2-8uM
Anti-CNGA3-D8	13.6uM
Anti-CNGA3-C9	2-3uM

d) *Western Blotting*

Up until now, all the experiments have been done on the synthesized peptide. To test the antibody's ability to recognize the endogenous full protein from an animal, western blotting was performed on retinal and whole eye lysates of rabbit, mouse, and chicken. Positive results were seen only when the tight binding anti-GBB5-H9 antibody was used (Figure 11). The blot shows recognition of a protein at around the expected size of the full length GBB5 protein (MW~40kDa) for each of the three animals, while the negative control (secondary antibody only) shows the non-specific binding of the anti-FLAG-HRP secondary antibody. The bands detected below 30kDa in the mouse lysate can be attributed to degradation of the GBB5 protein to a smaller size, and a large amount of additional unrelated protein. The antibody was also observed to recognize the recombinantly expressed and purified human version of the GBB5 (GNB5) in Western blot.

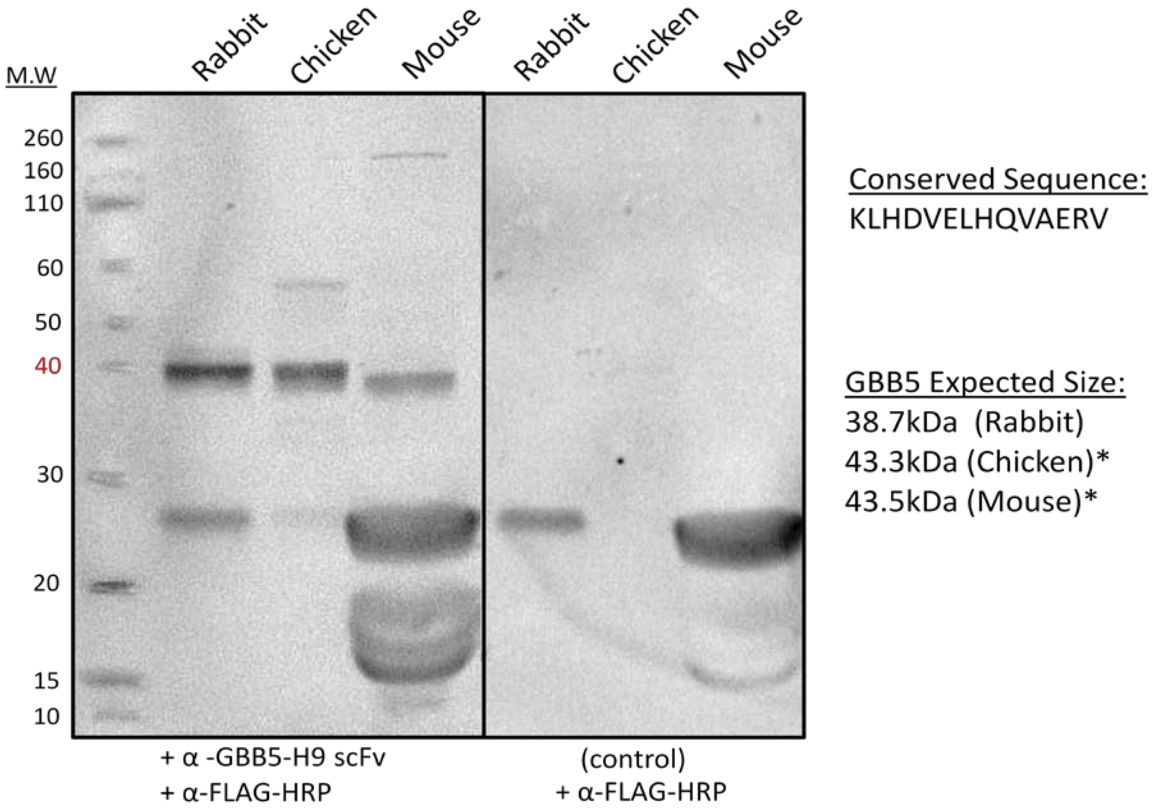

Figure 11. Western blot of retinal lysates using anti-GBB5-H9 scFv. The GBB5 endogenous protein is detected in rabbit, chicken, and mouse lysates at the expected sizes of around 40kDa. The right side shows the negative control of secondary antibody only

***the chicken and mouse expected sizes are predicted from cDNA.**

e) *Electrochemical Detection (ECD)*

The CombiMatrix 12K electrode microchip was chosen as an assay platform because of its small size, electrical output, and potential for a multiplexed array of antibodies to accommodate a biomarker panel. Each chip has 12,000 individually addressed electrodes that theoretically can detect an electrical signal from 12,000 deposited antibodies. However, since there is variation across electrodes and each antibody must be deposited in serial, only 4 antibodies can be practically used per chip to assay 4 biomarkers at this time.

f) *Formatting ECD platform for multiplex ELISA*

We optimized each step of deposition/detection protocol by using cytokines as target molecules. For most cytokines the lower limit of detection was around 100pg/ml, which is similar to conventional microwell plate-based ELISA (Figure 12). The capability of detecting a number of proteins in the same assay was demonstrated for three cytokines (Figure 13). Each cytokine was detected either individually or in the mixture. By using the tyramide signal amplification protocol, significant amplification of ECD signal from TNF-*a* target protein was observed. No increase in the background was detected (Figure 14).

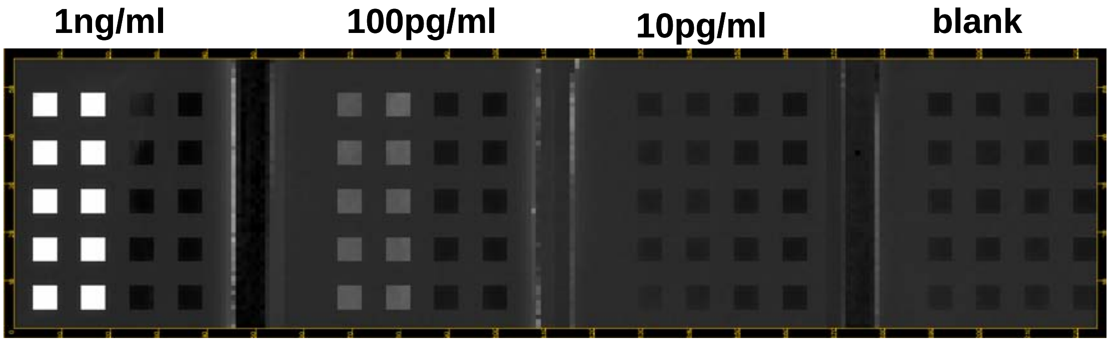

Figure 12. Lower limit of detection of IL-6 cytokine. Anti-IL-6 capture antibodies were deposited in the first two rows in each quadrant. The third and the forth rows were blank controls. Each quadrant was incubated with IL-6 at indicated concentrations. No target was applied to the fourth quadrant.

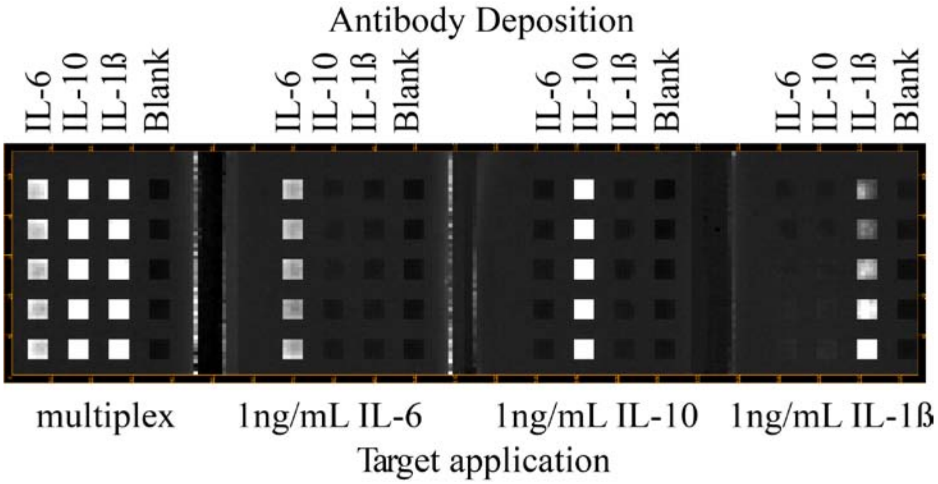

Figure 13. Detection of IL-6, IL-10, and IL-1β by protein microarrays. Anti-IL-6, anti-IL-10, and anti-IL-1 β antibodies were deposited in rows 1, 2, and 3 in each quadrant. Row 4 was a blank control. Each quadrant was incubated either with individual target or with the mixture of all three targets, as indicated.

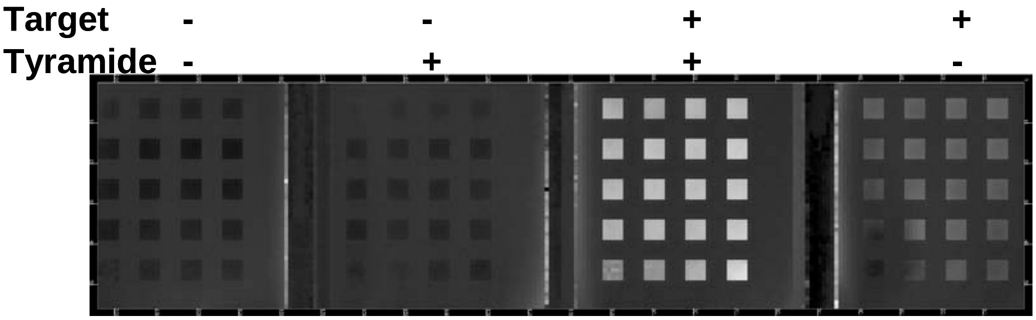

Figure 14. Signal amplification by tyramide in TNF-α detection assay. Anti-TNF-α antibody was deposited in all rows of each quadrant. Quadrants 3 and 4 were incubated with the target. No target was applied to quadrants 1 and 2. Tyramide was added to quadrants 2 and 3.

To deposit the anti-biomarker scFv antibodies to the surface of the poly-pyrrole coated platinum electrodes, the scFv antibodies were expressed with a C-terminal Alkaline Phosphotase (AP) fusion enzyme to allow adsorption at a region of the antibody that is not required for antigen binding. The AP protein adds around 40kD, to give a total size of about 70kD. Since the adsorption of the antibody to the polypyrrole is non-directional, there is a possibility that the antigen binding epitopes will be hidden if they adsorb “face down”. There is a good chance this will occur if only the scFv is used. The AP addition provides an increased surface area for adsorption as to allow the antigen binding epitopes of the scFv to be oriented in a way where binding can occur. To test this approach, the anti-CNGA3-A5 scFv was chosen. Three different antibodies were deposited in separate rows of 5x 25 electrode blocks in four quadrants of the chip. There were four rows in each quadrant with one of the following: an anti-CNGA3-A5, an anti-CACNA1F-Pep1, an anti-GBB5-A1, or casein to serve as a negative control. The other two antibodies were deposited to test for cross-reactivity. The orientation upon adsorption was favorable enough to get a concentration dependent electrical signal when differing concentrations of the CNGA3 peptide was incubated on each quadrant of the chip (Figure 15). The peptide could be detected down to 100 ng/ml with little to no cross reactivity from the other adsorbed scFvs.

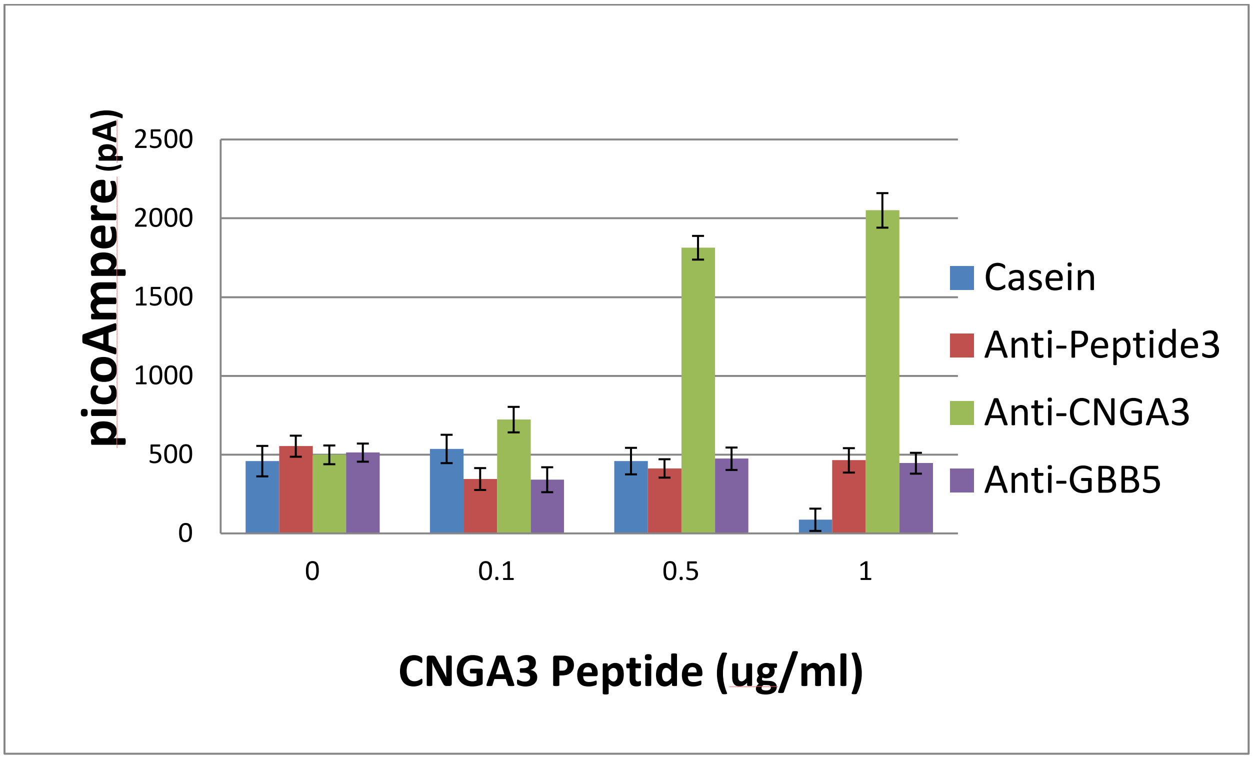

Figure 15. Electrochemical Detection using the anti-CNGA3-scFv. Detection is concentration dependent and does not cross react with unrelated peptides. The anti-CNGA3 antibody gives an electrical signal over background down to 0.1ug/ml of peptide.

Direct deposition of recombinant antibodies resulted in low signal, possibly due to lower affinity of single-chain antibodies compared to fully assembled endogenous antibody molecules. To lower detection limits further and provide multiplexed detection, a more consistent and directed method for orientation specific attachment was needed. The FLAG tag of the scFv antibody was utilized for this purpose.

To increase deposition of single-chain molecules we introduced a two-step deposition protocol, in which the mouse anti-FLAG antibody is deposited to polypyrrole and then incubated with the FLAG-tagged antibodies thereby depositing similar amounts of capture molecules regardless of their sequence. By using these modifications we demonstrated recognition of both GBB5 and CNGA3 targets by the corresponding single chain molecule. We also confirmed that by converting the scFv to an scFv-Fc molecule, binding of target to the GBB5 scFv antibody was increased (Figure 16).

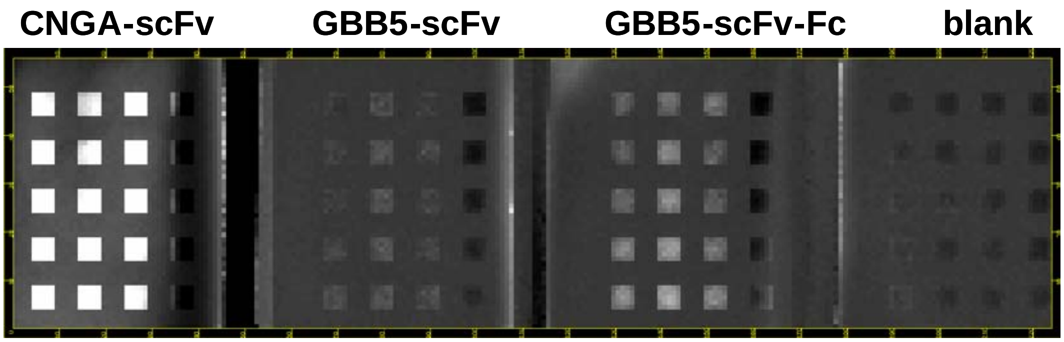

Figure 16. Detection of CNGA and GBB5 by protein microarrays. Anti-Flag antibody was deposited in all quadrants. Quadrants were incubated with the recombinant antibodies as indicated, followed by incubation with corresponding biotynlated target.

g) *Conversion to scFv-Fc Scaffold*

The conversion of the monovalent scFv into a divalent scFv-Fc was done to increase the binding affinity of the antibody through avidity (Figure 17). Since antibody binding is in equilibrium of being bound and unbound, having two epitopes that bind simultaneously to two antigens, decreases the off rate and allows the antibody to be present for longer. This is in fact what was seen on western blot in comparison of the anti-GBB5-H9 scFv and the anti-GBB5-H9-scFv-Fc. As seen in Figure 18, the scFv version can detect the GBB5 peptide-MBP fusion to a lower limit of 0.25ug total protein or 25ng/ml sample concentration, while the Fc version can detect a lower limit of 0.01ug or 1ng/ml sample concentration. This is a 25-fold improvement over the scFv version.

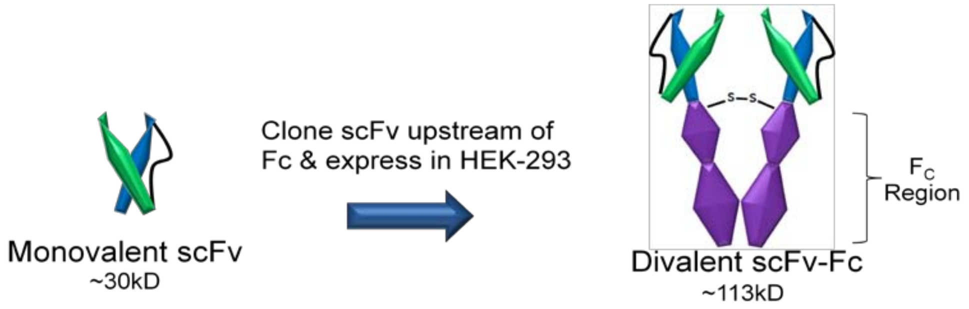

Figure 17. Conversion of the monovalent scFv to the divalent scFv-Fc. The scFv-Fc is expressed as two polypeptides in HEK-293 cells and comes together through a disulfide bond. The two binding domains provide stronger binding to the target through avidity.

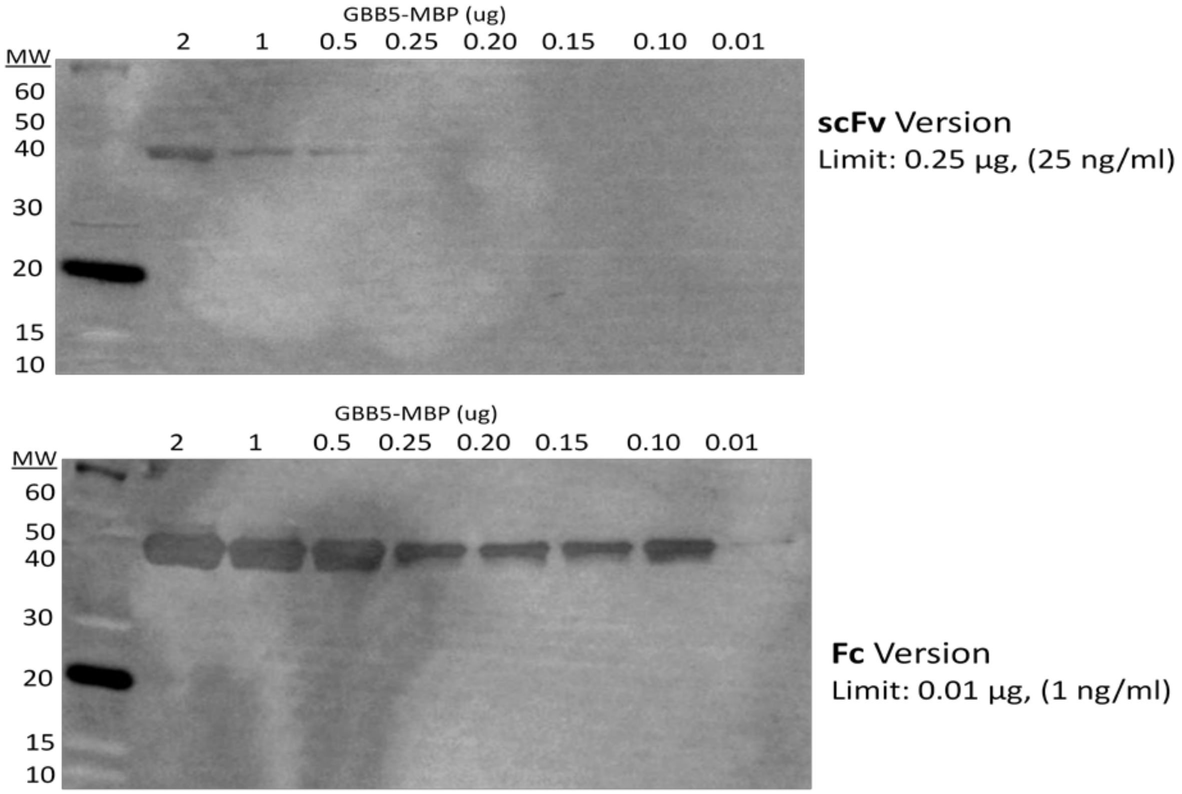

Figure 18. Western blot of GBB5-peptide-MBP using scFv-Fc. When the scFv is converted to the scFv-Fc divalent version, the lower detection limit decreases 25x to 0.01ug or a sample concentration of 1ng/ml.

viii. Plasmon Resonance

SPR is considered of the most accurate methods to determine dissociation constants of antibodies. When testing our antibodies on the instrument, the dissociation constants were about 100 fold higher than was found in FP. This may be due to the nature of the assay where the peptide is immobilized to a streptavidin coated gold surface and the antibody flowed over, while in FP the peptide is free to bind the antibody in solution. The anti-GBB5-H9 scFv gave a dissociation constant of ~50uM while the scFv-Fc version gave ~0.5uM. The off rate of the scFv-Fc version can be seen to increase dramatically with antibody binding persisting at nearly an hour, compared to the scFv that comes off the target in seconds with a continuous flow of buffer (Figure 19). The overall affinities are not as good as expected, however the 10-100 fold improvement with the scaffold change shows the potential for significantly increasing affinities of any of the anti-biomarker scFvs.

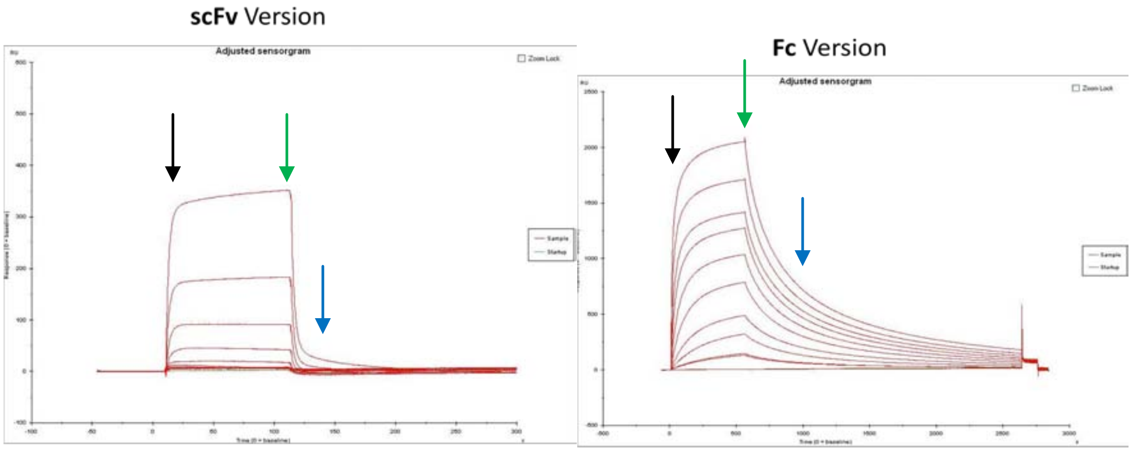

Kd: ~50uM

Kd: ~0.5uM

Figure 19. Surface Plasmon Resonance of scFv-Fc. The conversion to the scFc-Fc scaffold gives a 100 fold increase in binding affinity; however the overall dissociation constant is high. The black arrow shows the start of the antibody flow over the surface of the immobilized peptides. The increase in the y-axis shows real-time binding of antibody. The x-axis is time in seconds. The green arrow shows when only buffer begins to flow over the surface. The blue arrow shows the off rate of the antibody washing off of the peptide

5. Conclusions

Antibodies against the 4 most promising biomarkers (6 peptides) of laser eye injury were generated using a phage-display library of scFvs. They all are specific for the peptide they were selected to bind to and show no cross reactivity. Binding strengths were determined by three methods. Fluorescence Polarization gave dissociation constant ranges from 1-10uM for most of the antibodies, except the anti-GBB5-H9 which gave 10 fold less at 250-500nM. The photonic crystal biosensor assay gave similar values and confirmed the FP data. The SPR however yielded values that corresponded to 100x weaker binding antibodies. This difference could be due to the buffer flow system of the instrument as opposed to the in-solution or endpoint binding of the FP and photonic crystal biosensor, respectively. The anti-GBB5-H9 scFv was shown to recognize the endogenous GBB5 protein from mouse, chicken, and rabbit retinal lysates as well as the purified human form of the protein (data not shown). Conversion of this antibody to the scFv-Fc scaffold gave 10-100 fold improvement in binding affinity due to avidity of the divalent molecule. This also increased the sensitivity of the Western blot by lowering the detection limit 25x to 1ng/ml. Finally, an electrochemical detection protocol for multiplex sandwich was developed, the panel of custom antibodies was integrated into the assay, and the assay was formatted for detecting two biomarkers of laser eye injury.

6. References

1. Dill, K., et al., *Immunoassays based on electrochemical detection using microelectrode arrays.* Biosensors & Bioelectronics, 2004. **20**(4): p. 736-742.
2. Smith, G.P., *Filamentous Fusion Phage - Novel Expression Vectors That Display Cloned Antigens on the Virion Surface.* Science, 1985. **228**(4705): p. 1315-1317.
3. McCafferty, J., et al., *Phage antibodies: filamentous phage displaying antibody variable domains.* Nature, 1990. **348**(6301): p. 552-4.
4. Hanes, J., et al., *Ribosome display efficiently selects and evolves high-affinity antibodies in vitro from immune libraries.* Proceedings of the National Academy of Sciences of the United States of America, 1998. **95**(24): p. 14130-14135.
5. Hagemeyer, C.E., et al., *Single-chain antibodies as diagnostic tools and therapeutic agents.* Thrombosis and Haemostasis, 2009. **101**(6): p. 1012-1019.
6. Kotlan, B. and M.C. Glassy, *Antibody phage display: overview of a powerful technology that has quickly translated to the clinic.* Methods Mol Biol, 2009. **562**: p. 1-15.

F. Molecular Beacon Detection Scheme for Occupational Health and Safety Sensor

1. Summary

This aspect of the project explores the application of molecular beacons to sense threats to occupational health and safety. The first phase of this project was dedicated to a detailed study on the current uses of molecular beacons to identify and quantify targets associated with occupational health and safety. The outcome was a catalog and database displaying the current utilization of molecular beacons to track absorption and distribution in the body. The focus was the detection of heavy metal ions due to their extreme toxicity and the challenge they present as sub-nanoscale particles. The use of DNA aptamers as molecular recognition elements in biosensors for heavy metal ions makes a suitable platform for single molecule detection. The transduction mechanism used in the sensors is an energy transfer process between semiconductor quantum dots, which fluoresce when excited by light and acceptor molecules that can absorb the light emitted by the quantum dots. This phenomenon is distance dependent and can be coupled with the conformation change the DNA makes when it interacts with its target and thereby causes a decrease or increase in fluorescence. This change in fluorescence can be seen with the naked eye or detected using a spectrometer. Two different DNA sequences that interact with specific targets, known as aptamers were used to detect mercury, lead, zinc and cadmium. These probes were tested in a liquid assay as well as on a filter paper coupon, which the assay was applied to and allowed to dry. The use of Raman spectroscopy was also investigated in the detection of zinc ions using a zinc aptamer.

2. Introduction

The literature survey conducted on chemicals associated with occupational health and safety focused on the toxicity of heavy metals and how they are absorbed in the body. This information assisted in the development of heavy metal detection assays. Toxicity from the heavy metal ions lead (Pb), mercury (Hg), and cadmium (Cd) can all result in renal dysfunction [1]. While zinc is an ion required for normal physiological function, it can also result in toxicity upon excessive supplementation [2]. Toxicity from the heavy metal lead (Pb) can adversely affect several organs and body systems and potentially cause cardiovascular disease, hypertension, renal dysfunction, Autism and Parkinson’s disease. Determination of lead exposure can be done through measurement of blood, urine and bone Pb levels. These species are biomarkers for lead poisoning. Blood-Pb is an indicator for recent or acute exposure and urine-Pb levels provide information on the body burden over a longer period of exposure. The bone-Pb level tells what the body burden dose was from Pb over the lifetime of exposure. An independent study shows high risk of cardiovascular disease for individuals with Blood lead level (BLL) < 5 µg/dL. 15% of Pb exposed workers had BLL more than OSHA permissible limits. In another independent study of lead mobilization test on children, multiple positive correlations were found between the severity of autism and the urinary excretion of toxic metals. WHO and OSHA safety level for Pb are 1.45 µM (30 µg/dL) and 1.93 µM (40 µg/dL) respectively [3]. Above these safety levels concentration of lead in the body can be toxic.

Concentrated mercury also poses serious problems to human health, as bioaccumulation of mercury within the brain and kidneys ultimately leads to neurological diseases. To control mercury pollution and reduce mercury damage to human health, sensitive determination of mercury is important [4]. The concentration of mercury in drinking-water sources is usually less than 0.5 μg/liter, but sometimes groundwater can have higher concentrations. Many studies involving the observation of more than 1000 individuals indicate that the classical signs and symptoms of elemental mercury vapor poisoning (objective tremors, mental disturbances and gingivitis) may be expected to appear after chronic exposure to air mercury concentrations above 0.1 mg/m^3 (IPCS, 1991) [5]. Ingestion of 500 mg of mercury (II) chloride causes severe poisoning and sometimes death in humans. Acute effects result from the inhalation of air containing mercury vapor at concentrations in the range of 0.05–0.35 mg/m^3. Exposure for a few hours to 1–3 mg/m^3 may give rise to pulmonary irritation and destruction of lung tissue and occasionally to central nervous system disorders [5]. Among the high consumers of fish, the median concentrations of mercury were 8.6 μg/L in blood, 2.4 μg/g in hair, 10 pg/L in end-exhaled air, and 1.1 μg/g creatine in urine. The relationship between freshwater fish consumption and mercury was significant in all biological media. The high-consumption group had much higher mercury levels in blood (9-fold), hair (7-fold), alveolar air (3-fold), and urine (15-fold) than the low-consumption group [6 blood, urine, and alveolar air].

Cadmium is a contemporary metal with many industrial uses, and cadmium emissions to the atmospheric, aquatic, and terrestrial environment have increased over the years [7]. The kidneys are usually the most critically affected organs in occupational exposure to Cd; known to adversely interfere with the renal handling of plasma derived proteins. Tubular proteinuria should also be considered as an adverse effect attributed to Cd exposure, because it can lead to irreversible renal damage associated with an exacerbation of the age-related decline in glomerular filtration rate and a decrease in the filtration reserve capacity. The biological exposure thresholds for controlling health significant nephrotoxic effects in adults occupationally exposed to Pb and/or Cd are 700 μg Pb/L in blood and 5 μg Cd/L in blood [8]. The table below summarizes the toxic effects of the metals discussed.

Table 1: Summary of Heavy Metal Characteristics

Heavy Metal	Sources of Exposure	Toxicity Levels	Toxicity Effects
Lead (Pb)	Occupational, drinking water	WHO: <1.45 uM (30 ug/dL) OSHA: <1.93 uM (40 ug/dL)	Cardiovascular disease, hypertension, renal dysfunction, Autism, Parkinson's disease
Mercury (Hg)	Fish, drinking water, dental amalgams	OSHA: <0.1 mg/m^3 (time weighted avg.) EPA: max. contamination level for drinking water is 2ug/L (10 nM)	Cardiovascular disease, renal dysfunction, Autism
Zinc (Zn)	Supplementation (RDA is 15 mg/day)	100-300 mg Zn/d associated with toxicity	Copper deficiency, neutrapenia, anemia, adverse effect on ratio of LDL/HDL cholesterol
Cadmium (Cd)	Occupational, Cigarette smoke; food/drink	OSHA: 5 mg/m^3 ACGIH: Threshold Limit Values are 10 µg/m^3 total, 2 µg/m^3 inhalable fraction	Renal dysfunction, proteinuria, hepatotoxicity

3. Methods, Assumptions and Procedures

The use of molecular beacons and DNA aptamers in the fabrication of biosensors for the detection of threats to occupational health and safety are described below. The molecular beacons and DNA aptamers are used to synthesize optical probes using semiconductor nanocrystals or quantum dots along with quenchers. In addition, the fabrication of a substrate for enhanced Raman signals for the detection of metal ions using a DNA aptamer is described.

a) *Molecular beacons for pathogen detection*

For the detection of *Salmonella typhimurium* and *Listeria monocytogenes* the antisense beacon sequence for specific genes in these pathogens were ordered from Integrated DNA Technologies (IDT) (Coralville, IA). For Salmonella detection the target sequence is GCT CAG ACA TGC CAC GGT ACA ACG, which is specific to the *inv*A gene. The target sequence for Listeria detection is CAT CGT CCA TCT ATT TGC CAG GTA. For both molecular beacons the antisense sequence was ordered with a black hole quencher II (BHQ2) modification on the 3' end. BHQ2 is a dye that maximally absorbs light in the 559 nm to 670 nm range. The 5' end was functionalized with an amide group and 12 extra carbon atoms to provide a spacer between the DNA and the much larger quantum dot (QD). The quantum dots in this study were composed of a cadmium selenide (CdSe) core and a zinc sulfide (ZnS) shell and were purchased from eBioscience, Inc. (San Diego, CA). These QDs emit light at 605 nm when excited by a higher energy light source. The surface of the QDs was carboxyl functionalized for conjugation to the amide terminated DNA beacon. The cross-linker 1-ethyl-3-[3-dimethylaminopropyl] carbodiimide hydrochloride (EDC or EDAC) was used to bind the beacon to the QD. These molecular beacons in their folded form are shown in the figures below.

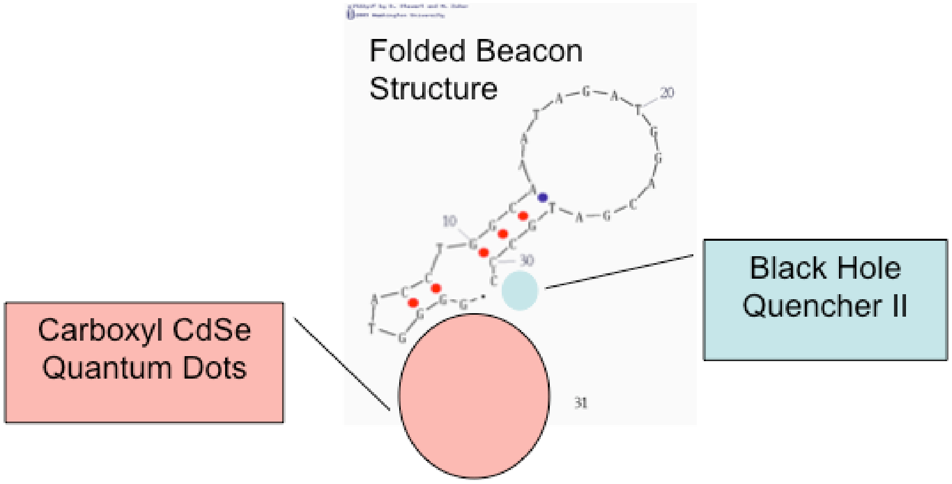

Figure 1. Molecular beacon for *Listeria monocytogenes*. Target is DNA sequence CAT CGT CCA TCT ATT TGC CAG GTA.

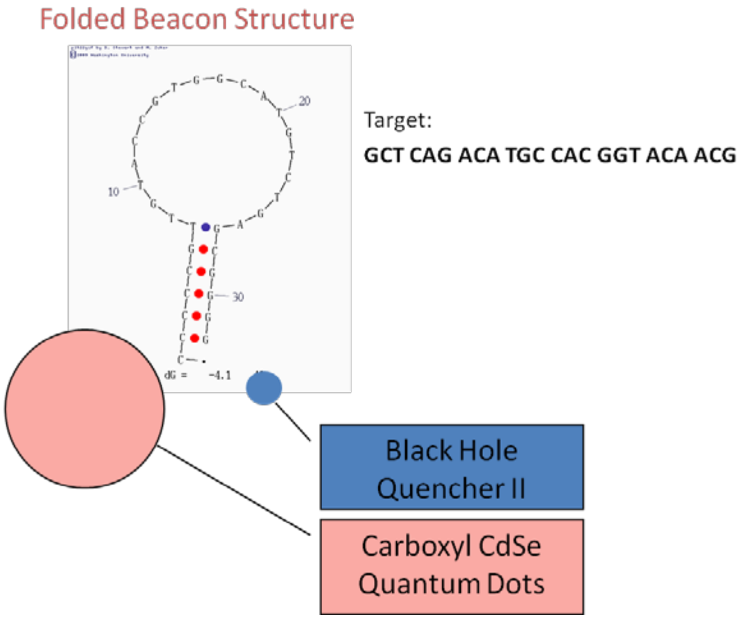

Figure 2. Molecular beacon for the detection of Salmonella *typhimurium* using a quantum dot and black hole quencher II.

While the probes are in their folded conformation the BHQ2 is close enough to absorb the light emitted by the QD. BHQ2 can absorb light through Fluorescence Resonant Energy Transfer (FRET), which is a distance depended energy transfer process [9]. It occurs when the QD and the BHQ2 are within close enough proximity to each other (1-10 nm). Once the target sequence is present, the folded complementary sequence opens up in order to hybridize with the target. This causes separation between the QD donor and the BHQ2 acceptor, thereby reducing the amount of energy transfer or quenching. The detection of the target is indicated by an increase in fluorescence.

b) *Zinc ion Detection with Raman Spectroscopy*

In order to investigate the potential for using microRaman spectroscopy as a method for remote detection of harmful chemical species, the Raman signature of a DNA aptamer that was selected for zinc was analyzed with and without zinc. This was done using a silver film over nanosphere (AgFON) substrate to enhance the signal. Van Duyne has shown these substrates to enhance the Raman signal via the phenomenon Surface Enhanced Raman Spectroscopy (SERS) [10]. The original aptamer, labeled Zn-6m2, which was selected by Rajendran and Ellington, was truncated to only include the segment involved in the folded structure [11]. The figure below shows the predicted folded structure of the zinc aptamer when interacting with zinc.

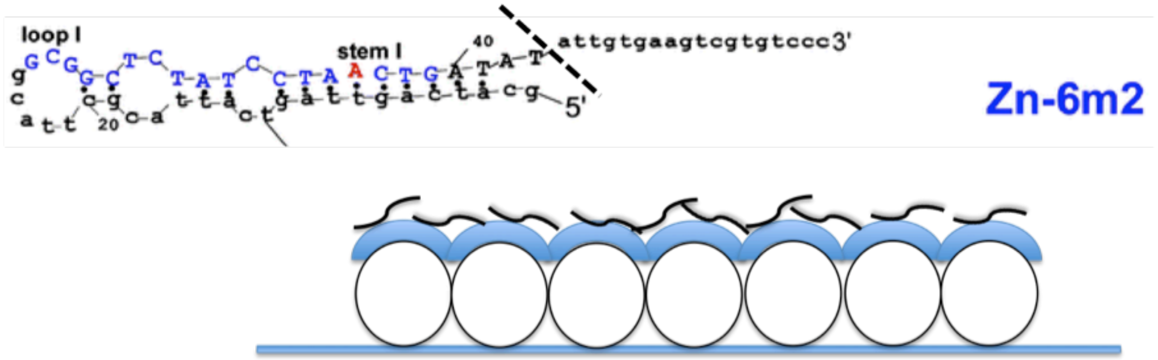

Figure 3. Top is the DNA sequence of aptamer Zn-6m2 in its predicted folded conformation with a dotted line indicating where the aptamer was truncated for this experiment. Bottom is the schematic of the SERS substrate, which consists of a layer of polystyrene beads covered with a thin film of silver (~100 nm). The aptamer was placed on the surface for analysis.

The aptamer for zinc in Figure 3 was ordered from Integrated DNA Technologies (Coralville, IA) with the segment to the right of the dashed line removed since this segment does not appear to be involved in the zinc interaction. The aptamer was dissolved in TE buffer at a concentration of 5 mM. Zinc chloride salt from Sigma-Aldrich (St. Louis, MO) was used to make a solution of aptamer with zinc ions.

The SERS substrate was created using nanosphere lithography as done previously by Van Duyne et al. [10]. Glass slides obtained from Fisher Scientific were cleaned using Piranha (1:3 30%H_2O_2:H_2SO_4) solution and then rendered hydrophilic by using 5:1:1 H_2O:NH_4OH:30% H_2O_2 with sonication for 1 hour. Surfactant-free, white carboxyl substituted polystyrene latex nanospheres with diameters of 390 nm from Duke Scientific, were used undiluted at 2 µl (10%wt/ wt %) and drop coated onto the glass slide. After drying, a thin layer (~100 nm) of silver was thermally deposited on the microsphere mask using the Varian e-beam deposition system at a rate of 1 Å/s at 10^{-7} torr pressure. After the substrates were prepared the two samples were drop cast onto the surface and allowed to dry. One with the aptamer at a concentration of 5 mM and the other with the aptamer plus 2 mM zinc (II) ions. The two sequences were analyzed using a Renishaw micro-Raman system with an Ar^+ -ion laser (514.5 nm wavelength). The power was 8 mW and the acquisition time was 120 s.

c) *Mercury (II) ion probe*

The modified thrombin binding aptamer (TBA), 5-/5AmMC12/GGT TGG TGT GGT TGG /3ThioMC3-D/-3 was purchased from Integrated DNA Technologies Inc. (Coralville, IA). The reagents Tris(2-carboxyethyl)phosphine) (TCEP) and (1-Ethyl-3-[3-dimethylaminopropyl]carbodiimide Hydrochloride) (EDC) were purchased from Pierce Biotechnology (Rockford, IL). The carboxyl-functionalized eFluor® 650 Nanocrystals (NC) or QDs were purchased from eBioscience, Inc. (San Diego, CA) and have a CdSe core and ZnS shell with a proprietary polymer coating. The emission wavelength is 650 +/- 3 nm. The 1.4 nm diameter Monomaleimido Nanogold® particles or gold nanoparticles (AuNP) were from Nanoprobes, Inc. (Yaphank, NY). All other chemicals were obtained from Sigma-Aldrich (St. Louis, MO).

The DNA was dissolved in Tris ethylenediamine tetraethyl acetate (EDTA) (TE) buffer (10 mM Tris, 1 mM EDTA) at pH 8.0. The dithiol group on the DNA 3' terminus was reduced using TCEP solution to a sulfhydryl (-SH) group before mixing with the Monomaleimido Nanogold particles. An excess of DNA was used at a ratio of 20 nmol DNA to 6 nmol Nanogold. An excess of DNA was used because the smaller molecular weight DNA is easier to separate. After this step, the solution was filtered using a 10K molecular weight cut off (MWCO) centrifugal device, which was centrifuged at 7,000 x g for 20 minutes, to remove any unbound DNA and excess TCEP. The TBA-Nanogold conjugates were then suspended in TE buffer for attachment to the QDs. Again, an excess of DNA was used for this conjugation. There were 10-fold more TBA-AuNP structures than QDs. The carboxyl groups on the QDs are activated with the crosslinker, EDC, followed by reaction with the amine-functionalized 5' terminus of the TBA. The mixture was then filtered with a 100K MWCO membrane to remove any unbound TBA-AuNP complexes. A schematic of the probe and how it works is illustrated in the figure below (Figure 4). Figure 5 shows how Hg ions interact with DNA through the nitrogen 3 atom of the nucleic acid thymine. This interaction is why a strand of DNA with 6 thymines in it will bind to Hg. Since the thymines are symmetric in their position, the TBA folds in half when the thymine-Hg-thymine structures form.

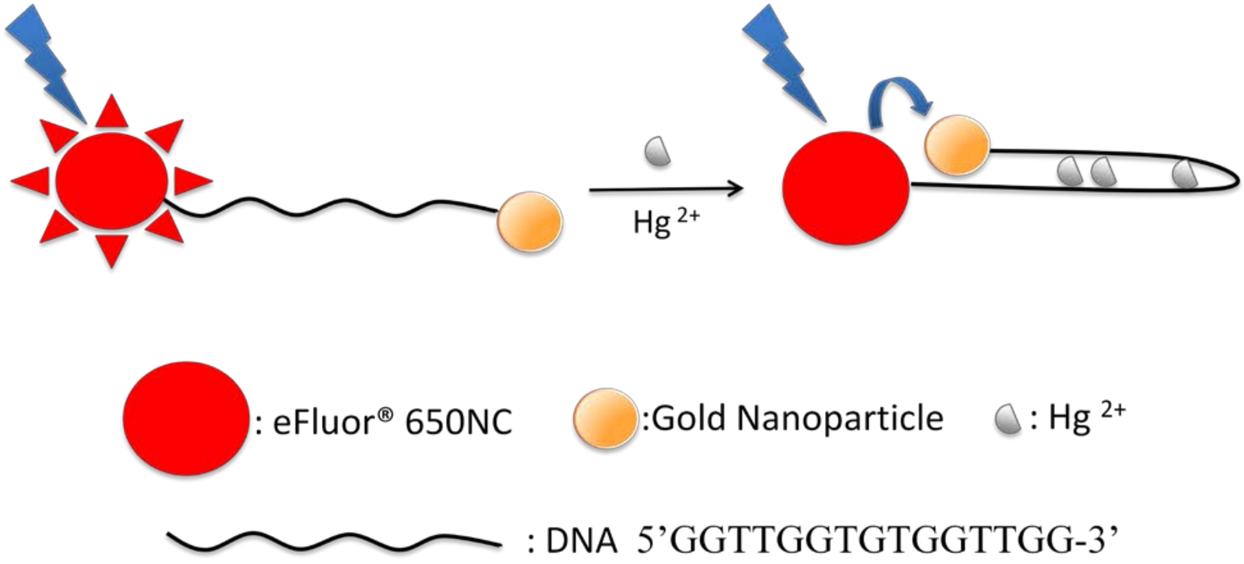

Figure 4. Schematic of the NSET based sensing mechanism of the TBA-Nanocrystal-Nanogold bioconjugate probe for detecting Hg^{2+} ions.

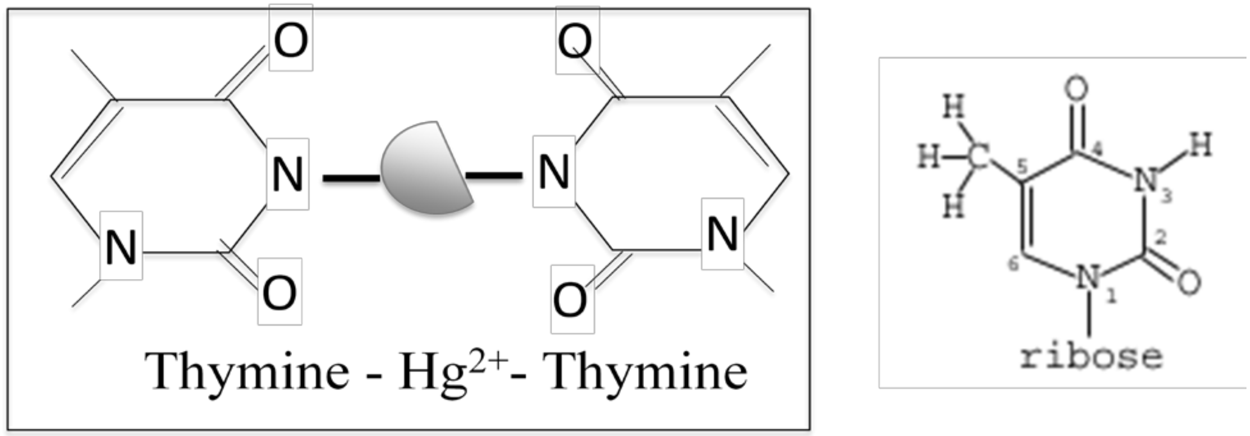

Figure 5. Mercury (II) ions interact with the nitrogen 3 atoms (N3) in the DNA base thymine.

d) *Lead (II) ion probe*

The TBA (5’-/AmMC12/GGT TGG TGT GGT TGG/3ThioMC3-D/-3’) was also used for detection of Pb ions, but the conformational change that occurs upon interaction is different. The TBA folds into a G-quadruplex when Pb is present. This is shown in figure 6.

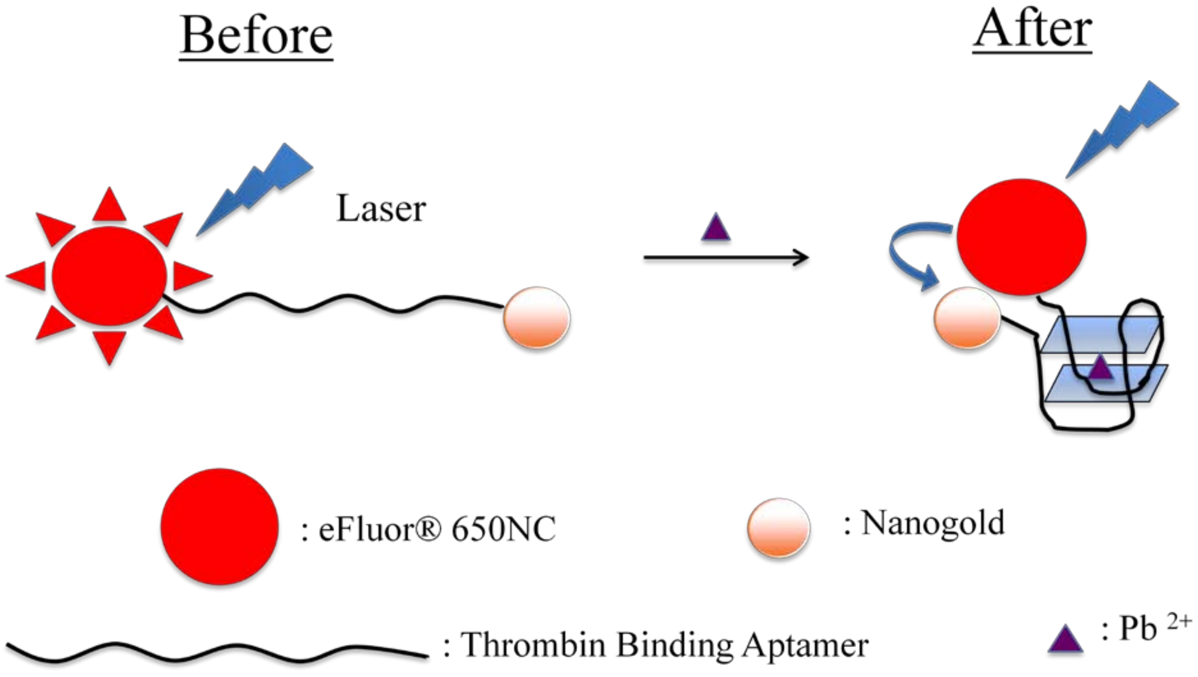

Figure 6. Schematic of the NSET based sensing mechanism of the TBA-Nanocrystal-Nanogold bioconjugate probe for detecting Pb^{2+} ions. The Pb ion causes the G-quadruplex formation.

The same materials were used for the Pb detection as for Hg. Nanosep® centrifugal devices in 3K and 100K molecular weight cutoffs (MWCO) were acquired from Pall Life Sciences (Ann Arbor, MI). Lead (II) chloride salt was obtained from Sigma Aldrich (St. Louis, MO).

The TBA was dissolved in Tris ethylenediamine tetraethyl acetate (EDTA) (TE) buffer (10 mM Tris, 1 mM EDTA) at pH 8.0. EDTA aids in protecting DNA from degradation by nucleases by chelating divalent cations, which are required for nucleases to function [12]. The dithiol group on the TBA was first reduced using TCEP and then mixed with activated Nanogold solution. Gold nanoparticles and DNA were incubated at a ratio of 7:1. Excess gold was used to ensure that each TBA attached to a QD has gold conjugated to its opposite end. This will help prevent QD photoluminescence from continuing at the same intensity while lead (II) ions are interacting with the TBA.

Next, the solution was filtered using a 3K MWCO centrifugal device at 14,000 x g for 15 minutes, to remove the excess TCEP. The TBA-AuNP conjugates were then suspended in TE buffer.

Two ratios of TBA-AuNP structures to QDs were tested for the TBA to QD conjugation, 10:1 and 5:1. The carboxyl groups on the QDs are activated with the cross-linker, EDC. Once activated, they react with the amine-functionalized end of the TBA for two hours at room temperature. The solution was then filtered with a 100K MWCO centrifugal device at 5,000 x g for 10 minutes to remove any unbound TBA-AuNP complexes [13].

The photoluminescence (PL) was measured using a USB4000 Ocean Optics (Dunedin, FL) spectrometer with a 380 nm LED for excitation. The liquid assay probe was tested in triplicate at different concentrations of Pb^{2+} ions, from 50 nM to 1 μM for both DNA to QD ratios. The PL intensity at 650 nm was recorded for the probe and the probe plus lead at a range of different lead concentrations. The average of three measurements was taken to gauge the uniformity of the probe. The liquid assay probe was placed in a UV cuvette for PL measurement.

e) *Zinc (II) ion and Cadmium (II) ion probe*

The aptamer Zn-6m2, which was selected for zinc by Rajendran and Ellington also has an affinity for cadmium ions [11]. The kinetics have been shown to be different for the two ions however, with the reaction being faster for zinc. In addition to investigating the use of this aptamer for the detection of zinc using Raman spectroscopy it was also evaluated as the molecular recognition element in an optical probe for detection Zn and Cd. A truncated form of the Zn-6m2 aptamer that was only 50 bases in length, but contained the nucleotides involved in the folding and binding to zinc ions, was purchased from Integrated DNA Technologies Inc. (Coralville, IA). Mfold was used to show the predicted folded structure of the truncated aptamer and the structure with the lowest free energy is shown in Figure 7 [14]. It was functionalized on the 5’ terminus with a disulfide group and the 3’ end contained an amine modification.

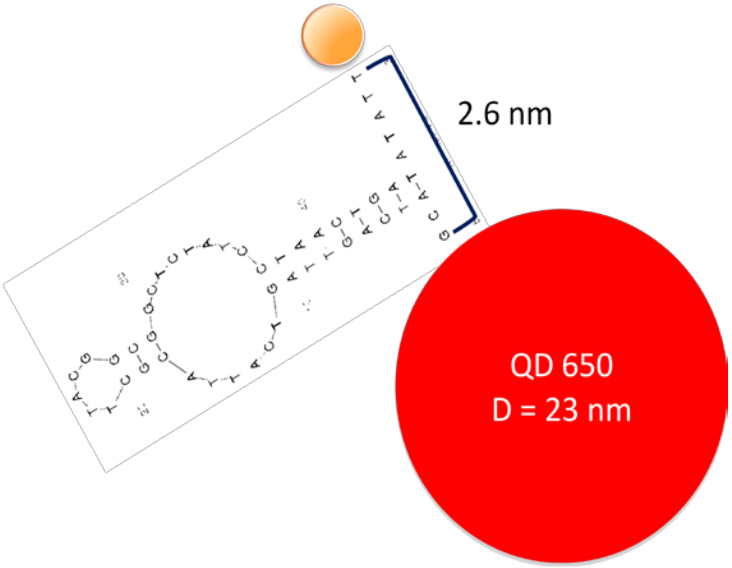

Figure 7. Schematic of probe for zinc and cadmium ion detection using a truncated version of the aptamer Zn-6m2 and a quantum dot and gold nanoparticle.

The carboxyl-functionalized eFluor® 650 Nanocrystals (NC) or QDs were acquired from eBioscience, Inc. (San Diego, CA). These QDs have a CdSe core and a ZnS shell with a polymer coating and an emission wavelength of 650 +/- 3 nm. The Monomaleimido Nanogold® particles of 1.4 nm diameter were obtained from Nanoprobes, Inc. (Yaphank, NY). The reagents TCEP and EDC were purchased from Pierce Biotechnology (Rockford, IL). Nanosep® centrifugal devices in 3K and 100K molecular weight cutoffs (MWCO) were acquired from Pall Life Sciences (Ann Arbor, MI). Zinc chloride solution (0.1 M) and cadmium nitrate solution were obtained from Sigma-Aldrich (St. Louis, MO).

For the DNA-AuNP conjugation a ratio of 7:1 gold to DNA was used and the reaction was incubated at room temperature for 2.5 hours. The mixture was filtered using the 3K MWCO centrifugal device at 14,000 x g for 15 minutes, then resuspended in borate buffer. Borate buffer is used because it does not contain amine groups, which could interfere with the QD conjugation. The DNA-AuNP nanoconstruct was then conjugated to the QDs at a ratio of 10:1 DNA-AuNP to QD. After activating the carboxyl groups on the QD surface using EDC, the DNA-AuNP was added and the mixture incubated for 2 hours while gently mixing. The reaction mixture was then filtered using a 100K MWCO centrifugal filtration device at 5,000 x g for 15 minutes to remove any unbound DNA or AuNPs. The filtration step was repeated twice using borate buffer to further wash away any unbound materials.

f) *VI. Filter paper coupons for portable handheld device*

In addition to detecting heavy metals or other chemical hazards using a liquid assay, filter paper coupons were fabricated to test the assay as a dried dot, which could be used in a hand held portable device for field use or as a point of care tool. The filter paper used was Immobilon®-FL filter paper from Millipore Corporation (Billerica, MA). The Immobilon®-FL filter paper is meant for use in fluorescence measurements, as it has low auto-fluorescence. The coupon is made by adhering filter paper to a plastic coverslip for rigidity. The probe assay is then pipette onto the coupon in a volume of 2 µl. This volume allows for a dried dot that is small enough in diameter to fit within the beam of the LED when tested. Each dot contains 0.6 picomoles of probe.

4. Results and Discussions

a) *Molecular beacons for pathogen detection*

The molecular beacon for *S. typhimurium* was tested by placing 100 µL of the molecular beacon at a concentration of 10 nM in a vial followed by addition of the target sequence. The vial was place under UV light to observe visible photoluminescence while in the quenched state (see Figure 8 – left). The target sequence was added to the beacon and an increase in light emission was seen, as shown in Figure 8. This increase in photoluminescence was visible with the naked eye.

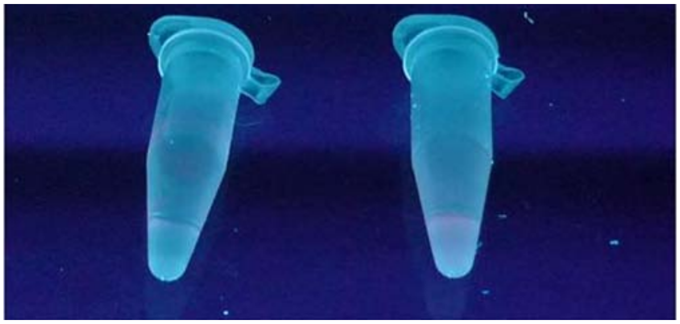

Figure 8. Vial containing S. typhimurium beacon in quenched state before target added (left) and beacon in unquenched state after addition of 1 mM target sequence (right). The decrease in photoluminescence is visible by the naked eye.

b) *Zinc detection with Raman spectroscopy*

The Raman spectrum of the zinc aptamer on the AgFON substrate for two spectra appear slightly different in the 1300 – 1500 cm^{-1} range as shown in Figure 9. The metal ion binding has likely interfered with the ring stretching modes in this region. The shifts in wavenumber are indicators of distortions of the DNA. A significant shift is evident from 1323 cm^{-1} for the aptamer alone to 1319 cm^{-1} for the aptamer plus zinc. This mode is attributed to the adenine mixed in-plane stretching mode of the 6-member ring. Most other differences are only 1 – 2 cm^{-1}.

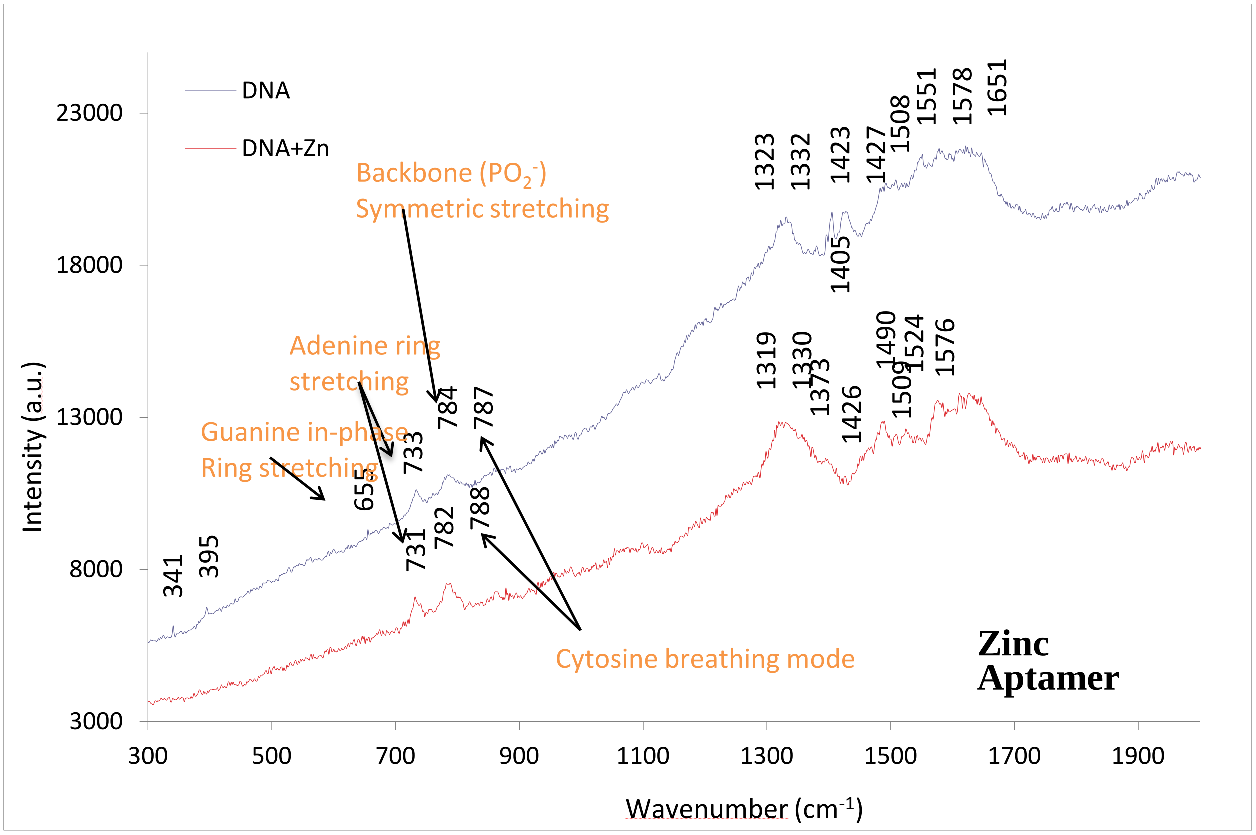

Figure 9. Drop coated sample of unmodified DNA aptamer (blue) and unmodified DNA aptamer + Zn^{2+} (red). Conditions: 8 mW laser power, 120 s exposure time.

A comparison between the Raman peaks seen with just the aptamer and the aptamer with Zn is shown in Table 2. It also lists the mode associated with each peak.

Table 2: A comparison between the Raman modes of the zinc aptamer alone and the modes produced by the zinc aptamer with zinc.

APTAMER	APTAMER + ZN^{2+}	MODE DESIGNATION
655		Guanine in-phase ring stretching of 6-member ring except C_4C_5
733	731	Adenine ring stretching
784	782	RS: cytosine breathing mode & symmetric stretch of phosphodiester bond
787	788	Cytosine ring breathing mode
	983	Cytosine C_5H breathing mode
1216		Thymine ring & C_5Me stretching
1323	1319	Adenine mixed in-plane stretching mode of 6-member ring
1332	1330	Guanine C_8N_9 & N_7C_8 stretching
1380	1373	Thymine C_5-Me bending
1508	1509	Cytosine N_3C_4 & N_1C_2 stretching
1578	1576	Purine line

c) *Mercury detection*

An optical probe for detecting mercury (II) ions was synthesized using a DNA aptamer, QDs, and gold nanoparticles. The photoluminescence data was taken using a USB4000 Ocean Optics (Dunedin, FL) spectrometer with a 380 nm LED for excitation. Three aliquots of TBA probe (10 nM) were prepared for analysis, one without Hg^{2+}, one containing 500 nM Hg^{2+} ions, and the third containing 824 µM Hg^{2+} ions. The three Hg^{2+} ion concentrations were also tested with 100 µL aliquots of QDs at 10 nM. This was done to determine if the mercury ions alone had any effect on the QD photoluminescence. Figure 10 shows the photoluminescence spectra of the three samples, where a decrease in luminescence peak is seen with Hg^{2+} ions present. The quenching efficiency, η was calculated as $[(I_0 - I_{Hg})/I_0]$, where I_0 is the peak luminescence intensity without Hg^{2+} for 10 nM TBA probe and I_{Hg} is the peak luminescence intensity with Hg^{2+} ions present. The 500 nM Hg^{2+} ion sample had a quenching efficiency of 62%.

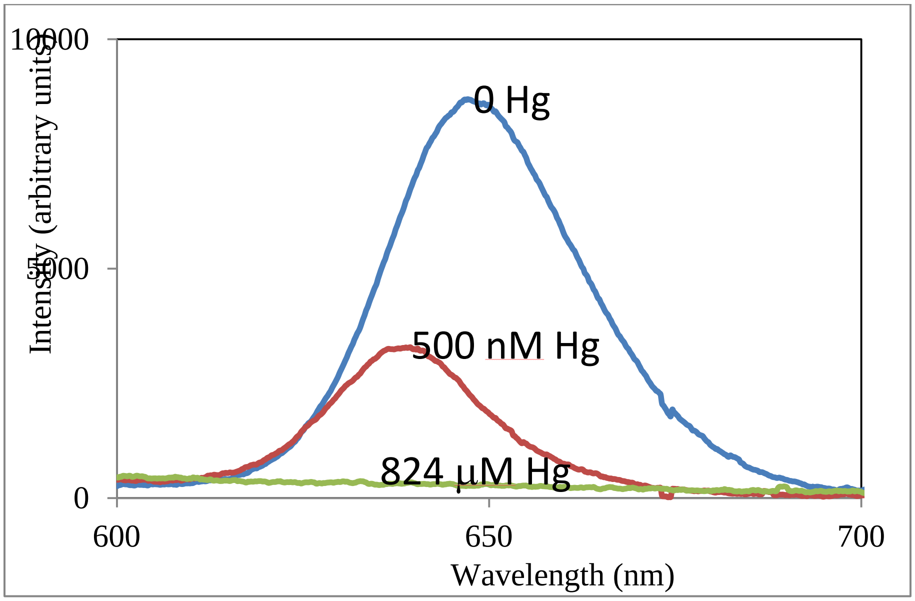

Figure 10. Fluorescence spectra of TBA probe (10 nM) without Hg^{2+}, with 500 nM Hg^{2+}, and with 824 mM Hg^{2+} present.

This was comparable with the work of Liu *et al*. who obtained 66% quenching efficiency using the TBA with the donor carboxyfluorescein (FAM) and the acceptor DABCYL for Hg^{2+} sensing at 500 nM [15]. Although the quenching efficiency was similar, Liu *et al.* did not show any shift in peak intensity. Another difference between the previously mentioned study and this work is the use of EDTA in the buffer. EDTA aids in protecting DNA from degradation by the enzyme DNase by chelating divalent cations such as Mg^{2+}, which are required for DNase to function. It is interesting to note that this decrease in luminescence was achieved in the presence of EDTA, which is capable of interacting with Hg^{2+} ions [12]. Perhaps the quenching efficiency could be improved beyond 66% without EDTA in the buffer. Given the amount of EDTA in the buffer, it could also be that the affinity between Hg^{2+} ions and thymine bases is stronger than it is for Hg^{2+} and EDTA.

When the large excess of Hg^{2+} ions, 824 μM, was tested there was no peak detected. This could be the result of complete quenching by the AuNPs due to the addition of Hg^{2+} ions. However, there is a slight chance that unconjugated QDs are present in the assay. A ratio of TBA:QDs of 10:1 gives a distribution of QDs with different quantities of TBA attached and there would be less than 0.01% of QDs with no TBA bound. If this were the case, the Hg^{2+} would not be able to cause the quenching through the expected mechanism for those unconjugated QDs and there would still be some fluorescence emission from the unbound QDs. There would have to be another means of extinguishing the fluorescence. Alternatively, the complete quenching observed could be the result of the Hg^{2+} ions interacting with the surface of the QDs and thereby affecting their emission. A quenching effect was seen in other work using L-cysteine capped CdS QDs when exposed to Hg^{2+} ions [16]. While it is unlikely that Hg^{2+} ions were able to interact with the polymer coated QDs, the photoluminescence was measured for QDs alone (no TBA-AuNP nanoconstruct attached) at 10 nM and with the previously tested Hg^{2+} ion concentrations (Figure 11). The peak intensity for the QDs alone (a) and the QDs with 500 nM Hg^{2+} ions is effectively the same. Interestingly, the addition of 824 μM Hg^{2+} resulted in the complete quenching of the QD luminescence, as seen in (c) of Figure 11.

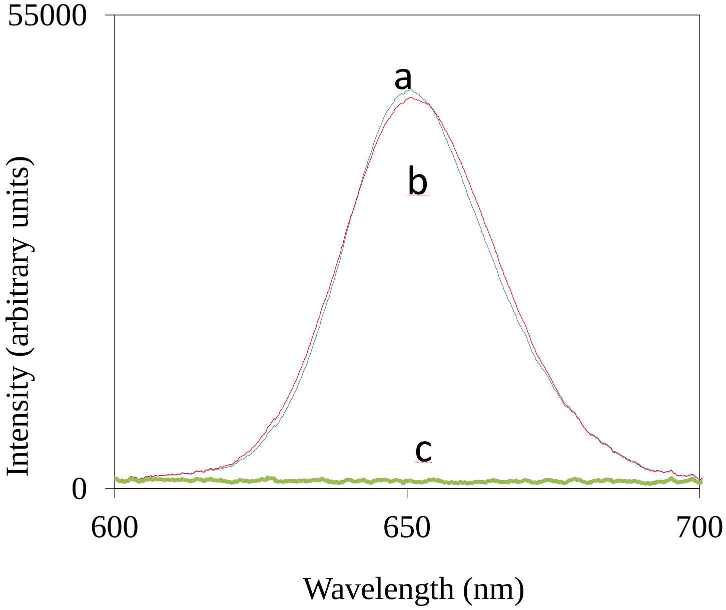

Figure 11. Fluorescence spectra of (a) QDs (10 nM), (b) QDs (10 nM) with Hg^{2+} (500 nM), and (c) QDs with Hg^{2+} (824 mM) present.

The quenching could be the result of mercury ions interacting with the QDs. The heavy metals Cu^{2+}, Fe^{3+}, and Zn^{2+} have been shown to eliminate QD fluorescence irreversibly [17]. Therefore, at a certain concentration, Hg^{2+} also eliminates QD fluorescence, but below this level the aptamer-based probe is necessary for detection. For a 10 nM sample of QDs complete inhibition of fluorescence occurs between 45 and 55 μM mercury (II) ions (Figure 12).

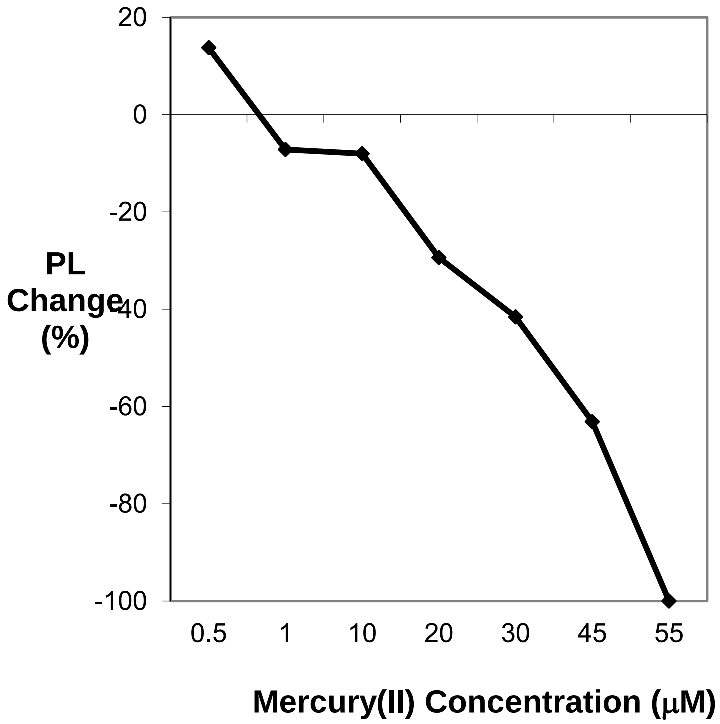

Figure 12. Change in PL of 10 nM QDs with increasing Hg2+ concentration.

In addition to the luminescence quenching seen with Hg^{2+} present, there was also a blue shift between the unquenched and quenched samples. The peak for '0 Hg' in Figure 10 is at 648 nm, whereas the peak for the quenched state with 500 nM Hg, is shifted 13 nm to 635 nm. This decrease in emission peak has been demonstrated previously in our group through an investigation of the energy transfer process between QDs and AuNPs, where a 12 nm blue shift was seen [18]. In both cases, 1.4 nm diameter Nanogold particles and CdSe/ZnS QDs were used.

While detection of mercury ions has been demonstrated, there has been variability in the probe performance. It was hypothesized that using an excess of DNA in the conjugation of the gold nanoparticles to the DNA may improve performance. This was based on the actual probe configuration as shown in Figure 13 where each QD has approximately 10 DNA strands attached. The ideal configuration would be just one DNA sequence per QD. However, the difficulty in separating QDs with different numbers of DNA strands attached prevents this. Given this configuration it is important that each strand of DNA is conjugated to an AuNP. If not, false negatives are more likely, as shown in the bottom row of Figure 13 where the QDs are not quenched in the presence of Hg. If Hg ions interact with DNA that does not have a gold nanoparticle attached, then the folding event will not result in quenching.

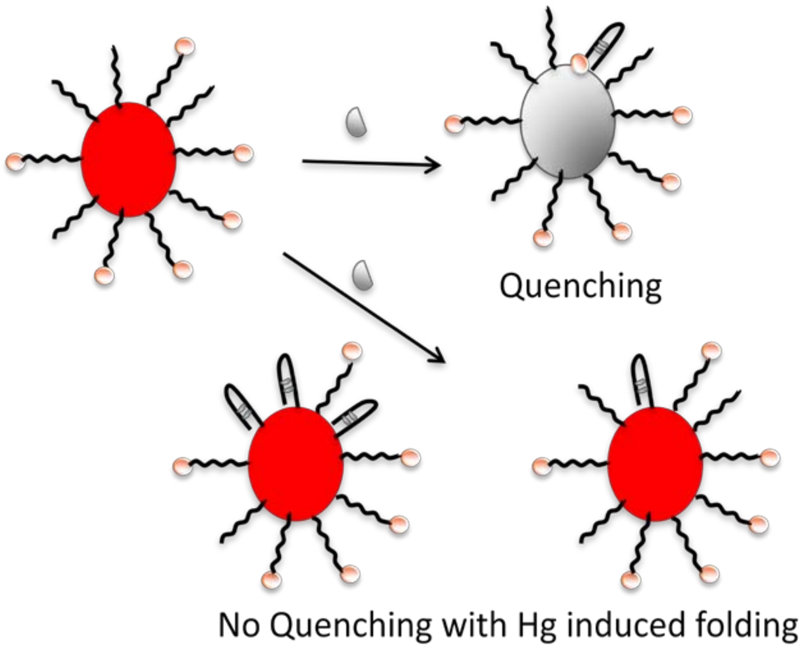

Figure 13. Actual probe configuration when using 10:1 DNA to QD ratio. Possible scenario if DNA does not have gold nanoparticle attached, which would cause a false negative.

In order to ensure that all DNA are conjugated to a AuNP, an excess of gold (10-fold) was tested in the gold conjugation step. Since the AuNPs are 1/20th of the diameter of the QDs, they will be removed during the filtration step of the QD conjugation. The excess gold showed better results so different ratios were tested. In addition to the 10:1, 7:1, 5:1, and 3:1 were evaluated. This was done to reduce materials used if possible. A ratio of 7:1 for AuNP:DNA was found to have the most consistent results as illustrated in Figure 14. All future probe synthesis was done using this optimized parameter.

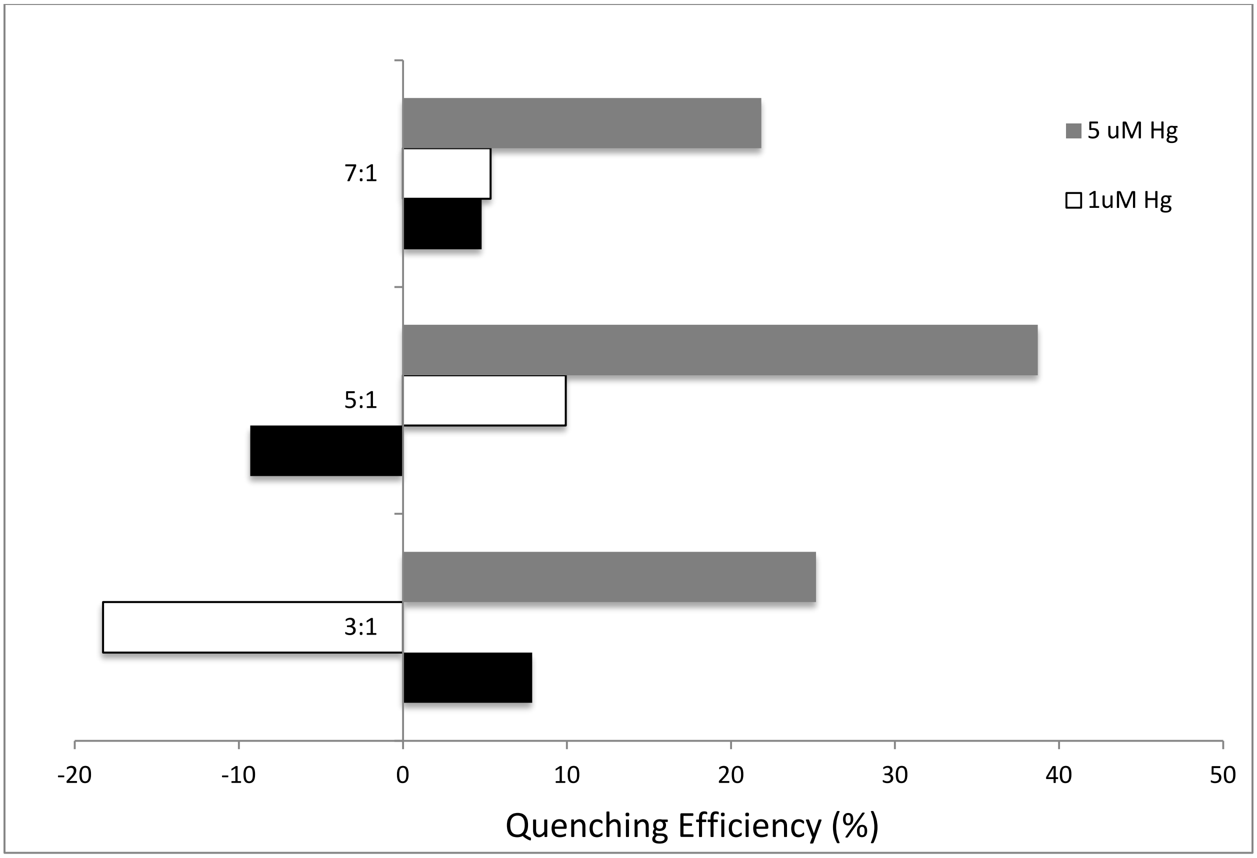

Figure 14. Quenching Efficiency at different Hg concentrations for probes made with different AuNP:DNA ratios liquid assays.

The ratio of DNA to QD used in the second conjugation step was also optimized through testing of DNA:QD ratio 5:1 against the control ratio of 10:1. A 5:1 ratio would produce mostly QDs containing 5 DNAs attached to each. The results for this test are shown if Figure 15.

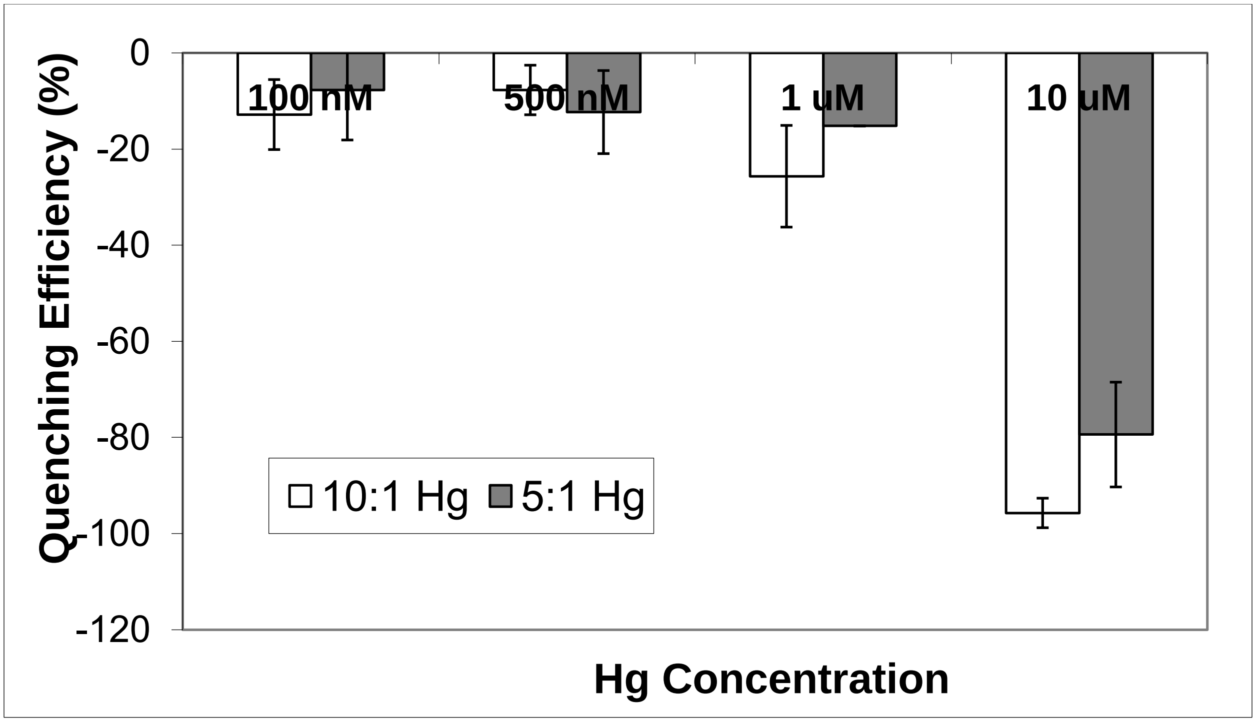

Figure 15. Quenching efficiency vs. Hg concentration for different DNA:QD ratios in liquid assay.

d) *Lead detection*

The probe at different lead concentrations for different DNA to QD ratios was tested in a liquid assay for the optimization of the probe. Quenching efficiency (η%) was calculated using the formula $\eta = (I-I_0)/I_0$, where I_0 is the intensity of probe and I is the intensity of the probe exposed to Pb^{2+} ions. Figure 16 shows the results of the liquid assay probe being tested against different concentrations of lead from 100 nM to 1 μM for 10:1 and 5:1 DNA to QD ratios. The quenching efficiency was calculated for three sets of readings and the average was taken. The quenching efficiency observed at 1 μM was -41 % for the 5:1 measurement and -39% for the 10:1 conjugation as shown in Figure 16. The probe was tested at this particular concentration range because the OSHA and WHO safety levels for lead intake are 30 μg/dL (1.45 μM) and 40 μg/dL (1.93 μM), respectively [3]. Blood lead levels above these thresholds are cause for concern. Therefore a significant quenching efficiency would be required for this range. As the error bars indicate in Figure 16, the 10:1 conjugation shows less variability than the 5:1.

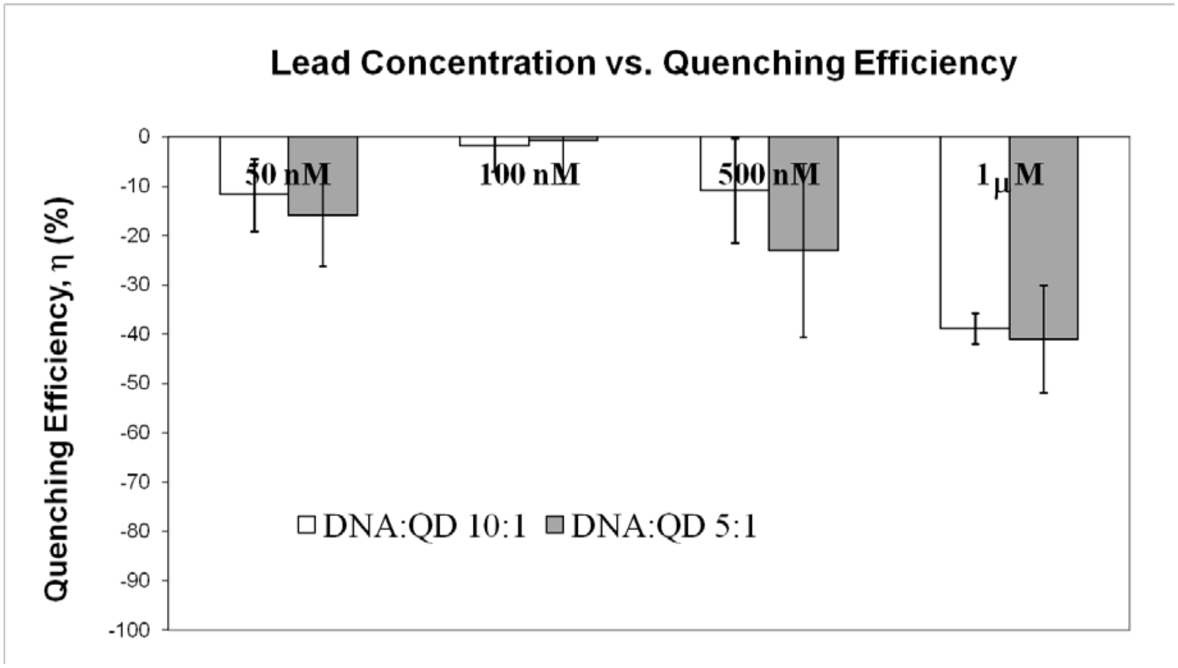

Figure 16. Quenching efficiency of the probe at different Pb concentrations for different DNA to QD ratios tested in a liquid assay

In addition, change in the PL was measured for different concentrations of Pb^{2+} ions with only the QDs to investigate any effect Pb^{2+} ions may have on the fluorescence of the QDs. This is shown in Figure 17. It has been shown that some heavy metals can eliminate QD fluorescence starting from a particular concentration of metal ion [17]. QDs alone when exposed to Pb^{2+} ions had significantly decreased fluorescence (-47%) at approximately 6 μM, which is approximately five times the safety level of lead. The aptamer-based probe, however, detected lead at the appropriate concentration range. This demonstrates that the probe performance for detecting Pb^{2+} ions at 1 μM was not due to the interaction of Pb^{2+} ions with the QDs. Rather; significant decreases at 1 μM lead are a result of the energy transfer process of the probe.

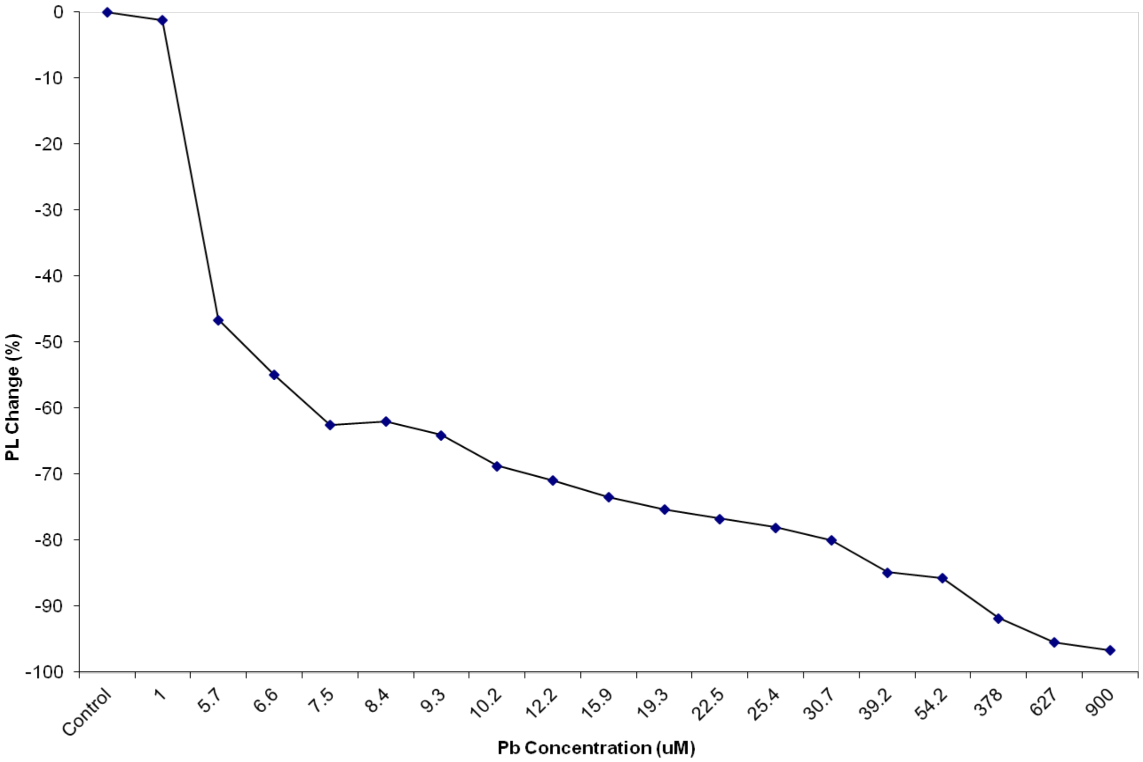

Figure 17. Change in photoluminescence (PL) intensity of 10 nM QD650 at different Pb concentrations from 0 to 900 mM.

e) *Zinc and Cadmium detection*

Samples were prepared for testing the Zn-6m2 probe against zinc and cadmium. 200 µL samples with a probe concentration of 10 nM were prepared. Each sample was comprised of 2 µL of probe and between 178 µL and 196 µL of tris-acetate buffer at pH 7.35. After the control intensity was measured the zinc or cadmium solution was added to make 200 µL. For Zn 100 µM, 800 µM, and 10 mM concentration was evaluated based on the upper limit of normal blood-Zn levels being approximately 20 µM. The calculated quenching efficiencies are shown in Figure 18 below. The integration time was 500 ms. Two measurements were taken for each concentration and averaged.

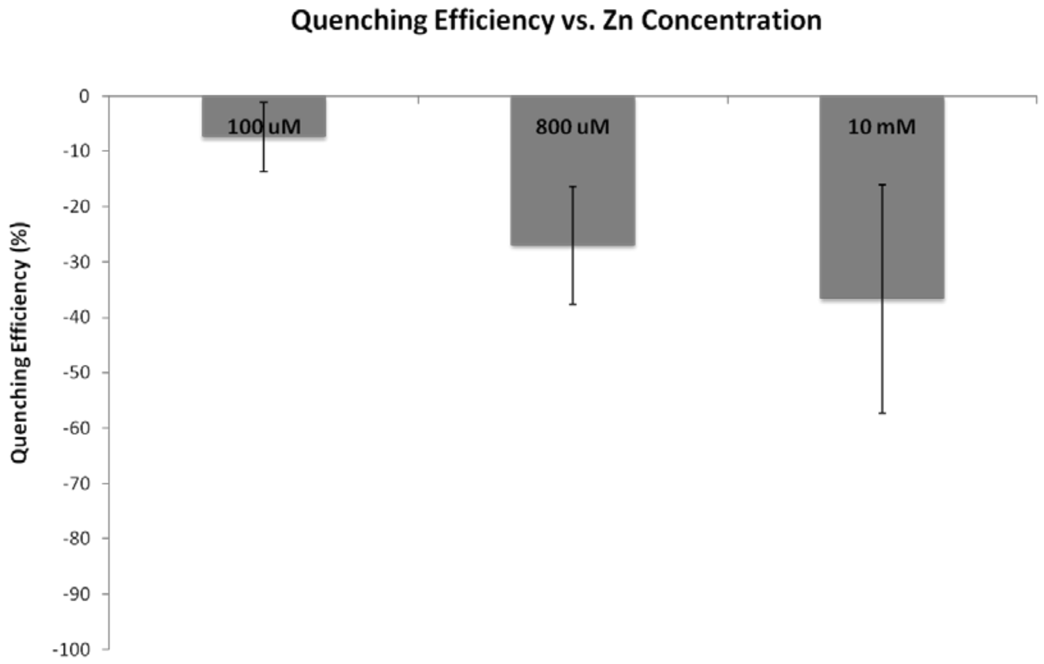

Figure 18. Zn-6m2 probe tested against different concentrations of zinc (II) ion in a liquid assay.

For cadmium a lower concentration range was tested. These samples also had a final volume of 200 μL and contained 10 nM concentration of probe. The quenching efficiencies are shown in Figure 19 for 100 nM up to 400 μM. Two measurements were taken and averaged. The Zn-6m2 probe performed well at 100 μM and 400 μM Cd concentrations with significant quenching efficiencies of -35% and -55% respectively.

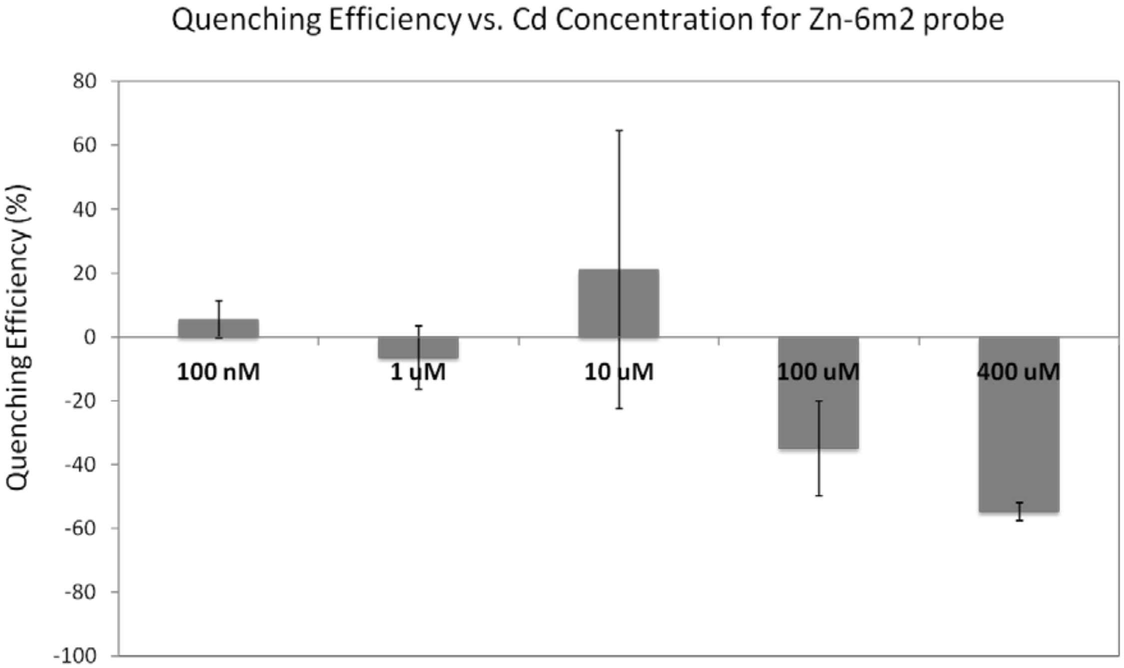

Figure 19. Zn-6m2 probe tested against different concentrations of cadmium (II) ion in a liquid assay.

f) *Filter paper coupons for portable handheld device*

The probes synthesized for Hg and Pb and Zn and Cd detection were applied to Immobilon®-FL (low auto-fluorescence) filter paper coupons. Each dot contained 0.6 pmoles of probe. Once dry, the peak fluorescence intensity of the dot is measured and recorded as the control intensity or I_0. After the control intensity is recorded a volume between 2 µL and 4 µL is applied to the dot via pipette and the intensity is measured again in order to calculate the quenching efficiency. The metal ion solution concentrations were determined to provide equivalent exposures as the liquid assays. Measurements were taken in duplicate for the filter paper testing. For Hg and Pb both DNA:QD ratios were evaluated. In Figure 20 the filter paper coupons made with the TBA probe are tested for a wide range of Hg concentrations. The quenching efficiencies were not significantly different for the 10:1 and 5:1 DNA to QD ratios.

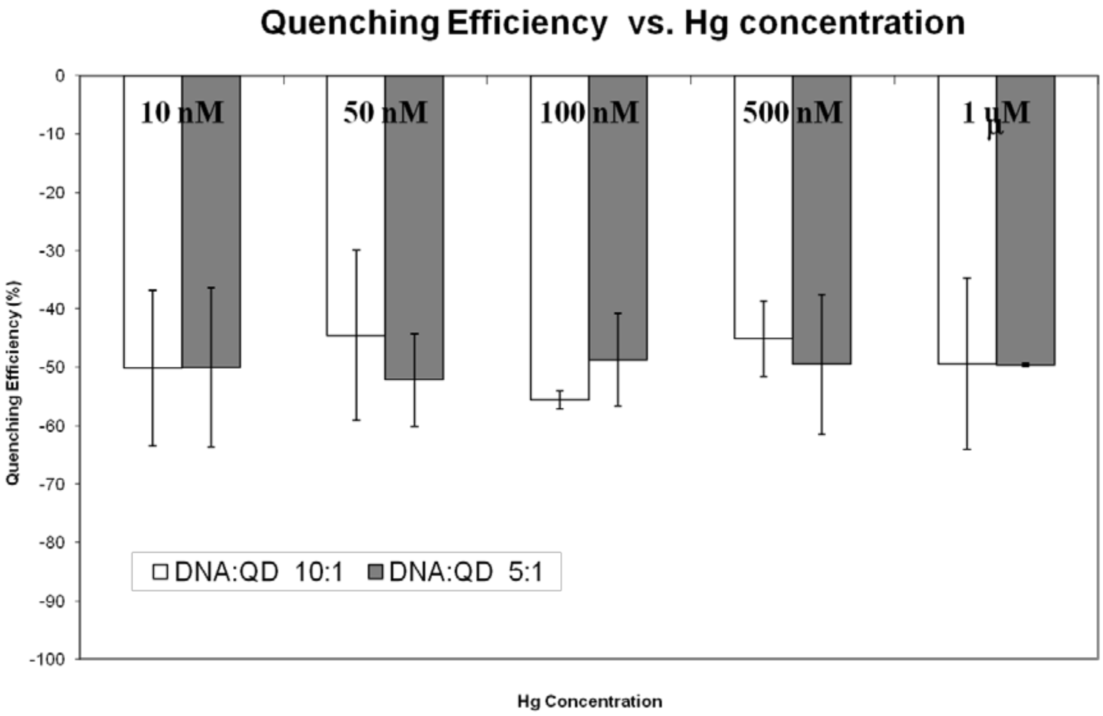

Figure 20. Quenching efficiency of the probe at different Hg concentrations for different DNA to QD ratios tested on filter paper coupon.

When tested against Pb, as shown in Figure 21 the quenching efficiency was -71% with almost no difference between the two measurements at 1 μM Pb^{2+} ion concentration for both 10:1 and 5:1 DNA to QDs ratio. Optimal performance at 1 μM is desired for Pb detection based on the WHO and OSHA standards.

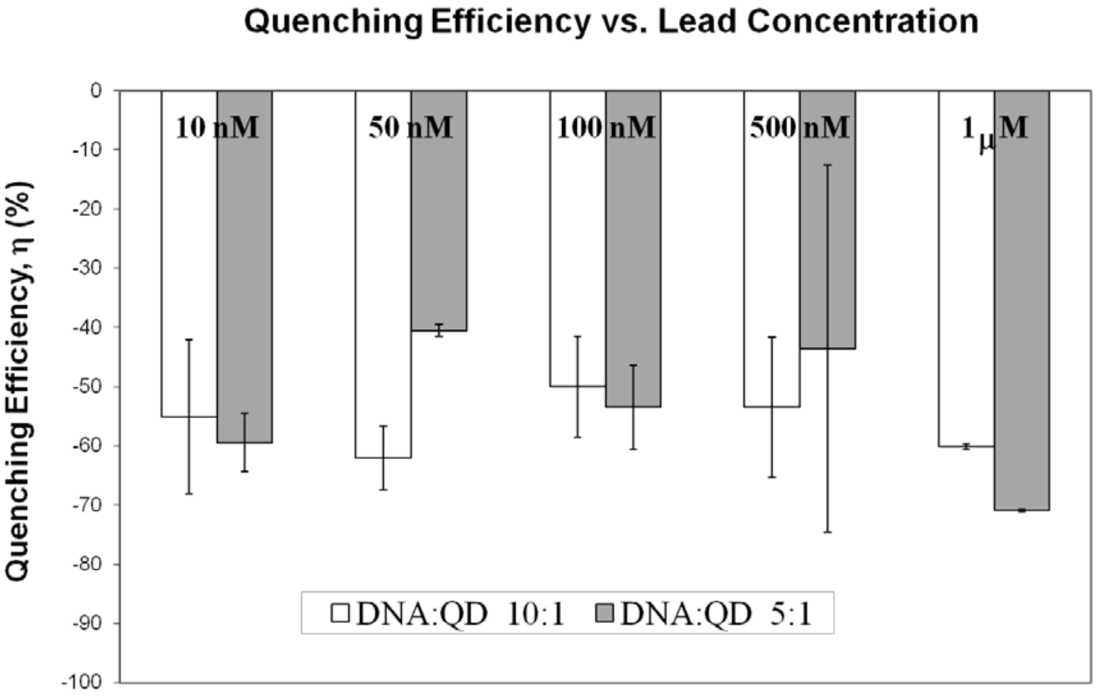

Figure 21. Quenching efficiency of the probe at different Pb concentrations for different DNA to QD ratios tested on filter paper coupon.

The filter paper coupon was tested against Cd at three different concentrations (Figure 22). All three concentrations had a quenching efficiency of approximately -60%. The Zn-6m2 probe was also tested against Zn on the filter paper coupons. The quenching efficiencies for 667 nM Zn, 67 μM Zn, and 3 mM Zn are shown in Figure 23.

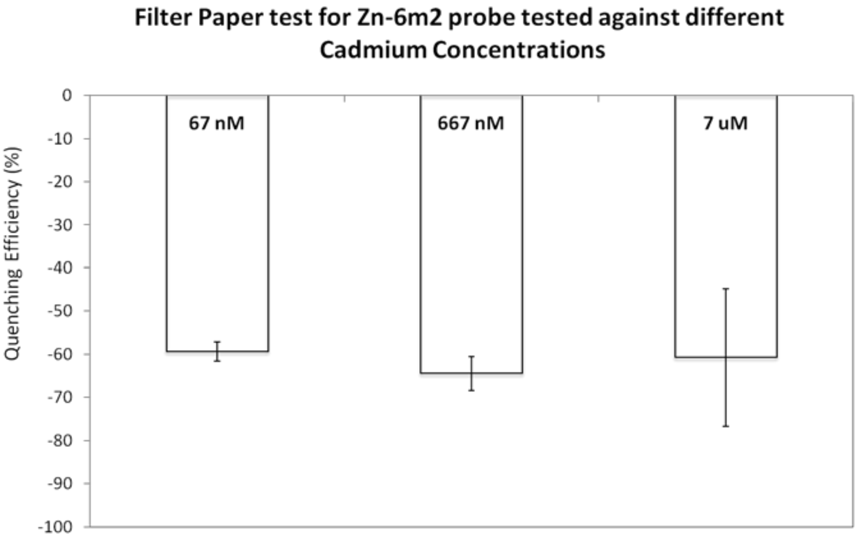

Figure 22: Filter paper coupon tested for three concentrations of cadmium (II) ion.

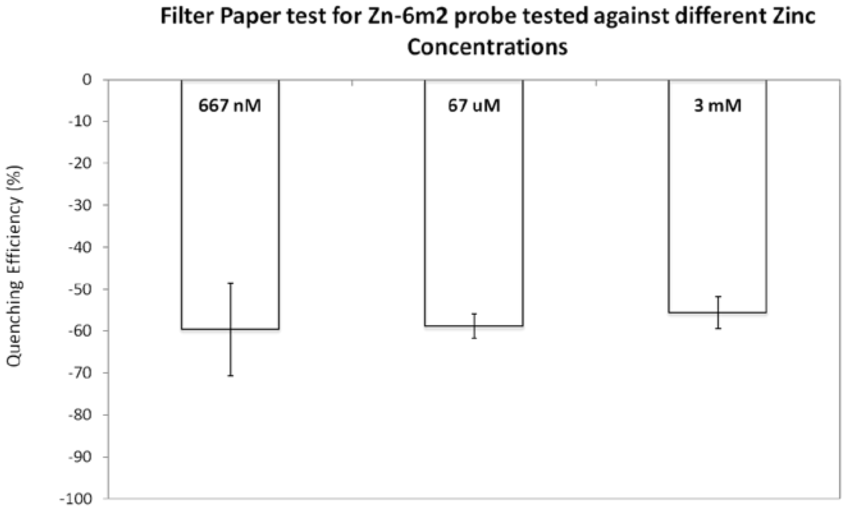

Figure 23: Filter paper coupon tested for three concentrations of zinc (II) ion.

The liquid assay for Hg/Pb has been shown to be fairly stable after storage at 2-4 °C for 3 weeks when tested on filter paper for Hg concentrations between 1.25 μM and 5 μM. The quenching efficiency for 2.5 μM was -56% when tested 1 week after it was synthesized and only decreased to -33% when tested 2 weeks later. The stability of the filter paper coupon dot was also evaluated. In this test the detection of Cd was tested at day 1 for 67 nM Cd with a quenching efficiency -59%. After making the coupons, they were stored at room temperature for 1 week, then tested against the same Cd concentration (Figure 24). The quenching efficiency decreased to -45% and had more variability between measurements but still had detection capabilities after being stored at ambient conditions for 1 week.

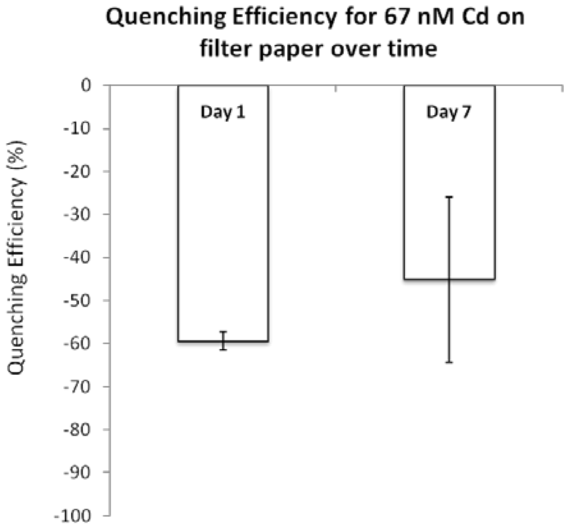

Figure 24: Filter paper coupon assay tested against 67 nM cadmium at two time points to evaluate stability of coupon.

5. Conclusions

Heavy metal ions, such as mercury and lead ions, can be detected using Thrombin Binding Aptamer (TBA) as it binds to Hg^{2+} ions via thymine bases and Pb^{2+} ions via guanine bases. Gold nanoparticles (Au-NP) containing a maleimide group are conjugated to sulfhydryl (-SH) group on TBA end.Au-NP-TBA conjugates are united to carboxyl-functionalized Cd-Se quantum dots (QD) with peak emission at 650-nm.Nanometal Surface Energy Transfer (NSET) between QD and Au-NP allows optical signal transduction upon target induced folding of the aptamer. This scheme could be used for detection of other heavy metal ions, such as Pb^{2+}, Cd^{2+}, or Zn^{2+}. The same scheme could also detect biomarkers using DNA aptamer. These QDs and gold nanoparticles make durable nanoconstructs for detecting heavy metal ions. The detection of mercury and lead ions at the nanomolar to micromolar level was achieved using the DNA aptamer and quantum dots. Probe assay applied to Immobilon-FL (low auto-fluorescence) filter paper-coverslip coupon enabled more consistent detection when compared with liquid assay tests. Also QDs alone exposed to Pb^{2+} ions and Hg^{2+} ions resulted in decreased fluorescence at approximately 5 times above safety levels, while the aptamer-based probe was sensitive enough to detect lead in the appropriate range. The Zn-6m2 aptamer was used for detecting Zn and Cd at different concentration ranges. Cd and Zn were also detected using filter paper coupons, which gave consistent results.

6. References

1. Ellis, K.J., et al., *DOSE - RESPONSE ANALYSIS OF CADMIUM IN MAN - BODY BURDEN VS KIDNEY DYSFUNCTION.* Environmental Research, 1984. **33**(1): p. 216-226.
2. Fosmire, G.J., *ZINC TOXICITY.* American Journal of Clinical Nutrition, 1990. **51**(2): p. 225-227.
3. Khan, D.A., et al., *Evaluation of lead body burden in occupational workers by lead mobilization test.* JPMA. The Journal of the Pakistan Medical Association, 2009. **59**(6): p. 350-4.
4. Selid, P.D., et al., *Sensing Mercury for Biomedical and Environmental Monitoring.* Sensors, 2009. **9**(7): p. 5446-5459.
5. Organization, W.H., *Mercury in Drinking-waterBackground document for development of WHO Guidelines for Drinking-water Quality*. 2005.
6. Johnsson, C., A. Schutz, and G. Sallsten, *Impact of consumption of freshwater fish on mercury levels in hair, blood, urine, and alveolar air.* Journal of Toxicology and Environmental Health-Part a-Current Issues, 2005. **68**(2): p. 129-140.
7. Rikans, L.E. and T. Yamano, *Mechanisms of cadmium-mediated acute hepatotoxicity.* Journal of Biochemical and Molecular Toxicology, 2000. **14**(2): p. 110-117.
8. Garcon, G., et al., *Biomonitoring of the adverse effects induced by the chronic exposure to lead and cadmium on kidney function: Usefulness of alpha-glutathione S-transferase.* Science of the Total Environment, 2007. **377**(2-3): p. 165-172.
9. Selvin, P.R., *The renaissance of fluorescence resonance energy transfer.* Nature Structural Biology, 2000. **7**(9): p. 730-734.

10. Zhang, X., C.R. Yonzon, and R.P. Van Duyne, *Nanosphere lithography fabricated plasmonic materials and their applications.* Journal of Materials Research, 2006. **21**(5): p. 1083-1092.
11. Rajendran, M. and A.D. Ellington, *Selection of fluorescent aptamer beacons that light up in the presence of zinc.* Analytical and Bioanalytical Chemistry, 2008. **390**(4): p. 1067-1075.
12. Vaz, J.L.L., et al., *Binary and ternary interactions of mercury(II) with seven pyrimidines and ethylenediaminetetraacetic acid.* Journal of Chemical Research-S, 1997(8): p. 280-281.
13. Brenneman, K., et al., *Aptamer-based optical bionano sensor for mercury(II) ions*, in *Nanotechnology Materials and Devices Conference (NMDC), 2010 IEEE*. 2010: Monterey, CA, USA. p. 221-224.
14. Zuker, M., *Mfold web server for nucleic acid folding and hybridization prediction.* Nucleic Acids Research, 2003. **31**(13): p. 3406-3415.
15. Liu, C.-W., C.-C. Huang, and H.-T. Chang, *Highly Selective DNA-Based Sensor for Lead(II) and Mercury(II) Ions.* Analytical Chemistry, 2009. **81**(6): p. 2383-2387.
16. Chen, J., et al., *Functionalized CdS quantum dots-based luminescence probe for detection of heavy and transition metal ions in aqueous solution.* Spectrochimica Acta Part a-Molecular and Biomolecular Spectroscopy, 2008. **69**(3): p. 1044-1052.
17. Zarkowsky, D., et al., *Heavy Metal Contaminants Can Eliminate Quantum Dot Fluorescence.* Cytometry Part A, 2011. **79A**(1): p. 84-89.
18. Vasudev, M., et al., *Energy transfer interactions of semiconductor quantum dot-nanogold particle complexes*.

G. Development and Sensor Testing

1. Summary

Sensing Strategies, Inc. (SSI) has carried out technology investigations and hardware prototype developments to support the AF/SG requirements for directed energy detection and characterization and occupational health/toxicology topic areas. The investigations involved laboratory measurements of novel detection approaches with an emphasis on identifying promising approaches and their limitations. Ideas that did not seem to merit further investigation were identified as well. For the prototype developments, the emphasis was on directed energy detection sensors and three different sensors were developed. The sensors have been used by a variety of organizations to satisfy different deployment and demonstration objectives. There is clear applicability of the devices used to AF medical and operational missions and considerable overlap with the needs of law enforcement personnel. Demonstrations were made of different data dissemination approaches to enhance the utility of collected data to enhance medical evaluations of exposed personnel and support safe operations for future missions.

2. Introduction

This work was performed under a subcontract with the University of Illinois at Chicago and made possible by contract number FA7014-07-C-0047 from HQ US Air Force Surgeon General and AFDW and its contents are solely the responsibility of the authors and do not necessarily represent official views of the HQ US Air Force Surgeon General and AFDW

Detecting and characterizing laser radiation has grown in importance over the last few years because of the rapid increase in the number of aircraft illumination incidents of both domestic and military aircraft. While many of these incidents are carried out by individuals with low power laser pointers, the illuminations at even eye safe irradiance levels can be distracting to a pilot during critical operations such as landing an aircraft. In addition to the laser pointer incidents, the military is concerned about pulsed laser illuminations since they have greater potential to be hazardous to personnel. Pulsed lasers are used for a variety of military missions such as rangefinders and designators. Furthermore, many of the militarily relevant lasers are not visible, so without some kind of sensing capability, the personnel being illuminated will be unaware of the occurrence which will be important from both situational awareness and personnel protection perspectives. Therefore, SSI's primary focus under this contract was to develop new designs and extend existing designs to provide innovative and effective ways to detect, classify, and characterize laser illuminations of military personnel.

SSI also investigated novel sensing approaches for detecting hazardous substances in air and water for occupational health and toxicological monitoring applications. SSI's investigations involved experimental evaluations of new detection concepts including Raman spectroscopy, aptamers on quantum dots, nanoparticles.

3. Methods, Assumptions and Procedures

Developing laser sensors from a medical health perspective is a relatively new problem area so there are not established methods or procedures for either developing requirements or implementing concepts of operation. Instead, SSI needed to work with various AF organizations to educate them about the laser illumination problem and explain what kind of data could be provided by specialized sensors. We also explained how the data could be used to improve personnel medical evaluations and to develop mitigation procedures to reduce the risk of injuries to personnel. In the discussions, the AF personnel expressed ideas and preferences regarding functional and parametric specifications that they believed were important. For example, some pilots recognized that pulsed lasers were of more potential hazard to their eyes and wanted a small portable sensor that addressed that part of the threat space.

Combining these interactions with our corporate history in building specialized laser sensors, SSI recommended a path of sensor development that is reflected in this report. The Personnel Protection Sensor (PPS) addresses the small format, pulsed laser detector problem. The M4 sensor was developed to prove the performance of more sophisticated sensors in a larger package with the expectation that the sensors would be used in an eventual geolocation sensor. While providing quantitative laser exposure data is a primary motivation for the sensors developed under this program, a universal desire from users is to geolocate the threats themselves. That is, identify the laser location on a map so the perpetrator can be apprehended or countered in some means. This goal is addressed by the M6 sensor which was completed late in the program and includes orientation sensors which, combined with the sensor location derived from GPS and the laser incidence angle from the M6 integrating sensor, allows for a laser location (and associated uncertainty) to be computed. There were not opportunities to fly the M6 sensors under this program so future work will be needed to establish their geolocation performance.

a) *Personnel Protection Sensor*

SSI developed a novel sensor for detecting and characterizing pulsed laser radiation that could be potentially hazardous to personnel and this sensor was called the personnel protection sensor (PPS). One of the goals for this sensor was for it to be battery operated and small enough to be carried in a pocket and held in place on a vehicle temporarily with Velcro. Functional and performance compromises were necessary to meet the size goals, so SSI developed an approach that could provide real-time feedback to an operator regarding ocular hazards without explicitly measuring all of the laser characteristics. The sensor provides amplitude for the pulsed lasers reported as fraction of maximum permissible exposure (MPE). The system was designed to provide this value across 110 degree full angle field of view (FOV) throughout the 400-1100 nm spectral range even though it does not specifically measure wavelength. The sensor also reports whether protective eye wear will be effective in blocking the laser radiation and by indicating hazard warnings on the back of the device. These functions are tied to an internal spectral filter representative of eye wear that might be used by AF personnel. Figure 1 shows the dimensions of the PPS sensor dimensions which include the internal, rechargeable battery. The sensor weighs less than 1 pound and will operate roughly seven hours on a charge.

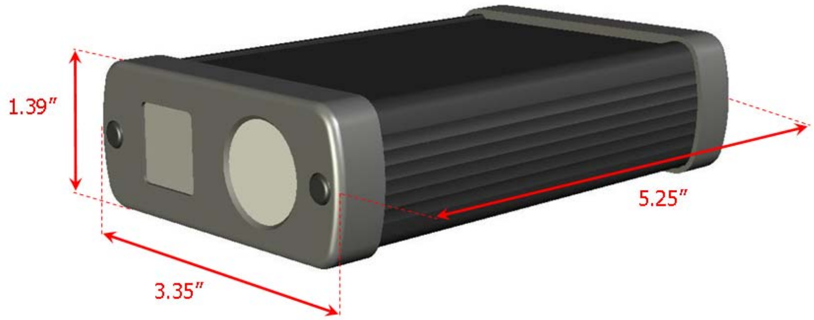

Figure 1. Personnel Protection Sensor (PPS) and its Dimensions

i. Sensor Operation

The PPS sensor shows threat information when pulsed lasers are detected. A power indicator and pulse repetition frequency are displayed along with a textual display regarding the laser exposure and potential hazard. At threshold (roughly .001 x MPE), a blue light emitting diode (LED) is lighted and the pulse repetition frequency (PRF) of the laser is displayed. As the incident laser fluence (Joules/square centimeter (J/cm2)) increases, a real-time text indicator displays information about the potential hazard. If the laser radiation can be blocked by the eye protection filters, the display shows "Use CM (Countermeasure)". If the eye wear are not able to block the laser radiation, the display shows "Vulnerable" and then "Danger" if the exposure exceeds the MPE. Figure 2 shows a sample display of the PPS for a laser illumination that is blocked by the laser filter. Note, it is critical that the filter used in the PPS and the users eyewear match for the displays to be meaningful.

Figure 2. PPS Sensor Display

The PPS sensor display is live and provides real-time indication regarding pulsed laser detections. The display and interface were designed to be useful from a demonstration perspective, but it is anticipated that a modified display or indication system would be desired by operators. The PPS design allows for repackaging the sensor and reformatting the data output in a future effort to suit requirements defined by the AF.

Table 1: PPS Specifications

Specification	Value
Field of View	110 degrees
Detection Threshold	$<10^{-9}$ J/cm^2 visible
Amplitude Measurement	Decade bins
Threat Characterization	Determines if signal is in protection bands or not

ii. Data Products

Data files from the PPS are downloaded to another computer and processed with an application called PPS Analysis Tool. The tool allows one to open files and display their contents as shown in Figure 3. In this case a 20 Hz laser is being fired at a target board and a range of amplitudes up to 3 (approximately equal to MPE) is observed. For the brighter pulses, the sensor displays live and shows in the recorded data that the laser eye protection countermeasure should be used (Protect = yes). A summary of statistics for the data file are provided and tabs are available for the GPS data and sensor diagnostic data. There are two output options with the tool. First, the plots seen in the display can be printed to bitmaps using the print button. This allows the analyst to easily incorporate results into briefing charts. The save button saves the data in a comma separated value (CSV) file for analysis or plotting by outside tools. Figure 4 shows an excerpt of a spreadsheet used to display the CSV file which includes the summary information, details on a pulse by pulse basis and the GPS data. The first column is seconds past midnight (SPM) followed by the date and details on the events. The data can be copied and pasted into other applications or used directly from the CSV file.

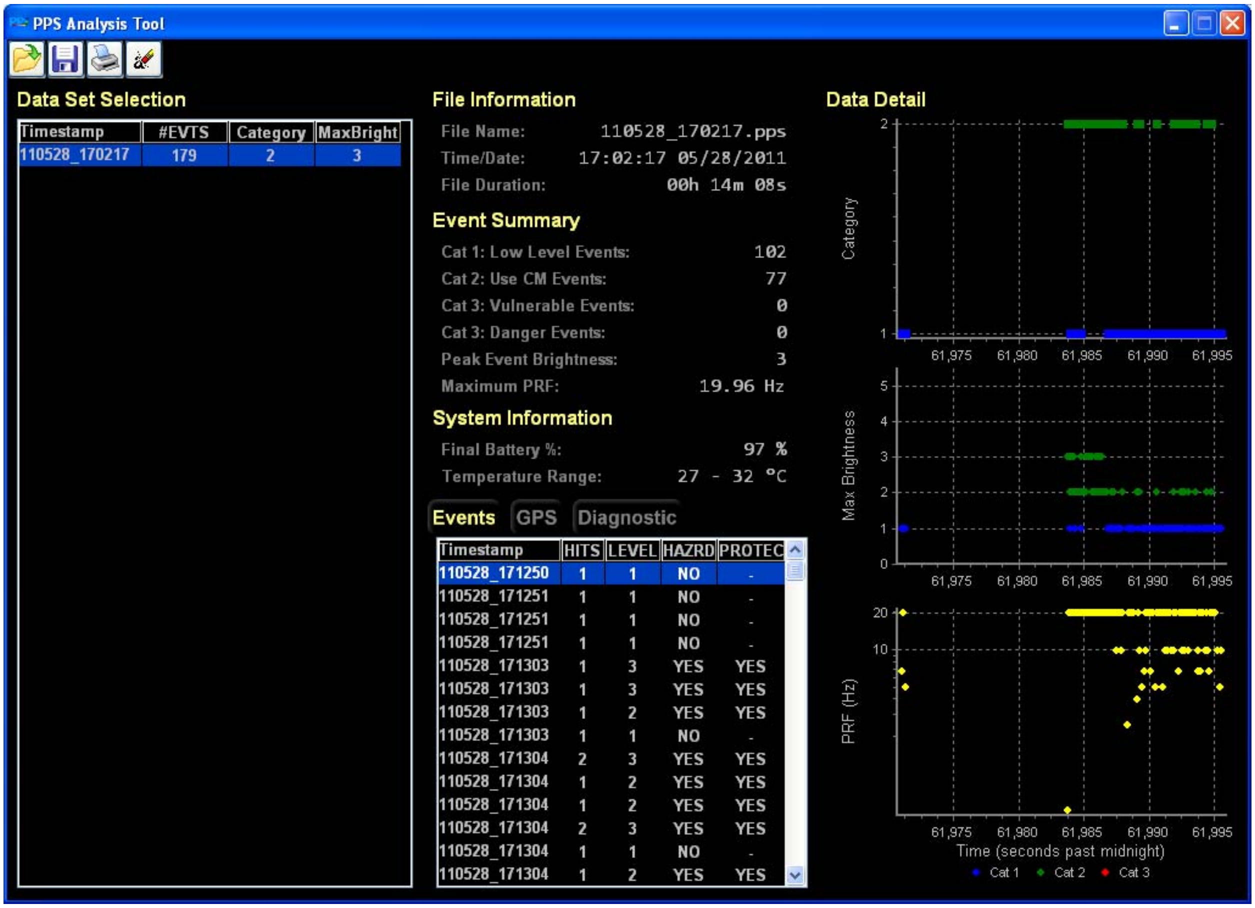

Timestamp	#EVTS	Category	MaxBright
110528_170217	179	2	3

File Name: 110528_170217.pps
Time/Date: 17:02:17 05/28/2011
File Duration: 00h 14m 08s

Cat 1: Low Level Events: 102
Cat 2: Use CM Events: 77
Cat 3: Vulnerable Events: 0
Cat 3: Danger Events: 0
Peak Event Brightness: 3
Maximum PRF: 19.96 Hz

Final Battery %: 97 %
Temperature Range: 27 - 32 °C

Timestamp	HITS	LEVEL	HAZRD	PROTEC
110528_171250	1	1	NO	-
110528_171251	1	1	NO	-
110528_171251	1	1	NO	-
110528_171251	1	1	NO	-
110528_171303	1	3	YES	YES
110528_171303	1	3	YES	YES
110528_171303	1	2	YES	YES
110528_171303	1	1	NO	-
110528_171304	2	3	YES	YES
110528_171304	1	2	YES	YES
110528_171304	1	2	YES	YES
110528_171304	2	3	YES	YES
110528_171304	1	1	NO	-
110528_171304	1	2	YES	YES

Figure 3. Sample PPS Analysis Tool Display

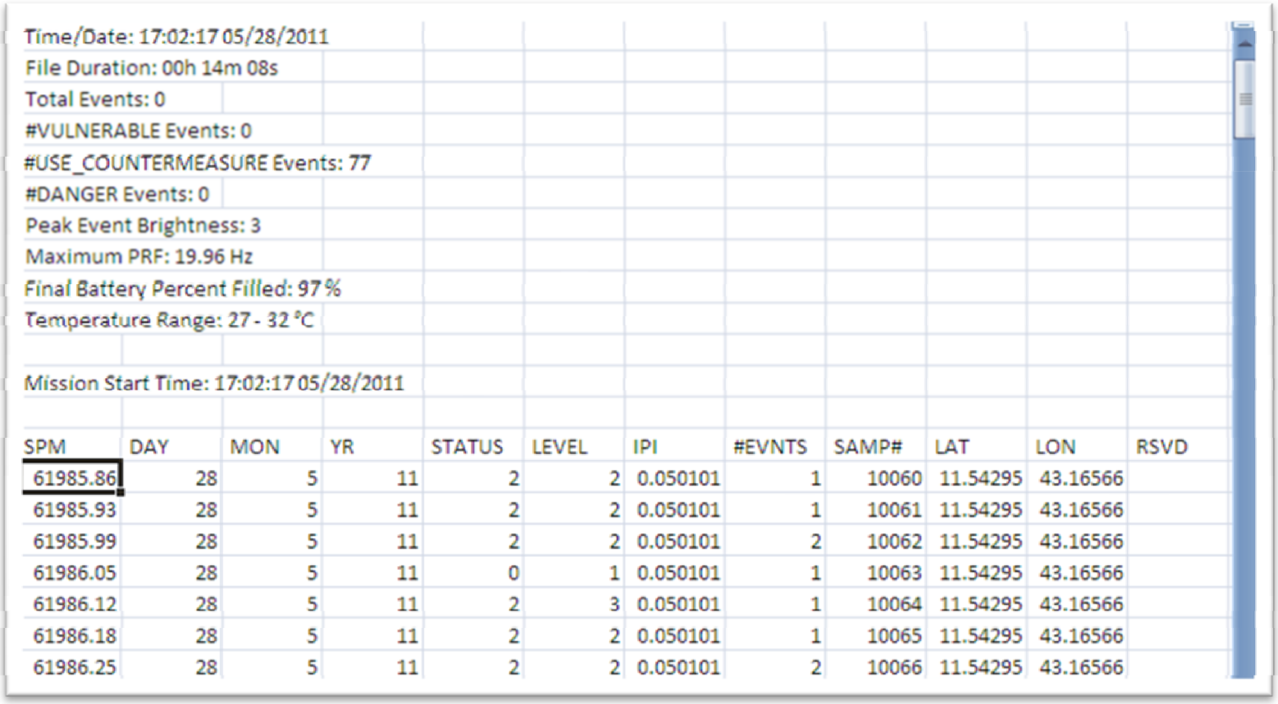

Time/Date: 17:02:17 05/28/2011
File Duration: 00h 14m 08s
Total Events: 0
#VULNERABLE Events: 0
#USE_COUNTERMEASURE Events: 77
#DANGER Events: 0
Peak Event Brightness: 3
Maximum PRF: 19.96 Hz
Final Battery Percent Filled: 97 %
Temperature Range: 27 - 32 °C

Mission Start Time: 17:02:17 05/28/2011

SPM	DAY	MON	YR	STATUS	LEVEL	IPI	#EVNTS	SAMP#	LAT	LON	RSVD
61985.86	28	5	11	2	2	0.050101	1	10060	11.54295	43.16566	
61985.93	28	5	11	2	2	0.050101	1	10061	11.54295	43.16566	
61985.99	28	5	11	2	2	0.050101	2	10062	11.54295	43.16566	
61986.05	28	5	11	0	1	0.050101	1	10063	11.54295	43.16566	
61986.12	28	5	11	2	3	0.050101	1	10064	11.54295	43.16566	
61986.18	28	5	11	2	2	0.050101	1	10065	11.54295	43.16566	
61986.25	28	5	11	2	2	0.050101	2	10066	11.54295	43.16566	

Figure 4. PPS Exported CSV File

iii. Moody AFB Demonstration

Two PPS sensors were sent to the 71st RQS (rescue squadron) located at Moody AFB for an extended deployment of the sensors by medical personnel. The sensors were used in a combination of C-130 airborne measurements as well as ground support measurements. The left-hand panel of Figure 5 shows the sensors operated on the C-130. A combination of flight and ground operations was used with the PPS sensor during the deployment. The aircrews provided feedback on the display and operation and identified items of interest observed in the data. The sensors were also used for characterizing potential hazardous irradiance levels in the vicinity of a ground target board used to boresight laser designators. The data from these tests were used to improve safe operating procedures associated with the laser firings. The right-hand panel of Figure 5 shows one of the set-ups used to characterize the signal reflections.

PPS Installed on C-130

Ground Target Reflection Geometry

Figure 5. PPS Sensor Use on 71st RQS Deployment

iv. Rapid Dissemination of PPS Sensor Data

One of the Tricorder program goals was to investigate and demonstrate methods for rapidly disseminating data collected by operators. Once there are laser illumination characterization sensors deployed, there needs to be a path for moving data quickly to other parties having a need-to-know about the incidents. Data sitting in an instrument's memory or on an operator's thumb drive is not adding to the situational awareness or mission planning required by medical and operational personnel. As one approach to meeting the rapid dissemination goal, SSI purchased a handheld computer with a wireless networking and phone capability. An application was written to download data from a PPS sensor through a cable between the devices (see Figure 6). The handheld computer presented a summary of lasing events and allowed the operator to page through a menu system to look at more detailed displays about the collected data. Figure 7 shows a summary of the data analysis and transmission functions. The handheld computer could send event summary messages via text messages to other phones and the data files were transferred wirelessly to a base station which had more processing and display capabilities than the handheld computer. A demonstration was carried out in which laser events were recorded and text messages sent out to various AF personnel to make them aware of the incidents. Data files were then emailed to AF medical analysts for review. This demonstration serves as one possible mechanism for rapid dissemination of laser incident data.

Figure 6. PPS Data Transfer to Handheld Computer

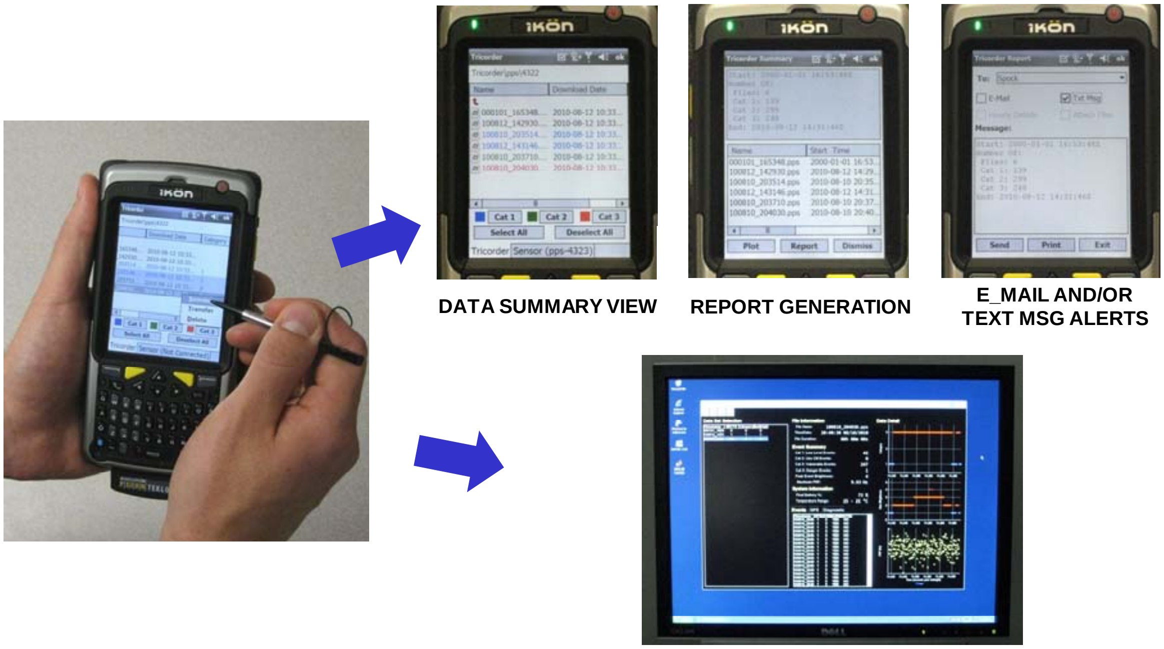

DATA SUMMARY VIEW

REPORT GENERATION

E_MAIL AND/OR
TEXT MSG ALERTS

DOWNLOAD DATA TO WORKSTATION FOR
DETAILED ANALYSES

Figure 7. PPS Sensor Data Analysis and Transmission on Handheld Computer

b) *M4B Sensor Development*

SSI developed a prototype sensor to verify performance of key sensor components to be used in a laser geolocation sensor and to expand the threat space addressed to include low power CW lasers. These low power lasers are a growing nuisance to domestic, law enforcement and military pilots because of their capability to distract or temporarily dazzle pilots at night. The distraction effects can be important even orders of magnitude below the MPE irradiance levels. Therefore, a significant goal of the M4B sensor is to collect laser signature data below one microwatt/cm^2 for visible laser radiation (roughly 3 orders of magnitude below the MPE). As shown in Figure 8, the M4B sensor has two independent sensor modules, an integrating sensor that detects pulsed and CW lasers and a pulse-optimized sensor. The sensor was built to be rugged enough for airborne applications or extensive field use.

Pulse-Optimized Sensor
- low fluence detection
- 400-1700 nm
- fluence amplitude
- pulsewidth binning
- pulse repetition freq.

Integrating Sensor
- Pulsed and CW
- laser pointer detection
- 400-1100 nm
- amplitude
- Wavelength ID
- Angle of arrival

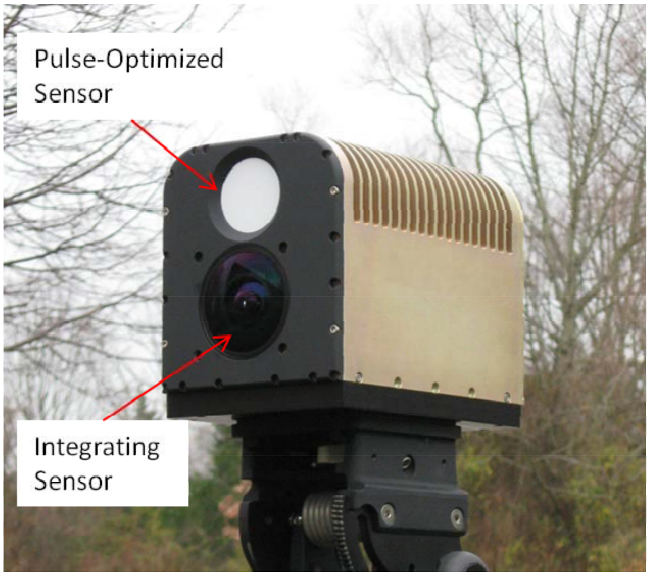

Figure 8. M4B Sensor Description

i. Sensor Performance

In its original configuration, the pulse-optimized sensor reports pulse amplitude, wavelength estimate (coarse), and pulse characteristics such as inter-pulse interval and pulsewidth binning. The integrating sensor provides higher accuracy wavelength estimates (+/- 10 nm), angle of arrival, and amplitude estimates (order of magnitude accuracy), but it is less sensitive and has lower probability of detection for pulsed lasers than the pulse-optimized sensor. Table 2 presents specifications for the M4B sensor. The goal of detecting irradiances below one microwatt/cm^2 at night was exceeded by roughly two orders of magnitude. It is noteworthy that even at 10^{-8} W/cm^2, an observer will still report a bright laser signal when their eyes are night adapted. Data from the sensor is displayed live on a graphical user interface on a laptop computer and stored for post-analysis.

Table 2: M4B Performance Specifications

Parameter	Integrating Sensor	Discrete Sensor
Field of View	120°	120 degrees
AOA Resolution	1°	N/A
Spectral Range	400-1080 nm	400-1700 nm
Spectral Resolution	+/- 10 nm	Coarse binning
Pulsewidth	N/A	Coarse binning
Pulse Repetition Frequency	N/A	<1 Hz to 5 kHz
Threshold Day	~10^{-5} W/cm^2	Same as night
Threshold Night	~10^{-8} W/cm^2	<10^{-10} J/cm^2

ii. M4B Cursor-on-Target Demonstration

The AF/SG office expressed its interest in carrying out a data dissemination demonstration like what was done with emailing data summaries and data files from the PPS sensor. However, in this instance, the goal was to move data on a communication network modeled after an actual military network. In conjunction with the AF/A3 office and the Naval Post graduate School (NPS), SSI supported sensor modifications and testing of the M4B sensor to display data on FalconView using a Cursor-on-Target (CoT) data format. NPS had the communication network hardware and SSI worked with NPS and Mitre to define data fields and the interface to send sensor data directly from the M4B head to the network. The goal was to have live data displayed at a “Tactical Operations Center” and archived for later analysis.

While the laser detection capability of the sensor is well understood, there is no standard for providing data products to medical users. Therefore, SSI defined a set of sensor data products in the expectation that it would spur discussions with the medical community regarding laser exposures and standards for reporting. The M4B data products are not represented as being a final solution to this problem, nor are they the only products that could be generated by the sensor. To achieve the CoT compatibility and generate the data products put forth in the ICD, sensor modifications were required as described below.

1) The wavelength and amplitude error bars for the pulse-optimized sensor in its original configuration are large which makes it difficult to assess the potential hazard caused by pulsed laser illumination. SSI modified the sensor to provide a data product directly related to maximum permissible exposure for all laser wavelengths in the 400-1100 nm band so that a hazard level could be determined and reported in the data. As a consequence of the modification, the sensor data could no longer be used to estimate wavelength so the reported range was 400-1100 nm. A second pulsed detection channel was provided to report eye safe laser rangefinders as an independent message for situational awareness purposes.
2) A second modification was made to uniquely distinguish pulsed and CW lasing events to remove ambiguities caused by having the two different sensors reporting on the same event. Specifically, it was the intention to have pulsed laser events declared by only the pulse-optimized sensors and the CW laser events declared by the integrating sensor.
3) Data output modifications were required to comply with the CoT format and to reflect the changes in the sensor data products. The data processing and formatting was all accomplished in the sensor head to eliminate the need for a laptop computer to be part of the system. In carrying out this modification, there was no capacity in the M4B to store its own data so the only data products from the test are those received over the CoT communication network.

In carrying out the CoT demonstration, there were two tests carried out. The first was a laboratory test at SSI in which NPS personnel brought a computer that was representative of the network to which the M4B sensor would be connected. This test provided a risk reduction that the messages and connections were appropriate and that the modified sensor was still operating properly. Figure 9 shows a picture of the sensor undergoing laser illumination while connected to the NPS network. The network computer and display are shown in the right-hand panel of Figure 9 and the laser event cursor shows up properly on the FalconView map. SSI verified that the laser icons changed appropriately for different fluence levels reflecting the hazardousness of the sources. The network connections and software were found to work as expected which verified the system's readiness to undergo testing at Camp Roberts with the actual NPS system.

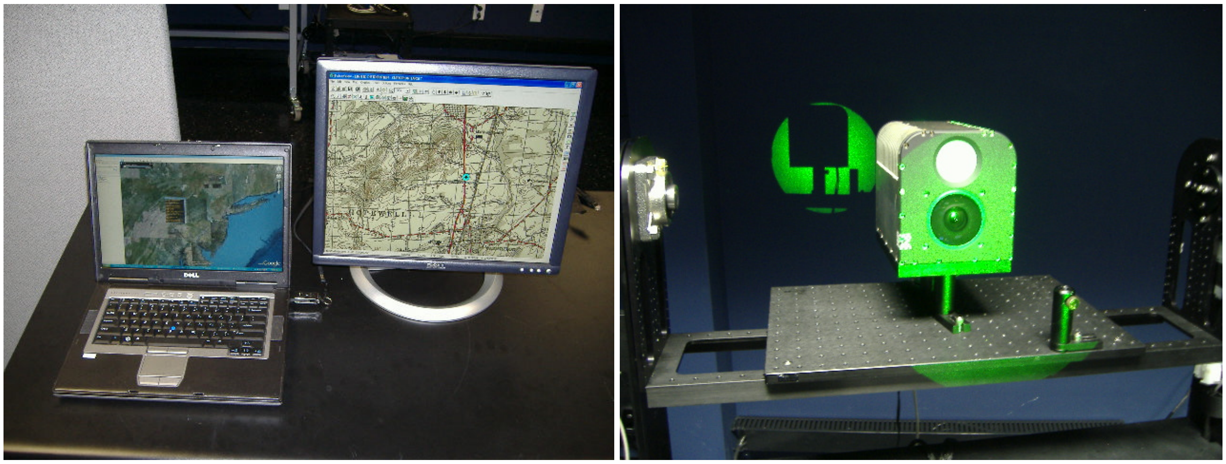

Figure 9. Risk Reduction Laboratory Testing of Cursor-on-Target Hardware

c) *2.3 Geolocation Sensor Development*

Under the Tricorder effort, SSI fabricated and tested three directed energy detection sensors with the capability to determine absolute heading to the source from the sensor's position. In the Tricorder statement of work, this sensor was called the Geolocation Sensor and SSI has given it a designation of M6. The M6 sensor components and performance specifications are similar to those in the M4B sensor providing time of event, the sensor location and the laser amplitude, wavelength, laser angle of arrival and pulse characteristics. However, the M6 sensor has additional components added that provide absolute heading and elevation angle of the sensor head. Using these data elements combined with the sensor location and the integrating sensor-derived angle of arrival of the laser source, the system computes a vector with heading and elevation to the source from the sensor location. How to best use this data is something to be determined by the application and user requirements. For example, if the sensor is on a ground vehicle and a laser beam is propagated horizontally to the sensor, the vector derived will be parallel to the ground and never intersect it. However, for an airborne sensor illuminated by a ground based laser, the vector computed can be intersected with the ground and the user preference for what mapping tool (e.g., FalconView) to use needs to be established. Tools to accommodate the user preferences will need to be written under a future effort.

i. M6 (Geolocation) Sensor Description

The M6 sensor, shown in Figure 10, is similar in appearance to the M4B sensor since the integrating sensor and discrete sensor designs are essentially the same. Some upgrades to the processing capability internal to the housing were made for future flexibility and the housing was slightly expanded on account of this change. An additional change is that a visible camera was added to the package to capture live video pictures (~1 Hz) when laser events are being detected.

This added data product will be useful in some situations to help identify from what the source originated in a visible scene.

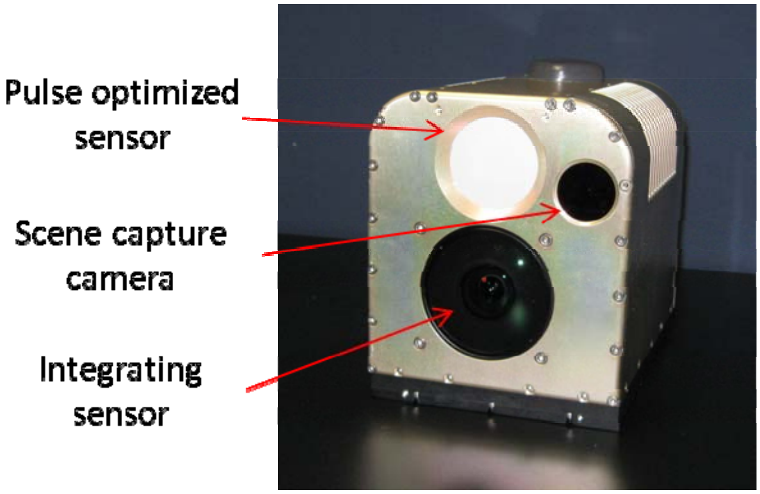

Figure 10. M6 Sensor Description

A new graphical-user-interface was written to display the M6 data in real-time. Figure 11 shows the display with results from measuring a laser in the laboratory. The data display is similar to the M4B display in terms of the laser parameters measured. The most significant new capability is the heading and elevation display which shows the vector to the source from the sensor location. This data is available because of the new sensors added to the M6 design along with new firmware to make the relevant computations. Another new feature added is a “history” display showing summary information about events that have occurred since the program was started. In this way, if an operator is not looking at the display when an illumination event occurs, they can still be aware that events have occurred based on the details of the history display.

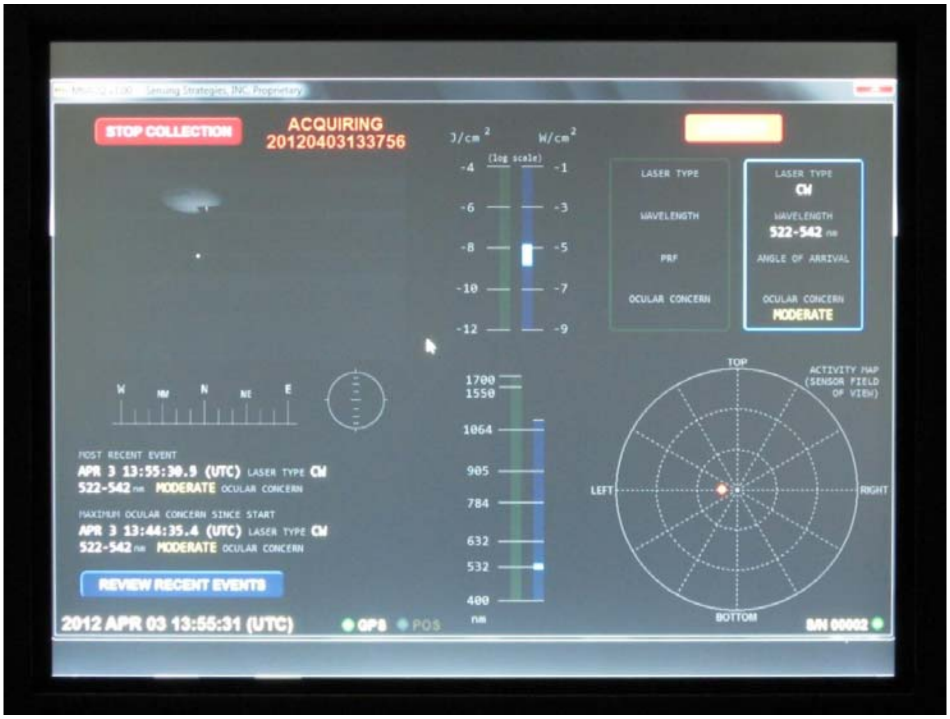

LASER TYPE CW
WAVELENGTH 522-542 nm
ANGLE OF ARRIVAL
OCULAR CONCERN MODERATE

MOST RECENT EVENT
APR 3 13:55:30.9 (UTC) LASER TYPE CW
522-542 nm MODERATE OCULAR CONCERN

MAXIMUM OCULAR CONCERN SINCE START
APR 3 13:44:35.4 (UTC) LASER TYPE CW
522-542 nm MODERATE OCULAR CONCERN

2012 APR 03 13:55:31 (UTC)

Figure 11. M6 Graphical User Interface

ii. Sensor Specifications

The sensor performance for the M6 sensors is unchanged from the M4B (see Table 3). Testing of the angle of arrival capability has been limited to ground tests at SSI's facility. To fully characterize this capability in relevant environments will require additional testing (e.g., flying the sensor on a C-130 or helicopter). A need for airborne measurements with lasers illuminating the sensor will also be essential in establishing baseline geolocation accuracy and this kind of testing was not able to be scheduled under the current effort.

Table 3: M6 Performance Goals

Parameter	Integrating Sensor	Discrete Sensor
Field of View	120°	120°
AOA Resolution	1°	N/A
Spectral Range	400-1080 nm	400-1700 nm
Spectral Resolution	+/- 10 nm	Coarse binning
Pulsewidth	N/A	Coarse binning
Pulse Repetition Frequency	N/A	<1 Hz to 5 kHz
Threshold Day	~10^{-5} W/cm^2	Same as night
Threshold Night	~10^{-8} W/cm^2	<10^{-10} J/cm^2

d) *Occupational Health and Toxicology Sensor Investigations*

An objective of the Tricorder program was to extend its capabilities to occupational health and toxicology applications. The goal is to have a capability for sensing toxic elements or species in air, soil or water samples without having to resort to “wet chemistry” experiments in the field. Therefore, SSI’s task was to investigate methods for optically or electrically sensing changes in a detection mechanism that could be carried out remotely or with a distributed direct-contact sensing network that could be queried by a central processing unit. Our emphasis for this effort was on detection techniques because the networking aspect of the approach is straightforward relative to coming up with a novel, reliable way of sensing the targets of interest. SSI’s investigation was focused on three different techniques: 1) surface attached gold nano particles with specialized ligands attached to the particle surfaces that would be selective to particular toxic compounds, 2) Raman spectroscopy for chemically sensing compounds of interest using a non-contact, remote sensing mechanism, and 3) quantum dots with target molecule specific aptamers attached to the dots. A summary of the three approaches is given below.

i. Surface Attached Nanoparticles

Previous work by AFRL and UES Corporation demonstrated their ability to prepare solutions of uniform size gold nano particles using multifunctional peptides to coat the gold particle surfaces.[1] The peptides stabilized the particles thereby reducing coagulation and provided a mechanism for detecting the presence of heavy metal ions. Gold nanoparticles exhibit Surface Plasmon Resonance (SPR) which gives them a characteristic color depending on the particle size. A shift in the emitted spectrum occurs when the peptides attach to the gold particles and this new spectrum changes when the solution contains a heavy metal that interacts with the peptide. This color shift has been proposed as a means for testing water samples for toxic metals.

For the Tricorder effort, the desire was to come up with either an electrical or optical method to sense the change in SPR based on detection of the target species. Discussions with UES Corporation were held to identify possible detection mechanisms and target species. The selection of toxic metals in water was made as an applicable problem set and one for which the solution-based nanoparticles had shown promise. Detector samples were purchased from UES who carried out particle depositions and chemical exposures. The detectors were made up of polished silicon wafers on which the particles were deposited in a chemical solution. Fluorescence measurements were made to confirm the presence of gold on the treated surfaces before shipping the detector samples to SSI.

SSI was responsible for carrying out optical reflectance measurements to determine if the changes in reflectance were detectable with a stabilized white light source and commercial spectrometer. Figure 12 depicts the set-up which in which a fiberoptically coupled white light source was directed at the surface and a spectrometer was used to measure the surface scattered radiation to try and detect the spectral shift associated with the SPR change. A variety of reflectance geometries were tested including glancing specular measurements as well as the diffuse scatter shown in the drawing. As discussed in section 3, the variability in reflectance between samples exceeded any changes in the spectral signatures associated with exposure to contaminants.

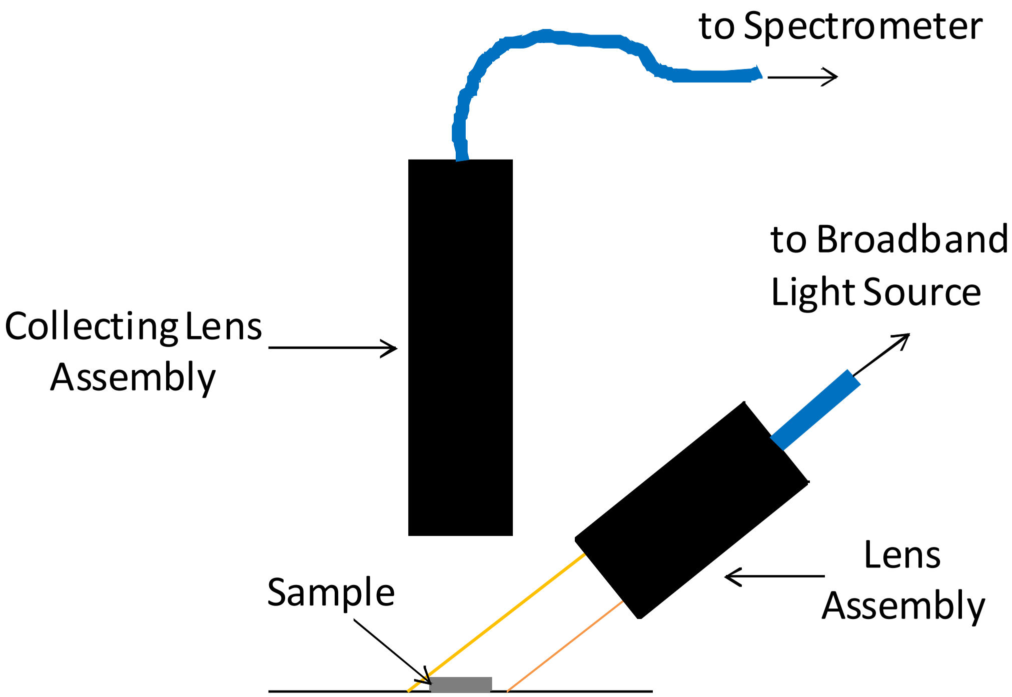

Figure 12. Surface Reflectance Measurement Set-up

ii. <u>Raman Spectroscopy</u>

As part of the Tricorder program, SSI investigated the feasibility of detecting specific amide and amine chemical groups in plants as they are the most prevalent alkaloids which provide anesthesia properties. The eventual goal of this task would be to build a handheld device that could be used in the field to quickly identify substances based on their chemical signature using a non-contact technique. While there are commercial items developed for this kind of species identification, none of them provide a stand-off capability like that desired for the AF mission. To support this activity, SSI acquired a commercial spectrometer designed for Raman Spectroscopy measurements using a 785 nm laser wavelength. This wavelength was selected because shorter wavelength lasers (e.g., 532 nm), which would be preferred from a Raman signal generation perspective, create substantially higher fluorescence signals which make the detection of weak Raman features more difficult. Going to longer laser wavelengths would require using InGaAs cameras to detect the Raman features which would add significantly to the system cost. Using a 785 nm laser creates Raman features detectable with a silicon camera technology and it is a mature diode laser technology which can be obtained commercially with high output power. These cost and data quality concerns drove the decisions as to which technologies to use for the signature measurements. Figure 13 shows sample data from two pain killers using the 785 nm wavelength based Raman system.

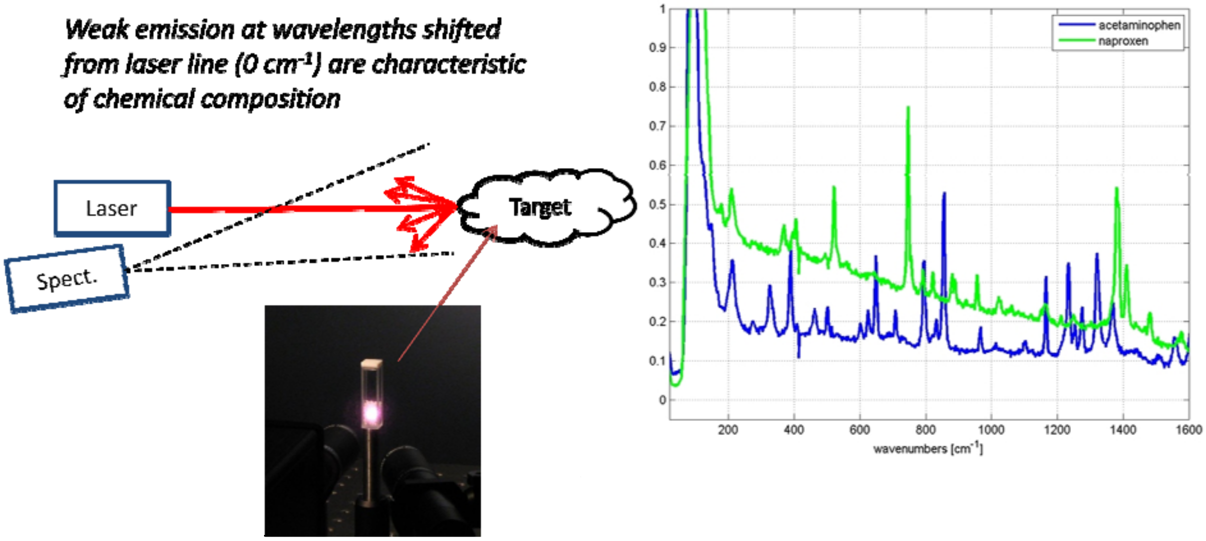

Figure 13. Raman Emission Testing for Chemical Species Detection

iii. Quantum Dot Based Toxicological Sensors

UIC has a history of using quantum dots as chemically selective sensors for biological and toxic species detection. Quantum dots have the unique feature that they fluoresce in spectral bands uniquely defined by their size and composition. The quantum dots are made selective to particular target species by attaching to them aptamers (specially selected biological molecules) which change in shape when the target species is present. By attaching a small gold particle to the end of the aptamer, the quantum dot fluorescence can be quenched when the apatmer molecule changes shape and the gold particle is in close proximity to the dot. This quenching mechanism provides a means to detect the presence of a target species based on the change in intensity of the dots (as opposed to a change in spectral characteristics like the gold nanoparticle surface plasmon resonance). This approach makes a sensor whose selectivity is determined by the effectiveness of the aptamer in uniquely identifying the target species combined with a means to determine when the quantum dots have “turned off”.

In the interest of developing a sensor concept for using quantum dots, SSI collected data on commercially available dots. The spectral characteristics of quantum dots are measureable with standard spectrometers and the data shown in Figure 14 was collected with an Ocean Optics spectrometer with a UV curing lamp illuminating two quantum dot samples. For this exercise, the dried samples of dots were roughly 1-2 mm in diameter and the spectrometer was held close to the emitters to collect the spectra versus time. Figure 15 shows the stability of the quantum dot emissions which indicate that signals on the order of 1% different should be distinguishable. This suggests that having control samples of dots, not modified with the apatamers, to compare with activated dots should be a viable means to determine when the activated quantum dots have been quenched. Discussions about a system approach will be presented in the Results and Discussions Section.

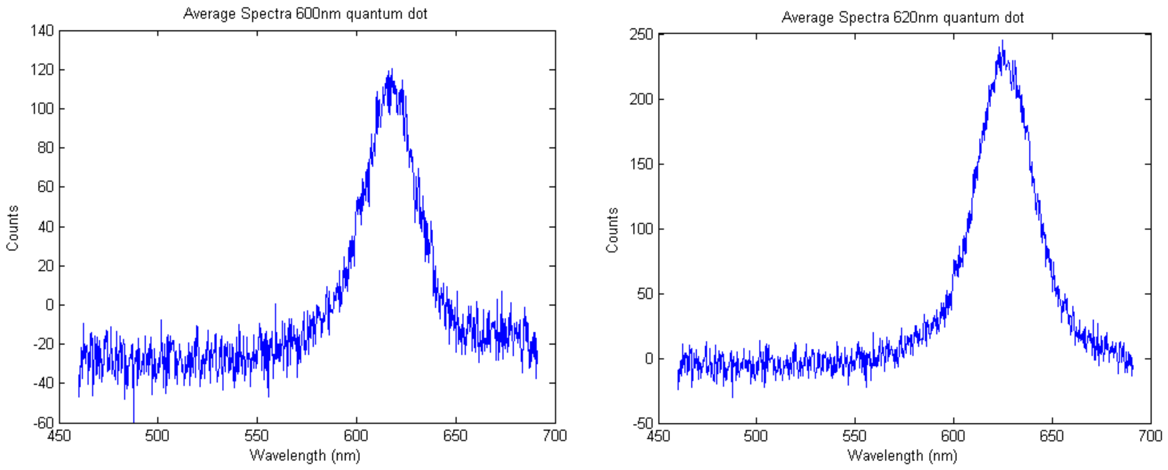

Figure 14. Quantum Dot Spectral Emission Data

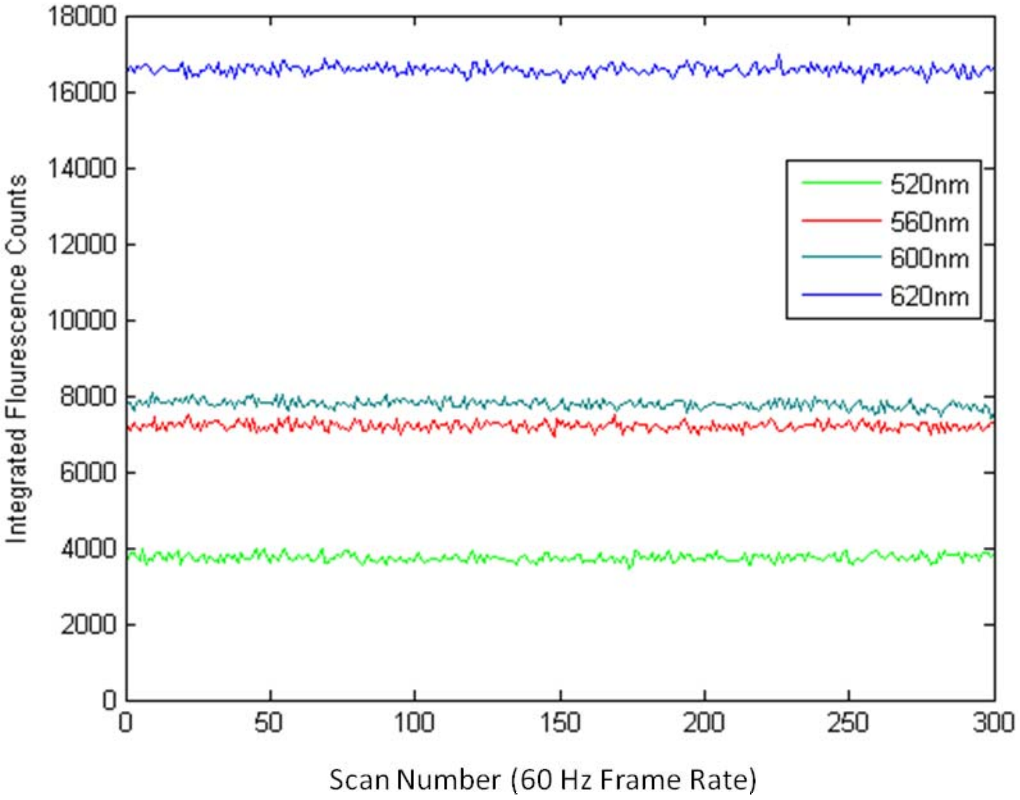

Figure 15. Temporal Stability of Integrated Quantum Dot Spectra (arbitrary units)

4. Results and Discussions

a) *PPS Test Results*

The PPS sensors were used on airborne and ground based tests during this program. Domestically, the sensors were used on controlled tests in which the sources and test conditions were known. On the 71st Squadron tests overseas, the conditions were less understood and controlled, but they provided valuable feedback on how the operators would use them and respond to the displays. Details about major test results are provided below.

i. 3.1.1 Field Test Results

The PPS sensor was tested at Fort AP Hill on December 21, 2009 using a laser designator to illuminate the sensor from roughly a 1 km range. The sensor correctly identified the irradiance levels as hazardous and displayed the “Use Countermeasure” message indicating that laser eye wear would be effective in protecting the sensor operator. The sensor operator walked over the available path (deep snow precluded a driving test) while being tracked by the laser to demonstrate the sensor’s ability to log sensor location during the illuminations.

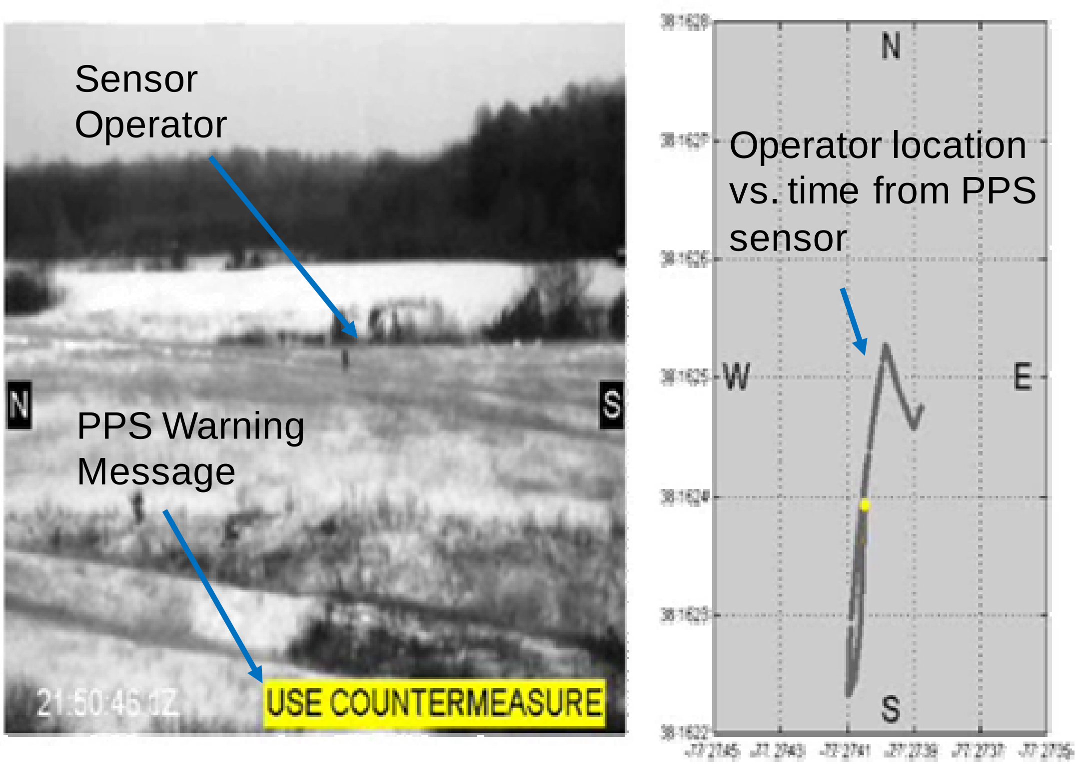

Figure 16. PPS Data from Fort AP Hill Test

SSI also loaned the sensor to Air National Guard personnel in Tucson, AZ to operate the sensor in a C-130 during a flight test involving laser illuminations of the aircraft. The PPS sensor was operated for sorties involving CW and pulsed lasers and the sensor correctly identified the pulsed laser events and did not respond to the CW illuminations. This experience further demonstrated the sensor’s utility for rapid alerting of aircrews regarding potentially hazardous illuminations.

ii. 3.1.2 71st RQS Deployment

Two PPS sensors were loaned to the 71st Rescue Squadron from Moody AFB to operate them over a 5.5 month deployment to Africa. The sensors were flown on C-130s and used for ground operations. In airborne operations, the pilots correlated PPS hits from a laser ceilometer as well as other assets in the base vicinity. However, given the scarcity of laser illumination events in that region, SSI recommended the 71st personnel locate areas where routine laser testing might be taking place and deploy the sensors there for additional practice. The 71st personnel were able to find a location on the base grounds where routine laser operations occurred. SSI iterated with the 71st personnel to develop measurements that could be useful from a range safety perspective. Specifically, the sensors were operated in a variety of positions near and behind the target board. The measurements did not detect any firings missing the target board (which would be of considerable concern for ocular hazards). However, measurements of reflections from the target boards did indicate potential hazards existed. The results were presented to the laser operators and their commanding officer which led to changes in the range operations to better control the area and ensure personnel safety, a feat the 71st personnel viewed as an excellent outcome for the deployment.

A variety of lessons learned from the activity were reported by the 71st personnel. First, the operators indicated that the display was easy to read and the indications were easily identified. However, they expressed that the display needed a “night mode” to reduce the intensity and make it more compatible with night vision goggles. There was also a strong desire for directional information to indicate the location (even quadrant) of the event to help identify the source location. Nevertheless, having the live indication of laser energy was found to be extremely useful and informal conversations with the 71st personnel showed that there will be a need for guidance to operators regarding what should be their response when the sensors indicate the presence of incident laser energy.

b) *3.2 M4B Test Results*

The M4B system served a variety of useful functions throughout this program. First, it was used to validate the sensor performance for the design that was to be used in the M6 geolocation sensor. As summarized below, the sensor performance met all expectations and provided the sensitivity needed to characterize and determine angle of arrival even for very low power CW lasers. Second, the sensor was used for automatic cueing of an imaging sensor to demonstrate the real time threat characterization and the ability of the system to be used in conjunction with other countermeasure techniques. Finally, the sensor was modified again to output data directly to a network connection in the NPS COT demonstration. In all three cases, the instrument served a useful function and provided important lessons learned that impacted the geolocation sensor design.

i. Sensor Performance Test Results

The M4B sensor was operated in indoor and outdoor environments to characterize its performance in terms of sensitivity, spectral range, wavelength resolution, field of view, angle of arrival accuracy, event timing accuracy, and amplitude measurement. Figure 17 shows sample data collected by the sensor in an outdoor collection in which the sun was in the sensor field of view. A CW green (532 nm) laser pointer was directed at the sensor and the amplitude and wavelength were measured continuously as the sensor was scanned throughout its field of view (120 degrees). Figure 17 shows that excellent wavelength data was collected even in the bright solar background and the amplitude distribution (broadened by atmospheric scintillation) was consistent with the low power level incident on the sensor.

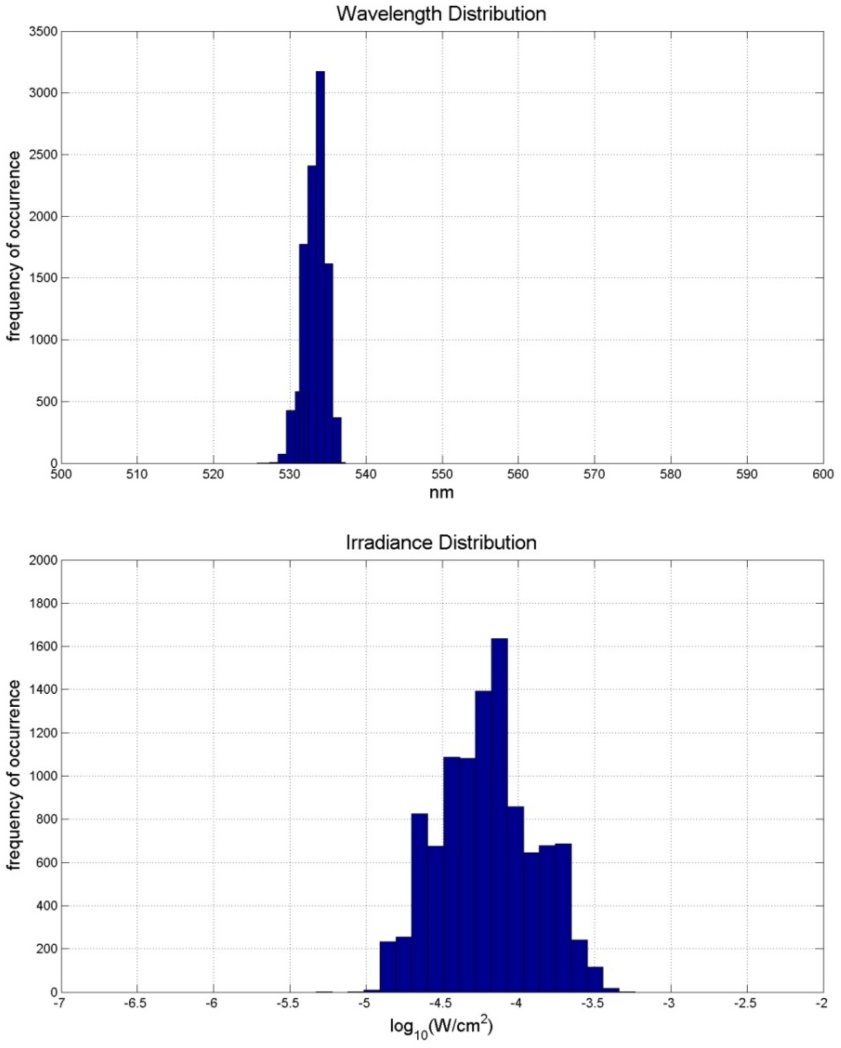

Figure 17. M4B Wavelength and Amplitude Measurement Results

ii. Automated Cueing Demonstration

In discussions with potential sensor operators, an interest was expressed in being able to capture images of laser perpetrators to identify their location, vehicle or other clues to apprehend and counter them. High resolution imagers capable of providing this kind of detail are narrow in field of view and unlikely to be pointing in the proper location to provide this kind of data. Furthermore, some lasers of interest are not visible, so the operators may not know that lasers are being fired based on visible pictures alone. Given this interest, SSI carried out a demonstration of the M4B's ability to automatically cue an imaging sensor on a pan/tilt head to a specified location to identify the source of laser radiation. The sensor identified the laser radiation and sent a message to the pan/tilt controller which was co-boresighted with the sensor so that incidence angle messages would be in a common coordinate frame. Real-time cueing could also be used to switch protective filters, shutters or warning messages to provide protection and situational awareness to personnel or cameras put at risk by the exposures.

iii. M4B Cursor-On-Target Test Results

The M4B sensor was operated at Camp Roberts on September 13, 2011 for the CoT test with NPS. Figure 18 shows the front of the sensor as well as a view from behind the sensor looking towards the laser site. Two laser sites were used for this test, 845 meters and 310 meters. The longer range site was used with the special operations forces laser aided marker (SOFLAM) and both a CW red laser and the SOFLAM were operated from 310 m. NPS operated the communication network and provided the SOFLAM source. As mentioned previously, the M4B sensor was modified to output laser characterization answers directly to the NPS network so the data would be displayed on the FalconView maps and be collected at a remote site that represented a tactical operations center. Figure 19 shows sample results from the test in which a laser icon is viewed on the FalconView map and the data contained in the message is displayed by clicking on the icon. The sensor correctly characterized pulsed and CW lasers under the limited test matrix possible for this test. The goal of transmitting data over the network was successfully accomplished both locally and at the remote operations center where the data was archived for later analysis. This test proved the approach of having live feedback and remote analysis of data products from DE sensors.

Figure 18. M4B Sensor at Camp Roberts for COT test

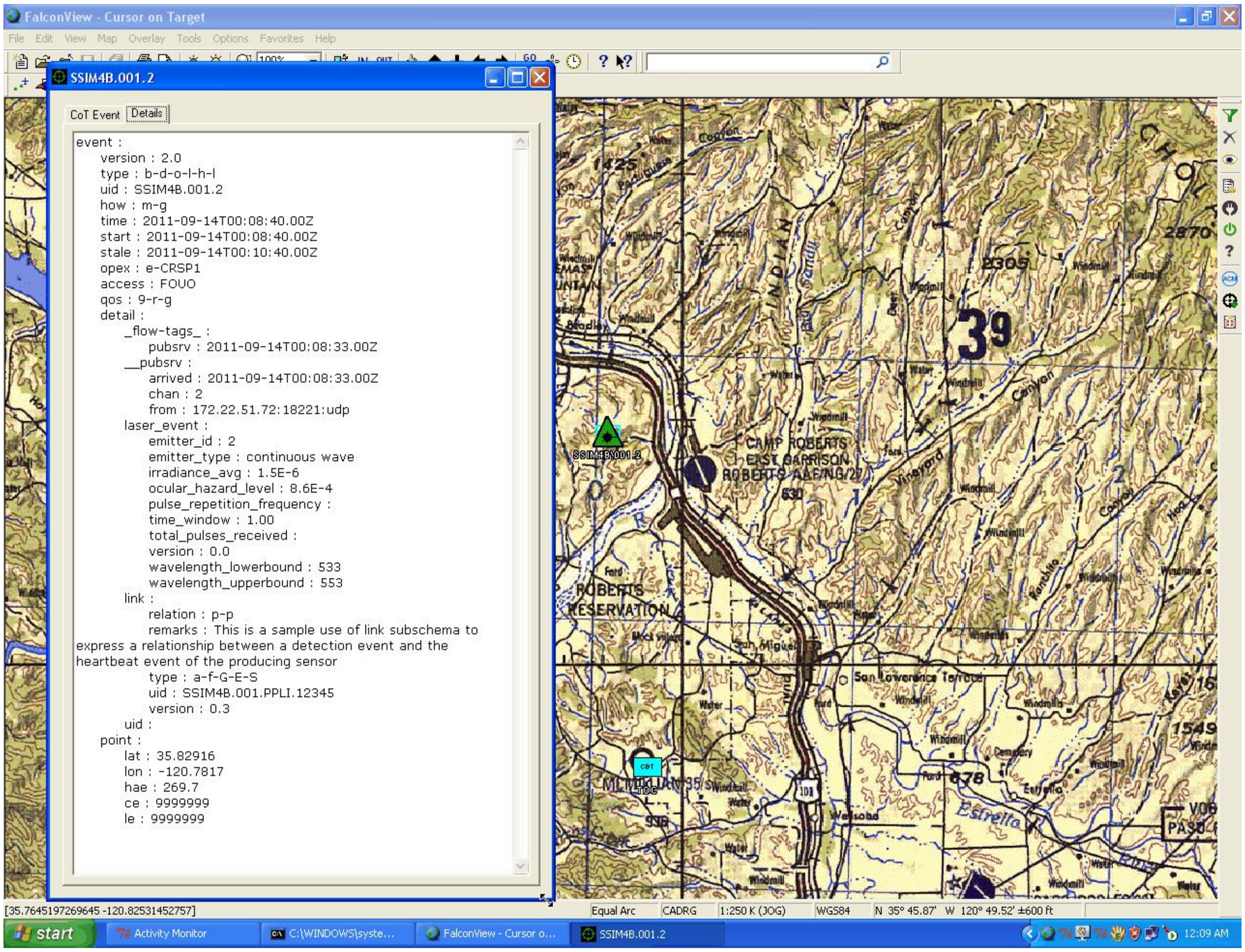

```
event :
    version : 2.0
    type : b-d-o-l-h-l
    uid : SSIM4B.001.2
    how : m-g
    time : 2011-09-14T00:08:40.00Z
    start : 2011-09-14T00:08:40.00Z
    stale : 2011-09-14T00:10:40.00Z
    opex : e-CRSP1
    access : FOUO
    qos : 9-r-g
    detail :
        _flow-tags_ :
            pubsrv : 2011-09-14T00:08:33.00Z
        __pubsrv :
            arrived : 2011-09-14T00:08:33.00Z
            chan : 2
            from : 172.22.51.72:18221:udp
        laser_event :
            emitter_id : 2
            emitter_type : continuous wave
            irradiance_avg : 1.5E-6
            ocular_hazard_level : 8.6E-4
            pulse_repetition_frequency :
            time_window : 1.00
            total_pulses_received :
            version : 0.0
            wavelength_lowerbound : 533
            wavelength_upperbound : 553
        link :
            relation : p-p
            remarks : This is a sample use of link subschema to
express a relationship between a detection event and the
heartbeat event of the producing sensor
            type : a-f-G-E-S
            uid : SSIM4B.001.PPLI.12345
            version : 0.3
        uid :
    point :
        lat : 35.82916
        lon : -120.7817
        hae : 269.7
        ce : 9999999
        le : 9999999
```

Figure 19. Sample Data from CoT test

c) *M6 Sensor Results*

The M6 sensors were tested in a combination of laboratory and outdoor performance tests at SSI. Figure 20 shows the three systems undergoing laboratory testing on a pan/tilt mount at SSI. Table 4 presents tests that were carried out with the sensors.

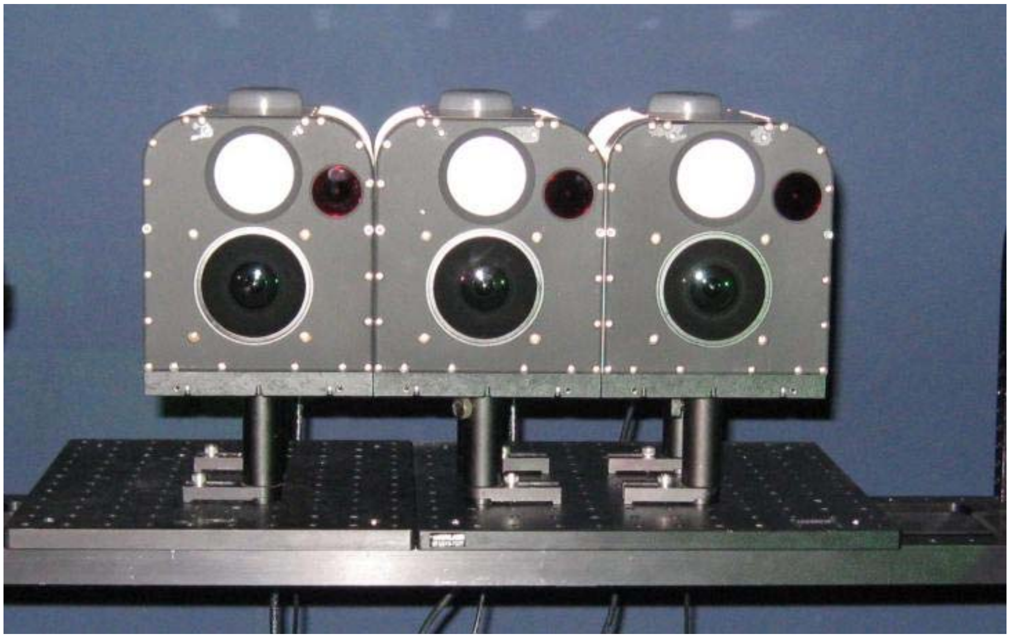

Figure 20. M6 Sensors Undergoing Laboratory Testing

Table 4: M6 Performance Summary

Test	Meets Performance Goal
Field of view	✓
CW Sensitivity	✓
Pulsed Sensitivity	✓
CW Wavelength Range (spectral resolution)	✓
Pulsed Wavelength Range (spectral resolution)	✓
Time Tagging	✓
Pulse Repetition Frequency	✓
Sensor Position	✓
Heading and elevation angle	✓

d) *Occupational Health and Toxicology Sensor Results*

All of the occupational/toxicology detection techniques investigated under this program had shortcomings which made their implementation in a handheld "Tricorder" device impractical. It is important to emphasize that the fundamental techniques themselves showed promise, but they will require more investigation or a modified approach to make them practical for a handheld instrument as discussed below.

i. Surface Attached Nanoparticle Results

SSI carried out fluorescence measurements of the bulk solution nano-particles to verify the kind of findings reported by UES. Figure 23 shows spectral transmission of the bio-functionalized nano-particle detectors after contamination by various metal species. The contaminant concentrations for these measurements were on the order of milli-molar which, though high, were used to verify the basic properties of the bulk nano-particle response. The shift in the surface plasmon resonance (SPR) is evident and the variation in spectral shift might be exploitable to allow identification of particular toxic metals. It is also likely that having multiple types of bio-functionalized detectors would improve the ability to deduce elemental impurities based on having multiple spectral shifts to analyze.

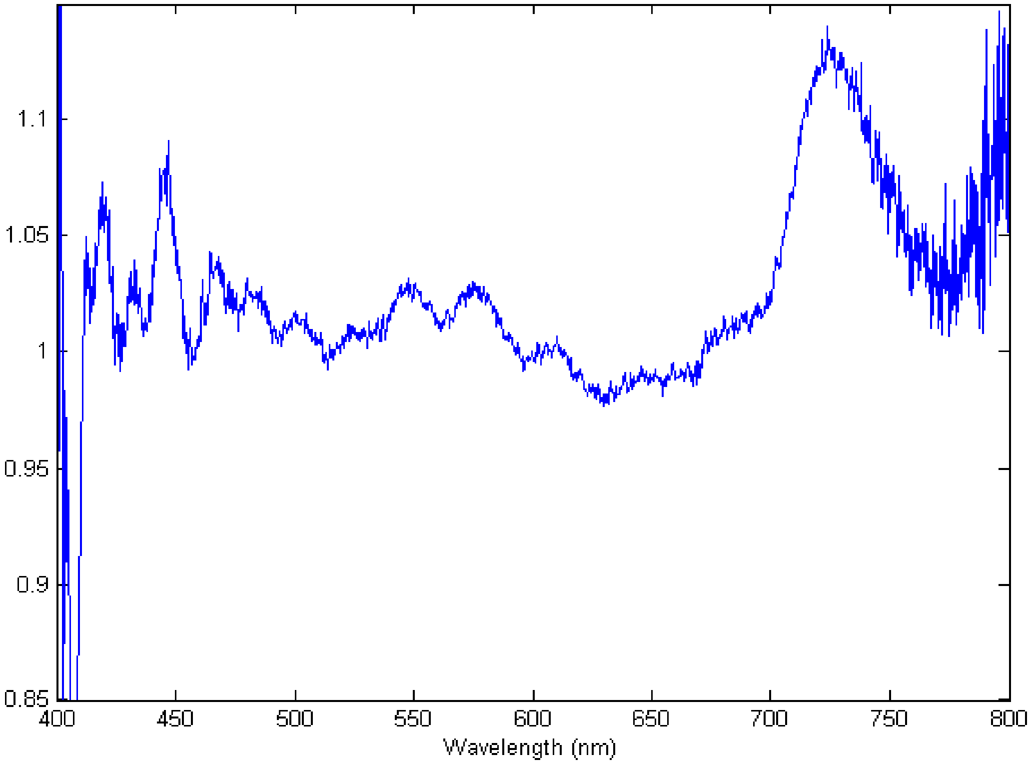

Figure 23. Ratio of One Silicon Wafer Blank to a Second Blank (no Nano-Particles)

UES used an approach to attach a self-assembling monolayer (SAM) on the silicon wafer and created the nano-particles in solution with the intention of developing bonds between the monolayer and the particles. UES tried different concentrations and structures of the monolayers and provided the samples to SSI to try and detect SPR and shifts associated with exposure to contaminants. SSI tried several geometries with the wafers and compared reflectance measurements at near grazing incidence to normal reflectance. The overall conclusion was that the SPR observed in the bulk solution could not be observed on the surface samples. Figure 24 presents spectra for one of the self assembled monlayers samples in which the silicon wafer was exposed to mercury (Hg^{2+}) which had created a SPR shift in the bulk solution. The top two panels are the measured spectra for a liquid contaminant droplet on the surface and the right hand panel is the same sample after the droplet had evaporated. The roll-off in amplitude at the ends of the visible spectrum are due to the lamp's spectral emission. The lower panels are the same spectra divided by the spectrum created from the same wafer in the same position prior to the contaminant exposure. This type procedure was used throughout the measurements, although variants were used to try and improve the results. For example, comparisons were made using the average of multiple sample orientations or using a consistent blank spectrum for all samples. SSI also used two different lamps to ensure that lamp intensity variations were not a cause of variations in the data. We had similar results using a NIST-traceable, current stabilized tungsten lamp as we did with the commercial white light source used for most of the measurements. While the lower right hand panel suggests a possible spectral feature, the results were not reproducible and could be created from other procedures. For example, Figure 25 shows a similar spectral feature for a blank sample that did not have nano-particles on the surface. SSI found that features that were suggestive of SPR were not reliable and concluded that more research at a fundamental level would be needed before this approach could be considered for a prototype development.

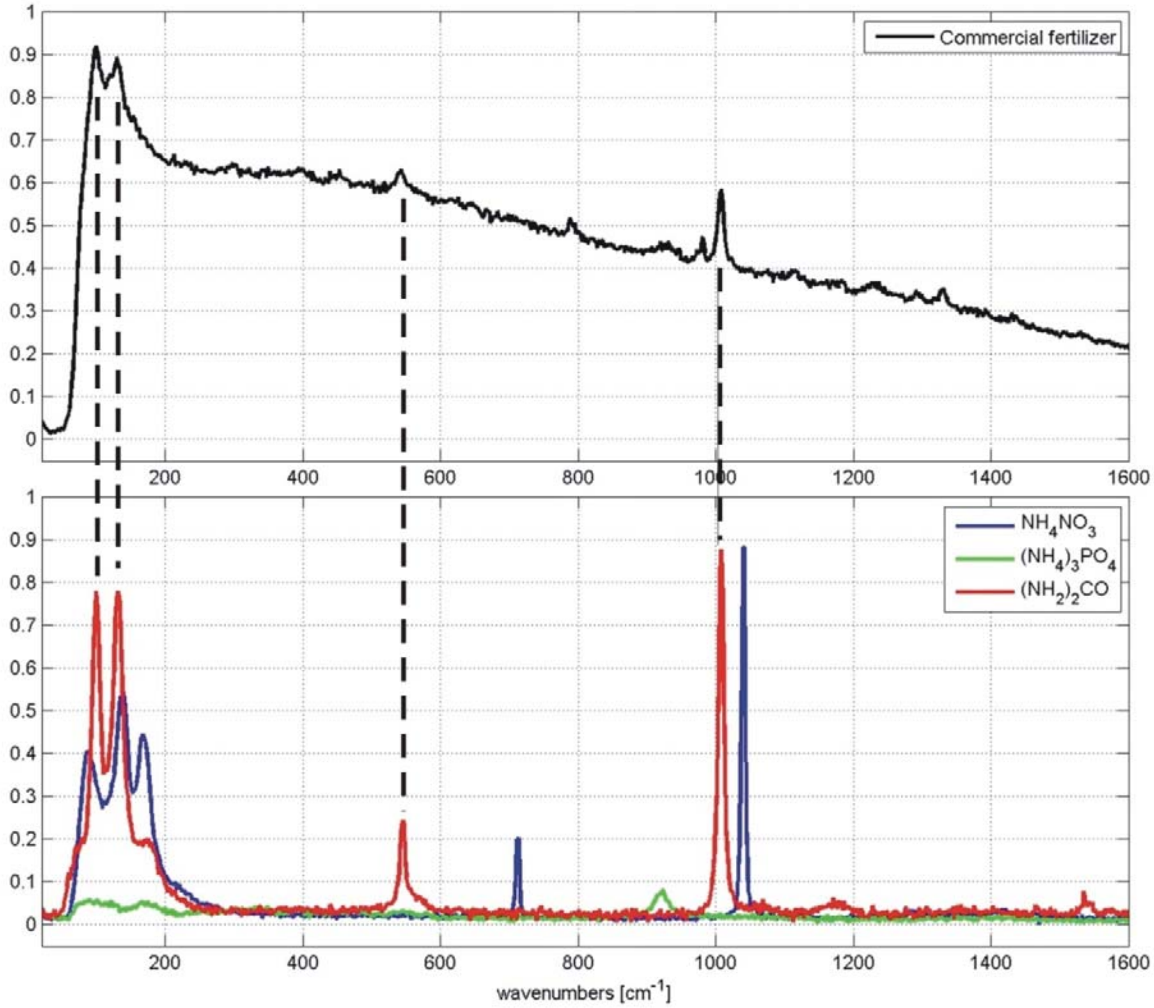

Figure 24. Raman Spectra of Known and Unknown Samples

ii. Raman Spectroscopy Result

SSI carried out measurements with a Raman spectrometer to establish an experience base that would be used to evaluate potential system concepts. The focus of the effort was on whether it was practical to develop a portable Raman instrument capable of detecting and characterizing substances from some 10s of meters away. Portable Raman systems are available commercially and can be used for point measurements essentially in contact with the sample of interest. SSI carried out measurements with leaf samples for characterizing possible alkaloids indicative of anesthetic-like molecules as well as powder samples typical of explosives. The working concept discussed with the Air Force was that a bio-environmental engineer would have responsibilities to identify potentially hazardous or dangerous substances and that a portable chemical species identifier would be a valuable addition to a medical kit.

Sample measurements with powder substances are shown in Figure 26. For this data collection, known substances (ammonium nitrate, ammonium phosphate, urea) were characterized with the spectrometer and a sample of yard fertilizer was measured as an unknown. As seen in the figure, there are a sufficient number of spectral features to help identify the composition of the unknown. However, a strong fluorescence from the unknown material contributed to the overall spectrum. This kind of emission is common to many of the plant measurements made by SSI it was typically the case that the fluorescence was so strong that no features could be detected. This result indicates that it would be advantageous to use a longer wavelength laser to reduce the fluorescence. Unfortunately, this path leads to using an InGaAs camera for the Raman feature measurement which leads to a more costly and cumbersome sensor design. For the powder substance measurements, SSI concluded that the power levels needed to obtain adequate signal to noise from a distance of 10's of meters would be eye hazardous to personnel without protective eye wear. Since the operational concept for the device would require using the device around unprotected personnel, it was dropped as a Tricorder approach for the purpose of this program. The approach of using higher power eye safe lasers (1.55 microns) and InGaAs camera arrays to detect the Raman features was leading to a cumbersome and very expensive solution that was also rejected for the purpose of this program.

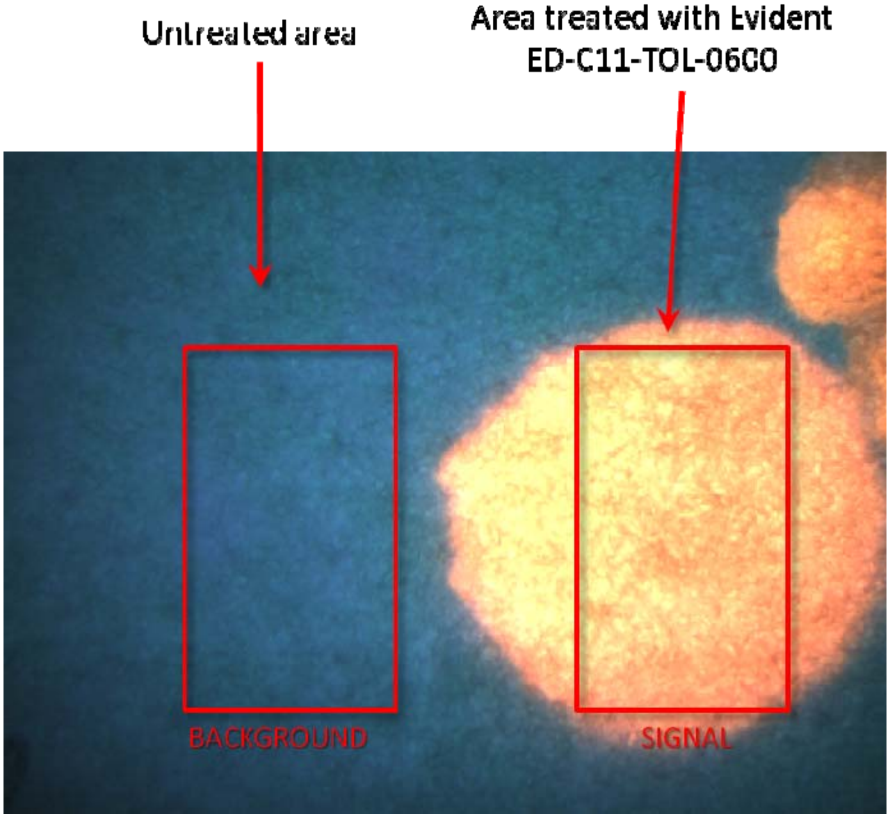

Figure 26. Image of Commercial QDs on Filter Paper Illuminated by UV Light

iii. <u>Quantum Dot Results</u>

The functionalized quantum dot (QD) sensors can make for an intriguing sensor design. Because the quantum dots change their emission state upon contact with the target species, a strictly radiometric approach can be used for identifying dots that have had a detection. This makes for a simpler design than one that requires a spectrum to be measured such as the surface plasmon resonance sensor with the gold nano-particles. The selectivity is based on the unique aptamer-target interaction and the sensor only needs to identify which samples of dots have changed. Figure 25 shows the concept of a sensor using a matrix of QD samples to multiplex a variety of detectors in a single device. In this approach, there would be samples that were control dots with no aptamers to serve as intensity references for the others. In this way, changes in lighting characteristics or contaminants on the surface of the sample being tested (dust layer) would not lead to a misinterpretation of the functionalized radiant emission.

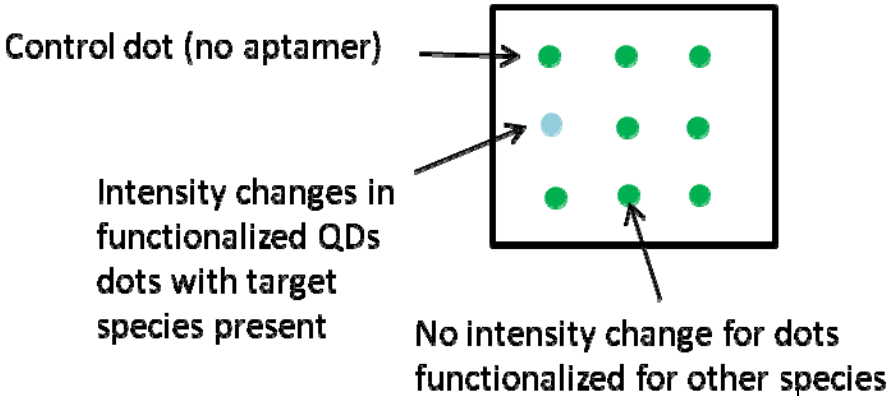

Figure 25. Concept for Using Grid of Functionalized Quantum Dots to Identify Multiple Target Species

SSI carried out an experiment to verify that an imaging approach could measure stable intensity levels from small QD samples. Commercially available QD samples were placed on filter paper and illuminated from the side using a UV curing lamp. The samples were imaged with a digital video camera using a microscope objective as a collection lens. Figure 26 shows an image of the sample and a background region. The radiometric signal from these areas was integrated and differenced to provide a measured QD signal versus time. Figure 27 presents the intensity versus time for the measured emission which shows that it is very stable and could be used for determining small intensity changes if compared to a reference. This conclusion shows that an imaging approach can be used to monitor the emission status of QD samples and a matrix of samples would allow simultaneous screening for a wide range of species with a very simple instrument. The sophistication is in the aptamer design and its selectivity and sensitivity to the target species. This chemistry aspect of the investigation was handled by UIC and the conclusions of that activity are presented in a separate volume.

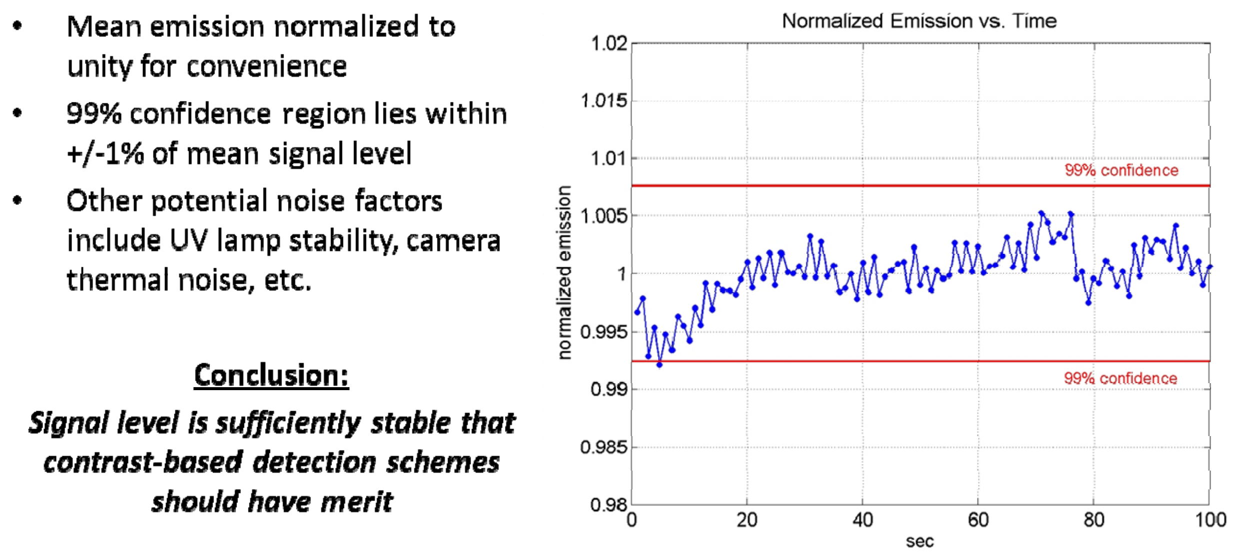

- Mean emission normalized to unity for convenience
- 99% confidence region lies within +/-1% of mean signal level
- Other potential noise factors include UV lamp stability, camera thermal noise, etc.

Conclusion:

Signal level is sufficiently stable that contrast-based detection schemes should have merit

Figure 27. Intensity vs. Time of Small QD Samples as Measured by Imaging Camera

5. Conclusions

SSI has fabricated and tested directed energy detection sensors suitable for characterizing pulsed and CW laser illuminations. Five PPS sensors were fabricated and delivered. These sensors were used in domestic and overseas ground and airborne tests and have elicited positive responses and lessons learned from operators regarding features and characteristics that are desirable from an operational perspective. The M4B sensor was effectively used to characterize low irradiance CW and pulsed lasers in laboratory and outdoor testing. The M4B served to prove the sensor approaches to be used in the M6 sensor which is designed to provide data for geolocating threat laser locations. Three M6 sensors were fabricated and tested in laboratory and outdoor tests and the sensor performance was consistent with expectations. The ability of the system to provide absolute vectors to the source origin was tested in ground sensor tests and will need additional flight test demonstration in the future.

Data dissemination techniques were investigated and proven in the program as well. Data from the PPS sensors was captured transmitted to a handheld computer for initial analysis. Summary threat messages were transmitted from the handheld computer by email to government personnel and the data sets were sent wirelessly to a work station for further analysis. An alternate real-time dissemination approach was implemented using the cursor-on-target protocol and a military-like network provided by the Naval Post-Graduate School. In this test, the M4B sensor firmware was modified to transmit threat data directly from the sensor head on to the network in a CoT-compatible format. Threat icons and data summaries were displayed on FalconView maps and the data was transmitted over the network to a ground station representing a tactical operations center. This demonstration proved the ability to collect laser threat data and transmit it in real time to users with a need for the information.

SSI investigated alternate detection approaches for occupational health and toxicological species monitoring. The use of surface deposited gold nanoparticles did not appear promising because of the variability in the reflected spectral signature. The surface Plasmon resonance features seen in bulk solution were not identified reliably in the samples available from UES Corporation.

SSI also investigated Raman spectral signature collection and concluded that for the remote sensing application (targets at 10s of meters away), it was likely that eye hazardous lasers would need to be used which conflicted with the operational use ideas for the medical community. Finally, SSI investigated sensor ideas for toxicological monitoring using functionalized quantum dots which change emission state when the target species is present. SSI concluded that an inexpensive and simple sensor can be fabricated using imaging sensors once the quantum dots are shown to have the proper selectivity and sensitivity to meet the toxicological monitoring requirements. This part of the research is presented under separate cover by UIC.

6. References

1. Slocik, J.M., M.O. Stone, and R.R. Naik, *Synthesis of Gold Nanoparticles Using Multifunctional Peptides.* Small, 2005. **1**(11): p. 1048-1052.

H. Sociotechnical Evaluation of the Tricorder

1. Summary

The social and technical concerns surrounding the use of any handheld device affect the ability of an end user to successfully use such devices in the field. The Tricorders (a health care technology) described fully in Chapter 3, detect laser radiation and might be used in a variety of CONOPs. Q-methodology was chosen to study the technical and the operational features of the Tricorder; focus groups and published literature were used for early instrument development. Through a number of Q-sort studies with civilians and air force personnel, features for future development of the Tricorder were identified. Some will be easy to deploy. Some will be challenging as a number of technical features were identified that are sufficiently controversial such that direction from the Air Force will be needed to make decisions to inform future development direction. Regarding the operational aspect of the data to be collected from the Tricorder, a significant diversity of opinion exists. In light of this diversity of opinions, careful planning and evaluation will be necessary during deployment of this technology, or the competing views could reduce acceptance of the technology *in situ*.

2. Introduction

The technical "correctness" of the Tricorder—it identifies what it should identify, when and where it should be identified—is only one component in the development of the Tricorder (which is described in Chapter 3). Sociotechnical aspects of the environment in which the Tricorder was to be used had not been identified during the technical discussions surrounding its development. There had been some discussion about who will use it, although this was broadly defined as "multiple user groups." This aspect of the research program sought to further define these user groups, to determine the sociotechnical issues that would enhance technology acceptance with each Aspect of the Tricorder project, and generate procedures to address sociotechnical issues in the future.

3. Methods, Assumptions and Procedures

a) *Building the Research Instrument*

The project began with a review of the literature regarding people and organizational issues surrounding health information technology (HIT). Information systems analysis (evaluation) methodology literature was included. Multiview, a method of information systems analysis, was identified, and literature located for potential adaptation to the Tricorder evaluation [1]. Another common framework for evaluation of HIT was also considered, developed by Harrison et al., exploring how technology affects and is affected by its social and operational environment [2].

Q-methodology [3, 4] was chosen for the evaluation given its ability to solicit a diversity of opinions among multiple users to reflect the multiple applications of the Tricorder device as it developed [5]. For a full description of the application of Q-methodology, please refer to the civilian report and the journal article [6] in appendix.

While the DE threat has been known for some time [7-23], the emerging nature of the threat to members of DOD necessitated a series of focus groups with members of the Air Force Air Combat Command, Air Medical Command, and Special Operations Command. The focused discussion of DE threats produced over 20 pages of notes during two focus groups, which were analyzed to build the draft research instrument for the Q study. The individual statements and observations were first collated by theme. These observations and focus group statements were augmented with information collected from literature. Statements with similar themes were merged; a consistent picture of themes emerged with two different areas: 1) the technical features of the Tricorder, and 2) the operational aspects of the Tricorder. Two different Q-sorts were created--operations and equipment--each with 34 statements. Conditions of Instruction were developed.

The Condition of Instruction for the equipment Q-sort was:

> *Which issues would be Most Important or Most Unimportant to you concerning devices or equipment issued to you for detection of lasers (DE)?*

The Condition of Instruction for the deployment/operations Q-sort was:

> *Which issues would be Most Important or Most Unimportant to you when you are operating in an environment having a known or anticipated high probability of directed energy activity?*

A third Q-sort was created with a separate Condition of Instruction about operational planning; however, during the contract period, the operational planning Q-sort was never performed due to the lack of research subject availability.

b) *Validating the Research Instrument*

In research, triangulation is one mechanism used to validate research instruments. This study completed triangulation through 1) seeking confirmation of concepts obtained from focus groups in the literature; 2) seeking out subject matter experts for additional insight; and 3) piloting the instrument with a sample of potential research participants and followed by a cognitive interview. Circumstances beyond the researchers' control prohibited the use of potential research participants; however, subject matter experts were identified who did assist in validating the draft instrument. Some statements from end users could not be validated by external sources (ruggedization for example, which is important to some end users). Such statements would not be in published reports, unless the report was about the failure of equipment in battle.

What follows are the instances of publicly available information on DE (with reference to the statements within the Q) that were used to validate the Q statements. Note: Condition 1 refers to Operational Planning; Condition 2 to Deployment/operations; and Condition 3 to Equipment.

- **Medical Encounter Forms.** After reviewing the presentations for the Heritage Foundation conference(25) on Directed Energy at ://www.heritage.org/Press/Events/ev021306a.cfm, one presentation mentioned the Air Force procedure regarding incidence reporting of Directed Energy exposure. Upon exposure to DE, an incident report is created and filed, similar to the FAA policy. While most of these reports are likely classified, Q-sort opinion statements reflect the DE environment based on these conference presentations.
    - **Validation of Condition/Statement:** Operations: Statements 2,5,7,32,34; Equipment: Statement 11

- **Laser Blinder.** Another interesting unclassified report came from Janes.com, "Chinese Laser 'Blinder' Weapon for Export" at (://www.janes.com/articles/Janes-Defence-Weekly-95/CHINESE-LASER-BLINDER-WEAPON-FOR-EXPORT.html). In 1995, several different arms shows demonstrated the ZM-87, which was specifically designed to blind the adversary. Subsequent outrage and international treaties now prevent devices specifically designed to blind soldiers.
    - **Validation of Condition/Statement:** Operations: Statements 2, 5, 7, 8, 11, 13, 23, 24, 26, 28, 32, 33, 34; Equipment: Statements 7, 9, 10, 11, 14, 17, 29
- **Effect of Directed Energy on Pilot Approaches: FAA Study** at (://www.faa.gov/library/reports/medical/oamtechreports/2000s/media/0409.pdf. [11] This study of directed energy on airplane landing approaches and pilot reaction had application to the Q-sort. The laser energy was low enough to cause no damage to the pilots in the simulators; however, at the level of 50 uW/cm^2, 26% of the landings were aborted. This demonstrates how directed energy, while not contributing to injury, does distract concentration in complex tasks. Another article [7] talking about its effect on pilots is "Aussie laser-pointer dazzle attacks on airliners: Bad" at ://www.theregister.co.uk/2008/04/03/australian_airliner_laser_attacks/.
    - **Validation of Condition/Statement:** This concern is reflected in Operations: Statements 7, 12, 11, 22, 23; Equipment: Statements, 5, 6, 7, 16
- **Economist Article** at ://www.economist.com/science/displaystory.cfm?story_id=12502799) [12]. Zeus is designed to disarm IED from a safe distance. While this article discusses the purposes of Zeus, it also mentions the Laser Area Defense System (LADS), providing protection from incoming shells and small rockets, and the Airborne Laser (ABL) that, when mounted on a 747, is designed to intercept large ballistic missiles. From the general descriptions of the DE items, both deployed and to be deployed, the focus group concerns were confirmed.
    - **Validation of Condition/Statement:** Operations: Statements 3,5,10,11,13,15, 21, 22, 32, 33, and 34; Equipment: Statements 7, 10, 13
- **Directed Energy Weapons on the Battlefield: A New Vision for 2025**, authored by John P. Geis II, Lieutenant Colonel, USAF [24]. The report claims that currently no pulsed weapon has been deployed in the battlefield. This paper was written in 2003, so the environment may have changed. Though not specifically validating any one comment in the Q-sort, the calculations and the future vision of the threats and opportunities do raise the stakes in the race for portable detection of Directed Energy.
- **B.E. Meyes GLARE GBD3C or GLARE MOUT** at ://www.bemeyers.com/index.php?option=com_product&catid=1&id=11 [25]. A product on the market that is designed as a long-range visual deterrent laser device and a primary non-lethal laser dazzler. While laser dazzlers are intended to warn or hail without causing damage, the specifications of the devices helped validate some of the statements.
    - **Validation of Condition/Statement**: Operations: Statements 7, 8, 9, 10, 21; Equipment: Statements, 7, 9, 10, 11, 13, 14, and 32
- **Unconfirmed Eye Damage** at ://www.forecastinternational.com/archive/eo/eo12338.htm [8]. This is the original citation referred to by a number of other studies. The threat of eye damage caused by lasers was spotlighted in April 1997 when a US Navy intelligence officer sustained a

retinal injury consistent with exposure to an Nd-YAG laser. The suspected source was the nearby Russian freighter *Kapitan Man*, but evidence was inconclusive.

- **Validation of Condition/Statement:** Operations: Statements, 7, 8, 9, 11; Equipment: Statements 10, 11, 14

c) *Implementing the Research*

A list of existing Q method software and hardware requirements was sent to the Air Force to begin the discussion about hosting the online Q-sort. The research instrument was loaded into Flash Q—software for online Q-sorting. The Flash Q software was beta tested. All visible coding errors were corrected. Due to circumstances outside the scope of contract, triangulation and validation of the research instrument with Air Force Personnel themselves proved infeasible. Permission to engage non-air force personnel was received and the necessary paper work filed.

The researchers approached the FBI as a surrogate users group, with no success. Following unsuccessful research subject recruitment within the FBI, surrogate users (pilots, paramedics, police officers, and first responders) were identified with whom to conduct the study. A draft IRB application was created for submission, describing a different source for research subjects. Revisions to the Q-sort were made, making it relevant to homeland security personnel. The UIC Internal Review Board (IRB) exemption was granted. Emails were sent out to pilots, paramedics, police officers, and first responders. After repeated outreach, a dozen responses were obtained from among the pilot study participants.

Following the Q-methodology study with civilians, outreach to the Air Force recommenced. A proposed amendment to the IRB to permit face-to-face Q-sorts was delayed in submission until the physical location of the next Q-sort was determined. Following significant numbers of meetings and approvals, the 183rd Air National Guard Unit in Springfield, Illinois, agreed to the researchers conducting a study at that location. Appropriate research permissions were required from both UIC and the Air Force. A new UIC IRB was submitted that reflected the change in research protocol. Permission was requested of the Air Force and granted, and the research was assigned Air Force Survey Control Number USAF SCN DAFSG10-073. The new pre-test, post-test protocol was to administer the operations and equipment Q-sorts prior to a briefing about the equipment, brief the research subjects about the Tricorder equipment, and then administer the same Q-sort about the equipment to the subjects.

Traditionally, Q-sorts are done manually face-to-face, with statements on small slips of paper, using a paper grid. With the understanding that future studies may have required hosting Q-sorts on computers face-to-face, we reviewed the Dell Mini 10 Netbook computer as an option. The screen resolution was too small to conduct the Q-sort. Laptops, owned by the department or rented by the department, remained the digital method available to conduct face-to-face computerized Q-sorts. The Flash-Q software was refined. Ultimately, laptops were rented to support Q data collection at the 183rd National Guard Unit in Springfield, Illinois. Paper versions of the Q-sort were prepared as backup if problems arose with the computer contract, software, or other technical difficulties. The Q software was modified in accordance with the revised research protocol that had been approved by UICs IRB.

Additional contacts with the Air Force about new user groups were planned as follow-up to leads from the Scientific Review, AMIA conference, and meetings with Richard Preston of SSI, a member of the research team. Dr. Preston provided Point of Contact information for Moody AFB. The IRB amendment process now reflected this change in protocol. A new Survey Control Number (SCN) was requested from the Air Force for the modified protocol as the previous SCN had expired, and some language had changed due to the delivery method of the proposed protocol. As the research subjects now to be recruited would already have exposure to the device, the pre- and post-design was no longer appropriate. The individuals would only complete the operations Q-sort and equipment Q-sort, and they would do it using traditional manual methods.

The support letter from the contracting officials was received, and the IRB approved protocol was submitted for amendment. The IRB approved the new site for the Q-study, a modified cover sheet was created, and the Q-sort was mailed to the individuals associated with Moody Air Force Base Rescue Squadron.

4. Results and Discussions

a) *Civilian Study*

A total of 12 respondents completed the Q-sort for the equipment and 9 respondents completed the Q-sort for operations. The self-reported job titles (more than one title was allowed) for the 12 respondents were: police officers (3), pilots (6), first responders (3), paramedics (2), and unknown (1). Eight subjects had military experience. Three confirmed, four denied, and five did not know their DE exposure status. The data were loaded in PQMethod 2.11 [26].

Factor analysis revealed four “stories” from the equipment responses and three stories from the operations responses. All of the stories were statistically significant. For an overview of the factors, see Figure 1. The nine respondents for the operations Q-sort factored into three groups: 1. *I View my Job within a Context of a Mission;* 2. *I Want to be Safe; and* 3. *Where is the DE Coming From?* (See appendix for more details about the individual factors.)

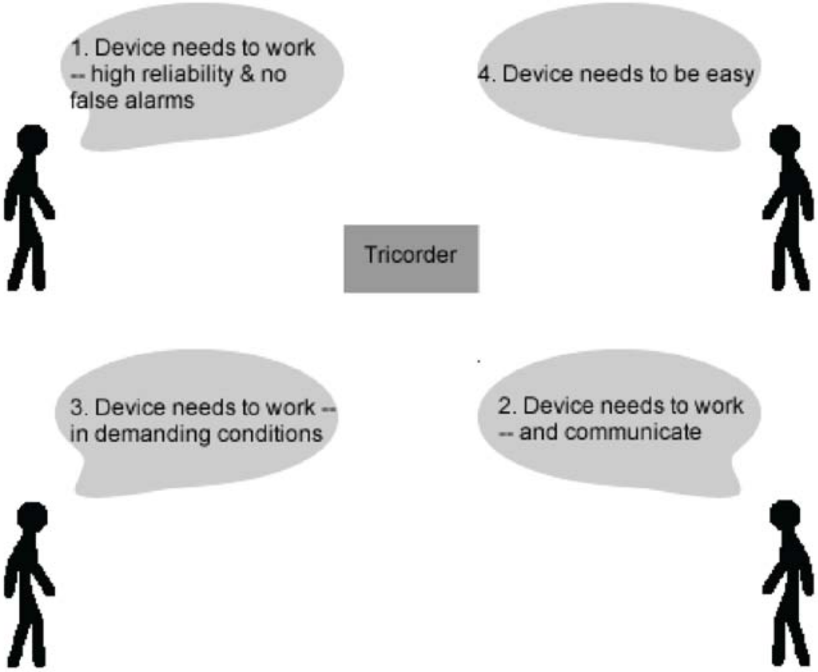

Figure 1. Factors that emerged from the equipment Q-sort in the civilian population.

The significant finding, through detailed analysis of individual responses of both the equipment and the operations Q-sorts for the civilian population, was that individuals, although having similar opinions about what features they desired, had differing opinions on the intended use of the device. When deploying devices, the multiple combinations of features on uses makes training more challenging.

b) *Air National Guard Study*

The Q-sort data were clustered using the software program PQMethod 2.11. Three factors (opinion groups) were uncovered for the operations Q-sort, equipment Q-sort pre-briefing, and equipment Q-sort post-briefing. The individuals did not align based on job title. In the two equipment Q-sorts (pre- and post-), a negative factor was uncovered. Individuals who align negatively hold the complete opposite opinion of those who align positively. Upon additional analysis, correlation between all of the equipment factors was minimal. Additional factors emerged from the data; however, only single individuals aligned to each of them. Future research is warranted to explore if others agree with these opinion groups.

i. <u>Pre-Briefing</u>

From Figure 2, three factors were revealed from the 29 individuals who responded to the Q-sort. Twenty-three individuals loaded onto three factors. One factor was bipolar, meaning one person believed the exact opposite of the other individuals. The factors were: Ease of Use, High Reliability and High sensitivity, Tactical Efficiency, Where am I & Do Others Know, and Special Ops Perspective.

Figure 2. Air National Guard Equipment Pre-Briefing Factors. The number is the number of individuals who loaded onto the factor.

ii. <u>Post-Briefing</u>

In the post-briefing Q-sorts (Figure 3), three factors were revealed, with one bipolar factor. The factors were: Medical Care & Alert, Tactical Efficiency, Works in Hostile Environment, and Alert & Fix. Tactical Efficiency was essentially the equivalent response pre- and post-Tricorder briefing in that the briefing demonstrating the desired features did not modify opinions post-briefing. The other factors, Medical Care & Alert, Works in Hostile Environment, and Alert & Fix, appeared modified by the briefing, as the post-briefing opinions of the respondents were different than the pre-briefing opinions.

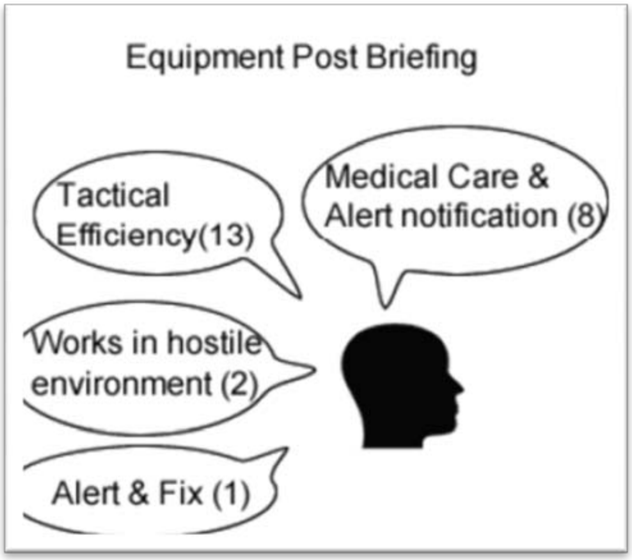

Figure 3. Air National Guard Equipment Post-Briefing Factors. The number is the number of individuals who loaded onto the factor.

Of the 27 individuals who answered both the pre- and post-equipment surveys, seven individuals retained their opinions following presentation of the Tricorder device under development. Of the 27 individuals who responded to both the pre- and post-briefing, 13 individuals remained on similar factors (Medical Care & Alert Notification was similar to Ease of Use, High Reliability and High sensitivity, although not identical). Of the seven individuals who did not change their minds, three of them were medics. Otherwise, neither job title nor exposure to directed energy revealed any information as to why the individuals loaded on any one factor.

c) *Rescue Squadron Field Study*

A total of four responses were received from the individuals who spent three months with the Tricorder. A preliminary analysis was performed with the four responses, and the research subjects at Moody Air Force base were invited to provide additional feedback to the research team. Drs. Boyd and Valenta and Melissa Naiman traveled to Moody Air Force Base for a follow up debriefing of Tricorder Q-results with those who had completed the Q-sort. The data had been submitted anonymously; thus, neither the researchers nor the research subjects could tell who said what. Multiple perspectives had been found, and the research team wanted to explore reasons as to why Q-sorters would respond in the manner identified through correlation and factor analysis of the data. The meeting resulted in the clarification of a number of statements in the research instrument.

- The end users specifically requested the Tricorder limit the amount of incoming sensor information to just minimum levels needed for decision-making and let the rest to be recorded for later.
- They were interested in its detecting safety issues like: irritant present (and what do I do about it), protective equipment works, dangerous exposure levels. They feel undertrained about the issue of directed energy.
- They were concerned about its sensing the direction from which the threats were coming.

- They envisioned the display to summarize the data for potential to be hurt and time to damage. Exploring this further, the concept of am I hurt was expressed NOT as a selfish concern, but they wanted to know if they could continue to perform their job.
- Having too bright a display could affect their ability to view with the night vision goggles.
- They want something comfortable to wear or to mount on the exterior of the plane.

d) *Air National Guard and Rescue Squadron Field Combined Data*

Further insight was sought through a process in Q that allows the combination of data over a series of Q-sorts. Combining data in this fashion increases the number of individuals who might load on each factor, reducing the potential for misleading results from having too few individuals in the study data.

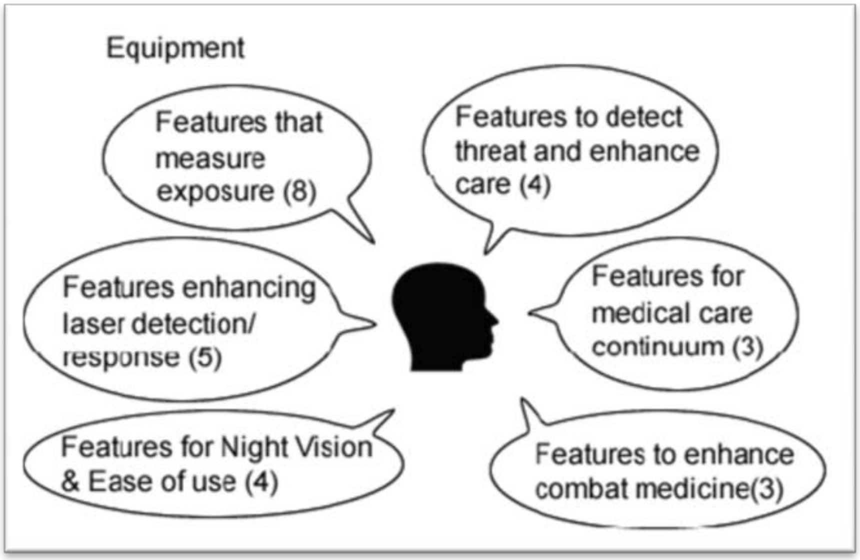

Figure 4. Equipment Q-sort Factors from the Combined Q-sorts of Air National Guard and Rescue Squadron. The number is the number of respondents who load on each factor.

When the equipment Q-sorts from the post-briefing of the Air National Guard were combined with those of the Rescue Squadron Field Study, six factors emerged (see Figure 4):

(1) Features that measure exposure;
(2) Features to detect threat and enhance care;
(3) Features enhancing laser detection/response;
(4) Features for night vision & ease of use;*
(5) Features for medical care continuum; and
(6) Features to enhance combat medicine.

In the combined factor analysis, all four responses from the Rescue Squadron loaded onto factors for both the operations and equipment factors. The asterisk* symbolizes the two factors on which the Rescue Squadron individuals loaded. (See appendix for presentation to TSRL for additional details.)

Due to the wide-ranging nature of the use of the Tricorder, a variety of different feature sets resulted. Some future design challenges relate to the expressed desire to measure the total amount of exposure. This is unique compared to the current prototype Tricorder display, which only shows the instant exposure levels and cannot currently handle the possibility of a number of different wavelengths. The highest ranking feature was "Detect in all directions." Currently, the device only detects a span of 120 degrees; given that the Tricorder's original focus was on eye protection. Users state they do not want to physically turn around to detect laser activity nearby.

Comparison to the Civilian population revealed little overlap in features requested, having a correlation of .64 between the different factors.

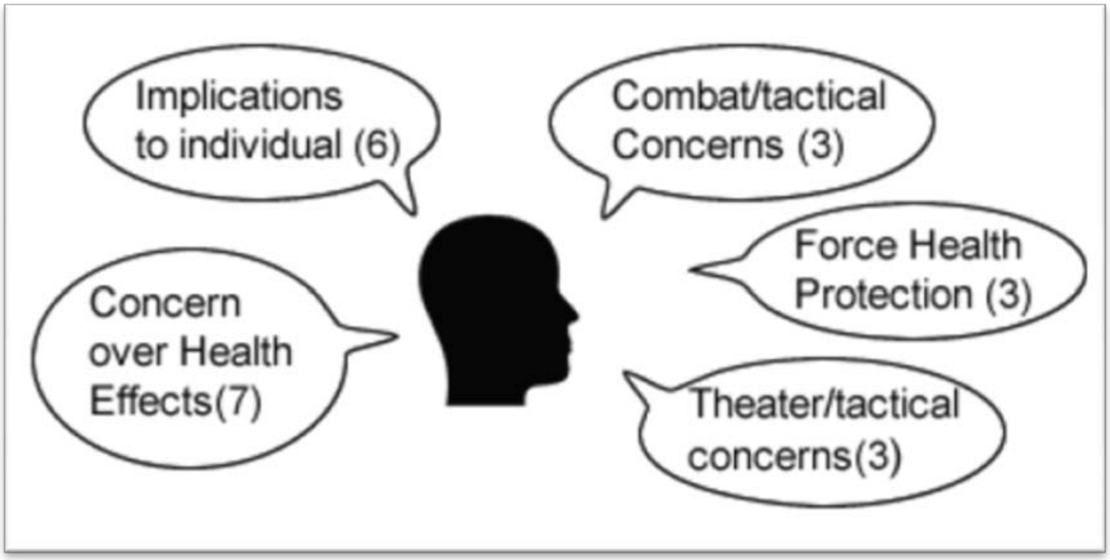

Figure 5. Operations Q-sort Factors from the Combined Q-sorts of Air National Guard and Rescue Squadron. The number is the number of respondents who load on each factor.

When a total of 29 responses to the operations Q-sort were merged between the Air National Guard and the Rescue Squadron, five factors were revealed (see Figure 5). Twenty-two individuals aligned on the five factors. All four individuals from the Rescue Squadron aligned on two of the factors. This suggests that the way these two groups would use this Tricorder data is completely different, based on their differing points of view. The operational concerns reveal a very complex picture (see TSRL presentation in appendix for more details and Table 1). As an example of this complexity, ”whether I can finish the mission” is rated Most Important in only one factor, not all five factors. During the Moody AFB debriefing, the concept of finishing the mission was not deemed important “since you *know* it will be finished.” This unwritten understood goal by all military personnel of the importance of finishing the mission could confound interpretation of this statement. Similarly, some factors were more concerned about whether or not they were hurt. In debriefing, the concern raised was whether they could finish their task, not whether they were hurt. This provides further evidence of the benefit of focus group follow-up to explore intent. The wide-ranging selection of statements about the operational use of this technology suggests the need for a more refined operational description for the purposes of training and evaluation.

Table 1. Most Important Individual Statements Across Factors. On a scale from +3 to -3, where +3 is Most Important.

	Concern for health	Combat/ tactical Concerns	Force health protection	Theater/ tactical concerns	Implication to individual
Whether I am exposed or not	2	3	2	1	1
Whether I am hurt or not	1	3	2	3	3
Whether I am protected or not	1	2	0	3	3
Whether my co-worker's position was revealed	-1	0	3	0	-1
I have exceeded my MPE (maximum permissible exposure)	3	-1	3	3	-1
Health effects of short intense exposure	3	-1	-1	0	0
Whether I can finish the mission	0	3	1	0	1
Whether I still have sufficient information to react	0	0	-3	-2	3
Confidence in PPE (personal protective equipment)	2	0	3	0	2
Time until permanent damage	3	-1	1	1	1

5. Conclusions

The sociotechnical evaluation study produced a research instrument that can be used within the Air Force to continue its exploration and development of Tricorder equipment. The social and organizational issues surrounding the Tricorder are complex and multifold. Through the collaboration among UIC researchers and subject matter experts from Sensing Strategies and the Air Force, the diverse needs and possible uses of the Tricorder have been explored in depth. While the original goal was to build one device with simple functionalities, some of the features of interest to the research participants (e.g., “Viewable with Night Vision Goggles”) are critical aspects for some, but not all, individuals. Figure 6 lists the features that are desired across users groups. Figure 7 lists the features that are controversial, and the Air Force will need to decide in which direction to take future research spirals. Figure 8 lists the features that are not desired by this study’s research participants, when compared against all other options. These features, however, *were* introduced by members of the initial focus groups when talking about the device development and the Air Force may find some personnel who do desire these features in future iterations of the Tricorder.

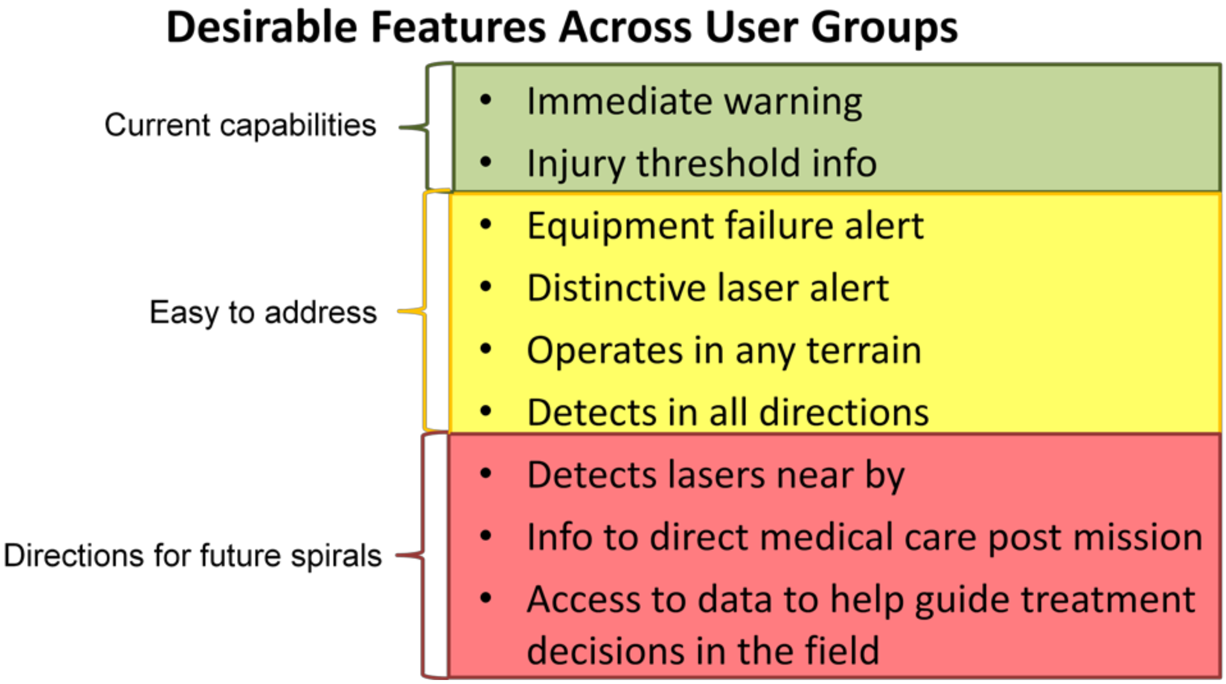

Figure 6. Desirable features across user groups.

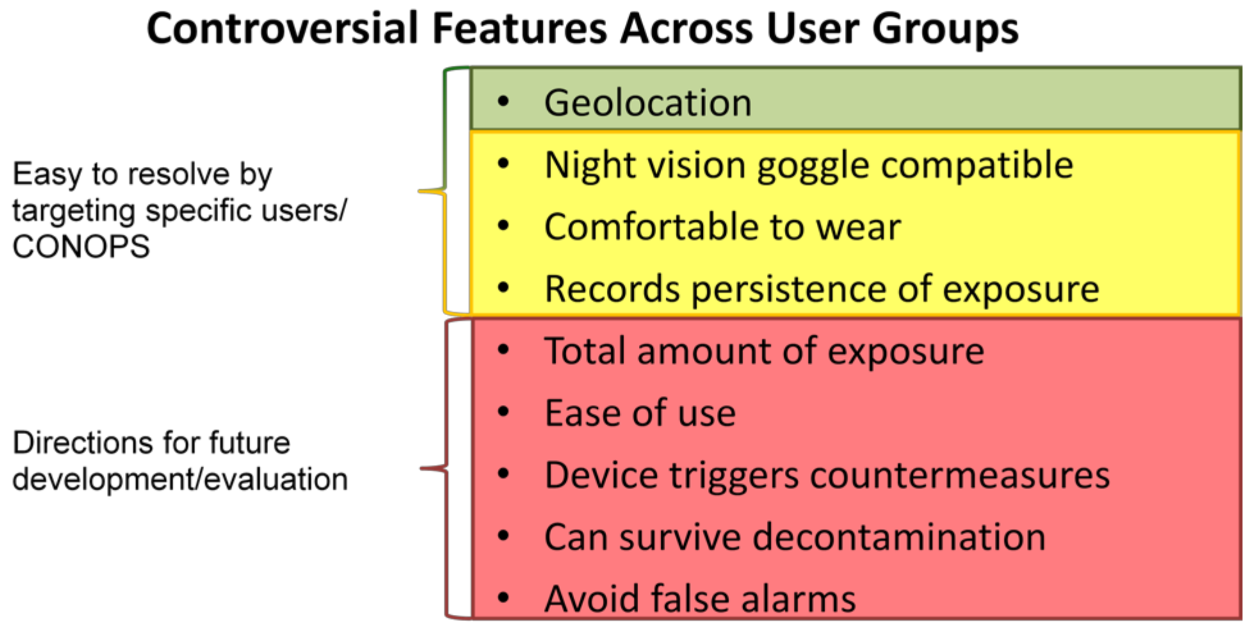

Controversial Features Across User Groups

Easy to resolve by targeting specific users/ CONOPS

- Geolocation
- Night vision goggle compatible
- Comfortable to wear
- Records persistence of exposure

Directions for future development/evaluation

- Total amount of exposure
- Ease of use
- Device triggers countermeasures
- Can survive decontamination
- Avoid false alarms

Figure 7. Controversial features across user groups.

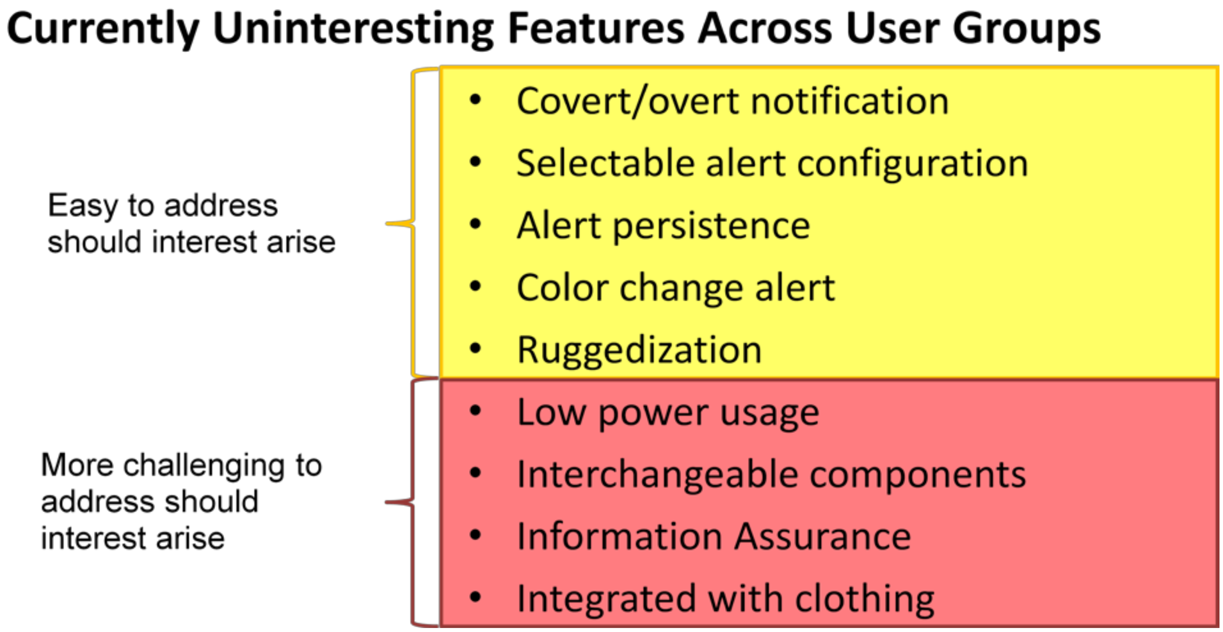

Currently Uninteresting Features Across User Groups

Easy to address should interest arise

- Covert/overt notification
- Selectable alert configuration
- Alert persistence
- Color change alert
- Ruggedization

More challenging to address should interest arise

- Low power usage
- Interchangeable components
- Information Assurance
- Integrated with clothing

Figure 8. Currently uninteresting features across all user groups

Based on feedback from the research subjects at Moody Air Force base, in future research projects, the following statements should be refined to improve the equipment Q-sort instrument. The subjects did not understand Information Assurance (statement 23), and Can perform multiple TOE functions (statement 30). Rather than Geolocation (statement 31), the participants preferred Range and Bearing for Source of DE.

Within the operations Q-sort, the statements identified as needing clarification were Whether I have reach-back (statement 20) and Whether I still have sufficient information to react (statement 19). The research subjects did not appreciate the statement, Whether my co-worker's position was revealed (statement 6), as they are normally in a plane.

A significant development direction emerged through the Q-sort factors of the combined Air National Guard and Rescue Squadron data. For statement 29, Access data to help make treatment in the field, four out of the six factors had this statement ranked as +2 or +3. This means users are stating clinical decision support in the field is a very important feature for the Tricorder. Decision support was not a subject of study for this Aspect. The medical engineering and radiation safety knowledge necessary to provide this level of decision support should be considered as a future research direction; it is outside the current specifications for the Tricorder. The Laser Injury Guidebook could be a source of important development guidelines that would need to be synthesized for future Tricorder functionalities [27].

During the presentation to TSRL, a number of questions arose about the current training of the end users regarding DE threats and appropriate protocols. The AF laser exposure protocol was shared with the researchers. The concern it expresses seems to be more about decreasing the anxiety of the individuals who are exposed than preparing for the event of future threat. Reconciling this difference (individual concern versus large-scale preparation) in future Tricorders will be challenging, since the sensor as currently developed will never be directly over the eye (individual concern) and the full intensity of the DE exposure will only be an approximate value.

From the diversity of operational uses of the data, careful deployment of the technology and appropriate operational expectation management will be needed to ensure success. Without this, the diversity could lead to unintended device failure or work-arounds, since it would be challenging to meet all of the operators' concerns in a first generation device.

6. References

1. Avison, D.E. and A.T. Wood-Harper, *Multiview : an exploration in information systems development*: Blackwell Scientific Publications.
2. Harrison, M.I., R. Koppel, and S. Bar-Lev, *Unintended consequences of information technologies in health care--an interactive sociotechnical analysis.* Journal of the American Medical Informatics Association : JAMIA, 2007. **14**(5): p. 542.
3. Barbosa, J.C., et al., *Statistical methodology: VII. Q-methodology, a structural analytic approach to medical subjectivity.* Academic emergency medicine : official journal of the Society for Academic Emergency Medicine, 1998. **5**(10): p. 1032.
4. Brown, S.R., *Political subjectivity: Applications of Q methodology in political science.* 1980: Yale University Press New Haven CT.
5. Colvard, M.D., et al., *Handheld directed energy sensor for environmental monitoring and clinician safety.* Aviation, Space, and Environmental Medicine. **81**(6): p. 602.
6. Boyd, A.D., et al., *Portable Devices to Detect Directed Energy: User Perceptions of Personal Risk and Protective Devices.* International Journal of Computational Models and Algorithms in Medicine, 2010: p. 1.
7. *Aussie laser-pointer dazzle attacks on airliners: Bad.* 2008 [cited 2008 September 30]; Available from: ://www.theregister.co.uk/2008/04/03/australian_airliner_laser_attacks/

8. *Eye damage to naval intelligence officer*. 2008 [cited 2008 September 30]; Available from: ://www.forecastinternational.com/archive/eo/eo12338.htm
9. Abrams, J. *Lasers aimed at planes targeted*. March 01 2011 [cited 2011 May 20]; 1]. Available from: ://voices.washingtonpost.com/dr-gridlock/2011/03/congress_targets_laser_abuse.html
10. Bunker, R.J. and D. Lindsay. *Recognizing Laser Threats*. 2008 Aprill 2008 [cited 2010 April 5]; Available from: ://www.fbi.gov/filelink.html?file=/publications/leb/2008/april08leb.pdf
11. Department of Homeland, S. *Daily Open Source Infrastructure Report for 30 March 2010*. 2010 [cited 2010 April 5]; Available from: ://www.dhs.gov/xlibrary/assets/DHS_Daily_Report_2010-03-30.pdf
12. Economist. *Zeus*. 2008 [cited 2008 September 30]; Available from: ://www.economist.com/science/displaystory.cfm?story_id=12502799
13. Hambling, D. *Soldiers Blinded, Hospitalized by Laser 'Friendly Fire'*. 2009 March 30 2009 [cited 2010 April 5 2010]; Available from: ://www.wired.com/dangerroom/2009/03/dont-lase-me-br/
14. Janes.com. *Chinese Laser 'Blinder' Weapon for Export*. 2008 [cited September 30 2008]; Available from: ://www.janes.com/articles/Janes-Defence-Weekly-95/CHINESE-LASER-BLINDER-WEAPON-FOR-EXPORT.html)
15. Johnson, D.A. *Laser Threats to Law Enforcement*. 1999 May 1 1999 [cited 2010 April 5 2010]; Available from: ://www.fbi.gov/publications/leb/1999/may99leb.pdf
16. Mainster, M.A., B.E. Stuck, and J. Brown, Jr., *Assessment of alleged retinal laser injuries.* Archives of Ophthalmology, 2004. **122**(8): p. 1210.
17. Mellerio, J., et al., *Battlefield laser weapons: an assessment of systems, hazards, injuries and ophthalmic resources required for treatment.* Lasers Light Ophthalmol, 1991. **4**: p. 41.
18. Nakagawara, V.B., et al., *The Effects of Laser Illumination on Operational and Visual Performance of Pilots During Final Approach*. 2004, Office of Aerospace Medicine: Washington, DC 20591.
19. Nakagawara, V.B., R.W. Montgomery, and K.J. Wood, *Aircraft accidents and incidents associated with visual effects from bright light exposures during low-light flight operations.* Optometry - Journal of the American Optometric Association, 2007. **78**(8): p. 415.
20. Nakagawara, V.B., K.J. Wood, and R.W. Montgomery, *Laser exposure incidents: pilot ocular health and aviation safety issues.* Optometry (St.Louis, Mo.), 2008. **79**(9): p. 518.
21. Thames Valley, P. *Five arrests following laser incidents - Reading*. 2009 Thursday 22 October 2009 [cited 2010 April 6]; Available from: ://www.thamesvalley.police.uk/newsevents/newsevents-pressreleases/newsevents-pressreleases-item.htm?id=105926
22. Tkachenko, M. *Russian airliners targeted by 'laser hooligans'*. July 5, 2011 [cited 2011 July 5]; Available from: ://www.cnn.com/2011/WORLD/europe/07/05/russia.laser.jetliners/index.html?hpt=hp_bn2
23. Wyrsch, S., P.B. Baenninger, and M.K. Schmid, *Retinal injuries from a handheld laser pointer.* The New England journal of medicine. **363**(11): p. 1089.

24. Geis Ii, J.P., *Directed Energy Weapons on the Battlefield: a New Vision for 2025*. Occasional Paper No. 32, 2003.
25. Meyes, B.E. *Non-blinding laser*. 2008 [cited 2008 September 30]; Available from: ://www.bemeyers.com/index.php?option=com_product&catid=1&id=11
26. Schmolck, P. *PQ Method 2.11*. 2002 July 7 2009 [cited 2009; Available from: ://www.lrz-muenchen.de/~schmolck/qmethod/downpqx.htm
27. Clark, P., et al., *United States Air Force School of Aerospace Medicine Laser Injury Guidebook*. 2008, Springfield, VA: NTIS.

I. List of Symbols, Abbreviations, and Acronyms

2D WB:	Two dimensional Western blot
ACGIH:	American Conference of Governmental Industrial Hygienists
AgFON:	Silver film over nanospheres
ALDC:	Fructose bisphosphate aldolase C
AP :	Atmospheric Pressure
ATOF-MS:	Ablation Time-of Flight Mass Spectrometry
AuNP:	Gold Nanoparticle
BHQ2:	Black hole quencher II
BSA:	Bovine Serum Albumin
CB:	Carbenicillin
Cd:	Cadmium
CI:	Confidence interval
Clu:	Clusterin
CMOS:	Complementary-Symmetry Metal–Oxide–Semiconductor
CNGA3:	Cyclic nucleotide gated channel alpha 3
CNGB3:	Cyclic nucleotide gated channel beta 3
CoT:	Cursor-on-Target
CSV:	Comma Separated Value
D:	Day
Da:	Dalton
DB:	Dutch belted
DE:	Directed Energy
DI:	Desorption ionization
DLC:	Diamond-Like Carbon
DNA:	Deoxyribonucleic Acid
DRP2:	Dihydropyrimidinase related protein 2
EC50:	Effective concentration at half the maximum
ECD:	Electrochemical Detection
ECL:	Electrochemiluminescence
EDC:	1-ethyl-3-[3-dimethylaminopropyl] carbodiimide hydrochloride (or EDAC)
EDTA:	Ethylenediaminetetraacetic acid

ELISA:	Enzyme-linked Immunosorbent Assay
FITC:	Fluorescein Isothisocyanate
FNCs:	Film Nanocomposites
FOV:	Field Of View
FP:	Fluorescence Polarization
FRET:	Fluorescence Resonant Energy Transfer
G test:	log likelihood ratio test for goodness of fit
GII:	Grade Two
GIII:	Grade Three
H&E:	Hematoxylin and eosin
Hg:	Mercury
HPLC:	High performance liquid chromatography
Hr:	Hour
HRP:	Horseradish peroxidase
HRP:	Horse Radish Peroxidase
IDT:	Integrated DNA Technologies
IgG:	Immunoglobulin G Antibody
J/cm^2:	Joules/square centimeter
Kan:	Kanamycin
LC-MS/MS:	Liquid chromatography/tandem mass spectrometry
LED:	Light Emitting Diode
LEP :	Laser Eye Protection
LIBS:	Laser-Induced Breakdown spectroscopy
LNCs:	Liquid Nanocomposites
MBP:	Maltose Binding Protein
MPE:	Maximum Permissible Exposure
MS:	Mass Spectrometry
MVL:	Minimally Visible Lesion
MW:	Molecular Weight
MWCO:	Molecular Weight Cut Off
NA:	Neutravidin
NC:	Nanocrystals
ND:YAG:	Neodimium Doped Yttrium Aluminum Garnet

NEOMED:	Northeastern Ohio Medical Universities
NLA:	Nonlinear Absorption
NLO:	Nonlinear Optical
NLS:	Nonlinear Scattering
NP:	Nanoparticles
NPM:	N-(1-pyrenyl) maleimide
NPS:	Naval Postgraduate School
OSHA:	Occupational Safety and Health Administration
Pb:	Lead
PBS:	Phosphate Buffered Saline
PCR:	Polymerase Chain Reaction
PDE6:	cGMP-specific 3',5'-cyclic phosphodiesterases
PKM2:	Pyruvate kinase isozymes M1/M2
PPS:	Personnel Protection Sensor
PVDF :	Polyvinylidene Difluoride
PWV:	Peak Wavelength
QD:	Quantum Dot
RPE:	Retinal Pigment Epithelium
RR:	Rate Ratio
RSA:	Reverse Saturable Absorption
SA:	Streptavidin
scFv:	Single chain Fragment of Variation
SDS-PAGE:	Sodium Dodecyl Sulfate Polyacrylamide Gel Electrophoresis
SERS:	Surface Enhanced Raman Spectroscopy
SOFLAM:	Special Operations Forces Laser Aided Marker
SPR:	Surface Plasmon Resonance
TBA:	Thrombin Binding Aptamer
TBS-T:	Tris buffer saline-tween
TCEP:	Tris(2carboxyethyl)phosphine
TCP-1-zeta:	T-complex protein 1 subunit zeta
TE:	Tris-EDTA
TEM:	Transmission Electron Microscope
TiOPc:	Titanyl Phthalocyanine

TMB:	3,3',5,5'-Tetramethylbenzidine
TOF:	Time-of Flight
TPA:	Two-Photon Absorption
TTR:	Thansthyretin
UIC:	University of Illinois at Chicago
VH:	Variable heavy chain
VL:	Variable light chain
WHO:	World Health Organization
Zn:	Zinc